UNIVERSITÀ DEGLI STUDI DI GENOVA

DIPARTIMENTO DI SCIENZE DELLA TERRA, DELL'AMBIENTE E DELLA VITA

SCUOLA DI SCIENZE E TECNOLOGIE PER L'AMBIENTE E IL TERRITORIO

DOTTORATO DI RICERCA IN BIOLOGIA APPLICATA ALL'AGRICOLTURA

E ALL'AMBIENTE

XXXV CICLO

S.D. BIO/11

EVALUATION OF THE CYTOTOXIC, GENOTOXIC AND INFLAMMATORY EFFECTS INDUCED BY THE EXPOSURE TO MINERAL FIBRES IN *IN VITRO* HUMAN CELLULAR MODELS

CANDIDATO:

SERENA MIRATA

RELATORE:

PROF. SONIA SCARFÌ (UNIVERSITÀ DI GENOVA)

Exposure to mineral fibres represents a serious occupational and environmental hazard, since it leads to chronic lung inflammation with the subsequent development of pneumoconiosis, fibrotic pulmonary diseases, lung cancer and malignant mesothelioma. However, since the toxicity and carcinogenicity of mineral fibres is profoundly interwoven with a broad variety of crystal-chemical-physical characteristics, the biogeochemical mechanisms through which mineral fibres, and especially asbestos, induce adverse effects in vivo *are yet to be completely understood.*

The first part of this study aimed at investigating the different possible toxicity mechanisms of UICC standard crocidolite, chrysotile from Balangero and erionite from Jersey, which are respectively representative of the classes of amphibole asbestos, serpentine asbestos and fibrous erionite. The acute damaging effects exerted by these mineral fibres during the first 24 h of exposure were evaluated by performing a comparative study in an in vitro *THP-1 cellular model of M0, M1 and M2 macrophages. The toxicity mechanisms of the three mineral fibres appeared to differ significantly. Crocidolite seemed to exert its toxic effects mostly as a result of its biodurability, ROS production, cytokine release and DNA damage. Chrysotile, due to its low biodurability, displayed toxic effects correlated with the release of toxic metals and the production of ROS and cytokines. Other mechanisms were involved in explaining the toxicity of biodurable fibrous erionite, which induced lower ROS and toxic metal release, but exhibited a cation exchange capacity able to alter the intracellular homeostasis of important cations. Interestingly, M2 macrophages, which are characteristically known for countering the inflammatory response, in the presence of asbestos fibres and erionite, exacerbated this process by secreting pro-inflammatory mediators.*

For the second part of this project, representative batches of short (length < 5 µm) and long (length > 5 µm) chrysotile fibres were prepared by cryogenic milling of a commercial chrysotile extracted from an open pit mine near Yasny (Russia). To gain new insights into the toxicity mechanisms of these size-separated fractions of chrysotile, their cytotoxic and genotoxic activity was investigated in an in vitro *cellular model based on human THP-1-derived M0 macrophages and HECV endothelial cells, both separately as well as in a co-culture setup. At all time-points, both chrysotile fractions displayed significant acute cytotoxic effects, with results that were comparable to the well-known damaging effects of crocidolite. In particular, the long fraction (> 5 µm) of chrysotile showed a notably higher cytotoxic potential, causing ROS production, DNA damage and the transcriptional upregulation of inflammatory mediators in M0 macrophages. On the other hand, the short fraction of chrysotile displayed a significant degree of cytotoxicity and genotoxicity* in vitro*, which is quite intriguing considering the ongoing debate regarding the potential toxicity of short asbestos fibres (< 5 µm). It should also be noted that in HECV cells the mineral fibres caused toxicity mainly as a result of direct cell membrane damage, whereas in M0 macrophages the apoptotic mechanism had a fundamental role in the induction of cell death.*

1. MINERAL FIBRES

"Mineral fibres" is a generic term encompassing all non-metallic inorganic fibres, defined by the World Health Organization (WHO) as elongated particles characterised by a length ≥ 5 μm, a width ≤ 3 μm and an aspect ratio (i.e., the length-to-width ratio) corresponding to a minimum of 3:1. Whether naturally occurring with a fibrous habit or industrially produced through slight modifications of raw materials, mineral fibres are globally widespread. Moreover, they frequently possess outstanding technological properties that have been commercially exploited for a staggering number of applications throughout human history (Della Ventura et al., 2018).

Among the naturally occurring mineral fibres, amphibole asbestos, serpentine asbestos, and the zeolite erionite are noteworthy because of both their versatile industrial applications and their severe consequences on human health. In fact, the microscopic fibrils constituting these mineral fibres may be released into the environment mainly by abrasion and, once inhaled, their short dimensions allow them to reach the lower respiratory tract inducing several lung diseases over time, such as pneumoconiosis, pleural plaques, pleural effusions, pleural fibrosis, diffuse malignant mesothelioma and lung cancer.

Asbestos is characterised by several unique properties, such as excellent thermal stability and tensile strength; additionally, it is an electrical and thermal insulator, is non-flammable and is resistant to heat, wear, humidity, alkalis, and acids. Therefore, asbestos has been extensively used in various manufacturing industries, especially since it is easily incorporated in various building materials, such as insulators, glue, plaster and concrete. Conversely, most commercial applications of natural zeolites rely on their ability to selectively absorb molecules from air or liquids. Thus, erionite has been employed as a noble-metal-doping catalyst in a hydrocarbon cracking process and has been studied as a potential fertilizer or odour control in livestock production (IARC, 1987; NTP, 2011). However, since these mineral fibres have been deemed carcinogenic to humans by the International Agency for Research on Cancer (IARC), erionite has been substituted by synthetic non-fibrous zeolites, whereas asbestos has been replaced wherever possible by glass fibres or Nomex (Dogan et al., 2008; IARC, 2012).

1.1. ASBESTOS

To date, there is no univocal definition regarding the term "asbestos", since the commercial, mineralogical and regulatory definitions occasionally contradict one another (Lowers and Meeker, 2002; Ross et al., 2008; Case et al., 2011; NIOSH, 2011; Gualtieri et al., 2018a; Militello et al., 2021). In fact, asbestos is a commercial term commonly used to describe six silicate minerals that

crystallize in nature with a characteristic fibrous morphology, which grants them a unique set of properties that have been widely exploited throughout human history. Indeed, in addition to its resistance to fire, heat and wear, asbestos represents an excellent electrical and thermal insulator, simultaneously displaying high tensile strength and flexibility. Because of these outstanding technological properties, asbestos has been used in a variety of commercial products over the years, leading to the manufacturing of more than 3000 asbestos-containing materials (Gualtieri, 2021). In fact, since it binds efficiently to various materials enhancing their strength and durability, asbestos was generally used for roof shingles, floor and ceiling tiles, cement pipes, insulators, and sealants in the construction industry field, as well as for brake linings and gaskets in the automotive industry field. Besides, chrysotile fibres were interwoven to obtain non-flammable fabrics that were employed for safety apparel, fire curtains in theatres and fire stop hangings in public buildings.

Archaeological studies have found evidence of asbestos being used during the Stone Age to strengthen ceramic pots, but the widespread employment of asbestos began in the second half of the 19th century, when the industrial revolution brought on the mechanization of the mining process, expediting the exploitation of amphiboles deposits in South Africa and of chrysotile mines in Canada, Russia, and Europe (Ross and Nolan, 2003). Only at the beginning of the 20th century the first sporadic reports of asbestos disease arose, followed by an ever-increasingly number of scientific studies associating the exposure to asbestos fibres in the working environment with fatal lung diseases. Since then, numerous cohort and case control studies have unequivocally established a correlation between asbestos exposure and occupational lung diseases, resulting in the classification of all six forms of asbestos as carcinogenic to humans (Group 1) by the International Agency for Research on Cancer (IARC, 2012). Thus, the massive use of asbestos in countless industrial applications turned out to be a global problem, since an individual may come into contact with its fibres as a result of (i) direct work-related exposure, which is common among workers in mines, shipyards and manufacturing companies; (ii) bystander exposure, that mainly involves electricians, masons and painters; (iii) environmental exposure, since asbestos was frequently employed for road surfaces, playground material, landfills and chemical paints.

The six naturally occurring silicate minerals recognised as asbestos (i.e., actinolite, amosite, anthophyllite, chrysotile, crocidolite and tremolite) are commonly classified in amphiboles or serpentines depending on the structure of their silicate anion. As the only serpentine form of asbestos, chrysotile is composed of Si_2O_5 subunits arranged in thin sheets of tetrahedra with the apical oxygens linked to hydrated magnesium molecules which are responsible for the high polarity of this mineral. These tetrahedral layers are further organised in concentric cylinders that run parallel to the fibre *c*-axis. In association to its high degree of dissolution, chrysotile easily breaks

into smaller fragments resulting in a short biopersistence of its fibres in the tissues. Conversely, amphiboles consist of Si_4O_{11} subunits assembled in a double chain of tetrahedra joined by corner-sharing of oxygen atoms along the fibre *c*-axis. Since the double chains are stabilised by the coordination with various cations, amphiboles exhibit an extremely wide range of crystal-chemical compositions, in contrast with chrysotile that presents a very limited number of variations from its ideal formula. Moreover, amphiboles display a high biodurability and biopersistence in tissues, due to the silica localised on the external side of their structure which provides strength and durability to their fibres (Whittaker, 1960; Craighead et al., 1980; Bernstein et al., 2005; Gualtieri et al., 2018b).

1.1.1. AMPHIBOLE ASBESTOS

Amphiboles are double-chain inosilicates composed of SiO_4 tetrahedra that are joined by corner-sharing of oxygen atoms, both within the same chain and between the adjacent chains. In each chain, tetrahedra with two bridging and two non-bridging oxygens are alternated with tetrahedra with three bridging and one non-bridging oxygens, forming subunits characterised by a Si(Al):O ratio of 4:11 and a length of approximately 5.3 Å. The double chains are laterally linked to each other due to several cation sites, which are typically classified according to their position in relation to the apices and bases of the tetrahedra. In particular, the small *M*(1), *M*(2) and *M*(3) sites are comprised between the opposed tetrahedral apices, whereas the *M*(4) site is localised between tetrahedral bases of adjacent chains. Moreover, the large *A* site, which lies between the rings formed by opposed tetrahedral bases in the chains, may be vacant, partially filled or fully occupied by Na^+ and/or Ca^{2+} (Leake, 1997).

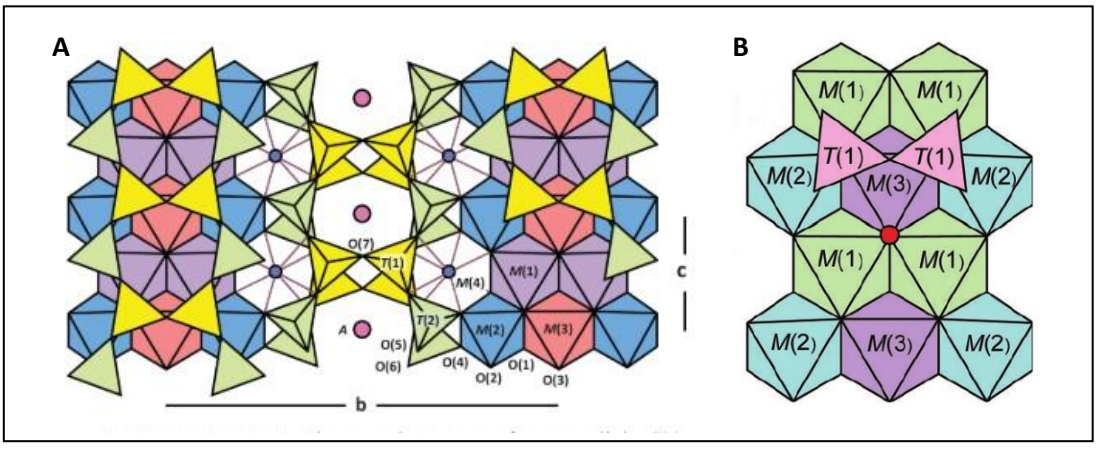

Figure 1. Schematic representation of amphiboles structure. (**A**) Crystal structure of a monoclinic *C*2/*m* amphibole projected onto (100). (**B**) Particular of the environment of the O(3) site in the *C*2/*m* amphibole structure. Images from Hawthorne et al. (2012) and Hawthorne (2016), respectively.

Since the oxygen atoms of the chains are coordinated not only to Si(Al) but also to a variety of other cations, amphiboles can be described with the simplified general formula $A_{0-1}B_2C_5T_8O_{22}W_2$ (Hawthorne et al., 2012; Ballirano et al., 2017), where A = Li^+, Na^+, K^+, Ca^{2+} (irregular cation sites with coordination ranging from 6-fold to 12-fold); B = Li^+, Na^+, Mg^{2+}, Ca^{2+}, Fe^{2+}, Mn^{2+} (less regular octahedral or 8-fold coordinated cation sites, occurring at the *M*(4) crystallographic site in monoclinic amphiboles); C = Mg^{2+}, Al^{3+}, Fe^{2+}, Fe^{3+}, Mn^{2+}, Mn^{3+}, Ti^{3+}, Ti^{4+} (fairly regular octahedral cation sites, corresponding to the *M*(1), *M*(2) and *M*(3) sites); T = Al^{3+}, Si^{4+}, Ti^{4+} (tetrahedral sites of the silicate chain, corresponding to the *T*(1) and *T*(2) crystallographic sites); and W = OH^-, F^-, Cl^-, O_2^- (anions occurring at the O(3) site). As a result of the chemical complexity of the amphibole group, in 1997 Leake revised the nomenclature previously approved by the International Mineralogical Association and presented an updated, more consistent, classification based on the atomic proportions of the major elements located in the various structural sites. Thus, according to the cations occupying the *M*(4) site, amphiboles are characteristically divided into four subgroups, namely the iron-magnesium-manganese amphibole group, the calcic amphibole group, the sodic-calcic amphibole group, and the sodic amphibole group (Leake, 1997).

Amphiboles typically exhibit several identifying features, such as two directions of cleavage intersecting at approximately 56° and 124°, specific gravity values varying from 2.9 to 3.6 and Mohs hardness ranging from 5 to 6. Moreover, their crystallographic habit is generally acicular or prismatic, although several amphiboles may also occur as asbestiform aggregates composed of bundles of thin fibrils displaying an aspect ratio ranging from 20:1 to 100:1, assembled in fibrous particles no wider than approximately 0.5 mm. Indeed, the family of amphibole asbestos includes five species: actinolite asbestos $Ca_2(Mg,Fe)_5Si_8O_{22}(OH)_2$, amosite $(Fe^{2+},Mg)_7Si_8O_{22}(OH)_2$ (the fibrous variety of cummingtonite-grunerite), anthophyllite asbestos $(Mg,Fe^{2+})_7Si_8O_{22}(OH)_2$, crocidolite $Na_2(Fe^{2+},Mg)_3Fe_2^{3+}Si_8O_{22}(OH)_2$ (the fibrous variety of riebeckite) and tremolite asbestos $Ca_2Mg_5Si_8O_{22}(OH)_2$. Due to the presence of strong bonds in their framework, they usually grow along the crystallographic *c*-axis exhibiting a marked needle-like crystal habit with a heterogeneous size distribution. Additionally, because of their chemical variability, amphiboles present an extremely wide range of possible chemical compositions, both in samples from the same outcrop and within the same crystal. This makes the identification and the classification of amphiboles extremely challenging, giving rise to both medical and legal issues linked to the exposure to amphibole fibres (Hawthorne et al., 2012; Belluso et al., 2017; Della Ventura et al., 2018). In particular, the commercial exploitation of amphiboles mainly involved amosite, anthophyllite and crocidolite that, due to their characteristic physical-chemical stability, were often employed in combination with chrysotile for asbestos-cement products, roofing, fire-proofing materials,

insulation pipes and boards. Conversely, tremolite had scarce industrial applications, although it has been frequently found as a contaminant in chrysotile, vermiculite, and talc (Virta, 2002).

Actinolite and tremolite

Actinolite and tremolite belong to the calcium amphiboles as part of the tremolite-actinolite-ferroactinolite series of isomorphic mixed crystals. Indeed, a solid solution series encompasses different minerals with a compositional range determined by the end-members of the series, which share the same basic chemical formula, but undergo a partial substitution of their elements. In this case, magnesium-rich tremolite [$^{A}\square^{B}\ Ca_2{}^{C}(Mg_{5.0\text{-}4.5}Fe^{2+}{}_{0.0\text{-}0.5})^{T}Si_8O_{22}{}^{W}(OH)_2$ with a $Mg/(Mg+Fe^{2+})$ ratio higher than 0.9] and iron-rich ferroactinolite [$^{A}\square^{B}\ Ca_2{}^{C}(Mg_{2.5\text{-}0.0}Fe^{2+}{}_{2.5\text{-}5.0})^{T}Si_8O_{22}{}^{W}(OH)_2$ with a $Mg/(Mg+Fe^{2+})$ ratio lower than 0.5] form a solid solution series in which Mg and Fe^{2+} ions can be freely exchanged in the crystal structure. Thus, since actinolite represents the intermediate member of the series, its ideal chemical composition is described by the formula $^{A}\square^{B}Ca_2{}^{C}(Mg,Fe)_5{}^{T}Si_8O_{22}{}^{W}(OH)_2$, in which the $Mg/(Mg + Fe^{2+})$ ratio falls in the range of 0.5–0.9 and the Si value ranges from 7.5 to 8.0 atoms per formula unit. In particular, the increasing content of Fe^{2+} in the chemical structure is correlated with a darkening in their colour, resulting in a spectrum of shades varying from the blackish green of iron-rich ferroactinolite to the creamy white of tremolite containing exclusively magnesium.

Since tremolite, actinolite and ferro-actinolite are *C*2/*m* monoclinic amphiboles, their crystallographic structure consists of two corner-linked *T*(1) and *T*(2) tetrahedral sites occupied by Si, which are assembled in double silicate chains connected together by strips of edge-sharing octahedrally coordinated sites. In particular the *M*(1), *M*(2) and *M*(3) octahedral sites typically contain Fe^{2+} and Mg, although these cations may sometimes be replaced by K^+, Al^{3+}, Mn^{2+}, Mn^{3+}, Ti^{3+}, Ti^{4+} or Cr^{3+}, while the anionic O(3) site responsible for their coordination is characterised by the presence of OH^-, F^-, Cl^- and/or O^{2-}. Moreover, the *M*(4) site that interconnects the tetrahedral siliceous double-chain and the octahedral cationic strip, is distinctively occupied by Ca in minerals classified as calcium amphiboles (Bloise, 2019).

The tremolite-actinolite-ferroactinolite series is commonly found in low-grade metamorphic rocks, in metamorphosed magnesium-rich limestones and metamorphic ultramafic rocks. According to their different crystalline habit, tremolite and actinolite may occur as both asbestiform and non-asbestiform structures. In fact, asbestiform species are composed of crystalline aggregations of parallel, needle-like fibres with a unidirectional growth, while non-asbestiform species are formed of elongated, lozenge-shaped prisms characterised by a multidirectional crystalline growth (Baietto et al., 2019). In particular, analyzing the compositional variability of asbestiform and non-

asbestiform samples in the actinolite series, it was determined that the fibrous habit is correlated with a lower amount of Al^{3+} in their crystal structure (Dorling and Zussman, 1987).

Apart from their occasional employment in small amounts for fire retardant devices, fibrous actinolite and tremolite are rarely mined with respect to more commercially widespread types of asbestos and, therefore, are mainly considered contaminants in chrysotile, vermiculite, and talc. Notably, tremolite asbestos was responsible for the contamination of the Libby mines in Montana, which provided the great majority of the vermiculite that was commercially distributed worldwide for construction materials, attic insulation, agricultural fertilizers, and potting soil mixes. Indeed, Libby vermiculite was mined under the trade name *Zonolite* until 1990, when the mine was closed due to the outstanding increase in asbestos-related illnesses among workers and residents in the nearby towns (Meeker et al., 2003; McDonald et al., 2004).

Amosite

Amosite is a trade name referring to the asbestiform amphiboles belonging to the cummingtonite-grunerite series and, in particular, to a rare asbestiform variety of iron-rich grunerite mined predominantly in the Limpopo province of South Africa, which was commonly referred to as *brown asbestos* due to its characteristic colour (Hart, 1988).

Cummingtonite and grunerite are part of the magnesium-iron-manganese amphibole subgroup, which contains monoclinic and orthorhombic minerals, classified according to the dominant element in their *M*(4) position, that form a solid solution series in which Mg, Fe and Mn are easily exchanged inside their crystallographic structure. Notably, the cummingtonite-grunerite series ranges from magnesium-rich magnesiocummingtonite [$^{A}\square^{B}\ Mg_2^{C}Mg_5^{T}Si_8O_{22}^{W}(OH)_2$] to iron-rich grunerite [$^{A}\square^{B}\ Fe_2^{C}Fe_5^{T}Si_8O_{22}^{W}(OH)_2$] as a result of the increasing substitution of Mg with Fe^{2+} in their chemical composition, while cummingtonite represents the series intermediate [$^{A}\square^{B}(Mg,Fe^{2+})_2^{C}(Mg,Fe^{2+})_5^{T}Si_8O_{22}^{W}(OH)_2$, with a $Mg/(Mg+Fe^{2+})$ ratio corresponding to 0.3–0.7] (Leake, 1978; Evans and Ghiorso, 1995; Della Ventura et al., 2018).

The amphiboles belonging to the magnesium-iron-manganese subgroup crystallize with different structures according to the size of their *M*(4)-site cations. Therefore, the homovalent substitution of Mg and Fe^{2+} is associated to an adjustment in their monoclinic symmetry, since magnesium-rich cummingtonite is $P2_1/m$ and iron-rich grunerite is $C2/m$. In fact, in the crystallographic structure of grunerite all octahedral sites are occupied by Fe^{2+}; instead, in cummingtonite, Fe^{2+} is preferentially coordinated in the *M*(4) site and Mg is mainly found in the *M*(2) site, while the two cations are equally distributed in the *M*(1) and *M*(3) positions (Della Ventura et al., 2018).

The minerals of the cummingtonite-grunerite series are relatively common since they are typically found in Ca-poor regionally and contact metamorphosed rocks. Nonetheless, the fibrous amphiboles of this series have been commercially exploited only in the metamorphic banded iron formations of the Limpopo province in South Africa. In fact, the trade name amosite ensued from the acronym Asbestos Mines of South Africa, since this type of asbestos was discovered in the Penge region in 1907 and extensively mined from 1914 to 1992, when the mining district was closed due to the serious health hazard posed by asbestos exposure (Hart, 1988). Although it was far from being as widely exploited as chrysotile, amosite was frequently employed in the construction industry for thermal insulation and for fireproofing applications, as well as in the manufacturing of loosely compacted mats for covering steam locomotives, jet engines and marine turbines.

Anthophyllite

Anthophyllite is characterised by the ideal composition $^{A}\square^{B}(Mg)_2{}^{C}(Mg)_5{}^{T}Si_8O_{22}{}^{W}(OH)_2$ and, due to the progressive exchange of Mg with Fe^{+2} in its crystal structure, forms a solid solution series with iron-rich ferro-anthophyllite $^{A}(\square)^{B}(Fe^{2+})_2{}^{C}(Fe^{2+})_5{}^{T}(Si)_8O_{22}{}^{W}(OH)_2$. According to the classification of the International Mineralogical Association, anthophyllite is part of the magnesium-iron-manganese subgroup, which comprises both orthorhombic and monoclinic amphiboles. Orthorhombic anthophyllite is compositionally similar and polymorphic with monoclinic cummingtonite which is a rare non-metastable form of magnesium-rich amphibole, whereas grunerite is the monoclinic polymorph of ferro-anthophyllite. Anthophyllite mainly grows in lamellar or fibrous aggregates, coloured in a range of shades varying from off-white to dull green, following the proportional increase in their Fe^{2+} content (Della Ventura et al., 2018).

Anthophyllite asbestos typically occurs in metamorphic magnesium-rich rocks of the lower to middle amphibolite facies (i.e., ultrabasic igneous rocks and impure dolomitic shales), as well as in serpentinized ultrabasic rocks as a retrograde metamorphic mineral. In particular, the principal mines of fibrous anthophyllite were in Finland and in Japan. In fact, the serpentinization of metamorphosed dunites and harzburgites created large deposits of this asbestos in Eastern Finland, prompting its commercial exploitation mainly in the mines of Paakkila and Maljasalmi. Indeed, Maljasalmi was a small mine in the Outokumpu commune that was active solely from 1944 to 1952, whereas the mine of Paakkila in the Tuusniemi commune represented the primary source of Finnish anthophyllite until its closure in 1975. Anthophyllite was industrially employed in limited amounts, mainly for insulation products, composite cement, and roofing materials, such as roof tiles or shingles. Moreover, it frequently occurs as a contaminant in chrysotile asbestos, vermiculite, and talc (Virta, 2002).

Crocidolite

Crocidolite represents the fibrous variety of riebeckite, which is classified in the sodic amphibole subgroup and is described by the ideal chemical formula $^{A}(\square)^{B}(Na)_2{}^{C}(Fe^{2+}{}_3,Fe^{3+}{}_2)^{T}(Si)_8O_{22}{}^{W}(OH)_2$. Nonetheless, its chemical composition is influenced by a broad variety of cationic substitutions in the *M*(1), *M*(2) and *M*(3) octahedral sites, such as the substitution of Fe^{3+} with Al and of Fe^{2+} with Mg, which lead respectively to the formation of ferro-glaucophane [$Na_2Fe^{2+}{}_3Al_2Si_8O_{22}(OH)_2$] and magnesium-riebeckite [$Na_2Mg_3Fe_2{}^{3+}Si_8O_{22}(OH)_2$]. Due to the elevated iron content in its chemical structure, riebeckite is typically found in a spectrum of shades varying from dark blue to black, leading to crocidolite being commonly referred to as *blue asbestos* because of its characteristic colour. Besides occurring as fibrous crocidolite in altered metamorphic rocks, riebeckite frequently forms long prismatic crystals with a diamond-shaped cross section that are generally of igneous origin (i.e. volcanic rock and pegmatites).

Crocidolite represented the most commercially employed amphibole, since it accounted for about 2%-3% of the worldwide production of asbestos and was extensively mined in Australia, Bolivia, and South Africa. The South African and Western Australian deposits occur in banded iron formations of Precambrian age, where crocidolite is found in seams parallel to their bedding. Indeed, crocidolite crystallizes in riebeckite fibres that are deposed perpendicular to the plane of the seam and are commonly associated with iron-rich magnetite. Conversely, the Bolivian deposit originates in slates and quartzites of Devonian age, in which crocidolite occurs as veins parallel to the bedding and as fracture fillings with irregular orientation, forming fibres of magnesium-riebeckite that are disposed at an acute angle. Similar geological and mineralogical features have been described in a deposit near Lusaka, in Zambia, which has never been exploited for commercial purposes.

Due to its characteristic tensile strength and heat resistance, crocidolite was mostly employed for steam engine insulation, cement products, pipe insulation, roofing tiles, spray-on coatings, guttering and cisterns. Moreover, there is also evidence that traces of crocidolite were found in the Kent Micronite cigarettes manufactured from March 1952 to May 1956, which amounted to approximately 13 billion cigarettes. Since each filter contained roughly 10 mg of Bolivian crocidolite, it has been estimated that smoking a pack of cigarettes per day would lead to the inhalation of an alarming amount of crocidolite (i.e., 131 million fibres) over the course of one year (Longo et al., 1995; Pauly et al., 2009).

The association between crocidolite exposure and mesothelioma was established in 1960, due to the significant incidence and mortality of this malignancy among the miners of Cape Province in South

Africa. Indeed, after crocidolite fibres are inhaled, their marked needle-like habit causes them to lodge in the pulmonary tissue, frequently leading to the insurgence of several asbestos-related diseases and, in particular, mesothelioma (Wagner et al., 1960; Bothman and Holt, 1972). The widespread mining of crocidolite ceased shortly after this discovery, albeit with a few exceptions, such as Bolivia, where the magnesium-riebeckite variety of crocidolite is still mined and used for asbestos-cement production.

1.1.2. SERPENTINE ASBESTOS

Serpentine minerals are a group of magnesium-rich phyllosilicates characterised by a layered structure in which tetrahedral sheets and octahedral sheets are arranged in a 1:1 ratio. In phyllosilicates, the tetrahedral sheet is composed of SiO_4 tetrahedra assembled in a continuous hexagonal network in which each SiO_4 subunit is linked to three adjacent tetrahedra by corner-sharing of its oxygen atoms. Their unshared oxygen atoms are all oriented in the same direction, connecting the silicon atoms of the tetrahedral sheet with the cations of the octahedral sheet. Indeed, the octahedral sheet is composed of edge-sharing octahedral sites occupied by divalent and trivalent cations (e.g., Fe^{2+}, Mg^{2+}, Al^{3+}) that are 6-fold coordinated with OH groups or O^{-} atoms. Considering that each hexagonal ring of tetrahedra encompasses three octahedral sites, when the octahedra contain a divalent ion such as Mg^{2+} or Fe^{2+}, the charge balance between the sheets is achieved when all three cation sites are occupied, forming a trioctahedral sheet. Conversely, when the octahedra contain a trivalent ion such as Al^{3+} or Fe^{3+}, only two-thirds of the octahedral sites are occupied, resulting in a dioctahedral sheet in which the vacant site is significantly larger than the occupied sites that, consequently, become severely distorted (Putnis, 1992).

Serpentine minerals are characterised by the ideal chemical formula $Mg_3(OH)_4Si_2O_5$, in which the trioctahedral sites are occupied by Mg^{2+} forming a brucite layer. Since they are characteristically arranged in a 1:1 layer structure with one Si-centred tetrahedral sheet (T) per one Mg-centred octahedral sheet (O), serpentines are composed of TO layers stacked together with the unshared oxygen atoms facing towards the centre. Nevertheless, the ideal linkage between a flat tetrahedral sheet and an octahedral sheet requires an octahedral cation radius of approximately 0.70 Å, i.e., slightly smaller than Mg^{2+}. Therefore, serpentine minerals generally occur in three polymorphs (i.e., chrysotile, antigorite and lizardite), each reflecting a different attempt at coping with this tetrahedral-octahedral mismatch (Putnis, 1992).

Serpentines typically exhibit several identifying features, such as specific gravity values varying from 2.2 to 2.9 and Mohs hardness ranging from 2.5 to 4. They are non-flammable and resistant to heat, albeit susceptible to strong acids. Serpentines are typically found in a broad spectrum of

shades ranging from white to grey, yellow to green, brown to black. They are often speckled and veined, with a diaphaneity varying from translucent to opaque.

Chrysotile

Chrysotile, which is the most common asbestos mineral, is a trioctahedral hydrous layer silicate belonging to the serpentine group, with the ideal chemical formula $Mg_3(OH)_4Si_2O_5$. Chrysotile has only limited variations from its ideal crystal–chemical composition; indeed, Mg^{2+} may be replaced by small amounts of other cations, such as iron, chromium, manganese, cobalt, or nickel. Chrysotile is characterised by a 1:1 layer structure with one Si-centred tetrahedral sheet (T) covalently bonded to one Mg-centred octahedral sheet (O). However, the lateral dimension of an ideal tetrahedral Si-centred T sheet (*b*=9.1Å) is smaller than the lateral dimension of an ideal octahedral Mg-centred O sheet (*b*=9.43Å), leading to a differential strain between the two sides of the layer. The strain of this misfit is partly relieved by rolling the TO layer around the fibril *c*-axis, forming a cylindrical lattice responsible for the typical fibrous crystal habit of chrysotile (Pauling, 1930; Ballirano et al., 2017). Since each TO layer has a thickness of approximately 7.3 Å, chrysotile fibres are generally composed of about 12–20 TO layers that are joined together by mechanical interlocking, forming concentric cylinders with the larger Mg-centred octahedral sheet of each layer on the outer side of the fibre and the smaller Si-centred tetrahedral sheet on its inner side (Whittaker, 1953; 1957; Titulaer et al., 1993; Bernstein, 2022).

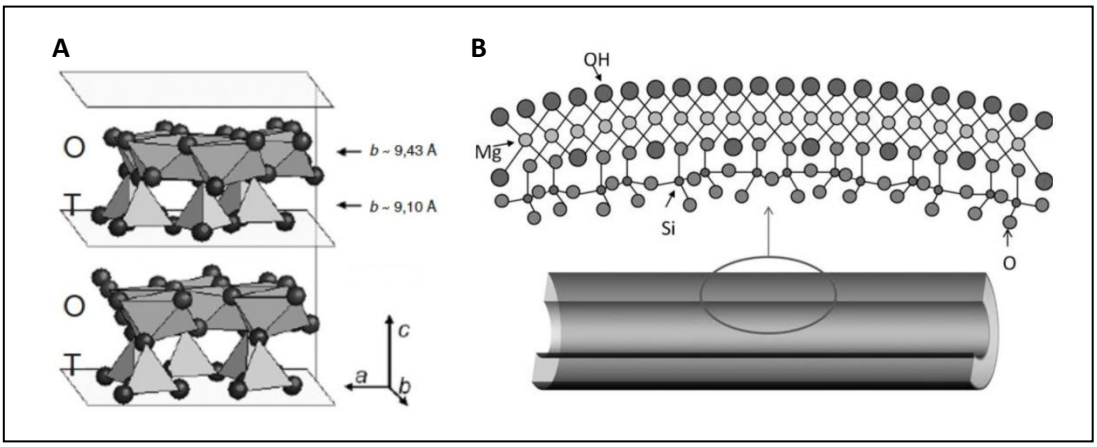

Figure 2. Schematic representation of chrysotile structure. (**A**) Layer structure of chrysotile showing the mismatch between the lateral dimension of the Si-centred tetrahedral sheet (light grey) and the Mg-centred octahedral sheet (dark grey). (**B**) Cylindrical lattice of chrysotile showing the Mg-centred octahedral sheet on the outer side of the structure. Images from Piperno et al. (2007) and Kononova et al. (2018), respectively.

Chrysotile, as well as the other minerals of the serpentine group (i.e., antigorite and lizardite), is formed by the retrograde hydrothermal alteration of ultrabasic rocks such as dunite, peridotite, and pyroxenites; besides, it is also found in association with thermally metamorphosed siliceous dolomitic limestones. Because of its high natural availability and low manufacturing cost, chrysotile accounted for about 95% of all asbestos commercially employed worldwide. In fact, due to its outstanding physical and technological properties, chrysotile was extensively used for construction products (i.e., asbestos-cement, asphalt, electric insulators, roof sealants, elevator brakes) and automotive parts (i.e., brake shoes, disk pads, clutches). Moreover, its long, curly fibres were frequently interwoven to obtain non-flammable fabrics that were employed for safety apparel, fire curtains in theatres and fire stop hangings in public buildings, while its short fibres were added as a reinforcing agent in paper, millboard, and plastic products (Roggli, 2013).

Chrysotile is the only type of asbestos belonging to the serpentine category and, as such, is currently classified as carcinogenic to humans (Group 1) by the International Agency for Research on Cancer. Nonetheless, since amphiboles and chrysotile differ in chemical compositions, structure models, properties and biopersistences, one of the controversies that have arisen over the years is that only amphibole asbestos are hazardous, whereas chrysotile does not present a detectable risk to health. As a result, this mineral is still largely employed in about 65% of the countries worldwide, giving rise to the so-called "global chrysotile issue" (Roggli, 1995; Hodgson and Darnton, 2000; Roggli and Vollmer, 2008; Mossman et al., 2011; IARC, 2012; Bernstein et al., 2013; Garabrant and Pastula, 2018).

1.2. ZEOLITES

Zeolites are a group of hydrated aluminosilicate minerals characterised by a crystal structure with a three-dimensional framework of SiO_4 and AlO_4 tetrahedra linked by corner-sharing of the oxygen atoms. Since this tetrahedral framework encloses interconnected cavities in the form of channels and cages, zeolites display a peculiar microporous structure that accommodates H_2O molecules and metal cations. In fact, the substitution of Al^{3+} for Si^{4+} in the tetrahedral sites causes a charge imbalance to the overall crystal structure that is compensated by the presence of large cations such as Na^+, K^+, Ca^{2+} and Mg^{2+} in the extra-framework cavities. However, since these cations are loosely bonded to the tetrahedral structure, they are readily exchanged with a surrounding solution of another ion, resulting in one of the most important properties of natural and synthetic zeolites. In fact, due to their cation exchange property, zeolites are employed for water softeners and soil conditioners, for the removal of ammonium in sewage treatment, for the sequestration of radioactive particles from nuclear waste and for the absorption of heavy metals from contaminated

soils. Moreover, since their water molecules are weakly bonded to the framework atoms, dehydrated and rehydrated zeolites maintain their overall structure intact, prompting their use as desiccants in the removal of water from petroleum and other hydrocarbons. Besides, dehydrated zeolites are employed as molecular sieves since the dimension of the cavities in their structure can be used to separate gases and ions based on their molecular or ionic size.

The zeolite group includes about 60 naturally occurring minerals that are typically found in fissures of mafic volcanic rocks, as well as in diagenetic and low-grade metamorphic settings. Additionally, more than 200 zeolite species have been manufactured synthetically to obtain a wide variety of extremely regular microporous structures that interact selectively with adsorbed molecules depending on their size, shape, and chemical characteristics. Thus, zeolites have been employed for numerous industrial applications, such as for selective heterogeneous catalysis, for separation of hydrocarbons in petroleum refining and for pollution control by selective molecular adsorption (Klein and Philpotts, 2016).

1.2.1. ERIONITE

Erionite is a naturally occurring fibrous zeolite which is described by the general formula $K_2(Na,Ca_{0.5})_7[Al_9Si_{27}O_{72}]\cdot 28H_2O$. However, its remarkable chemical variability prompted the identification of three different species (i.e., erionite-Na, erionite-K and erionite-Ca) according to the most abundant extra-framework cation in their structure. Erionite belongs to the so-called ABC-6 family, which comprises zeolites formed by six-membered rings of $(Si,Al)O_4$ tetrahedra that are stacked along the *c*-axis in a repetitive 6-layer scheme. Since the stacking sequence of erionite corresponds to AABAAC, its framework contains two double-6 rings, two cancrinite cages and two erionite cages per unit cell. The extra-framework cations are enclosed in the cancrinite and erionite cages, where they are coordinated by the H_2O molecules arranged around the axis of the erionite cavity. Indeed, the cancrinite cage contains a 6-fold coordinated K^+ ion located at the centre of the cavity, whereas several extra-framework cation sites are placed along the *c*-axis of the erionite cage (Gualtieri et al., 2016; Ballirano et al., 2017).

Erionite is typically found in deposits of prismatic-to-acicular crystals that occur as diagenetic product in sedimentary environments, as product of hydrothermal alterations or in the vugs of altered basalts (Gualtieri et al., 2016). Natural fibrous erionite is abundantly found in the volcanic tuff of the Cappadocia region in Turkey, where it was frequently employed as building material. At the end of the 1970s, in Turkish villages where inhalable erionite fibres were detected in air samples, several studies reported an increased incidence of pleural mesothelioma and pleural fibrosis, along with the detection of erionite fibres in the lungs of affected individuals (Panou et al.,

2015). The ensuing *in vivo* studies unambiguously correlated the environmental exposure to erionite with the respiratory diseases observed in several villages of Cappadocia (i.e., Sarihidir, Tuzköy, and Karain). Fibrous erionite resulted significantly more carcinogenic than chrysotile and crocidolite, leading to the classification of this zeolite as carcinogenic to humans (Group 1) by the IARC (IARC, 1987; Coffin et al., 1992). Therefore, erionite has not been mined for commercial purposes since the late 1980s, although fibrous erionite is frequently found as a contaminant associated to other zeolites, such as clinoptilolite and clinoptilolite-phillipsite (NTP, 2011).

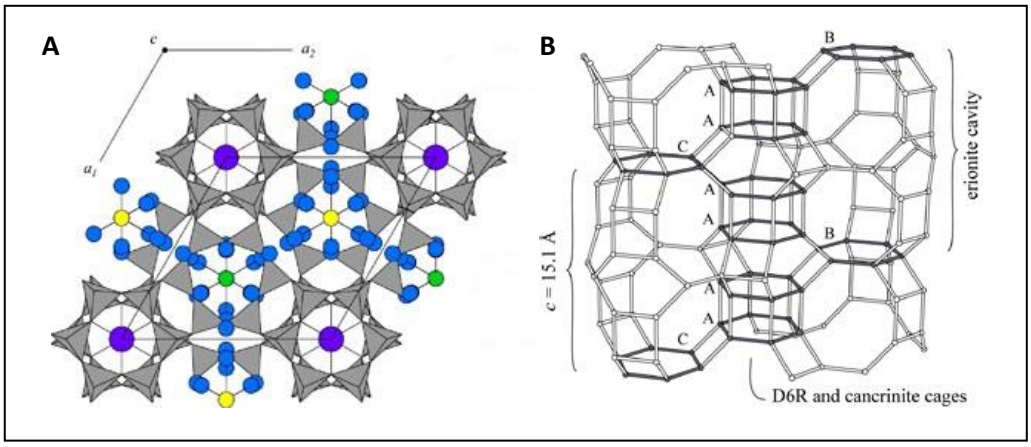

Figure 3. Schematic representation of erionite structure. (**A**) Crystal structure of erionite with the cancrinite cages containing K^+ ions (purple) and the erionite cages containing water molecules (blue) and the remaining extra-framework cations (yellow and green). (**B**) Diagram of erionite framework showing the characteristic stacking sequence AABAAC forming two double-6 rings, two cancrinite cages and two erionite cages per unit cell. Images from the International Zeolite Association (2005).

2. MINERAL FIBRE BIOLOGICAL INTERACTION

Since numerous cohort and case control studies have unequivocally established a correlation between asbestos exposure and occupational lung diseases, all six forms of asbestos have been classified as carcinogenic to humans (Group 1) by the International Agency for Research on Cancer and, as a result, sixty-nine countries have banned all six asbestos minerals (IARC, 2012; International Ban Asbestos Secretariat, 2023). Nonetheless, despite the unambiguous position of the International Agency for Research on Cancer in considering chrysotile carcinogenic to humans, this mineral is still largely employed in about 65% of the countries worldwide including China, India, Kazakhstan, and Russia. In fact, even if all amphiboles are banned globally, these countries still allow a "safe use" of chrysotile, authorizing its controlled manipulation as long as precautionary measures are in place (i.e., measuring the concentrations of airborne asbestos dust in the workplace so that it does not exceed 2 fibres/cm^3 of air on an eight-hour time-weighted average, monitoring the exposure of workers to asbestos at regular intervals, limiting the release of asbestos dust into the air, providing individual protection devices to workers) (Asbestos Convention 1986, ILO 162).

This dispute is known as the so-called "global chrysotile issue" and is deep-rooted in the assumption that only amphibole asbestos forms are hazardous, whereas chrysotile does not present a detectable risk to health since amphiboles and chrysotile differ in chemistries, structure models, properties and biopersistences. One of the controversies that have arisen over the years is that chrysotile is less potent in the induction of malignant mesothelioma and that it can cause disease only at extraordinarily large doses (Roggli, 1995; Hodgson and Darnton, 2000; Roggli and Vollmer, 2008; Mossman et al., 2011; Bernstein et al., 2013; Garabrant and Pastula, 2018).

This hypothesis is supported by the markedly lower biopersistence of chrysotile with respect to amphibole asbestos. In fact, the long-term toxicity of a mineral fibre is influenced by its biopersistence, which measures whether an exogenous particle can escape the physiological clearance mechanisms of the human body, and by its biodurability, which assesses the fibre capability of enduring physical and chemical processes such as dissolution, leaching, breaking, and splitting in a physiological environment. For this purpose, *in vivo* tests are employed to evaluate the fibres biopersistence in the lungs by analyzing their retention behaviour, while *in vitro* methods determine their degree of dissolution by measuring the decrease in the fibres sample mass or the concentration of ions released into the simulated body fluid in order to appraise the fibres biodurability (Oberdörster, 2000; Bernstein et al., 2005; Utembe et al., 2015; Gualtieri et al., 2018b). Among the *in vitro* dissolution tests, cellular assays require the treatment of cultured cells (usually alveolar macrophages) with mineral fibres, so that changes in the size and composition of

the intracellular fibres are determined by microscopic examination. Instead, acellular tests are based on the leaching of the fibre constituents into dissolution mediums, known as simulated lung fluids, both at pH=4.5 and pH=7.4, to simulate the intracellular phagolysosome and the extracellular milieu, respectively (Potter and Mattson, 1991; Lundborg et al., 1995).

In literature, the results of both *in vitro* biodurability studies and *in vivo* biopersistence tests have shown that chrysotile is markedly less biodurable/biopersistent than amphibole asbestos in the body (Bernstein et al., 2005; IARC, 2012; Utembe et al., 2015). For instance, considering a fibre with a diameter of 0.25 μm, the calculated dissolution time for chrysotile amounts to 94-177 days, which is considerably lower respect to the 49-245 years necessary for amphiboles (Gualtieri et al., 2018b). Moreover, when chrysotile is phagocytosed by alveolar macrophages *in vivo*, the acid environment of the intracellular phagolysosome induces its fibres to undergo a rapid dissolution, with a progressive leaching of Mg and the production of amorphous silica relicts, whose structure and toxicity are yet to be completely understood (Bernstein et al., 2013; Gualtieri et al., 2019a). In fact, chrysotile dissolution consists of a fast decomposition of the octahedral layer due to Mg leaching and a slower dissolution of the silica layer, whose rapidness determines the dissolution rate of chrysotile (Jaurand et al., 1977; Hume and Rimstidt, 1992).

At a first glance, this low biodurability could lead to the assumption that chrysotile has a lower toxic potential with respect to amphibole asbestos and thus is less capable of inducing adverse effects in the lung (Mossman, 1993). However, the amorphization of chrysotile induces the formation of a silica-rich fibre skeleton with silanol groups (Si-OH) and ionized silanol groups ($Si\text{-}O^-$). The subsequent dissolution of this reactive silica surface may be a possible source of ROS, in addition to surface iron species (Pollastri et al., 2014; Gualtieri et al., 2019a). Additionally, mineral fibres contain trace elements that may have a synergetic role in the insurgence of pulmonary diseases, since there are both epidemiological and experimental evidences that trace elements, and in particular trace metals, may provoke lung cancer (IARC, 1993; Nemery, 1990). In both chrysotile and amphiboles, trace metals are mainly localised in the octahedral site which is usually occupied by Mg or Fe, so they are released in the extracellular fluid of the lungs when asbestos fibres are dissolved during phagocytosis. In chrysotile samples, high amounts of trace metals such as Cr, Mn, Co, Ni, and Cu have been detected, since they represent an almost exclusively isomorphous substitution for Mg (Bloise et al., 2009a; 2009b; 2010; 2016; Deer et al., 2009). Therefore, the fast dissolution rate of chrysotile fibres could lead to a rapid mobilization of their content of trace elements, playing a significant role in causing disease in the lungs.

In this vein, another frequent misconception regards the anatomopathological detection of a certain number of asbestos bodies in the tissues as a required hallmark to ascertain heavy asbestos exposure. In fact, despite being partly removed by the mucociliary clearance mechanism of the lungs, these microscopic bundles of fibrils may reach the distal regions of the pulmonary parenchyma, leading to the formation of asbestos bodies in the septum of the alveolus. Indeed, they typically appear as yellow-brown nodules with a core of asbestos fibres that have been encased by macrophages in an iron-rich material derived from proteins such as ferritin and hemosiderin. Since this iron-rich coating does not contribute to the production of ROS, it has been suggested that asbestos bodies represent a protective mechanism to diminish the potential toxicity of the fibres by sequestering the redox-active metals on the fibre surface and thus reducing the metal-catalyzed oxidative stress, as evidenced by both *in vivo* and *in vitro* studies demonstrating that asbestos bodies induce a lower degree of cytotoxicity and fibrosis in comparison to uncoated asbestos fibres (Davis, 1970; Governa and Rosanda, 1972; Churg and Warnock, 1981; McLemore et al., 1980; Ghio et al., 1997; Governa et al., 1999; Ghio et al., 2004; Roggli, 2013).

Interestingly, the core of asbestos bodies isolated from human lungs rarely contains chrysotile (2%) with respect to other commercial amphiboles (96%), although the former represents the vast majority of the industrially employed asbestos. Considering that asbestos bodies predominantly occur on fibre bundles longer than 20 μm, the infrequency of chrysotile asbestos bodies may be ascribed to the rapid dissolution and fragmentation of chrysotile into shorter fibrils. Indeed, chrysotile asbestos bodies are generally formed only on relatively thick fibre bundles, which are mainly found in the lungs of miners and millers routinely exposed to long fibres of chrysotile. Moreover, in tissues containing chrysotile the number of uncoated fibres considerably exceeds the number of coated fibres, confirming that asbestos bodies represent a poor measure of the pulmonary burden caused by chrysotile exposure (Pooley, 1972; Morgan and Holmes, 1985; Dodson et al., 1989; Kohyama and Suzuki, 1991; Roggli, 2013; Frank, 2020).

Another factor that could influence the formation of asbestos bodies is the crystal habit (i.e., whether a fibre possesses a curly or a needle-like crystal shape), which determines the deposition depth of asbestos fibres in lung tissues, and thus has an indirect effect on carcinogenicity. In fact, the curvy and flexible fibres of chrysotile frequently remain in the upper part of the respiratory tract, where they are readily removed by the mucociliary clearance mechanism. Conversely, since the straight and rigid fibres of amphibole asbestos usually align with the airstream, they are carried deeper into the distal airways and alveolar regions, where they are cleared at a much slower rate prompting their permanence in the pulmonary tissue for longer periods (Gualtieri, 2023). The limited alveolar penetration of chrysotile bundles may also account for the apparent lack of

association between the exposure to its fibres and the development of malignant mesothelioma in human cohorts. On the contrary, when asbestos fibres reach the lower respiratory tract, they persist at the site of deposition triggering a chronic inflammatory process driven by HMGB1 secretion and by inflammasome activation, which promotes the activation of NF-κB and PI3K pathways in mesothelial cells (Mossman et al., 1990; Dostert et al., 2008; Carbone et al., 2019; Gualtieri et al., 2021).

The carcinogenicity of mineral fibres is also influenced by the dimensions of the inhaled fibres, since their length and width have a fundamental role in determining toxicity, inflammation and, ultimately, pathogenicity. Indeed, several studies highlighted the involvement of fibre dimensions in tumorigenesis, with long (> 5 μm), thin (< 0.5 μm diameter) fibres having a greater carcinogenic activity and proliferative capability than short fibres (Dogan et al., 2005; Donaldson, et al., 2010). In particular, the importance of fibre size goes back to the work of Stanton, in which fibres of a particular dimension (length > 8 μm and width < 0.25 μm) appeared more carcinogenic than others when implanted within the pleural cavity of rat specimens. Interestingly, in this model system, smaller fibres were likewise carcinogenic, although they induced tumours less frequently than thin fibres longer than 5 μm. Nonetheless, this early work presented several limitations, i.e., the small groups of studied animals, the unrealistic method of asbestos exposure, and the problematic preparation of fibres aliquots with an accurate size (Stanton et al., 1981; Frank, 2020). Since the ensuing reviews of *in vitro*, *in vivo*, and epidemiologic data evidenced contradictory results regarding the harmful effect of short asbestos fibres, their potential toxicity remains widely debated in the scientific community. This endless dispute also regards the potential toxicity of chrysotile short fibres, since one side claims that short asbestos fibres are toxic and carcinogenic (Egilman and Tran, 2016), while the other side argues that chrysotile fibres with length < 5 μm do not contribute to the negative effects of asbestos on human health (Bernstein, 2022).

According to the work of Goodglick and Kane (1990), both long and short crocidolite fibres caused a significant toxicity in macrophages *in vitro* via an iron-dependent ROS-mediated mechanism; conversely, the short fibres were cytotoxic *in vivo* only when their dose abundantly exceeded the clearance capacity. These results could be explained by the assumption that either short fibres are inherently less harmful or that they are less injurious *in vivo* because they are cleared more efficiently than larger fibres from sites of potential damage. In fact, when short asbestos fibres localise in the pulmonary tissue, they can be removed by the mucociliary clearance mechanism, by the local macrophages through phagocytosis, or by the lymphatic system which prompts their accumulation in the surrounding lymph nodes (Bernestein, 2022).

Studies on animal models associated the inhalation of asbestos fibres longer than 5 μm with the insurgence of asbestosis, mesothelioma, and lung cancer, whereas shorter fibres displayed no convincing evidence of a pathogenic effect. Besides, in several epidemiologic studies on asbestos textile workers, the exposure to long fibres was correlated with a markedly higher incidence of lung cancer (Stayner et al., 2008; Loomis et al., 2009; 2010; 2012; Roggli, 2015). As a result, the Agency for Toxic Substances and Disease Registry declared that there is strong evidence that asbestos fibres shorter than 5 μm are unlikely to cause cancer in humans (ATSDR, 2004; Barlow et al., 2017). However, the assumption that short asbestos fibres are not harmful to human health is still open to debate, since some authors noted that exposure to short, thin fibres was still associated with lung cancer risk. Indeed, several reviews reported that asbestos fibres of all lengths induce pathological responses, and therefore it is particularly challenging to determine whether fibres of a particular size have no role in causing disease (Dodson et al., 2003; Boulanger et al., 2014).

Hence, the toxicity and carcinogenicity of mineral fibres is profoundly interwoven with a broad variety of crystal-chemical-physical characteristics, such as fibre length and width, crystal curvature and habit, fibre density, chemical composition, total iron and Fe^{2+} content, heavy metals presence, ability to produce ROS, surface activity, zeta potential, dissolution rate, velocity of iron and metals release, biopersistence and biodurability. As a result, the biogeochemical mechanisms through which mineral fibres, and especially asbestos, induce cytotoxic and genotoxic damage *in vivo* are yet to be completely understood (Mossman and Gualtieri, 2020). Indeed, the exposure to mineral fibres represents a serious occupational and environmental hazard, since it leads to chronic lung inflammation with the subsequent development of pneumoconiosis, fibrotic pulmonary diseases, and various malignancies, such as lung cancer and malignant mesothelioma. One of the consequences is a high number of casualties and elevated costs for the healthcare systems of countries worldwide. Thus, understanding the mechanisms of toxicity and carcinogenicity of inhalable mineral fibres constitutes a fundamental step towards the quantitative classification of the toxicity/carcinogenicity of mineral fibres for preventive medicine and the development of effective treatments for both at-risk workers and the general population.

In this regard, a very useful experimental model is the human monocytic cell line THP-1, since these cells can be easily differentiated into the various macrophage phenotypes involved in the inflammatory response *in vivo* (Chanput et al., 2014). In fact, the exposure to mineral fibres happens mainly by inhalation, causing their localization in the pulmonary tissue where alveolar macrophages constitute the first and foremost line of defence against detrimental inhaled stimuli. Indeed, macrophages represent the major effector cells of the innate immune system, since they

have a fundamental role in both triggering and maintaining the inflammatory response that develops in the tissues as a consequence of harmful stimuli. Macrophages comprise a population of myeloid cells, whose formation is the result of a progressive maturation of blood and bone marrow precursors in response to M-CSF (i.e., monocyte colony stimulating factor). Circulating monocytes remain in the bloodstream for a few days before accumulating into different tissues throughout the body, where they differentiate into a broad variety of tissue-resident macrophages with specific functions and morphologies (e.g., Kupffer cells in the liver, microglial cells in the brain, osteoclasts in the bone and alveolar macrophages in the lung). In case of cell damage, which is a required step in triggering the inflammatory response of immune cells, the chemokines released from injured cells prompt the accumulation of monocytes in the tissue and their subsequent differentiation to macrophages that can adapt their phenotype in response to different local stimuli (Gordon, 2007; Tsou et al., 2007; Vannella and Wynn, 2017).

In the lung, a limited number of macrophage sentinels, known as resident alveolar macrophages, rapidly localise at the site of injury and initiate the inflammatory process. The inflammation prompts the release of chemokines with the function of recruiting circulating monocytes, causing their extravasation and maturation in the tissue to non-activated (M0) macrophages. Once they are localised in the lung, the newly differentiated M0 macrophages are further polarised to classically activated (M1) and alternatively activated (M2) macrophages by the local mediators in the tissue microenvironment. Classically activated M1 macrophages are found at the site of damage shortly after injury or infection, with their phenotype developing in the presence of bacterial endotoxin (LPS) and IFN-γ or TNF-α. They release pro-inflammatory cytokines (i.e., TNF-α, IL-1β, IL-6, IL-12 and IL-15) and promote the production of cytotoxic reactive oxygen species (ROS), proteolytic enzymes and bioactive lipids. Conversely, M2 macrophages, which can be polarised by IL-4 and/or IL-13, may appear later at the site of inflammation and counteract the pro-inflammatory activity of the M1 phenotype by secreting anti-inflammatory mediators (i.e., IL-10, CCL18 and CCL22) and tissue-repair-promoting factors, such as TGF-β, VEGF and FGF. However, while M1 and M2 cells were initially assumed to be phenotypically and functionally distinct subpopulations with opposite roles in the inflammatory response, it is now recognised that macrophages exist as several subpopulations with different levels of M1/M2 markers and activities (Mantovani et al., 2004a; Martinez et al., 2007; Hussell and Bell, 2014; Arora et al., 2018; Laskin et al., 2019; Abdelaziz et al., 2020).

For this purpose, the human monocytic cell line THP-1 represents a valuable experimental model, since it provides interesting insights into the modulation of macrophage behaviour and functions. In fact, these cells can be easily polarised into the different macrophage phenotypes (i.e., M0, M1 and

M2 cells) involved in the inflammatory response and can be challenged with a broad variety of stimuli (i.e., infectious agents, asbestos and pollutants), as well as co-cultured with a plethora of different cell types to mimic tissue-specific interactions (Chanput et al., 2014). Therefore, this *in vitro* human cell model has been employed in several studies—which mainly focused on THP-1-derived M0 macrophages—to obtain a more in-depth understanding of the mechanisms underlying the acute toxicity and the inflammatory response induced by toxic and carcinogenic mineral fibres (Dostert et al., 2008; Li et al., 2012; Morris et al., 2015; Lee et al., 2018; Munson et al., 2018; Boyles et al., 2019; Gualtieri et al., 2019a; Corti et al., 2020; Skuland et al., 2020; Ventura et al., 2020; Di Giuseppe et al., 2021a; Ito et al., 2021; Larson-Casey et al., 2021).

3. ASBESTOS-RELATED DISEASES

The widespread employment of asbestos began in the second half of the 19th century, when the industrial revolution brought on the mechanization of the mining process, prompting the manufacturing of more than 3000 asbestos-containing materials in the following decades (Ross and Nolan, 2003; Gualtieri, 2021). Only at the beginning of the 20th century the first sporadic reports of asbestos disease arose, due to the surprising number of early deaths and lung problems in asbestos-mining towns (Case and Marinaccio, 2017). In this regard, while conducting a post-mortem investigation, Dr. Hubert Montague Murray discovered for the first time asbestos traces in the lungs of an asbestos textile worker who had died from pulmonary fibrosis in the early 1900s. Following an increasing number of scientific studies associating the exposure to asbestos fibres in the working environment with fatal lung diseases, the turning point was the cohort study carried out in 1955 by Sir Richard Doll, in which the association between lung cancer and exposure to asbestos fibres was indisputably demonstrated for the first time (Doll, 1955). Since then, numerous cohort and case control studies have unequivocally established a correlation between asbestos exposure and occupational lung diseases, resulting in the classification of all six forms of asbestos as carcinogenic to humans (Group 1) by the International Agency for Research on Cancer (IARC, 2012). Thus, the massive use of asbestos in countless industrial applications turned out to be a global problem, since the inhalation of its fibres may induce asbestosis, pleural plaques and effusions, malignant mesothelioma, and lung cancer after a latency period of decades (Manning et al., 2002).

In fact, the risk of developing asbestos-related diseases is extremely high for workers in fields with high asbestos exposure and for their families, due to the accumulation of dust on their work clothes. In addition, since asbestos was extensively used in the construction industry field prior to the restrictions implemented by several countries, the aging of such buildings may cause its fragments to be released in the environment creating a potential hazard. In fact, the microscopic bundles of fibres constituting asbestos may be released into the environment mainly by abrasion and, once they are inhaled, their short dimensions allow them to enter the upper and lower respiratory tracts. Some of the inhaled fibres are removed by the mucociliary clearance mechanism of the lungs but long thin asbestos fibres may reach the alveoli, where they can remain for many years, prompting the activation of the local immune system. For this reason, prolonged exposure to asbestos has been associated with chronic lung inflammation and tissue damage, oftentimes leading to various diseases in both lung and pleura, such as asbestosis, pleural plaques, pleural effusions, pleural fibrosis, diffuse malignant mesothelioma and lung cancer (Manning et al., 2002).

3.1. NON-MALIGNANT ASBESTOS-RELATED DISEASES

3.1.1. ASBESTOSIS

Pneumoconiosis is a general term used to identify a broad spectrum of pulmonary diseases characterised by interstitial fibrosis due to the inhalation of different mineral dust. For this reason, pneumoconiosis assumes specific names according to the type of noxious inhalant, such as coal (black lung or anthracosis), asbestos (asbestosis), silica dust (silicosis), iron (siderosis) or talc (talcosis). Indeed, the effect of mineral dust exposure on the lungs is influenced by their many variables, such as size, shape, solubility, and reactivity. For instance, it is unlikely that particles longer than 5 μm can reach the distal airways, whereas particles shorter than 0.5 μm are often exhaled without substantial deposition in the alveoli. However, particles that are 1-5 μm in diameter get lodged at the alveolar duct bifurcations and are engulfed by macrophages, although most inhaled dust is entrapped in the mucus and rapidly removed by the ciliary movements. Alveolar macrophages are known for their fundamental role in the initiation, and subsequent development, of lung injury and fibrosis since inhalable particles stimulate the release of mediators involved in the inflammatory response, fibroblast proliferation and collagen deposition. Thus, the main pathological consequences of pneumoconiosis include chronic pulmonary inflammation and progressive pulmonary fibrosis, which can eventually lead to impaired lung function and, depending on its extent and severity, to respiratory and cardiac failure. Moreover, although some medical treatments are aimed at slowing down pneumoconiosis progression and relieving symptoms, the lung damage cannot be reversed once the disease has been diagnosed. Pneumoconiosis usually manifests after years of dust exposure in the workplace environment and is therefore among the most common occupational diseases in the world, in particular in developing countries (Heppleston, 1988; Fujimura, 2000; Chong et al., 2006; Qi et al., 2021).

In particular, asbestosis results from a prolonged exposure to a relatively large amount of asbestos fibres, which penetrate deeply into the lungs prompting the activation of alveolar macrophages. However, due to asbestos natural resistance to degradation in the phagolysosome environment, the immune system is not able to remove the inhaled fibres, leading to a chronic inflammatory reaction. In fact, the macrophages release pro-inflammatory mediators (e.g., transforming growth factor [TGF]-β, tumour necrosis factor [TNF]-α, fibronectin, insulin-like growth factor [IGF]-1, platelet-derived growth factor [PDGF]), attracting more macrophages at the site of the injury and stimulating fibroblasts recruitment to synthesise fibrous scar tissue. This fibrotic scarring usually begins around terminal bronchioles and alveolar ducts and, in heavily exposed individuals, may even reach the alveolar walls, resulting in a reduction of the lung capacity due to their thickening. Moreover, characteristic findings of heavy asbestos exposure are the so-called asbestos bodies,

which typically appear as yellow-brown nodules in the septum of the alveolus after tissue staining. These microscopic structures usually have a rod- or dumbbell-shaped body with multiple segmentations, since they represent asbestos fibres that have been encased by macrophages in an iron-rich material derived from proteins such as ferritin and hemosiderin (Roggli et al., 2013; Weinberger et al., 2019). In patients with asbestosis, asbestos bodies are commonly seen by light microscopy, although in advanced cases they may be associated with cyst formation, subpleural honeycombing and pleural diseases. In fact, asbestosis continues to progress in the lung even if no further fibres are inhaled, with symptoms that become apparent only after a significant amount of time has passed from the initial exposure. Unfortunately, there is no cure available for asbestosis, only a palliative treatment of symptoms.

3.1.2. PLEURAL PLAQUES

Pleural plaques are non-cancerous well-circumscribed areas of hyaline fibrosis that form in the lining of the lungs after prolonged exposure to asbestos. They consist of mature collagen fibres densely arranged in an open basket-weave pattern, covered by flattened or cuboidal mesothelial cells. Although the pathogenesis of pleural plaques is yet to be completely understood, the most likely explanation is that accumulation of inhaled asbestos fibres in the pleural space through the lymphatic system irritates the lung tissue. Therefore, the pleural macrophages initiate an inflammatory reaction and, in the long term, induce collagen deposition leading to the substitution of the healthy lung parenchyma with fibrotic tissue. Additionally, nearly one in five patients experiences a partial calcification of the pleural plaques, due to the deposition of calcium in the thickened tissue over time. The majority of pleural plaques develop on the parietal pleura which lines the inside of the rib cage, although they are also found, albeit more rarely, on the visceral pleura enveloping the lungs and on the domes of the diaphragm. These hyaline growths are the most common evidence of past asbestos exposure, affecting up to 58% of asbestos-exposed workers (Peacock et al., 2000). Pleural plaques are typically asymptomatic and thus are often diagnosed because of incidental findings while performing chest X-ray or CT scans.

3.1.3. DIFFUSE PLEURAL THICKENING

Prolonged asbestos exposure may also be responsible for triggering diffuse pleural thickening, which is a non-circumscribed fibrous thickening of the visceral pleura leading to its adherence to the parietal pleura with the obliteration of the pleural space (Yates et al., 1996). According to the standard classifications, diffuse pleural thickening is characterised by unilateral or bilateral pleural thickening in continuity with an obliterated costophrenic angle and is conventionally diagnosed upon finding a continuous sheet of pleural thickening more than 5 cm wide, more than 8 cm long

and more than 3 mm thick, although these widespread fibrotic areas may extend up to the entirety of a lobe or lung (Currie et al., 2009; ILO, 2011). Their thickness ranges from less than 1 mm to more than 1 cm and is often associated with fibrous strands, known as crow's feet, extending for a few millimetres into the lung parenchyma from the thickened pleura (American Thoracic Society, 2004). Due to the sizable adhesions of the visceral and parietal layers of the pleura, this condition prevents the lungs from fully expanding and thus significantly impairs pulmonary function, causing a decrease in total lung capacity and in diffusing capacity (Kee et al., 1996; Yates et al., 1996).

3.1.4. PLEURAL EFFUSIONS

Diffuse pleural thickening is often preceded by pleural effusion, which is the build-up of fluid in the pleural space between the visceral and the parietal layers. This condition, known as benign asbestos pleural effusion, is prompted by an excessive production of pleural fluid due to asbestos exposure and the subsequent pulmonary irritation. In fact, in a physiological condition, the pleural fluid is continuously secreted by parietal pleural capillaries and is maintained by lymphatic absorption at a stable volume of 5–15 mL, in order to provide a functional vacuum between the layers of the pleura. Conversely, due to the accumulation of an excessive amount of fluid within the pleural space, the increased resistance against lung expansion may significantly impair the pulmonary function causing shortness of breath and pain. Although pleural effusions can sometime progress to diffuse pleural thickening, they are typically asymptomatic since they last a few months before spontaneously resolving, from which derives their classification as “benign” conditions. The diagnosis of benign asbestos pleural effusion is usually based on a history of asbestos exposure, paired with the presence of exudative effusion (often haemorrhagic with lymphocyte dominancy) and the exclusion of other possible causes, such as tuberculous pleuritis, bacterial pleuritis, collagen diseases, heart failure and malignant conditions (Epler et al., 1982; Hillerdal and Ozesmi, 1987; Roggli, 2013; Fujimoto et al., 2015).

3.2. ASBESTOS-RELATED MALIGNANCIES

According to the most recent report of the International Agency for Research on Cancer (IARC), asbestos is a well-established cause for four primary types of cancer, namely malignant mesothelioma, lung cancer, laryngeal cancer and ovarian cancer. In fact, although several studies have also suggested a correlation between asbestos exposure and the insurgence of malignancies in other organs (i.e., pharynx, stomach, colon and rectum), the experimental evidence has not yet unequivocally established asbestos role in inducing these types of cancers. Additionally, the exact pathogenesis of asbestos-related cancers, and its underlying mechanisms, are still not yet completely understood and thus regarded with intense interest (IARC, 2012).

Since asbestos particles are released into the environment mainly by abrasion, the most common asbestos-related cancers are malignant mesothelioma and lung cancer, both caused by the inhalation of asbestos fibres that penetrate deeply into the lung tissue. Due to their resistance to pulmonary clearance mechanisms and phagolysosome degradation, asbestos fibres remain in the pulmonary tissue leading to chronic inflammation and irritation. In fact, asbestos fibres are phagocytosed by epithelial cells and macrophages and, since they are characterised by the presence of active iron at their surface, the subsequent respiratory burst promotes the production of reactive oxygen species (ROS) via a Fenton-like reaction chain (Gualtieri, 2021).

In particular, the frustrated phagocytosis of long fibres induces a chronic ROS production which is thought to be partly responsible for asbestos carcinogenicity, since it damages proteins and DNA, causes membrane damage through lipid peroxidation and prompts fibre encapsulation by collagen and iron-rich proteins (Manning et al., 2002). Indeed, as a result of prolonged asbestos exposure, DNA accumulates multiple mutations in critical genes that can be divided in proto-oncogenes, which act as positive regulators of cell growth and invasion after they are activated by point mutations, chromosomal translocations and gene amplification, and tumour suppressor genes, which lose their function as negative regulators in cancer development due to their inactivation by chromosome loss, gene deletions and point mutations (Barrett, 1994). Moreover, it is likely that cellular responses to asbestos are partly the result of the multiple signalling pathways and transcription factors which are activated through ROS-dependent pathways (Manning et al., 2002).

Thus, the pathogenesis of asbestos-related cancers is associated with a persistent inflammatory response initiated directly or indirectly by ROS, cytokines, chemokines, growth factors and pro-inflammatory factors. For this reason, asbestos-related cancers typically develop after a long latency period from the exposure to its fibres and are often diagnosed after they have already metastasized throughout body, leading to a significant worsening of the outcome.

3.2.1. LUNG CANCER

Asbestos-related lung cancer is a malignant condition characterised by an uncontrolled cell growth in the lung which is clinically associated with asbestos exposure. In fact, asbestos has been associated with all major histological types of lung malignancies although asbestos-related lung cancer is virtually indistinguishable in both morphology and symptoms from lung cancer induced by other causes. Since cancer histological characteristics and its anatomic location have no diagnostic value in ascertaining whether asbestos is the primary cause of this condition, its identification is typically based on the parameters established in Helsinki Criteria for Diagnosis and Attribution. According to these guidelines, evidence of past asbestos exposure is a distinctive and

necessary marker, proven by the detection of a conspicuous amount of asbestos fibres in the lung tissue (i.e., a count of 5,000-15,000 asbestos bodies per gram of dry lung tissue, or an uncoated fibre burden of 2 million amphibole fibres (> 5 μm) per gram of dry lung tissue, or 5 million amphibole fibres (> 1 μm) per gram of dry lung tissue, or 5-15 asbestos bodies per mL of bronchoalveolar lavage fluid), by an occupational exposure exceeding 25 fibres/cm^3 of air per year, by a previous diagnosis of asbestosis or by the presence of pleural plaques. Interestingly, it should be noted that the recommendations involving fibre analysis apply only to amphibole fibres, since occupational history is considered a better indicator of lung cancer risk correlated with chrysotile exposure because of the faster clearance of its fibres from the pulmonary tissue. Finally, although the risk of developing lung cancer depends mainly on duration and intensity of asbestos exposure, there are several other crucial risk factors such as tobacco smoking and the individual susceptibility towards this malignancy (Wolff et al., 2015).

Clinical signs of lung cancer, and consequently of asbestos-related lung cancer, include chest pain, chronic cough (including coughing up blood), breathlessness, wheezing, chronic respiratory infections, weight loss and fatigue. The insurgence of asbestos-related lung cancer is associated with a long latency period (15-35 years), therefore the slow onset of its symptoms often leads to a misdiagnosis or an underestimation of the disease seriousness. In fact, the symptoms typically become detectable only after lung cancer has reached the late stage of its development and, additionally, they are sometimes mistakenly correlated to other illnesses hindering the diagnostic process. As a result of the difficult detection of asbestos-related lung cancer in the early stages, at the time of diagnosis, this malignancy often has already reached an advanced-stage, leading to a significant worsening of the outcome. In case of an early stage diagnosis, the treatment of choice is the surgical removal of the cancer by resecting a small portion of the lung (wedge resection), one of the lung lobes (lobectomy) or the entire lung (pneumonectomy). Conversely, when lung cancer has already spread from the initial tumour, care options include chemotherapy, radiotherapy and immunotherapy with pembrolizumab or nivolumab, since they are more apt at killing fast-growing cancer cells, slowing tumour growth and preventing the formation of further metastasis (Mamdani et al., 2022; Pastis et al., 2022; Rivera et al., 2022).

It has been estimated that asbestos-related lung cancer accounts for only a small percentage (3%-8%) of all lung cancers (McCormack et al., 2012). Nonetheless, lung cancer is the second most commonly diagnosed cancer and the leading cause of cancer death to this day, representing respectively the 11.4% of cancer diagnosis and the 18.0% of cancer deaths, which correspond approximately to 1.8 million deaths worldwide. Moreover, lung cancer prognosis is generally poor,

considering that in most countries only about 10%-20% of lung cancer patients survive after five years of being diagnosed (Sung et al., 2021).

Asbestos exposure has been associated with two main forms of primary lung cancer, conventionally distinguished in small cell lung cancer (SCLC) and non-small cell lung cancer (NSCLC) according to the dimension of their cells. However, in rare cases, lung cancer exhibits histological components of SCLC commingled with components of NSCLC and is therefore classified as combined small-cell lung carcinoma (C-SCLC), although it is usually treated as a "pure" SCLC (Travis et al., 2015).

Small Cell Lung Cancer (SCLC)

SCLC accounts for about 10%-15% of all lung cancer cases (Dayen et al., 2017). SCLC is an extremely aggressive carcinoma that mainly develops in the pulmonary hilum, involving the upper part of the respiratory tract. This form of lung cancer arises in the submucosal layer due to the malignant transformation of neuroendocrine cells belonging to the APUD system localised in the bronchial epithelium (Champaneria et al., 2006). As a result of its neuroendocrine nature, SCLC can produce large amounts of ectopic hormones (e.g. ACTH and ADH) promoting the insurgence of several paraneoplastic conditions, such as Cushing's syndrome, Lambert-Eaton myasthenic syndrome (LEMS) and the syndrome of inappropriate anti-diuretic hormone hypersecretion (SIADH) (Mitchell et al., 2007; Titulaer et Verschuuren, 2008).

SCLC cells have a round shape with well-defined margins, as well as a characteristic small size due to the scarce cytoplasm; the nuclear material is finely dispersed in the cells, while the nucleolus is often barely noticeable. Because of SCLC high mitotic rate, the formation of cell clusters with neither squamous nor glandular organization is a common histological finding. Genomic profiling of SCLC reveals extensive chromosomal rearrangements and a high mutation burden, almost always inducing the over-expression of the anti-apoptotic gene *Bcl-2* and the functional inactivation of the tumour suppressor genes *TP53* and *RB1*, therefore explaining the rapid neoplastic progression and the ability to elude apoptosis of this type of cancer. Moreover, SCLC expresses a variety of neuroendocrine markers such as chromogranin, synaptophysin and Leu-7 (Rosti et al., 2006; Robbins et al., 2005).

Due to its aggressive nature, at the time of diagnosis over two-thirds of SCLC patients already show metastatic growth in various organs such as liver, adrenal glands, bone and brain. For this reason, surgical removal is rarely an option and the treatment of SCLC is usually carried out employing chemotherapy and radiotherapy in order to reach cancer cells all throughout the body. According to its clinical and pathological characteristics, the stage of SCLC at the time of diagnosis is usually

classified in: localised (cancer well-circumscribed in the lung, known as limited stage SCLC); regional (cancer migrating from the lung has spread to lymph nodes within the chest, corresponding to an intermediate stage between limited and extensive stage SCLC); distant (cancer has metastasized to distant parts of the body, also identified as extensive stage SCLC). The American Cancer Society notes that the five-year survival rate for localised SCLC is 29%, while it drops to 3% when the cancer has already spread to distant parts of the body before detection. The overall five-year survival rate for SCLC is 7%, while the ten-year survival rate lowers to 3.5%, although it is influenced by individual factors including age, gender and race (American Cancer Society, 2022).

Non-Small Cell Lung Cancer (NSCLC)

NSCLC accounts for around 85% of all lung cancer cases and encompasses any type of epithelial lung cancer other than SCLC, due to their similar behaviour and prognosis. The most common histological types of NSCLC are adenocarcinoma, squamous-cell carcinoma and large-cell carcinoma, although there are several other types that occur less frequently, e.g., adenosquamous carcinoma, sarcomatous carcinoma, carcinoid tumour, salivary gland carcinoma and unclassified carcinoma (Pikor et al., 2013).

Adenocarcinoma accounts for about 40% of all lung cancers and arises from the malignant transformation of type II pneumocytes, which have a fundamental role in secreting pulmonary surfactants that reduce the surface tension in the alveoli and, for this reason, are characterised by the presence of secretory organelles known as lamellar bodies. Since adenocarcinoma insurgence appears to be stepwise, the earliest recognizable lesion is atypical adenomatous hyperplasia, which is a small well-circumscribed area of atypical epithelial proliferation with irregular borders. These pre-cancerous lesions typically form along the alveolar septa as a single cellular layer composed of cuboidal to low-columnar alveolar cells that resemble Clara cells or type II pneumocytes, although they may show various signs of cytologic atypia, such as hyperchromasia, pleomorphism and prominent nucleoli. Atypical adenomatous hyperplasia often progresses to adenocarcinoma in situ, a small non-invasive tumour that exhibits a localised distribution in the alveolar lining, prompting a lepidic growth which is characteristic of adenocarcinoma earliest stages. Since its growth is limited to the alveolar spaces with no invasion of the surrounding lung, it may be completely removed by surgical resection with an excellent prognosis; otherwise it may progress and become overtly invasive and malignant. Genomic profiling of adenocarcinoma reveals a plethora of mutations in oncogenes and tumour suppressor genes, copy number amplifications in oncogenes such as *TERT*, *MDM2*, *EGFR*, *MET* and *MYC*, deletions of tumour suppressor genes like *CDKN2A*, fusions or rearrangements in the membrane-

associated tyrosine kinase receptors *ALK*, *ROS1* and *RET* (Mitchell et al., 2007; Cancer Genome Atlas Research Network, 2014; Herbst et al., 2018).

Squamous-cell carcinoma represents about 25%-30% of all lung cancers and it originates from the neoplastic transformation of the respiratory epithelium lining the upper airways of the lung. The first clinical sign of its insurgence is the presence of squamous metaplasia, which causes the replacement of the ciliated pseudostratified columnar epithelium in the bronchi with a stratified squamous epithelium, formed by flattened cells arranged in several layers and thus more resistant to injury. As a result of the continuous exposure to noxious inhalants, squamous cells display an escalating degree of dysplasia, correlated with cytological abnormalities, loss of cellular maturation and increasing thickness of the epithelium. These premalignant lesions can progress to squamous carcinoma in situ, which is a non-invasive cancer characterised by variations in nuclear size and shape, uneven chromatin distribution, mitoses all throughout the stratified epithelium and discordance of maturation between nucleus and cytoplasm (dyskaryosis). When squamous carcinoma in situ is not removed through surgery or radiotherapy, it may advance to invasive squamous cell-carcinoma, which causes early metastasis in the adjacent lymph nodes, although its further spread in the body is slower in comparison to other types of lung cancer (Auerbach et al., 1961; Auerbach et aI., 1978; Saccomanno, 1982; Keith et al., 2000; Hirsch et al., 2001; Ishizumi et al., 2010; Gupta et al., 2019). Its genetic profiling shows an abundance of mutations and copy number alterations, mainly in pathways involved in the initiation and progression of the tumour, e.g. *KEAP1* and *NFE2L2*, belonging to the oxidative stress response pathways, are altered in 34% of the cases, while *SOX2*, *TP63* and *NOTCH1*, pertaining to squamous cell differentiation pathway, are altered in 44% of the tumours (Cancer Genome Atlas Research Network, 2012; Campbell et al., 2016)

Large-cell carcinoma accounts for about 5%-10% of all lung cancers and comprises a heterogeneous group of poorly differentiated malignancies lacking the cytological characteristics associated with adenocarcinoma, squamous-cell carcinoma or other cancers with well-defined histological properties. As a result, this type of lung cancer is mainly identified with a diagnosis of exclusion. Large cell carcinoma is considered a peripheral tumour due to its preferential well-circumscribed subpleural localization, although it rapidly spreads along the pleura metastasizing in mediastinal lymph nodes, bones, liver and, in very advanced cases, brain. Large-cell carcinoma cells appear large and round, with voluminous vesicular nuclei immersed in a moderate amount of eosinophilic cytoplasm. They are characterised by a high degree of anaplasia, associated with alterations in the regulatory pathways of *RAS*, *EGFR* and *PTEN* (DeVita et al., 2008). Moreover,

large-cell carcinoma often presents a neuroendocrine variant similar to SCLC, with specific alterations of *TP53* and *Bcl-2*, a typical palisade cell growth and neuroendocrine markers such as synaptophysin and chromogranin (Devereux et al., 1996).

Although this forms of cancer typically grow and spread more slowly than SCLC, about one-third of NSCLC patients already have metastases at the time of diagnosis. Since in most cases they are relatively insensitive to chemotherapy and radiotherapy, NSCLCs are mainly treated by surgical resection of the tumour, although recently chemotherapy has been increasingly employed both preoperatively and postoperatively (American Cancer Society, 2022).

Additionally, the clinical approach to NSCLC treatment is further influenced by the presence of mutations in the epidermal growth factor receptor (*EGFR*) and in the anaplastic lymphoma kinase (*ALK*). In fact, *EGFR* exhibits drug-sensitizing mutations in approximately 10%–35% of NSCLCs. When these mutations result in hyperactive forms of the protein, cancers are more likely to have adenocarcinoma histology and to be sensitized to drugs based on tyrosine kinase inhibitors that block the EGFR, such as erlotinib, gefitinib, afatinib and osimertinib. Conversely, 3%–7% of NSCLCs are characterised by *EML4-ALK* translocations or *ROS1* mutations that induce an abnormal activation of these tyrosine kinases. As a result, the vast majority of patients develops adenocarcinomas and is often successfully treated with ALK inhibitors like crizotinib, ceritinib, alectinib and lorlatinib. Since these two genetic markers are routinely profiled in NSCLC tumours, several studies have shown that *EGFR* activating mutations and *ALK* rearrangements are typically mutually exclusive, although they are increasingly reported together due to more sensitive detection methods, therefore estimating that 1.3% of NSCLC have both mutations (Kris, 2005; Hirsch and Bunn, 2009; Gainor et al., 2013; Gainor and Shaw, 2013). Other frequent alterations occur in genes belonging to the cell proliferation and survival pathway, including *KRAS*, *BRAF*, *HER2/neu*, and *MET*, that can be employed for targeted therapies in advanced stage cases (Yang et al., 2014).

In NSCLC, these genomic alterations are commonly interconnected with the epigenetic silencing of DNA repair genes. In fact, various cancers have been correlated with deficiencies in DNA repair mechanisms caused by mutations in DNA repair genes or more frequently by epigenetic alterations that reduce or silence their expression. Regarding NSCLC in particular, at least nine DNA repair genes are known to be repressed by promoter hypermethylation impairing homologous recombination repair, non-homologous end joining, base excision repair and mismatch repair, while *FEN1* is an essential enzyme in microhomology-mediated end joining, which is characteristically over-expressed due to the promoter hypomethylation (Nikolova et al., 2009; Gomes et al., 2014).

According to the American Cancer Society, the overall five-year survival rate for NSCLC amounts to 26%; in fact, the five-year survival rate for localised NSCLC is 64%, while it diminishes to 8% when the cancer exhibits metastasis at the moment of diagnosis (American Cancer Society, 2022).

Combined-Small Cell Lung Carcinoma (C-SCLC)

C-SCLC is a rare subtype of SCLC which is estimated to account for 2%-5% of all lung cancers, although the exact proportion of SCLCs with mixed histological features is still quite controversial. This malignant tumour is characterised by a combination of SCLC and NSCLC components, where the identified NSCLC subtype is typically adenocarcinoma, squamous cell carcinoma, large cell carcinoma or, albeit more rarely, sarcomatoid and giant cell carcinoma (Adelstein et al., 1986; Mangum et al., 1989; Nicholson et al., 2002; Zhao et al., 2017). In most cases of C-SCLC, the divergence of their morphological components occurs when a SCLC cell is transformed into a cell with the potential to develop NSCLC characteristics and, after acquiring further genetic and epigenetic alterations, the tumour develops cytohistological features of both SCLC and NSCLC.

Since SCLC is generally considered the most aggressive type of lung cancer due to its dreadful long term prognosis and survival rates, malignant lung tumours containing any proportion of SCLC cells are clinically classified as C-SCLC. In fact, while the overall survival rate between C-SCLC and pure SCLC is similar, C-SCLC patients have a better prognosis since surgery is the treatment of choice, unlike pure SCLC. Moreover, because of the NSCLC component, this type of cancer is relatively less sensitive to chemotherapy and radiotherapy, although targeted therapy has been successful in variants exhibiting *EGFR* mutations, which account for about 15%–20% of C-SCLC. Additionally, the majority of C-SCLC expresses estrogen and/or progesterone receptors that contribute to lung carcinogenesis promoting the progression of the established cancer (American Cancer Society, 2022).

3.2.2. MALIGNANT MESOTHELIOMA

Malignant mesothelioma is a rare aggressive cancer that originates in the mesothelium, which represents the epithelial lining protecting and enclosing the serous cavities of the body. Indeed, the mesothelium consists of a monolayer of flattened squamous-like cells that are specialised in the production of a lubricating fluid, which is entrapped by the microvilli on their luminal surface, providing a smooth surface for the movement of internal organs. Depending on the morphology of their cells, these malignancies are typically classified in three histological subtypes, namely epithelioid mesothelioma, accounting for approximately 50%–70% of cases; sarcomatoid mesothelioma, representing about 10%–20% of cases; and biphasic mesothelioma, amounting to roughly 20%–30% of cases. Although it represents the most common form of mesothelioma,

epithelioid mesothelioma seldom originates metastases, since it mainly grows as clusters of cuboidal cells with a single, well-defined nucleus in their centre. Therefore, it presents a more favourable prognosis and overall life expectancy with respect to sarcomatoid mesothelioma, which is an extremely aggressive form of cancer that spreads quickly to distant organs, resulting in a particularly difficult treatment. Indeed, while organised in fibrous nodes or discrete lesions, sarcomatoid cells commonly display a characteristic oval, spindle-like shape, which is frequently associated with the presence of multiple large nuclei. Lastly, biphasic mesothelioma comprises a combination of epithelioid and sarcomatoid cells, that are mainly distinguished by the immunohistochemical staining for calretinin, since it is an established diagnostic marker for epithelioid cells (Rdzanek et al., 2006; Kawai et al., 2016; American Cancer Society, 2022).

The insurgence of malignant mesothelioma is typically associated with a long latency period of approximately 20-50 years after the initial exposure to carcinogenic fibres. Indeed, according to the International Agency for Research on Cancer (IARC), the prolonged exposure to asbestos is indisputably considered the major cause of malignant mesothelioma, as evidenced by the fact that 80% of patients have been directly or indirectly exposed to its fibres in the past (Roggli et al., 2002). Furthermore, erionite has been correlated to the insurgence of malignant mesothelioma in the Cappadocia region of Central Anatolia, leading to the classification of this zeolite as carcinogenic to humans (Group 1) by the IARC. In fact, in Turkish villages where inhalable erionite fibres were detected in air samples, several studies reported an increased mortality due to malignant mesotheliomas, along with the detection of erionite fibres in the lungs of affected individuals (Panou et al., 2015).

Indeed, after these inhalable mineral fibres reach the parenchyma of the lung, they may lodge in the pleura causing a persistent state of inflammation that, coupled with the heightened proliferation of mesothelial cells due to macrophages releasing potent mitogenic factors (e.g., PDGF and TGF-β), may result in the development of cancerous lesions. As a result, pleural mesothelioma represents the most common type of mesothelioma, since about 75% of cases arise in the pleural tissue enveloping the lungs. Conversely, the mechanisms underlying the insurgence of peritoneal mesothelioma, which accounts for approximately 20% of cases, are yet to be completely understood, although it has been suggested that the mineral fibres may reach the abdominal lining through ingestion of contaminated sputum or transport from the lung via the lymphatic system. Moreover, in rare cases mesothelioma may also develop in the lining of the heart (i.e., pericardial mesothelioma) or the testes (i.e., testicular mesothelioma) (American Cancer Society, 2022).

According to its genomic profiling, mesothelioma exhibits a characteristic distribution in the numerical aberrations of its chromosomes, with monosomy of chromosome 22 and structural rearrangements in the 1p, 3p, 9p and 6q chromosome arms as the most common abnormalities (Lechner et al., 1997). In particular, several studies have found that the tumour-suppressor gene *BAP1*, which is located on the short arm of the chromosome 3, presents inactivating mutations in approximately 60% of mesothelioma cases, suggesting that its deficiency is correlated with an increased risk of developing cancer. Although its mechanism of action is still partially unknown, it has been hypothesized that BAP1 is implicated in chromatin modulation and transcriptional regulation during cell cycle progression through deubiquitination of the Histone H2A in nucleosomes and interaction with nuclear factors, such as HCFC1 (Cigognetti et al., 2015; Sahtoe et al., 2016).

Furthermore, the development of this malignancy has been correlated to the homozygous deletion and/or mutation of several tumour suppressor genes involved in the regulation of the cell cycle, such as *NF2* and *CDKN2A/ARF*. Indeed, approximately 40%−50% of mesotheliomas are characterised by inactivating mutations in *NF2* that encodes for Merlin, a scaffolding protein which is mainly located in adherens junctions, where it connects actin filaments to the cell membrane or to membrane glycoproteins. As a result, it has been hypothesized that its tumour suppressor properties may be associated with contact-mediated growth inhibition. In fact, when functioning properly, Merlin inhibits cell proliferation by repressing both *Cyclin D1* expression and CDK4 kinase activity, halting the cell cycle progression due to dephosphorylation, and thus activation, of pRB. Conversely, Merlin deficiency in malignant tumours prompts an aberrant upregulation of *Cyclin D1*, which promotes the advancement of the cell cycle by phosphorylating pRB and activating the transcription factor E2F1 (Xiao et al., 2005; Lin and Gutmann, 2013).

In this regard, another important tumour suppressor gene involved in the regulation of the cell cycle progression is *CDKN2A/ARF*, which encompasses two overlapping tumour suppressor genes frequently mutated or deleted in malignant mesothelioma. Among its several transcript variants, p16INK4 is an inhibitor of the cyclin-dependent kinase CDK4, while p14ARF promotes the transcriptional activity of the tumour suppressor protein p53 (Ouelle et al; 1995). p16INK4 displays a fundamental role in repressing cellular proliferation by indirectly allowing pRB to remain associated with E2F1, preventing the transition from G1 to S phase. In fact, in case of p16INK4 deficiency, the association between CDK4 and Cyclin D forms the active protein complex necessary for phosphorylating pRB, with the activation of the transcription factor E2F1 and the subsequent progression of the cell cycle (Witkiewicz et al., 2011; Rayess et al., 2012). p14ARF

exerts its tumour suppressing activity by sequestering HDM2, which represents the main inhibitor of p53 transcriptional activity. Furthermore, HDM2 belongs to the E3 ligase family and induces ubiquitination of p53, causing its exportation from the cell nucleus to the cytoplasm for degradation by the proteasome complex. By antagonizing HDM2, p14ARF promotes p53 transcriptional activity, which is involved in several crucial mechanisms preventing tumour development, such as cell cycle arrest and apoptosis (Zhang et al., 1998; Sherr, 2006; Zhang et Lu, 2009; Lo et al., 2015; Wienken et al., 2016).

Moreover, receptor tyrosine kinases are frequently overexpressed, such as *EGFR*, responsible for promoting angiogenesis, resistance to apoptosis, cellular proliferation and motility; *C-Met*, known for triggering tumour growth by stimulating angiogenesis and metastasis; *Axl*, implicated in tumour progression and epithelial-to-mesenchymal transition; *PDGFRB*, essential for vascular development (Jänne et al., 2002; Levallet et al., 2012; Pinato et al., 2013; Tsao et al., 2014; Davidson, 2015). Conversely, some of the hallmarks of most cancers are uncommon in malignant mesothelioma, for example activation of the *Ras* oncogene and inactivation of the tumour suppressor genes *TP53* or *RB1* (Nishiyama et al., 1995; Ni et al., 2000; Papp et al., 2001; Mossman et al., 2013).

The most common clinical signs of pleural mesothelioma include chest pain, chronic cough, haemoptysis, breathlessness, wheezing, accumulation of fluid in the pleural space, weight loss and fatigue; however, as these symptoms are quite common in a variety of lung conditions, sometimes they may be mistakenly ascribed to other illnesses. In most cases mesothelioma is already too widespread at diagnosis to be removed completely by surgery; therefore, the treatment of choice typically entails surgical resection in combination with radiotherapy and/or chemotherapy. Extra pleural pneumonectomy is potentially the most effective method to surgically remove all cancer cells, since it involves the removal of the lung on the side of the cancer, along with the corresponding section of parietal pleura lining the inside of the chest. In addition, part of the diaphragm and the pericardium are removed as well, although they are usually rebuilt with synthetic materials or autologous tissues afterwards. This operation is mainly employed in cases of epithelioid mesothelioma that has not spread to the lymph nodes but, considering that it causes substantial complications in about one-third of patients, it is rarely performed. As a result, a less invasive operation is preferred, pleurectomy/decortication where the surgical resection concerns the pleura enveloping the affected lung, the mediastinum and the diaphragm, while the lung parenchyma and the diaphragm muscle are not removed (Mossman et al., 2013).

Since this malignancy is extremely aggressive, radiotherapy and chemotherapy are frequently given simultaneously as a consolidative treatment in addition to surgery, either preoperatively or

postoperatively. For mesothelioma, chemotherapy typically requires a combination of two different types of drugs, a platinum compound (e.g., cisplatin or carboplatin) and an antifolate (e.g., pemetrexed or raltitrexed). Other than through intravenous delivery, chemotherapy may be directly administered intrapleurally or intraperitoneally so that the malignant cells receive the highest concentration of drugs. In particular, in hyperthermic chemotherapy the drugs are heated to 40−48°C before the treatment, which may occur right after surgical resection of the cancer in a procedure known as heated intraoperative chemotherapy that is frequently used for peritoneal mesothelioma. For cancers that cannot be removed with surgery, the main treatment is chemotherapy, although the Food and Drug Administration (FDA) recently approved immunotherapy based on a combination of nivolumab and ipilimumab, two monoclonal antibodies that act in synergy to decrease tumour growth by enhancing T cell function since they block the target proteins PD-1 and CTLA-4, respectively (Vogelzang et al., 2003; Mossman et al., 2013; Nakajima et al., 2022).

Nonetheless, malignant mesothelioma has a poor prognosis, since the overall five-year survival rate for pleural mesothelioma is approximately 12% and the average life expectancy is between 12 and 21 months, depending on the stage of disease at diagnosis. In fact, while the five-year survival rate for patients diagnosed with localised cancer amounts to 20%, this rate decreases to 16% in case the cancer has spread to nearby organs and it further diminishes to 8% in individuals with metastasis in distant parts of the body, such as the pleura of the other lung, liver or bones (American Cancer Society, 2022). However, when patients with pleural mesothelioma receive a multimodal treatment based on surgery in combination with chemotherapy and radiotherapy, their life expectancy increases from 13.7 months to 23.4 months in case of epithelioid mesothelioma, from 5 months to 10.8 months in case of sarcomatoid mesothelioma and from 8.1 months to 13.9 months in case of biphasic mesothelioma (Nelson et al., 2017).

3.2.3. LARYNGEAL CANCER

Laryngeal cancers account for only a small percentage of malignancies (2%-3%). They are mainly squamous-cell carcinomas caused by chronic exposure to noxious inhalants, which induce the neoplastic transformation of the squamous cells lining the three parts of the larynx, namely the supraglottis, the glottis and the subglottis. The International Agency for Research on Cancer (IARC) recognised asbestos as a proven cause of laryngeal cancer in 2006. In fact, since inhaled asbestos fibres pass though the larynx along their descent to the lungs, they can easily become lodged in its respiratory epithelium, causing a persistent state of irritation and inflammation which promotes the insurgence of squamous-cell carcinomas. Moreover, the chronic inflammation induced

by tobacco-smoking, alone or in combination with alcohol consumption, damages the protective cellular layer of the larynx, predisposing to the accumulation and deposition of asbestos fibres (IARC, 1988; IARC, 2004; Institute of Medicine (US), 2006).

According to the site of insurgence, laryngeal cancers exhibit slightly different clinical signs, although the most common symptoms are shortness of breath, severe coughing, difficulty swallowing, choking, voice hoarseness and chronic pneumonia. Therefore, laryngeal cancers are easily detectable, often leading to an early diagnosis while they are still well-circumscribed to the cells lining the larynx and thus significantly improving the effectiveness of the subsequent treatment. Among the therapeutic procedures available, several types of surgery are commonly employed with a high success rate, such as endoscopic surgery, vocal cord stripping, laser surgery, partial or total laryngectomy. Moreover, radiotherapy can be used in the early stages in order to remove the cancer without risking further damage to the vocal cords by performing a surgical resection, while chemotherapy is the treatment of choice when laryngeal cancer has already reached an advanced stage and metastasized to lungs, liver or bones. Additionally, chemotherapy and radiotherapy are frequently applied in combination with surgery both preoperatively and postoperatively (American Cancer Society, 2022).

As a result of early detection and treatment, the overall five-year survival rate for laryngeal cancer amounts to approximately 60%. In fact, the five-year survival rate for glottic cancer amounts to 77%, while it decreases to 46% for supraglottic cancer and to 49% for subglottic cancer (American Cancer Society, 2022).

3.2.4. OVARIAN CANCER

Ovarian cancer accounts for only a small percentage of malignancies (1.6%). Although there are different types of ovarian cancer according to the site of insurgence, the most common malignant form is epithelial ovarian carcinoma, which accounts for 85%-90 % of cases and develops on the outer surface of the ovary. The International Agency for Research on Cancer (IARC) recognised asbestos as a proven cause of ovarian cancer in 2009, due to several studies reporting a significant increase in the insurgence of ovarian cancer in women directly exposed to its fibres in the working environment or indirectly exposed through their digestive, respiratory and reproductive tracts (Acheson et al., 1982; Wignall and Fox, 1982; Germani et al., 1999; Berry et al., 2000; Langseth et al., 2007; Magnani et al., 2008; IARC, 2012).

Whereas the exact mechanism explaining how asbestos fibres reach the ovaries is still under debate, it has been suggested that inhaled or ingested fibres may be transported through the bloodstream and/or the lymphatic system. Additionally, asbestos fibres may localise in the ovaries by travelling

through the reproductive tract because of the application of asbestos-contaminated talcum powder to the genitals after showering or bathing, although this hypothesis has not been completely ascertained (O'Brien et al., 2020; Vimercati et al., 2021). In particular, since asbestos-contaminated talcum powder has shown to cause cancer after a prolonged inhalation, it is also suspected of being one important source of exposure in ovarian cancer. Indeed, seeing that asbestos and talc are created by the same geological processes, it is quite common to find underground formations of the two minerals so closely together that the mining practices cannot keep them separated. As a result, the asbestos naturally present in many sources of talc went undetected for years, resulting in the manufacture and distribution to the public of products containing asbestos-contaminated talc.

The most frequent symptoms of ovarian cancer include bloating, pelvic pain, abdominal swelling, constipation and loss of appetite; however they are often confused for clinical signs of more common illnesses, resulting in a delay of its diagnosis. Moreover, the diagnostic process is further hindered because of ovarian cancer similarities with other malignancies, such as peritoneal mesothelioma, which is also caused by asbestos. In fact, despite the recent improvements in the pathological techniques, the differential diagnosis between peritoneal mesothelioma and ovarian cancer is still challenging, leading to their misclassification in several cases (Slomovitz et al., 2021).

Regardless of the subtype of ovarian cancer, in case of well-differentiated malignant tumours confined to the ovary, treatment usually involves surgical resection. Conversely, for more aggressive cancers where complete removal is not an option, the tumour mass is reduced as much as possible in a procedure called debulking surgery, which sometimes implies the partial removal of other organs as well, such as the small intestine, colon, liver, bladder, spleen and/or gallbladder. Additionally, debulking surgery is frequently combined with radiotherapy or, more routinely, chemotherapy to better reach the remaining cancer cells. For ovarian cancer, chemotherapy typically requires the intraperitoneal or intravenous administration of a combination of two different types of drugs, a platinum compound (e.g., cisplatin or carboplatin) and a taxane (e.g., paclitaxel or docetaxel) (American Cancer Society, 2022).

The overall five-year survival rate for all stages of ovarian cancer is approximately 49%. In fact, while the five-year survival rate for patients diagnosed with cancer localised to a single ovary amounts to 93%, this rate decreases to 75% in case the cancer has spread to other parts of the pelvis, and it further drops to 31% in individuals with late-stage cancer characterised by distant metastasis (American Cancer Society, 2022).

4. SCOPE OF THE PROJECT

Since the toxicity and carcinogenicity of mineral fibres is profoundly interwoven with a broad variety of crystal-chemical-physical characteristics, the long-term project "*FIBRES: A multidisciplinary mineralogical, crystal-chemical and biological project to amend the paradigm of toxicity and cancerogenicity of mineral fibres*" has been in progress since 2017, with the purpose of investigating the biogeochemical mechanisms through which mineral fibres, and especially asbestos, induce adverse effects *in vivo*. This thesis, which has been conceptualised and carried out within the aforementioned Italian Research Project of National Interest (PRIN), aims at obtaining a more in-depth understanding of the biochemical mechanisms underlying the cytotoxic and genotoxic effects caused by the exposure to different types of mineral fibres.

In particular, the first part of this work focused on the acute damaging effects of three carcinogenic mineral fibres, i.e., Union for International Cancer Control (UICC) standard crocidolite, chrysotile from Balangero mine (Turin, Italy) and erionite from Jersey (Nevada, USA). These mineral fibres, which are respectively representative of the classes of amphibole asbestos, serpentine asbestos and fibrous erionite, are all classified as carcinogenic to humans (Group 1) by the International Agency for Research on Cancer (IARC), although the mechanisms by which they induce cytotoxic and genotoxic damage are not yet completely understood. Therefore, the first part of this study aimed at investigating the different possible toxicity mechanisms exerted by these mineral fibres during the first 24 h of exposure by performing a comparative study in an *in vitro* THP-1 cellular model of M0, M1 and M2 macrophages. In fact, all three macrophage phenotypes (i.e., non-activated M0, pro-inflammatory M1 and alternatively activated M2 cells) can be present at the site of injury and contribute to the outcome of the inflammatory process. Thus, the cytotoxic action of these mineral fibres was studied by measuring the level of cell death by either cell lysis or apoptosis in THP-1-derived macrophages. Then, the intracellular oxidative state, the intracellular toxic metal release, the presence of DNA damage and the inflammatory response were evaluated, since they are recognised factors that occur early during the cell-fibre interaction, contributing to instauration of an inflammatory response which may result in the onset of chronic diseases and malignancies in the long term.

For the second part of this project, representative batches of short (length < 5 μm) and long (length > 5 μm) chrysotile fibres were prepared by cryogenic milling of a commercial chrysotile extracted from an open pit mine near Yasny (Russia). Then, the cytotoxic and genotoxic activity of these size-separated fractions of chrysotile was investigated *in vitro* in comparison to UICC crocidolite, an amphibole asbestos commonly employed as a positive carcinogenic standard, and to wollastonite

NYAD G, a calcium inosilicate mineral characterised by non-biodurable fibres, scarce metal content and low toxicity (Di Giuseppe et al., 2021b). To this aim, their potential damaging effects were studied in an *in vitro* cellular model based on human THP-1-derived M0 macrophages and HECV endothelial cells, both separately as well as in a co-culture setup. In fact, alveolar macrophages are the first line of defence against detrimental inhaled stimuli since they rapidly localise at the site of injury and initiate the inflammatory process by releasing pro-inflammatory mediators. Apart from recruiting circulating leukocytes, these chemokines promote the activation of the surrounding pulmonary endothelium, which contributes to the instauration of a persistent inflammatory state by prompting the extravasation of immune cells into the tissue parenchyma. Moreover, while the pulmonary vasculature can be indirectly stimulated by pro-inflammatory factors secreted by other cell types in response to asbestos fibres, it can also be damaged by the direct contact with fibres that accumulate along capillaries, embed into endothelial cells, or penetrate within the capillary lumen (Treadwell et al., 1996). Therefore, the cytotoxic activity of the two size-separated fractions of chrysotile was investigated by measuring the level of cell death by either cell lysis or apoptosis in M0 macrophages and HECV cells. Afterwards, the intracellular oxidative state, the presence of DNA damage and the inflammatory response were evaluated in the two cell lines. Moreover, the effect of the pro-inflammatory mediators secreted by asbestos-treated M0 macrophages on HECV endotheliocytes was examined in a co-culture system at several time points (24 h, 48 h, and 7 days).

5. MATERIALS AND METHODS

5.1. CHEMICALS

All reagents were acquired from SIGMA-ALDRICH (Milan, Italy), unless otherwise stated.

5.2. MINERAL FIBRES

The following mineral fibres have been selected for this study:

– UICC standard crocidolite (South Africa, NB #4173-111-3) with chemical formula $(Na_{1.96}Ca_{0.03}K_{0.01})_2(Fe^{2+}_{2.34}Fe^{3+}_{2.05}Mg_{0.52})_{4.91}(Si_{7.84}Al_{0.02})_{7.86}O_{21.4}(OH)_{2.64}$. It is characterised by long fibres (mean length of 16.1 µm and width of 0.64 µm), high density (3.3 g/cm^3), very high iron content (FeO=17.42 wt% and Fe_2O_3=17.87 wt %), and high biodurability (estimated dissolution time of 66 years for a 0.25 µm thick fibre). Sample contains minor impurities of hematite, magnetite, and quartz (Gualtieri et al., 2018b; Pacella et al., 2019).

– Chrysotile from Balangero (Turin, Italy) with chemical formula $(Mg_{5.81}Fe^{2+}_{0.15}Al_{0.27}Fe^{3+}_{0.09}Cr_{0.01})_{6.33}Si_{3.97}O_{10}(OH)_{7.11}$. It has very long fibres (mean length of 34.7 µm and width of 0.59 µm), low density (2.53 g/cm^3), scarce iron content (FeO=2.50 wt% and Fe_2O_3=0.40 wt%), and low biodurability (estimated dissolution time of 124 days for a 0.25 µm thick fibre). Sample contains minor impurities of antigorite, balangeroite, calcite, clinochlore, diopside, dolomite, magnetite, microcline, plagioclase, and talc (Pollastri et al., 2016; Gualtieri et al., 2018b).

– Fibrous erionite-Na from Jersey (Nevada, USA) with chemical formula $(Na_{5.35}K_{2.19}Ca_{0.15}Mg_{0.11}Ti_{0.05})_{7.85}(Si_{28.01}Al_{7.90})_{35.91}O_{72}\cdot 28.13H_2O$. It is characterised by short fibres (mean length of 9.4 µm and width of 0.55 µm), low density (2.11 g/cm^3), minimal iron content (FeO=0.12 wt% and Fe_2O_3=0.30 wt%), and high biodurability (estimated dissolution time of 181 years for a 0.25 µm thick fibre). Sample contains traces of clinoptilolite (Gualtieri et al., 2016; Pollastri et al., 2016).

– Fibrous wollastonite NYAD G from Willsboro-Lewis mining district (New York, USA) with chemical formula $(Ca_{0.997}Fe^{2+}_{0.0053}Fe^{3+}_{0.0024}Mn_{0.0025}Mg_{0.0009}Si_{0.9786}O_3)$. It has very long fibres (mean length of 46.6 µm and width of 3.74 µm), high density (2.98 g/cm^3), minimal iron content (FeO=0.33 wt% and Fe_2O_3=0.17 wt%), and low biodurability (estimated dissolution time of 30 days for a 0.25 µm thick fibre) (Di Giuseppe et al., 2021b).

– Chrysotile from Yasny (Orenburg Oblast, Russia) with chemical formula $(Mg_{2.870}Fe^{2+}_{0.027}Fe^{3+}_{0.044}Al_{0.034}Cr_{0.005}Ni_{0.006})_{2.986}(OH)_4Si_{1.982}O_5$. It is characterised by very long fibres (mean length of 33.9 µm and width of 0.70 µm), low density (2.58 g/cm^3), scarce iron content (FeO=0.70 wt% and Fe_2O_3=1.27 wt%), and low biodurability (estimated dissolution time of 129 days for a 0.25 µm thick fibre). Sample contains minor impurities of lizardite, magnetite, hydromagnesite, and possibly calcite (Di Giuseppe et al., 2021c).

In particular, the first part of this study focused on UICC standard crocidolite (South Africa, NB #4173-111-3), chrysotile from Balangero (Turin, Italy) and fibrous erionite-Na from Jersey (Nevada, USA). Conversely, the mineral fibres selected for the second part of this study were UICC standard crocidolite (South Africa, NB #4173-111-3), wollastonite NYAD G (New York, USA) and chrysotile extracted from an open pit mine near Yasny (Russia) by the Orenburg Minerals company. Two fractions of Orenburg chrysotile were prepared by cryogenic milling, which produces fibres of a precise size while preserving the physical-chemical properties of the original fibre. Since fibre length is strictly regulated by the milling time under cryogenic conditions, the short fraction (CHR-S, 95% L < 5 μm) was obtained by cryogenic milling for 40 min, while the long fraction (CHR-L, 88% L > 5 μm) required a milling time of 10 min (Scognamiglio et al., 2021).

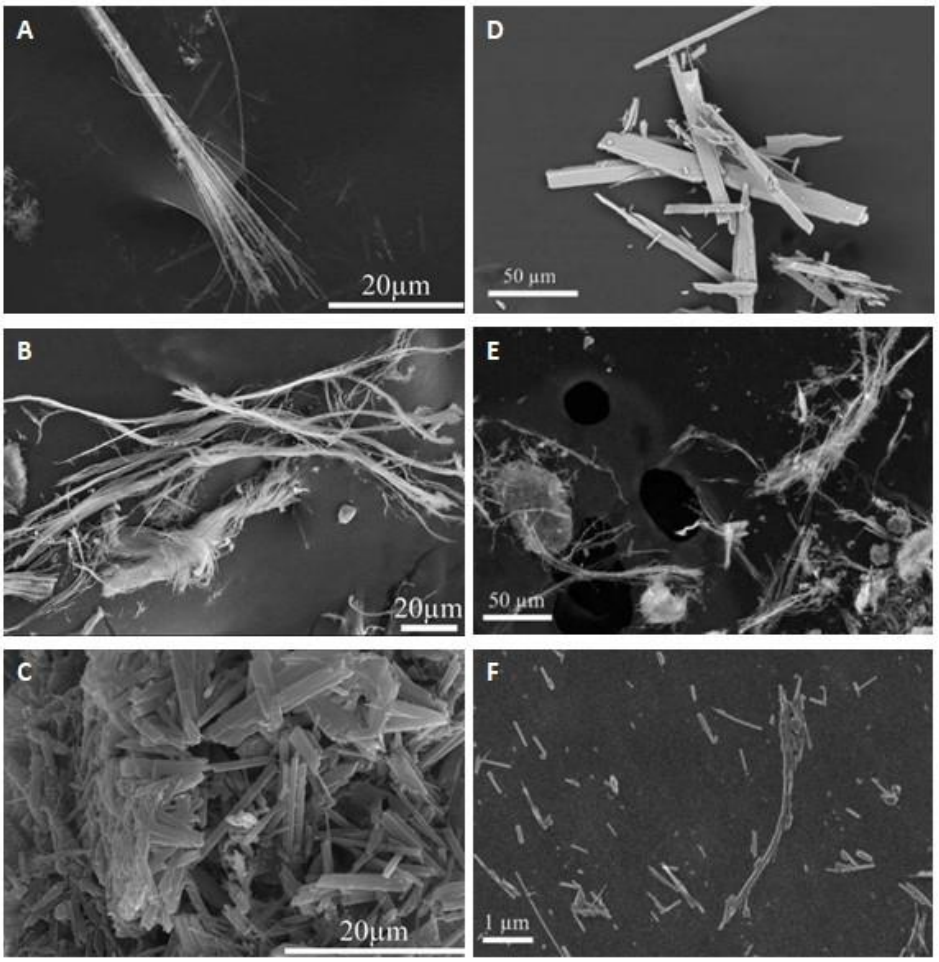

Figure 1. High-resolution FEG-SEM microphotographs of the investigated mineral fibres. (**A**) UICC standard crocidolite (South Africa, NB #4173-111-3), from Di Giuseppe et al. (2021a). (**B**) Chrysotile from Balangero (Turin, Italy), from Di Giuseppe et al. (2021a). (**C**) Erionite-Na from Jersey (Nevada, USA), from Di Giuseppe et al. (2021a). (**D**) Fibrous wollastonite NYAD G from Willsboro-Lewis mining district (New York, USA), from Di Giuseppe et al. (2021b). (**E**) Chrysotile from Yasny (Orenburg Oblast, Russia) after 10 min of cryogenic milling (CHR-L, 88% L > 5 μm), from Scognamiglio et al. (2021). (**F**) Chrysotile from Yasny (Orenburg Oblast, Russia) after 40 min of cryogenic milling (CHR-S, 95% L < 5 μm), from Scognamiglio et al. (2021).

5.3. CELL CULTURE

The human monocytic cell line THP-1 and the human vascular endothelial cell line HECV used in this study were obtained from the American Type Culture Collection (LGC Standards srl, Milan, Italy) and cultured at 37 ◦C in a humidified 5% CO_2 atmosphere. THP-1 cells were cultured in RPMI-1640 with 2 mM L-glutamine (Euroclone, Milan, Italy) supplemented with 10% FBS (Euroclone), 50 μM β-mercaptoethanol and penicillin/streptomycin as antibiotics (Corning Inc, Corning, NY, USA), whereas HECV cells were cultured in high glucose DMEM with 2 mM L-glutamine (Biowest, Nuaillé, France), supplemented with 10% FBS (Euroclone) with penicillin/streptomycin as antibiotics (Corning Inc).

5.4. MACROPHAGES DIFFERENTIATION

To evaluate the biological responses of differentiated macrophages in contact with mineral fibres, THP-1 monocytes were induced to polarise into non-activated M0 macrophages by adding 20 ng/mL phorbol-12-myristate 13-acetate (PMA, PeproTech EC, London, UK) to the culture medium. After 48 h, non-adherent cells were removed, and M0 macrophages were either employed for experiments or further polarised to pro-inflammatory M1 macrophages by treatment with 20 ng/mL interferon-gamma (IFN-γ) and 200 ng/mL lipopolysaccharide (LPS) for 24 h, or to alternatively activated M2 macrophages by using 20 ng/mL interleukin 4 (IL-4, PeproTech EC, London, UK) for 24 h (Morón-Calvente et al., 2018; Baxter et al., 2020).

5.5. CELL–FIBRE INTERACTION IMAGING AND FIBRE SURFACE CHARACTERISATION

For the detection and identification of the different mineral fibres with Micro-Raman spectroscopy, THP-1 monocytes were seeded at 300,000 cells/well in 6-well plates containing a 24 × 24 mm glass coverslip. Briefly, a 200 μL drop containing 300,000 cells was seeded on each coverslip, and after 2 h at 37 ◦C, the rest of the medium was added to the wells of the 6-well plate before the macrophages were differentiated as described above. Following their incubation with 50 μg/mL of fibres for 24 h, cells were washed twice with PBS and then fixed with 4% paraformaldehyde in PBS at 4 ◦C. After 2 h, the glass coverslips were washed three times with sterile deionised water, and once the paraformaldehyde was completely removed, the coverslips were dried under a laminar flow hood. Micro-Raman measurements were performed with a HORIBA Jobin Yvon LabRam (HORIBA Scientific, Kyoto, Japan) confocal micro-spectrometer (300 mm focal length) with an integrated Olympus BX40 microscope with 4×, 10×, 50× ULWD and 100× objectives, 1800 grooves/mm grating, an XY motorised stage and a Peltier cooled silicon CCD. The Raman signals of the fibres were acquired in two spectral ranges: the lattice and internal vibrational modes were collected in the

low-wavenumber spectral range (120–1200 cm^{-1}) by using a He-Ne 632.8 nm laser line as the excitation source; the OH stretching signals were detected in the high-wavenumber spectral range (2700–4000 cm^{-1}) by using a frequency-doubled Nd:YAG 473.1 nm laser line to distinguish the mineral phase among varieties whose spectra are similar in the low range. The system was calibrated with the 520.6 cm^{-1} Raman peak of silicon in the low-wavenumber range and with the emission lines of a gas lamp in the high-wavenumber range. The spectral resolution was ~2 cm^{-1} with the 632.8 nm line and ~4 cm^{-1} with the 473.1 nm line. The minimum spatial resolution was ~1 µm using the 100× objective. To avoid heating effects, density filters were used to reduce the laser power. The typical accumulation time was 60 s repeated 10 times. Data analysis was performed with the LabSpec 5 software. The fluorescence background was removed by subtracting a polynomial curve as the baseline. The Raman signals were deconvoluted with Gaussian–Lorentzian curves to determine the peak parameters and identify the mineralogical phases.

5.6. CELL VIABILITY WITH CALCEIN GREEN-AM

To measure the short-term cytotoxicity of mineral fibres, THP-1 monocytes were seeded in eight-well Lab-Teck chambered slides (Nalge Nunc Int., Naperville, IL, USA) at a density of 75,000 cells/well. After their differentiation, the macrophages were incubated with 50 µg/mL of fibres for 4 h, and then stained with 2 µM calcein green-AM (Life Technologies, Milan, Italy) following the manufacturer's instructions. To assess cell viability, confocal microscopy images were obtained using a Leica TCS SL confocal microscope equipped with an HCX PL APO CS 20.0× objective (Leica Microsystems, Wetzlar, Germany). Indeed, images of living cells (2.5 × digital zoom) were acquired in single stacks, both in phase-contrast mode and in fluorescence mode, acquiring the green fluorescence of calcein green-positive cells in the emission range of 500–550 nm.

5.7. CYTOTOXICITY ASSESSMENT BY MTT

To evaluate the cytotoxic effect of the exposure to crocidolite, chrysotile from Balangero and fibrous erionite, THP-1 monocytes were seeded in quadruplicate at 50,000 cells/well in 96-well plates and differentiated in M0, M1 and M2 macrophages according to the aforementioned treatments. Subsequently, the three mineral fibres (10 µg/mL, 50 µg/mL and 100 µg/mL final concentrations) were added to each well, and the plates were incubated for 24 h at 37 ◦C. Conversely, the cytotoxicity induced by crocidolite, wollastonite and the two factions of Orenburg chrysotile was evaluated in HECV endotheliocytes and in M0 macrophages at different time points. Briefly, HECV cells were seeded in quadruplicate at 10,000 cells/well in 96-well plates, whereas THP-1 cells were plated in quadruplicate at 50,000 cells/well in 96-well plates and induced to polarise into M0 macrophages. Then, the four different types of mineral fibres (25 µg/mL, 50

µg/mL and 100 µg/mL final concentrations) were added to each well, and the plates were incubated for 24 h or for 48 h. At the end of the experiments, cell viability was evaluated by the MTT assay (0.5 mg/mL final concentration) as previously reported in Pozzolini et al. (2016). Data are the means ± SD of three independent experiments performed in quadruplicate.

5.8. PLASMA MEMBRANE DAMAGE ASSESSMENT WITH LDH

Plasma membrane perturbation, which can lead to cell lysis, was quantified by measuring LDH release in the cell media through the quantification of enzymatic activity. Briefly, THP-1 cells and HECV cells were seeded in quadruplicate on 96-well plates, and the experiment was performed as described for the MTT assay. After 24 h or 48 h of incubation with the different mineral fibres, the LDH release in the cell media was measured by transferring 100 µL of cell medium from each well into wells of a new 96-well plate and adding 100 µL of assay buffer (686 µM iodonitrotetrazolium chloride, 291 µM 1-methoxyphenazine methosulphate, 1.35 mM µ-NAD and 55.5 mM lithium L-lactate in 200 mM TRIS, pH 8.2). The plate was then incubated at room temperature for 30 min, and then the reaction was blocked by adding 50 µL of 1 M acetic acid. The absorbance was read at 490 nm in a plate reader (BMG Labtech, Ortenberg, Germany). Data are the means ± SD of three independent experiments performed in quadruplicate.

5.9. APOPTOSIS DETECTION BY CONFOCAL MICROSCOPY

The level of cell apoptosis was assessed by confocal microscopy imaging using the annexin/propidium iodide staining as reported in Scarfì et al. (2020). Indeed, THP-1 monocytes were plated at 75,000 cells/well in eight-well Lab-Teck chambered slides and induced to polarise into the different macrophage phenotypes, whereas HECV cells were seeded at 10,000 cells/well in the same conditions. After cells were incubated with the mineral fibres (10 µg/mL or 50 µg/mL) for 24 h, they were stained with the Annexin V, FITC Apoptosis Detection Kit (Dojindo EU, Munich, GmbH) according to the manufacturer's instructions. Images were acquired employing a Leica TCS SL confocal microscope with argon/He-Ne laser sources and an HCX PL APO CS 20.0 × objective. The images of apoptotic cells (2.5 × digital zoom) were obtained in phase-contrast mode and in fluorescence mode, acquiring the green fluorescence of annexin-positive cells and the red fluorescence of propidium iodide-positive cells (emission range of 500–550 nm and 600–670 nm, respectively) in single stacks. In the resulting images, early apoptotic cells (i.e., annexin-positive and propidium iodide-negative cells) were detected by a purely green fluorescence, while late apoptotic cells (i.e., annexin-positive and propidium iodide-positive cells) were identified by a concomitant green/red fluorescence.

5.10. ROS INTRACELLULAR DETECTION

The intracellular production of ROS induced by the exposure to mineral fibres was measured as described in De La Fuente et al. (2020). Briefly, HECV endotheliocytes were seeded at 10,000 cells/well in 96-well plates, whereas THP-1 monocytes were plated at 50,000 cells/well in 96-well plates and differentiated according to the aforementioned treatments. After being washed once with HBSS, cells were incubated for 45 min at 37 ◦C with 10 µM 2',7' -dichlorodihydrofluorescein diacetate dye in HBSS (Life Technologies) and then washed with HBSS to remove excess dye. ROS production was evaluated after 2 h of exposure to 100 µg/mL of mineral fibres at 37 ◦C, while the positive control was treated with 200 µM H_2O_2. Then, the plates were read on a FLUOstar® Omega multi-mode microplate reader (BMG Labtech) with 485/520 excitation/emission wavelengths. Data are the means ± SD of two independent experiments, in which each condition was tested eight times.

5.11. EVALUATION OF DNA DAMAGE

Since mineral fibres are known to induce genotoxic damage, the double-strand breaks in DNA were analysed by evaluating nuclear γ-H2AX histone foci. Indeed, THP-1 cells were seeded in eight-well Lab-Teck chambered slides at a density of 75,000 cells/well, and the differentiated macrophages were incubated with 50 µg/mL of fibres. After 24 h, cells were stained with anti-gamma H2AX antibody (Abcam, Cambridge, UK), while the nucleus was coloured with 2 µg/mL propidium iodide. Images were obtained with a Leica TCS SL confocal microscope equipped with an HCX PL APO CS 63.0 × 1.40 oil objective. In the acquired nuclei images (4.0 × digital zoom), the fluorescent foci of double-strand breaks in DNA are green and the propidium iodide-positive nuclei are red (excitation at 488 nm for both and emission range of 500–550 nm and 600–670 nm, respectively).

5.12. INTRACELLULAR SILICATE QUANTIFICATION

The intracellular levels of silicic acid released by the mineral fibres during phagocytosis were quantified as described in Scarfì et al. (2009). Briefly, THP-1 cells were seeded in 12-well plates at 200,000 cells/well and, after their differentiation into M0 macrophages, they were treated with 50 µg/mL of mineral fibres for 24 h. Afterwards, cells were washed twice with 0.9% NaCl, and their content was extracted with 1 mM perchloric acid. This extract was then centrifuged at 12000× g in a microfuge, and silicic acid in the supernatant was quantified using the Spectroquant® Silicate (Silicic Acid) Test (Merck KGaA, Darmstadt, Germany) according to the manufacturer's instructions. Absorbance was measured at 650 nm using a Beckman spectrophotometer (DU 640),

and the silicic acid concentration was obtained by comparison with a calibration curve based on different concentrations of sodium metasilicate (0.1–5 µg/mL). Data are the means ± SD of three independent experiments performed in duplicate.

5.13. INTRACELLULAR TRACE METAL QUANTIFICATION

The concentration of metals was evaluated in the cell lysate of M0 macrophages treated for 24 h with mineral fibres. Indeed, THP-1 monocytes were seeded in 10 cm plates at 3×10^6 cells/plate and induced to polarise into M0 cells that were then incubated with mineral fibres at a final concentration of 50 µg/mL. After 24 h, their content was extracted with 3 mL of 1 mM perchloric acid and the cell lysate was centrifuged at maximum speed for 10 min to remove debris and fibres. Concentrations of Al, Fe, Mg, Ni, Co and Cr in the cell lysate were determined using a Thermo Scientific iCAP™ TQ Inductively Coupled Plasma–Mass Spectrometer (ICP-MS). The iCAP TQ ICP-MS was configured to ensure the detection of analytes even at low concentrations and with small amounts of sample. Prior to measurements, plasma and interface settings were automatically tuned using the dedicated Thermo Scientific software. The analyses were conducted with the application of TQ-O_2 and SQ-KED measurement modes. TQ-O_2 is triple quadrupole mode with collision/reaction cell (CRC) pressurised with oxygen as a reaction gas. SQ-KED is single quadrupole mode with CRC pressurised with helium as a collision gas and kinetic energy discrimination (KED) applied.

5.14. EXTRACELLULAR RELEASE OF INFLAMMATORY CYTOKINES

To measure the extracellular release of cytokines involved in the inflammatory process, THP-1 monocytes were seeded in 12-well plates at 200,000 cells/well, and the differentiated macrophages were treated with 50 µg/mL of mineral fibres for 24 h. The content of IL-1β, MCP-1 and TNF-α in the cell media was quantified by ELISA kit (Human IL-1beta ELISA Kit, TNF-alpha Human ELISA Kit and Human MCP1 SimpleStep ELISA® Kit, Abcam) following the manufacturer's instructions. Data are the means ± SD of two independent experiments performed in duplicate.

5.15. CO-CULTURE VIABILITY WITH MTT

To obtain a better understanding of the cytotoxic effect exerted on HECV cells by the molecular mediators secreted by M0 macrophages in response to mineral fibres, the viability of a co-culture setup with M0 macrophages and HECV endotheliocytes was assessed at different time points, namely 24 h, 48 h and 7 days. Indeed, the co-culture was prepared seeding HECV cells in quadruplicate at 50,000 cells/well (24 h and 48 h time points) or at 10,000 cells/well (7 days' time point) in 24-well plates, whereas M0 macrophages were differentiated from THP-1 cells plated at

100,000 cells/well in Transwell® PET inserts with a 0.4 μm-pore size (Greiner Bio-One, Milan, Italy). Afterwards, the mineral fibres were added to M0 macrophages at a final concentration of 50 μg/mL (24 h and 48 h time points) or 10 μg/mL (7 days' time point). At the end of the experiments, cell viability was evaluated by the MTT assay (0.5 mg/mL final concentration) as previously described (Pozzolini et al., 2016).

5.16. RNA EXTRACTION, cDNA SYNTHESIS AND qPCR ANALYSES

To evaluate the mRNA production of pro-inflammatory cytokines, THP-1 monocytes were seeded in 6-well plates at 500,000 cells/well, and once differentiated, the macrophages were incubated with 50 μg/mL of mineral fibres for 6 h, 24 h and 48 h, or with 10 μg/mL of mineral fibres for 7 days. Moreover, the gene expression profile of HECV endotheliocytes both directly exposed to mineral fibres and co-cultured with fibre-treated M0 macrophages was assessed at different time points. Briefly, HECV cells were seeded in 6-well plates at 250,000 cells/well (24 h and 48 h time points) or at 100,000 cells/well (7 days' time point), with or without M0 macrophages differentiated from THP-1 cells plated at 250,000 cells/well in Transwell® PET inserts with a 0.4 μm-pore size (Greiner Bio-One, Milan, Italy). Afterwards, the mineral fibres were added to HECV endotheliocytes (direct exposure) or to M0 macrophages (co-culture setup) at a final concentration of 50 μg/mL for 24 h and 48 h, or 10 μg/mL for 7 days.

In both THP-1-derived macrophages and HECV endotheliocytes, the gene expression profile of inflammatory mediators interleukin-1β (IL-1β, a.n. NM_000576.3), interleukin-6 (IL-6, NM_031168.2), interleukin-8 (IL-8, NM_000584.4), tumour necrosis factor-alpha (TNF-α, a.n. NM_000594.4) and monocyte chemoattractant protein-1 (MCP-1, NM_002982), was evaluated by qPCR relative to untreated cells. Moreover, in HECV endotheliocytes the gene expression of transforming growth factor-beta 2 (TGF-β2, a.n. NM_001135599.3), intercellular adhesion molecule-1 **(**ICAM-1, a.n. NM_000201.2), vascular endothelial growth factor (VEGF, a.n. NM_001025370.1), fibronectin (FIBRO, a.n. NM_002026), alpha-smooth muscle actin (α-SMA, a.n. NM_001141945.1), collagen 1A (COL-1A, a.n. NM_000088.3) and matrix metalloproteinase-9 (MMP-9, a.n. NM_004994.2) was likewise evaluated by qPCR relative to untreated cells. Total RNA was extracted using the NucleoSpin RNA, Mini kit (MACHEREY-NAGEL, Dueren, Germany) according to the manufacturer's instructions. The quality and quantity of RNA were analysed using a NanoDrop spectrophotometer (Nanodrop Technologies, Wilmington, DE, USA). The cDNA was synthesised from 1 μg of RNA by using an iScript cDNA Synthesis Kit (Bio-Rad Laboratories, Milan, Italy). Each PCR reaction was performed in 10 μL containing: 4× master mix (biotechrabbit GmbH, Henningsdorf, Germany), 0.2 μM of each primer and 5 ng of cDNA. All

samples were analysed in triplicate. The following thermal conditions were used: initial denaturation at 95 ◦C for three minutes, followed by 45 cycles with denaturation at 95 ◦C for 15 s, and annealing and elongation at 60 ◦C for 60 s. The fluorescence was measured at the end of each elongation step. Values were normalised to HPRT-1 (housekeeping gene, a.n. NM_000194.3) mRNA expression for THP-1-derived macrophages, whereas they were normalised to GAPDH (housekeeping gene, a.n. NM_002046) mRNA expression for HECV endotheliocytes. All primers (Table 1) were designed using the Beacon Designer 7.0 software (Premier Biosoft International, Palo Alto, CA, USA) and obtained from TibMolBiol (Genova, Italy). Data analyses were obtained using the DNA Engine Opticon® 3 Real-Time Detection System Software program (3.03 version), and to calculate the relative gene expression compared to the untreated control sample, the comparative threshold Ct method was used (Vandesompele et al., 2002) with the Gene Expression Analysis for iCycler iQ Real Time Detection System software (Bio-Rad, Milan, Italy).

GENE	GenBank (a.n.)	Forward	Reverse	Size (bp)
IL-1β	NM_000576.3	TGATGGCTTATTACAGTGGCAATG	GTAGTGGTGGTCGGAGATTCG	140
IL-6	NM_001318095.2	CAGATTTGAGAGTAGTGAGGAAC	CGCAGAATGAGATGAGTTGTC	194
IL-8	NM_000584.4	AATTCATTCTCTGTGGTATC	CCAGGAATCTTGTATTGC	127
TNF-α	NM_000594.4	GTGAGGAGGACGAACATC	GAGCCAGAAGAGGTTGAG	113
MCP-1	NM_002982	CTTCTGTGCCTGCTGCTC	CTTGCTGCTGGTGATTCTTC	156
TGF-β2	NM_001135599.3	AACCTCTAACCATTCTCTACTACA	CGTCGTCATCATCATTATCATCA	149
ICAM-1	NM_000201.2	CAACCGGAAGGTGTATGAAC	CGAGGTGTTCTCAAACAGCTC	390
VEGF	NM_001025370.1	TTCGGGCTGTTCTCGCTTC	CTCTCCTCTTCCTTCTCTTCTTCC	142
FIBRO	NM_002026	CCAGCAGAGGCATAAGGTTC	GGTCAAAGCACGAGTCATCC	95
α-SMA	NM_001141945.1	TTGAGAAGAGTTACGAGTTG	GGACATTGTTAGCATAGAGG	189
COL-1A	NM_000088.3	CTTTGCATTCATCTCTCAAACTTAG TTTT	CCCCGCATGGGTCTTCA	163
MMP-9	NM_004994.2	AACCAATCTCACCGACAGG	CGACTCTCCACGCATCTC	85
HPRT-1	NM_000194.3	GGTCAGGCAGTATAATCCAAAG	TTCATTATAGTCAAGGGCATATCC	144
GAPDH	NM_002046	CCTGTTCGACAGTCAGCCG	CGACCAAATCCGTTGACTCC	100

Table 1. List of primer pairs used for qPCR experiments in human THP-1-derived macrophages and in human HECV endotheliocytes.

5.17. STATISTICAL ANALYSIS

Statistical analysis was performed using one-way ANOVA plus Tukey's post-test (GraphPad Software, Inc., San Diego, CA, USA). Results with p values < 0.05 were considered significant.

6. ACUTE TOXICITY OF MINERAL FIBRES: RESULTS AND DISCUSSION

To refine the existing models explaining the toxicity and pathogenicity of mineral fibres, it is of paramount importance to obtain a better understanding of the fine biochemical mechanisms through which mineral fibres, and especially asbestos, induce adverse effects *in vivo*. For this purpose, a valuable experimental model is the human monocytic cell line THP-1, since these cells are easily polarised into the different macrophage phenotypes (i.e., non-activated M0, pro-inflammatory M1 and alternatively activated M2 cells). Over the years, this *in vitro* cell model has been extensively employed for investigating the acute toxicity and the inflammatory response in human macrophages challenged with carcinogenic mineral fibres (Di Giuseppe et al., 2021a). Nonetheless, to date, no comparative data have been obtained from the concomitant analysis of the inflammatory response induced by different mineral fibres in the three macrophage phenotypes. In fact, the previous studies focused on THP-1-derived M0 macrophages which were usually exposed to the most important commercial asbestos fibres, namely chrysotile and crocidolite (Dostert et al., 2008; Li et al., 2012; Ventura et al., 2020; Ito et al., 2021; Larson-Casey et al., 2021). However, non-activated M0, pro-inflammatory M1 and alternatively activated M2 macrophages can all be present at the site of injury and contribute to the outcome of the inflammatory process.

Therefore, in the first part of this project, the three macrophage phenotypes obtained from THP-1 cell differentiation were used to study the acute effects of three carcinogenic mineral fibres, namely Union for International Cancer Control (UICC) standard crocidolite, chrysotile from Balangero mine (Turin, Italy) and erionite from Jersey (Nevada, USA). These mineral fibres are respectively representative of the classes of amphibole asbestos, serpentine asbestos and fibrous erionite, which are all classified as carcinogenic to humans (Group 1) by the International Agency for Research on Cancer (IARC). Although they are recognised toxic and pathogenic agents, the mechanisms by which they induce cytotoxic and genotoxic damage are not yet completely understood. Therefore, this study aimed at investigating the different possible toxicity mechanisms exerted by these mineral fibres during the first 24 h of exposure by performing a comparative study in an *in vitro* THP-1 cellular model of M0, M1 and M2 macrophage phenotypes. At first, their cytotoxic action was studied by measuring the level of cell death by either cell lysis or apoptosis. Subsequently, the intracellular oxidative state, the intracellular toxic metal release, the presence of DNA damage and the inflammatory response were evaluated, since these processes occur early during the inflammatory response and contribute to the onset of chronic diseases and malignancies in the long term.

6.1. CELL–FIBRE INTERACTION IMAGING AND FIBRE SURFACE CHARACTERISATION

In all three types of polarised macrophages (M0, M1 and M2), the mineral fibres were detected inside the cells and identified by micro-Raman analyses after 24 h of incubation. As expected, chrysotile (CHR), crocidolite (CRO) and erionite (ERI) fibres showed different morphologies (Figure 1A).

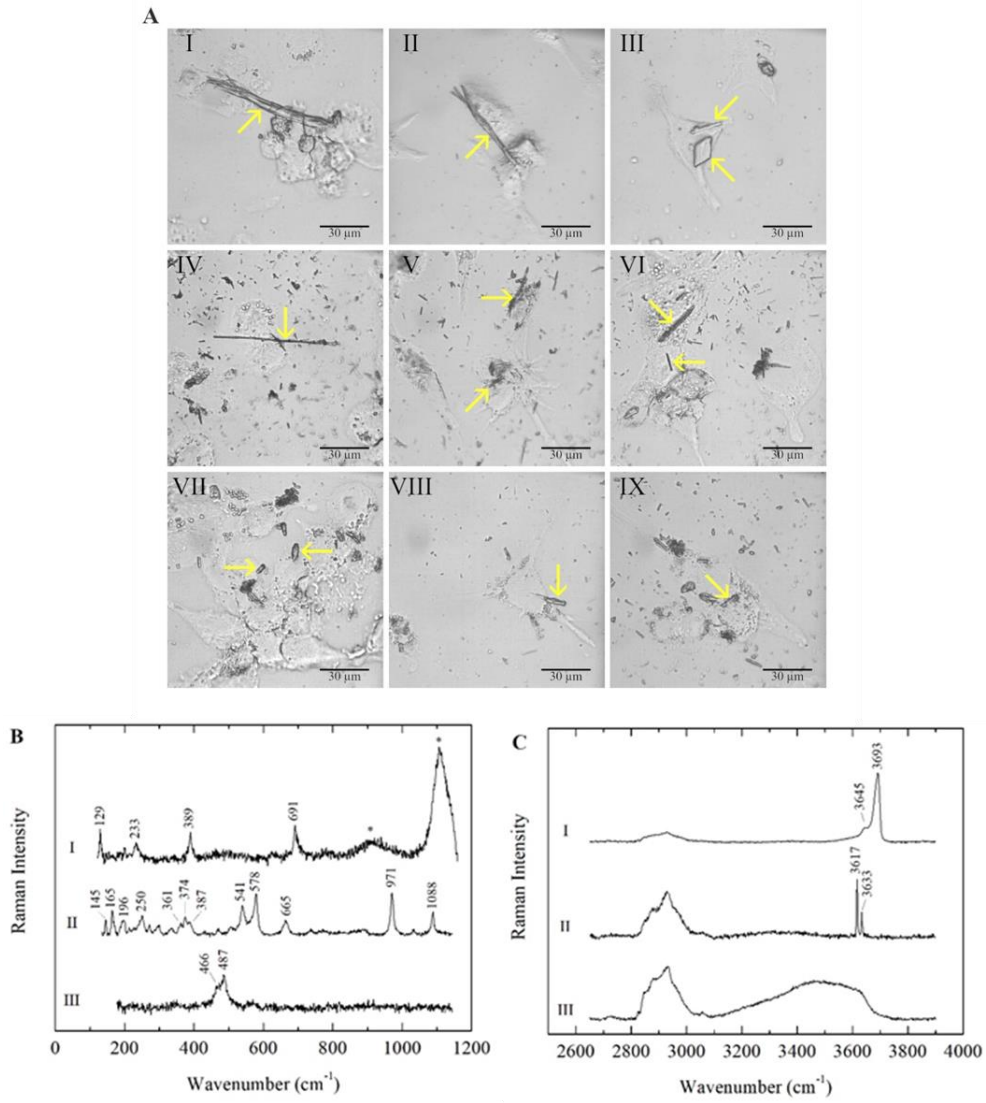

Figure 1. (**A**) Microscope images of M0, M1 and M2 macrophages in the presence of mineral fibres chrysotile, crocidolite and erionite. Panels I-II-III: chrysotile-treated M0, M1 and M2 macrophages, respectively. Panels IV-V-VI: crocidolite-treated M0, M1 and M2 macrophages, respectively. Panels VII-VIII-IX: erionite-treated M0, M1 and M2 macrophages, respectively. Typical morphologies of the fibres are highlighted with yellow arrows. The scale bar represents 30 µm. (**B**) Raman spectra of the mineral fibres chrysotile (I), crocidolite (II) and erionite (III) in M0 macrophages, acquired in the low-wavenumber spectral range. Photoluminescence bands of Cr^{3+} emissions are marked with asterisks (*). (**C**) Raman spectra of the mineral fibres chrysotile (I), crocidolite (II) and erionite (III) in M0 macrophages, acquired in the high-wavenumber spectral range. The Raman bands between ~2800 and 3100 cm^{-1} are attributed to CH stretching modes due to the cellular signals.

In all three investigated mineral fibres, impurities consisting of non-fibrous micrometric crystals were detected inside the cells along with fibrous phases, as previously reported in the literature (Table 1). In CHR-treated macrophages, bundles of curvilinear chrysotile fibres with splayed/frayed terminations and thinner and shorter single fibres were observed (Figure 1A, panels I, II and III); minor contributions of other minor fibrous and lamellar phases (balangeroite and antigorite, respectively) were also detected in addition to the non-fibrous content. CRO fibres showed a thin and rigid morphology with variable lengths (Figure 1A, panels IV, V and VI). ERI fibres were typically shorter than the other mineral fibres, exhibiting a more uniform size distribution (Figure 1A, panels VII, VIII and IX). The mineral fibres inside the three types of differentiated phagocytic cells were identified by their characteristic Raman spectra, acquired in both the low- and high-wavenumber spectral ranges, and the positions of the main peaks were highlighted (Figure 1B and 1C). For serpentine minerals, the lattice and internal vibrational modes were similar in different polymorphs, demonstrating that OH stretching signals are distinctive characteristics for the identification of the mineralogical phase in CHR-treated cells (Petriglieri et al., 2015; Rinaudo and Croce, 2019). In addition to CHR (curve I in Figure 1B and 1C), the lamellae of antigorite and balangeroite fibres were detected as minor contributions (Table 1) (Groppo and Compagnoni, 2007). Additionally, micrometric crystals consisting of impurities were observed in CHR-treated macrophages, highlighting the presence of iron compounds (Table 1) (Pollastri et al., 2016). Furthermore, in the low range, it was possible to detect the photoluminescence bands of Cr^{3+} emissions at ~671 and 680 nm due to the presence of chromium as a trace element in the CHR fibres (marked with asterisks in curve I in Figure 1B) (Bloise et al., 2016). In CRO-treated macrophages, CRO was identified by its peculiar Raman spectrum (curve II in Figure 1B and 1C)

Mineral fibre	**Impurities**	**Fibre Length (µm)**	**Fibre Width (µm)**
Chrysotile (Balangero, Turin, Italy)	Antigorite, balangeroite, calcite, clinochlore, diopside, dolomite, magnetite, microcline, plagioclase, talc, mackinawite, hematite, ilmenite, lepidocrocite, Fe-Ni sulphide, Fe-Mg carbonate	Min: 4.02 Mean: 34.7 Max: 188	Min: 0.18 Mean: 0.59 Max: 1.17
Crocidolite (UICC)	Hematite, magnetite, quartz, talc, lizardite, calcite, siderite, minnesotaite	Min: 2.52 Mean: 16.1 Max: 131	Min: 0.23 Mean: 0.64 Max: 1.98
Erionite (Jersey, Nevada, USA)	Clinoptilolite, iron-rich nanoparticles, iron oxides/hydroxides, nontronite	Min: 3.23 Mean: 9.39 Max: 55.0	Min: 0.25 Mean: 0.55 Max: 6.70

Table 1. General information on the mineral fibres investigated in this study. Impurities detected in the present work and in (Gualtieri et al., 2016; Pollastri et al., 2016; Della Ventura et al., 2018; Pacella et al., 2019). Fibre lengths and widths as reported in Di Giuseppe et al. (2021a).

(Croce et al., 2018; Lewis et al, 1996), and minor phases—including iron-bearing micro-crystals—were observed (Table 1) (Della Ventura et al., 2018; Pacella et al., 2019). Erionite was the main fibrous mineral phase detected in ERI-treated macrophages, with minor tabular clinoptilolite (Tsai et al., 2021). Here, iron-bearing impurities— as identified in SEM and TEM analyses in previous studies (Gualtieri et al., 2016)—were not observed through micro-Raman analyses, as they are generally smaller than the minimum detectable size, considering the spatial resolution of the spectrometer. It is noteworthy that for all three types of polarised macrophages, the Raman signals of cells were always found along with those of the analysed mineral fibres, and no differences in the signals were detected for each mineral fibre in the three types of differentiated macrophages. Cellular signals were especially clear from their CH stretching bands in the spectral range ~2800–3100 cm^{-1} (Figure 1C).

6.2. ACUTE TOXICITY OF MINERAL FIBRES

To analyse the cell viability and the phagocytic ability of M0, M1 and M2 macrophages, the differentiated cells were incubated with the three mineral fibres. After 4 h of incubation, we used calcein-AM staining—a green-fluorescent dye used to label live cells—to determine if the phagocytic cells had engaged and internalised the particles and if this had already affected cell viability (Figure 2).

For all three macrophage types, M0 (Figure 2A), M1 (Figure 2B) and M2 (Figure 2C), there were no differences in fluorescence positivity between control cells (panels AI-II, BI-II and CI-II for M0, M1 and M2 macrophages, respectively) and fibre-treated cells (panels III-IV CRO, panels V-VI CHR and panels VII-VIII ERI, respectively). In fact, in all experimental conditions, cells showed intense green cytoplasmic fluorescence, meaning that after 4 h of treatment with the fibres, no signs of cytotoxicity were visible yet. Nonetheless, in all types of macrophages, it was possible to observe the presence of the different types of mineral fibres inside the cytoplasm of the cells when the size of the fibres was short enough to allow their phagocytosis. From a qualitative point of view, M2 macrophages showed a higher number of mineral fibres dispersed at the bottom of the well, especially for CRO (panel C-IV) and ERI (panel C-VIII), compared to M0 and M1 macrophages (panels A and B), which had already captured many fibres or were in direct contact with them. The observed phenomenon may indicate that M2 macrophages are less able to engulf the mineral fibres compared to the other two phenotypes. This is plausible since this type of macrophage polarisation should have a more anti-inflammatory role (Laskin et al., 2019).

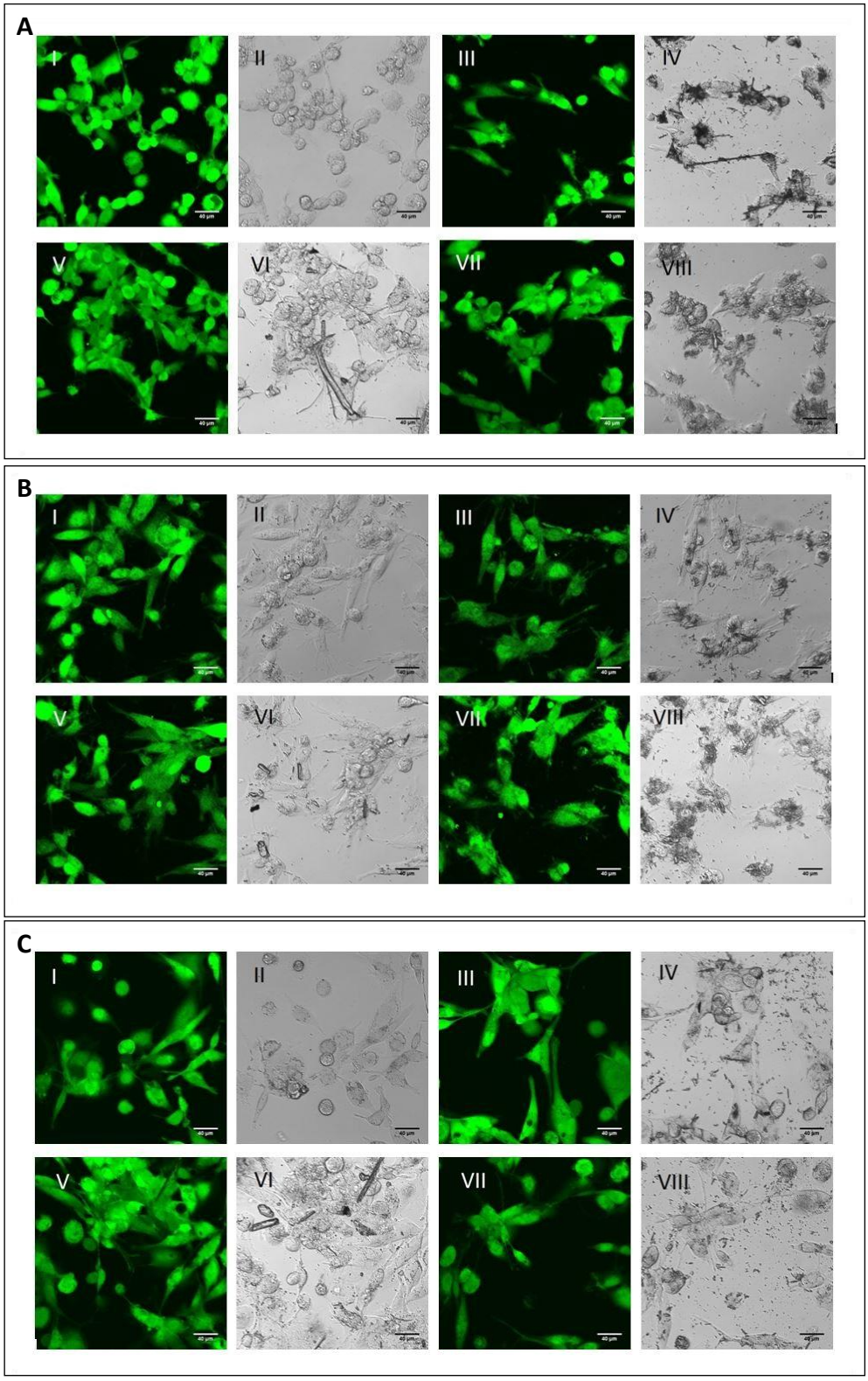

Figure 2. Qualitative evaluation of the short-term cytotoxicity. (**A**) Visualization by confocal microscopy analysis (2.5 × digital zoom) in fluorescence mode (panels I-III-V-VII) and in phase contrast (panels II-IV-VI-VIII) of M0 macrophages following 4 h incubation in the presence or absence of mineral fibres at 50 µg/mL and staining with calcein-AM. Panel I-II: Control; panel III-IV: CRO; panel V-VI: CHR; panel VII-VIII: ERI. The white bar represents 40 µm. (**B**) Visualization of pro-inflammatory M1 macrophages in the same conditions as cells in panel (**A**). (**C**) Visualization of alternatively activated M2 macrophages in the same conditions as cells in panel (**A**).

Since the qualitative assessment of macrophage viability by calcein staining showed no significant signs of toxicity after 4 h of fibre treatment, the MTT test was used to evaluate the cytotoxic effects of CRO, CHR and ERI (Figure 3, panels A–C, black, grey and white bars, respectively) in macrophages after 24 h. This assay measures mitochondrial enzyme activity by quantifying resultant alterations of energy metabolism and, ultimately, cell death. The viability index showed that there was a dose-dependent toxic effect resulting in a significant cell death rate in both M0 and M1 macrophages after exposure to all three fibres, while CRO exhibited a similar behaviour only in M2 cells. In M0 macrophages (Figure 3A, black bars), CRO caused a dose-dependent cell death rate of 57%, 49% and 22% at 100, 50 and 10 µg/mL, respectively, compared to control cells. Similarly, CHR (grey bars) induced cell death rates of 49%, 46% and 14% at the same fibre concentrations compared to control cells. In M0 macrophages, ERI (white bars) showed slightly lower toxicity compared to asbestos fibres, with significant death rates (45% and 35%) only at the two highest fibre concentrations (100 and 50 µg/mL, respectively) compared to control cells. Exposure to the three mineral fibres also induced a relevant cytotoxic effect in M1 macrophages (Figure 3B). The dose-dependent cell death rate after exposure to CRO was higher in M1 cells than in M0 cells (66%, 49% and 14% at 100, 50 and 10 µg/mL, respectively, compared to control cells). CHR at 100 and 50 µg/mL was also more cytotoxic in M1 than in M0, with cell death percentages ranging from 61% to 53%, respectively, compared to control cells. Regarding ERI, a strong cytotoxic effect was observed at 100 and 50 µg/mL (68% and 41%, respectively, compared to control cells). M2 macrophages (Figure 3C) demonstrated a dose-dependent cytotoxic effect during exposure to CRO, although the cell death rates were lower than those found in M0 and M1 cells, with percentages ranging from 30% to 21% at 100 and 50 µg/mL, respectively, compared to control cells. CHR showed minor but significant cytotoxicity; cell death values were similar at all concentrations and around 14–15% compared to control cells ($p < 0.005$ vs. C for all). Finally, ERI slightly induced cell death in M2 cells only at 100 and 50 µg/mL, with a 19% reduction in viability at both concentrations compared to control cells ($p < 0.05$ vs. C for both).

Overall, CRO and CHR showed a higher acute toxicity rate, strongly affecting energy metabolism and causing a significant cell death rate, than ERI in M0, M1 and M2 macrophages. In particular, for CRO treatment, our results are in line with a previous work (Ventura et al., 2020), where a similarly high THP-1 macrophage cytotoxicity rate was observed in the first 24 h of exposure. Furthermore, lower fibre-induced cytotoxicity was observed in M2 macrophages compared to the other two phenotypes; this finding can be ascribed to their anti-inflammatory role and consequent lower phagocytic activity, leading to a reduced cell death rate due to frustrated phagocytosis.

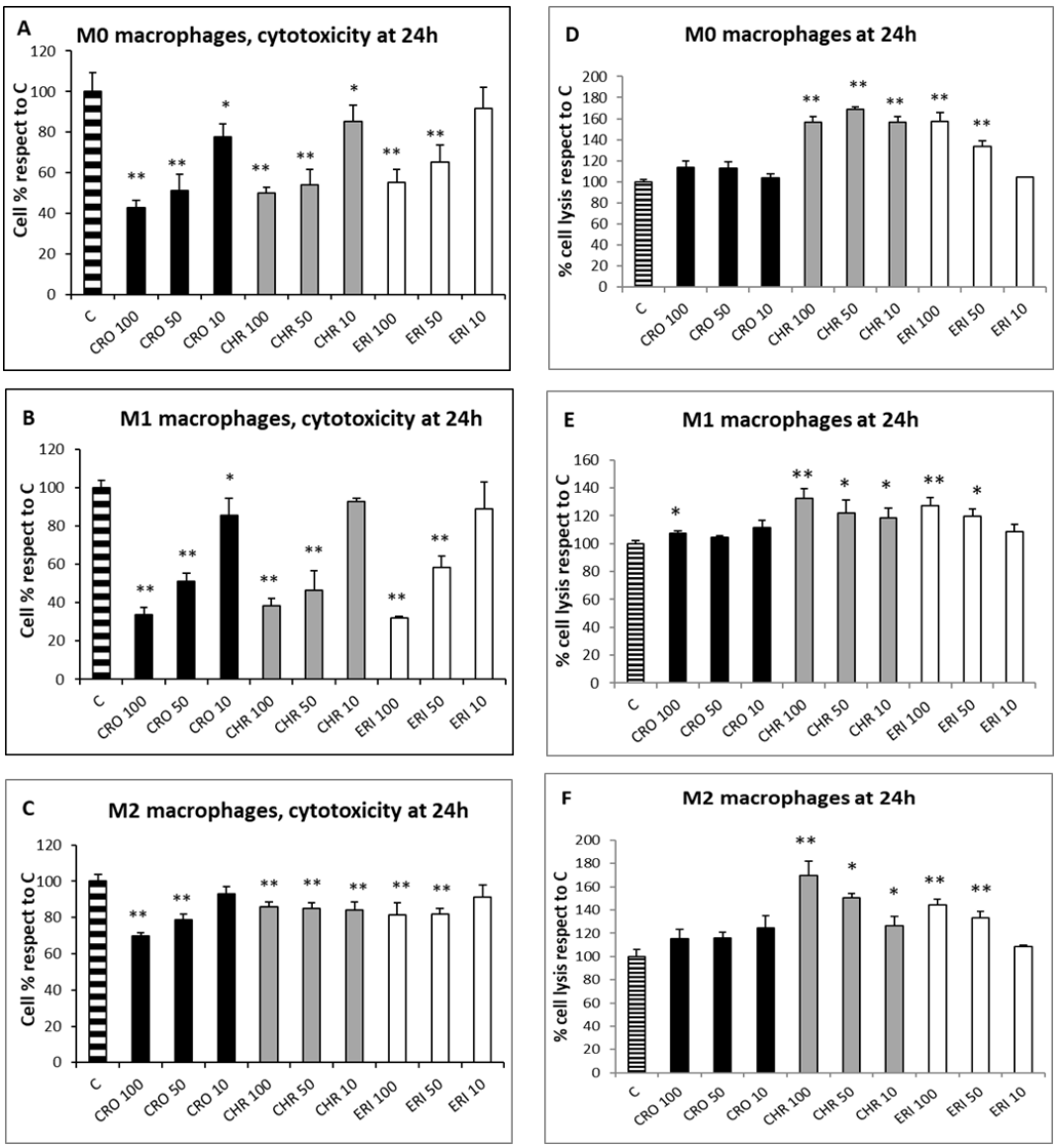

Figure 3. Cell toxicity evaluation and cell lysis assessment after exposure to mineral fibres. (**A**) M0 macrophage cytotoxicity evaluation by the MTT test at 24 h in the presence of 100, 50 and 10 μg/mL of the mineral fibres CRO (black bars), CHR (grey bars) and ERI (white bars). Results are expressed as cell percentages with respect to control cells (striped bar) and are the mean ± SD of three independent experiments performed in quadruplicate. Asterisks indicate the significance in a paired Tukey test (ANOVA, $p < 0.0001$; Tukey vs. C: * $p < 0.05$, ** $p < 0.005$, respectively). (**B**) Pro-inflammatory M1 macrophages cytotoxicity evaluation in the same conditions as (**A**). ANOVA, $p < 0.000005$; Tukey vs. C: * $p < 0.05$, ** $p < 0.005$, respectively. (**C**) Alternatively activated M2 macrophages cytotoxicity evaluation, in the same conditions as (**A**). ANOVA, $p < 0.000001$; Tukey vs. C: ** $p < 0.005$. (**D**) Cell lysis assessment measured by quantification of LDH release in the cell medium at 24 h in M0 macrophages after incubation with 100, 50 and 10 μg/mL of the mineral fibres CRO (black bars), CHR (grey bars) and ERI (white bars). Results are expressed as percentage of cell lysis relative to control cells (striped bar) and are the mean ± SD of three experiments performed in quadruplicate. Asterisks indicate significance in paired Tukey test (ANOVA, $p < 0.0005$; Tukey vs. C: ** $p < 0.005$). (**E**) Cell lysis assessment measured in the same conditions as (**D**) in pro-inflammatory M1 macrophages. ANOVA, $p < 0.01$; Tukey vs. C: * $p < 0.05$, ** $p < 0.005$, respectively. (**F**) Cell lysis assessment measured in the same conditions as (**D**) in alternatively activated M2 macrophages. ANOVA, $p < 0.01$; Tukey vs. C: * $p < 0.05$, ** $p < 0.005$, respectively.

To assess the nature of macrophage cell death, two analyses were performed: the lactate dehydrogenase (LDH) assay, which can be considered a cell death marker since the leakage of this cytosolic enzyme in the cell medium occurs following plasma membrane disturbance, and the annexin/propidium iodide positivity assay, measured by confocal microscopy to establish the level of cellular apoptosis. The LDH assay was performed on the three types of differentiated macrophages in contact with the fibres at three concentrations (100, 50 and 10 µg/mL) for 24 h to quantify cell death caused by plasma membrane damage (Figure 3D–F). The assay showed that, for all of the polarised macrophages, the rates of cellular damage observed after exposure to CRO were comparable to the control (Figure 3D–F, black bars). Conversely, all types of differentiated macrophages showed a certain degree of plasma membrane cell damage during treatment at all concentrations of CHR (grey bars) and at the two highest concentrations of ERI (100 and 50 µg/mL, white bars). In particular, in M0 cells (Figure 3D), the degree of cellular damage induced by CHR was not dose-dependent, and the relative values of LDH release were 1.56-, 1.68- and 1.56-fold higher than control cells at 100, 50 and 10 µg/mL, respectively, while for ERI, significant dose-dependent plasma membrane cell damage was observed, with values 1.58- and 1.33-fold higher than control cells at the two highest fibre concentrations. The trend was similar in M1 macrophages (Figure 3E), although levels of cell membrane damage were observed to be lower compared to M0 cells. In particular, for CHR treatment, the increase in necrotic events compared to control cells was 1.32-, 1.22- and 1.18-fold at 100, 50 and 10 µg/mL, respectively, while for ERI, it amounted to 1.27- and 1.19-fold compared to control cells at 100 and 50 µg/mL. The same trend was also evident in M2 cells (Figure 3F), since all tested concentrations of CHR induced an increase in cell lysis (1.69-, 1.50- and 1.26-fold increase at 100, 50 and 10 µg/mL, respectively), as was also observed with 100 and 50 µg/mL of ERI (1.44- and 1.33-fold for 100 and 50 µg/mL, respectively).

In general, in all differentiated macrophages, exposure to CRO was not able to induce cell lysis, meaning that the high rates of cytotoxicity, measured by the alteration of energy metabolism through the MTT test at 24 h for the same fibre (Figure 3A–C), are the result of other death mechanisms. On the other hand, significant levels of cell lysis were observed after treatment with CHR or ERI. Indeed, in the case of ERI, our results confirm recent findings in the U937 monocyte cell line model, which also demonstrated the direct damage of cell membranes in contact with the fibres (Cangiotti et al., 2018). The level was higher for CHR compared to ERI, and this result may point towards multifactorial cytotoxic activity, with cell membrane alteration at least partially capable of inducing cell death. To test this hypothesis, cells were treated with the mineral fibres for 24 h and analysed by confocal microscopy using annexin/propidium iodide staining to both qualitatively (Figure 4) and quantitatively (Figure 5) assess their apoptotic state.

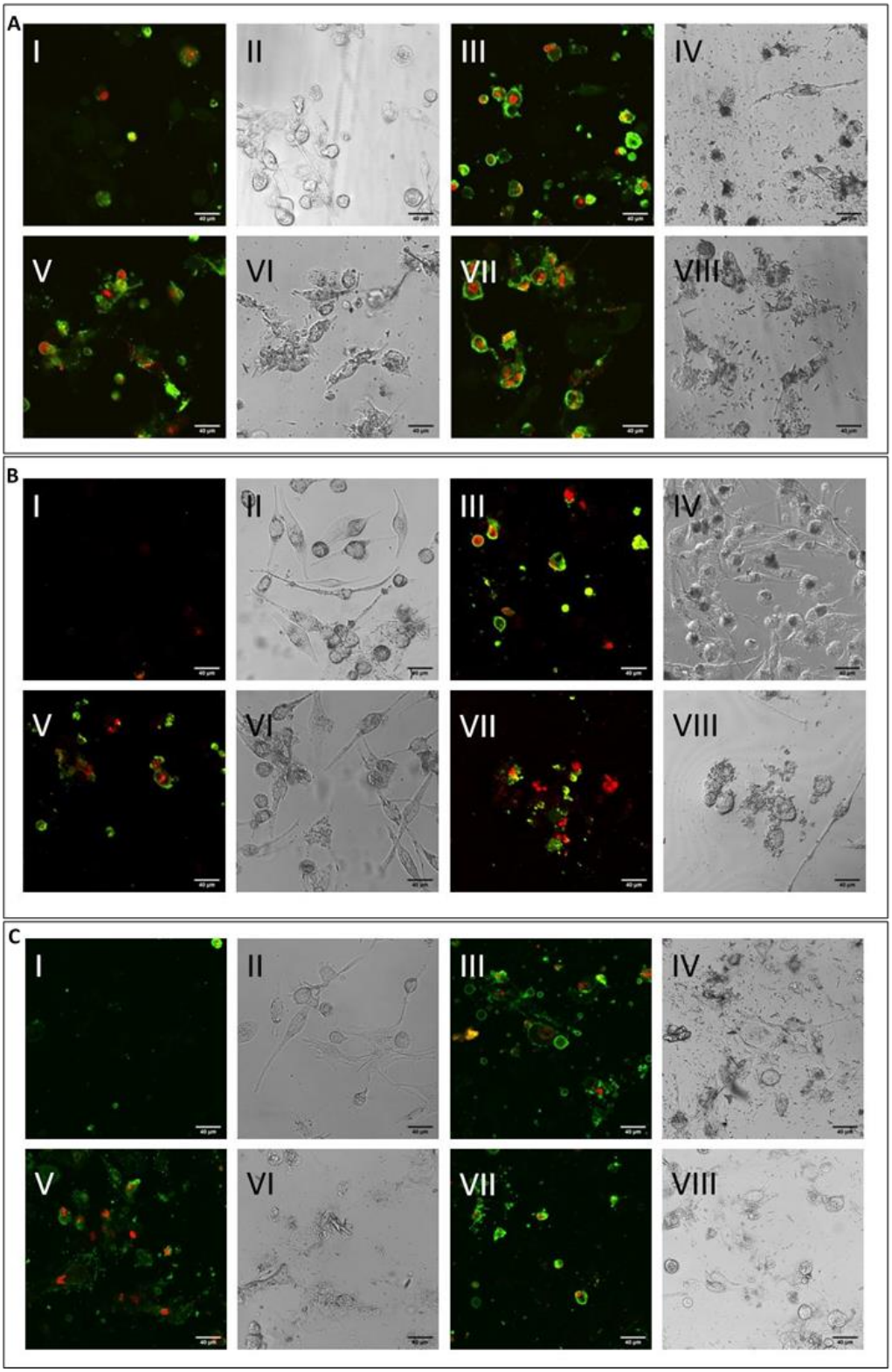

Figure 4. Cell apoptosis assessment by confocal microscopy analysis. (**A**) Visualization by confocal microscopy (2.5 × digital zoom) in fluorescence mode (panels I-III-V-VII) and in phase contrast (panels II-IV-VI-VIII) of M0 macrophages following 24 h incubation in the presence or absence of mineral fibres at 50 µg/mL and staining of annexin-positive (green) and/or propidium iodide-positive (red) cells. Panels I-II: control; panels III-IV: CRO; panels V-VI: CHR; panels VII-VIII: ERI. The white bar represents 40 µm. (**B**) Visualization of pro-inflammatory M1 macrophages in the same conditions as cells in panel (**A**). (**C**) Visualization of alternatively activated M2 macrophages in the same conditions as cells in panel (**A**).

Confocal microscopy analysis indicated that in all types of differentiated macrophages (Figure 4A, M0 macrophages; 4B, M1 macrophages; 4C, M2 macrophages), although at different rates, all fibres (Figure 4A–C: panels III-IV CRO, panels V-VI CHR and panels VII-VIII ERI, respectively) caused the significant induction of both early (only green positivity) and late apoptosis (concomitant green/red positivity) compared to control cells (Figure 4A–C: panels I-II).

The quantitative assessment of the apoptotic state, obtained by counting and calculating the mean of only green and red–green cells in five different fields of confocal microscope images for each treatment, is shown in Figure 5. In M0 cells (panel A), CRO induced the highest levels of early signals of apoptosis at both concentrations tested (white bars, 98% and 86% for 10 and 50 µg/mL CRO, respectively, $p < 0.005$ vs. C, for both bars). Early apoptosis signals after exposure to CHR and ERI were nonetheless significant and dose-dependent, although lower than those after exposure to CRO (white bars, 24% and 84% for 10 and 50 µg/mL CHR, and 41% and 64% for 10 and 50 µg/mL ERI, respectively, $p < 0.005$ vs. C for all bars). In contrast, regardless of the concentration used, the number of late apoptotic cells after 24h of treatment was similar for all fibres (black bars, from ~20 to ~40%, $p < 0.005$ vs. C). These data, showing an increase in apoptotic levels for all fibres, are in agreement with the apoptosis assessment in THP-1 M0 cells in our previous work (Di Giuseppe et al., 2021a), which was performed with a shorter incubation time (8 h), indicating further progression of the apoptotic phenomenon in these cells over time. On the other hand, compared to M0 cells, M1 macrophages (panel B) showed slightly reduced levels of apoptosis. Indeed, in M1 cells, the highest rates of early apoptosis were 31% for both 10 and 50 µg/mL CHR (white bars, $p < 0.005$ vs. C for all), although all values of early apoptosis were found to be significant compared to control cells (~20% for 10 and 50 µg/mL ERI with $p < 0.005$ vs. C for both bars, 11% for 10 µg/mL CRO and 29% 50 µg/mL CRO with $p < 0.05$ and $p < 0.005$ vs. C, respectively). In addition, all mineral fibres induced late apoptosis to a certain degree (black bars), ranging from ~10% to ~19%, with the highest values measured for 10 and 50 µg/mL ERI and 50 µg/mL CRO ($p < 0.05$ vs. C for all bars). Finally, M2 macrophages (panel C) showed the highest rates of early apoptosis after CHR treatment (white bars, 37% and 62% for 10 and 50 µg/mL CHR, respectively, $p < 0.005$ vs. C for both) and a lower rate for CRO (37% and 43% for 10 and 50 µg/mL CRO, respectively, $p < 0.005$ vs. C for both) and ERI (41% and 26% for 10 and 50 µg/mL ERI, respectively, $p < 0.05$ vs. C). Regarding late apoptosis, in these cells, it was significantly increased only by the highest concentrations of CHR and CRO compared to control cells (black bars, 37% for 50 µg/mL CHR and 27% for 50 µg/mL CRO, respectively, $p < 0.005$ vs. C for both). Conversely, both concentrations of ERI appeared to induce significant levels of late apoptosis (24% and 17% for 10 and 50 µg/mL ERI, respectively, $p < 0.05$ vs. C for both).

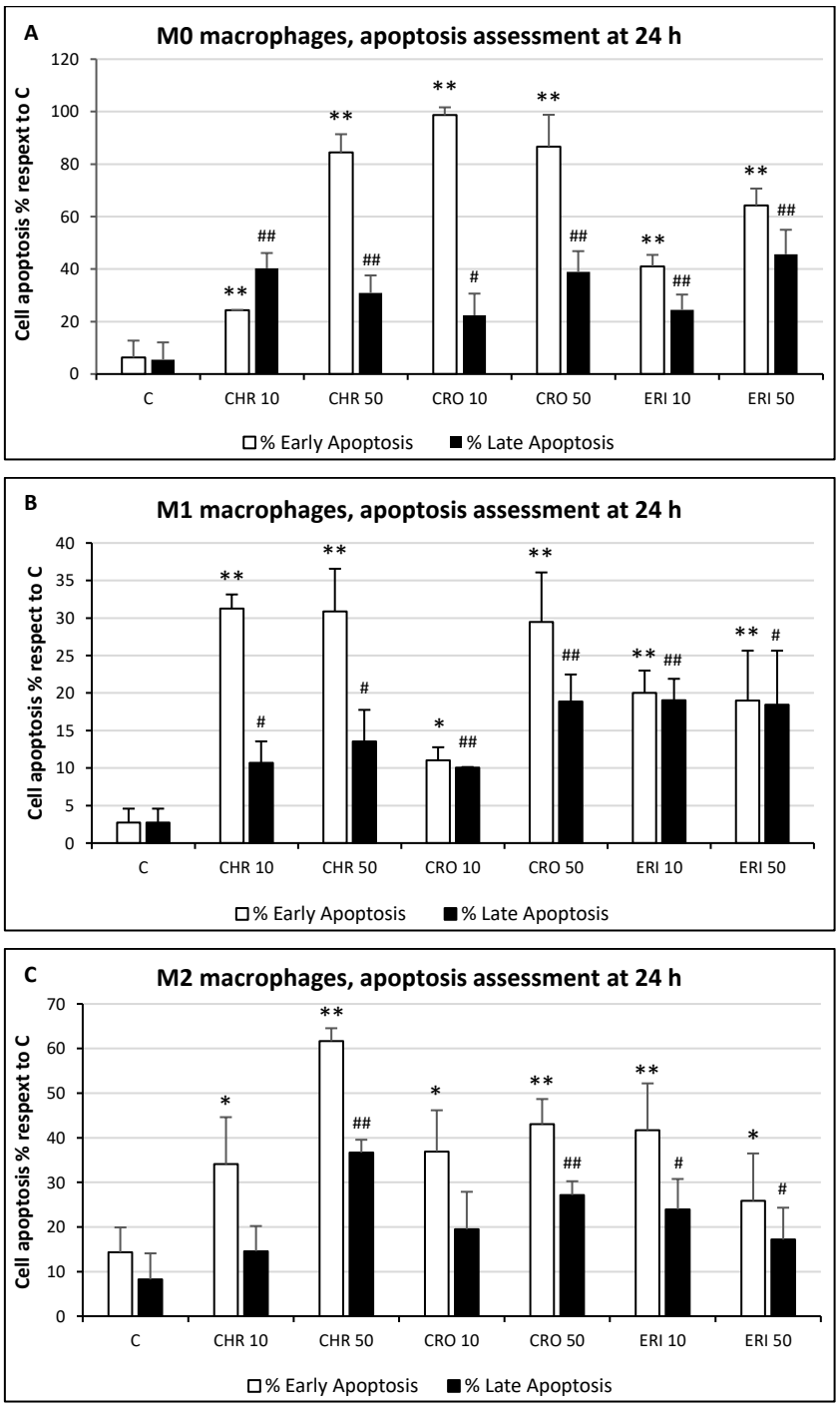

Figure 5. Cell apoptosis quantification. (**A**) The quantitative analysis of early (annexin-positive, white bars) and late (both annex-in-positive and propidium iodide-positive, black bars) apoptotic M0 THP-1 cells treated with 50 and 10 µg/ml of CRO, CHR and ERI relative to the total number of cells observed by confocal microscopy after 24 h; results are the mean ± SD of counts from five microphotographs. Asterisks indicate significance in Tukey test (ANOVA for white bars $p < 0.000001$; Tukey vs. C, ** $p < 0.005$, * $p < 0.05$, respectively; ANOVA for black bars $p < 0.0005$, Tukey vs. C, ## $p < 0.005$, # $p < 0.05$, respectively). (**B**) The same analysis in pro-inflammatory M1 macrophages. ANOVA for white bars $p < 0.00005$; Tukey vs. C, ** $p < 0.005$, * $p < 0.05$, respectively; ANOVA for black bars $p < 0.0001$, Tukey vs. C, ## $p < 0.005$, # $p < 0.05$, respectively. (**C**) Same analysis in alternatively activated M2 macrophages. ANOVA for white bars $p < 0.00001$; Tukey vs. C, ** $p < 0.005$, * $p < 0.05$, respectively; ANOVA for black bars $p < 0.00005$, Tukey vs. C, ## $p < 0.005$, # $p < 0.05$, respectively.

Overall, our data indicate that the three types of fibres are able to induce significant damage, resulting in the alteration of energy metabolism, cell membrane lysis and/or apoptosis and likely macrophage activation through phagocytosis. The overall phenomena, together with the incapability of macrophages to completely digest engulfed fibres and the induction of apoptosis resistance in macrophages by the fibres through activation of mitochondrial NOX4 over time (Larson-Casey et al., 2021), lead to a state of prolonged local inflammation and the release of inflammatory cytokines prodromal to the onset of cancer (Coussens and Werb, 2002; D'Arcy, 2019). Furthermore, macrophages internalising small fibres may survive in the short term and may act as carriers that transport particles towards the inner lung parenchyma and the mesothelium. The chronic inflammatory state caused by undigested fibres in activated macrophages at these new sites, as well as the direct interaction of the transported fibres with epithelial and mesothelial cells, will then set up a favourable microenvironment for cell transformation and carcinogenesis.

6.3. ROS PRODUCTION AND DNA DAMAGE

In the lungs, lung-resident macrophages are key contributors to triggering and maintaining the inflammatory response to harmful stimuli (Aggarwal et al., 2014). Macrophage cells are known to undergo a respiratory burst following cellular activation and phagocytic events, thus modifying the oxidative state of the cells through the intracellular production of ROS (Iles and Forman, 2002). In addition to constituting a physiological response that is also very important for signal transduction (Iles and Forman, 2002), the ROS increase can be further exacerbated by the physical-chemical nature of the phagocytosed particles, which, in the case of the three mineral fibres, present several redox-active metals on their surfaces that are able to promote ROS generation (see results in Figure 1 and Table 1). Thus, significant oxidative stress is to be expected by their administration to living cells and organisms (Gualtieri et al., 2019b). Specifically, to measure intracellular ROS production, the different types of macrophages, M0, M1 and M2 (Figure 6, panels A, B and C, respectively), were challenged with the mineral fibres for 2 h, and the ROS increase was compared to that in the untreated control cells (C) and to positive control cells stimulated by 200 µM H_2O_2. This time point was chosen because ROS production is a documented early signal of the inflammatory response (Iles and Forman, 2002) and because it was previously observed that further increases in ROS production in THP-1 cells after 2 h are not significant, remaining almost the same up to 4 h after the challenge with mineral fibres (Di Giuseppe et al., 2021a).

In all types of differentiated macrophages, the three mineral fibres were able to significantly increase intracellular ROS production after 2 h compared to the untreated control cells, with no significant differences among the three types of cells. The extent of this increase was comparable to

that in the positive control (H_2O_2 stimulus, from 1.5-fold to 1.63-fold increase in all differentiated macrophages compared to C) for CRO and slightly lower but still significant if compared to untreated control cells for CHR and ERI. In particular, the exposure of M0, M1 and M2 macrophages to CRO, CHR and ERI fibres increased intracellular ROS production by ~1.6-fold, ~1.4-fold and 1.2–1.35-fold compared to untreated control cells (panels A–C), respectively.

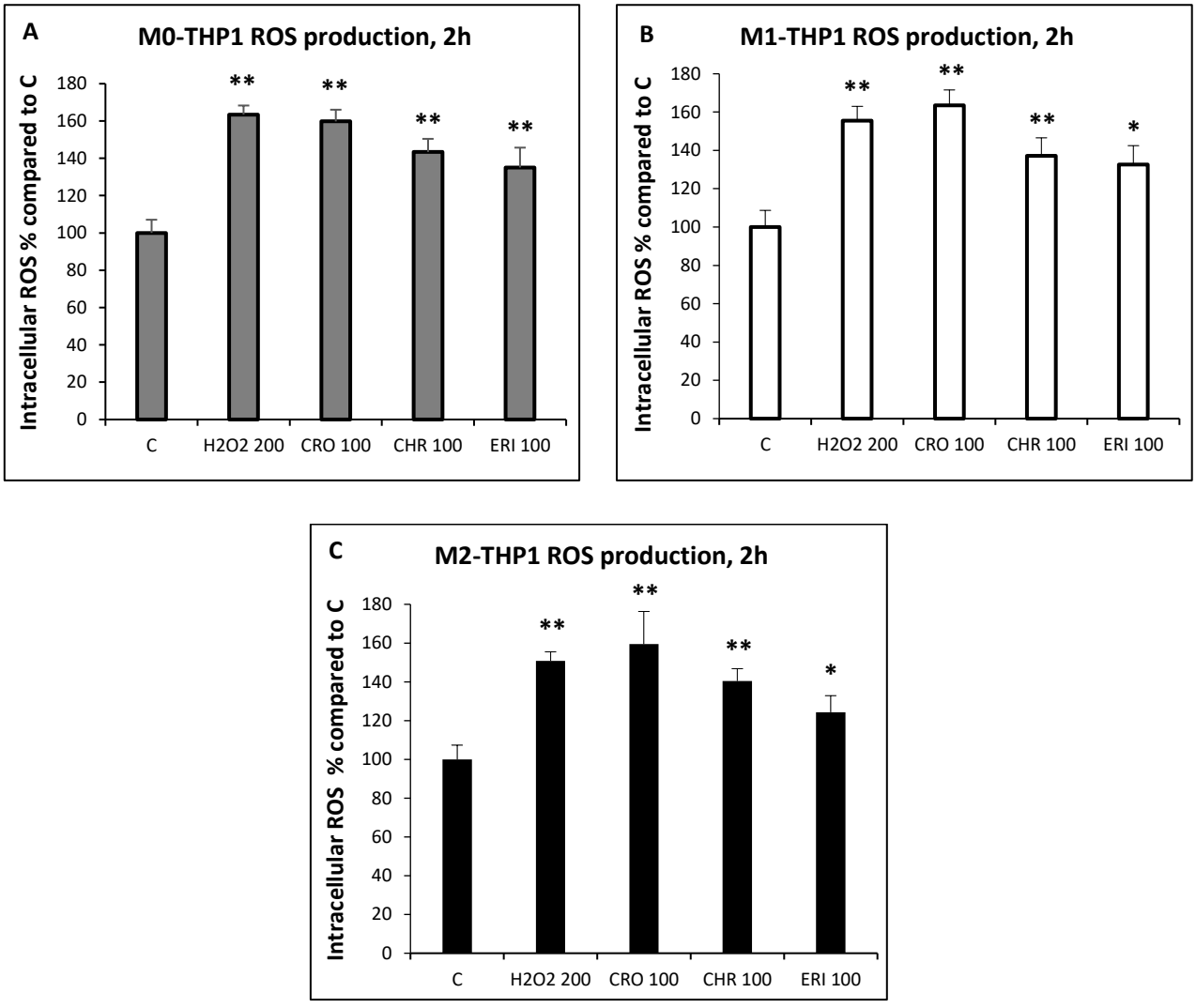

Figure 6. Intracellular ROS evaluation. (**A**) Intracellular ROS production measured by 2′,7′-dichlorodihydrofluorescein diacetate fluorometric analysis in M0 macrophages incubated for two hours in the presence or absence of 100 µg/mL of mineral fibres CRO, CHR and ERI. Cells stimulated with 200 µM H_2O_2 are the positive control. Results are expressed as percentages of ROS production compared to the untreated control (C) and are the mean ± SD of three experiments, in which each condition was tested eight times. Asterisks indicate significance in Tukey test (ANOVA $p < 0.000001$; Tukey vs. C, ** $p < 0.0001$). (**B**) Intracellular ROS production in pro-inflammatory M1 macrophages in the same conditions as (**A**). ANOVA $p < 0.000001$; Tukey vs. C, * $p < 0.005$, ** $p < 0.0001$, respectively. (**C**) Intracellular ROS production in alternatively activated M2 macrophages in the same conditions as (**A**). ANOVA $p < 0.000001$; Tukey vs. C, * $p < 0.005$, ** $p < 0.0001$, respectively.

ERI showed a lower ability to increase intracellular ROS production in the three types of macrophages compared to the other two asbestos fibres. This lower cellular response is likely due to the different metal ion compositions of the fibres. In fact, CRO is able to release significant amounts of intracellular iron (see Figure 8B), and CHR releases several redox-active metals (i.e., Mg, Fe, Cr, Ni and Co, see Figure 8A–D). Conversely, ERI hosts significantly lower amounts of redox-active metals. It was also found that ERI only releases Al from the surface of the fibres (dealumination) into the cytoplasm in quantifiable amounts (see Figure 8B) after 24 h. On the other hand, ERI seems to affect the intracellular Na^+ and Ca^{2+} concentrations in M0 macrophages due to its cation-exchange capacity (CEC), reportedly resulting in a significant cytoplasmic rise in Na^+ and a measurable depletion of Ca^{2+} (Gualtieri et al., 2019b; Di Giuseppe et al., 2021a). It is well known that Ca^{2+} is a fundamental stimulus for intracellular ROS production, both for cytoplasmic NADPH oxidase isoform activation and for mitochondria-mediated ROS production (Görlach et al., 2015). Thus, the reduced release of redox-active metals from the surface of ERI fibres, together with the alleged depletion of Ca^{2+} caused by the CEC, may explain the lower propensity of ERI to generate intracellular ROS compared to the other two asbestos fibres.

The increase in the oxidative state of the cells due to asbestos fibres contributes to the induction of various forms of DNA damage (Okayasu et al., 1999) with the subsequent onset of various malignancies, namely, diffuse malignant mesothelioma and lung cancer. In fact, exposure to asbestos fibres results in the appearance of DNA double-strand breaks (DSBs) in lung cells, particularly through the production of ROS (as quantified in Figure 6), which can reach the cell nucleus and attack the DNA backbone as well as the four DNA bases (Mossman, 2018). Thus, after 24 h of exposure to fibres, DNA DSBs (Figure 7) were qualitatively (panel A) and quantitatively (panel B) evaluated in M0, M1 and M2 cells by confocal microscopy through the staining of γ-H2AX foci. The ratio between the number of foci in treated cells compared to the number of foci in untreated cells (panel B) was then quantified. As expected, after exposure to mineral fibres, a significant rate of DSBs was found in the macrophages, regardless of the type of differentiation that they underwent, with no significant differences among the various fibre treatments. Specifically, the foci ratios measured in treated M0 cells compared to the untreated control (mean number of treated M0 foci/mean number control M0 foci) were ~17, 12 and 17.2 for CRO (black bars), CHR (grey bars) and ERI (white bars) ($p < 0.001$ vs. C for all bars, respectively), whereas in M1 macrophages, the ratio corresponded to 23.3, 21.6 and 20.5 for CRO, CHR and ERI, respectively ($p < 0.001$ vs. C for all bars). Finally, in M2 cells, the foci ratio amounted to 18, 18.2 and 22.1 for CRO, CHR and ERI, respectively, relative to untreated control cells ($p < 0.0005$ vs. C for all bars).

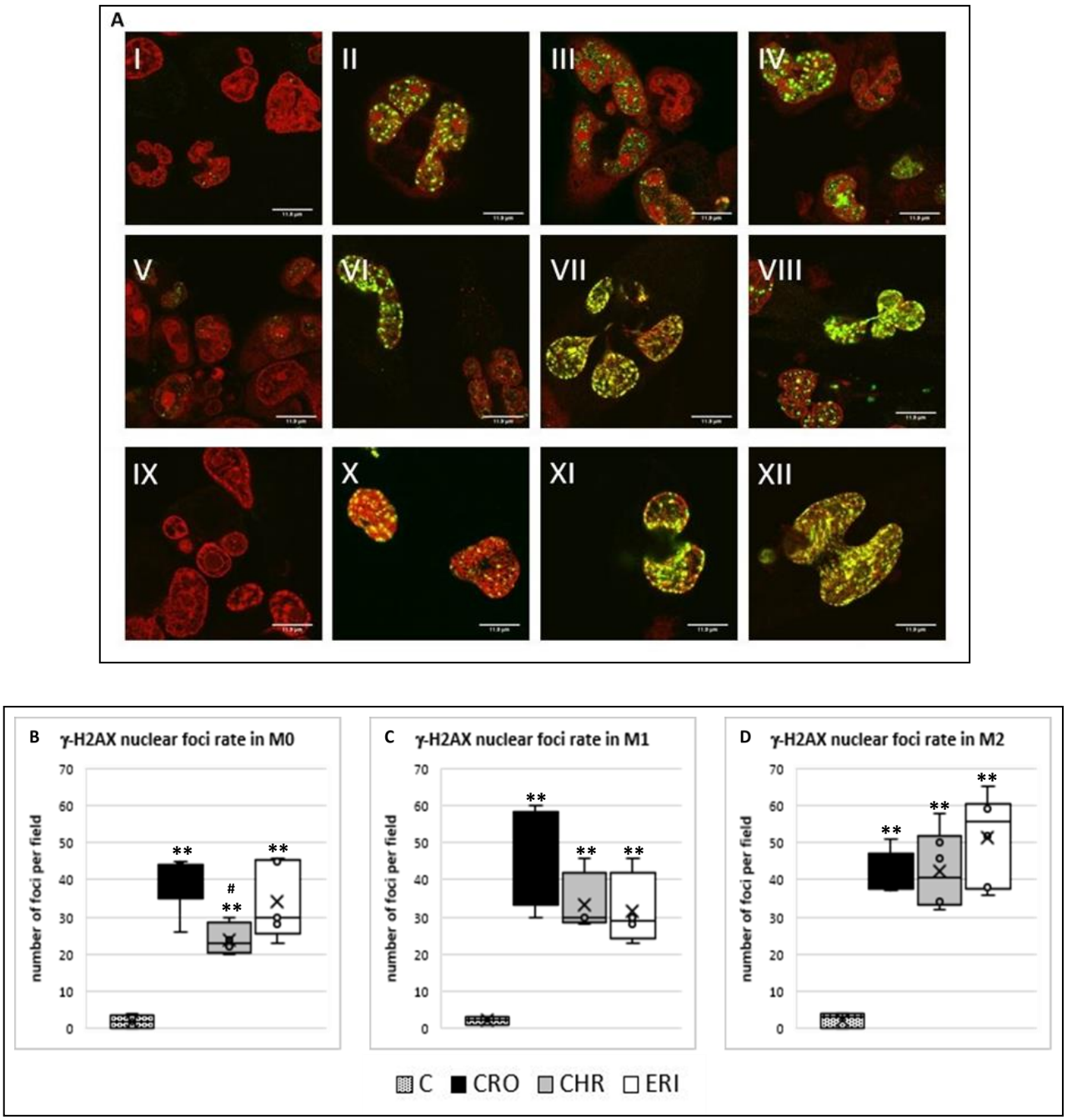

Figure 7. Quantification of the genotoxic damage. (**A**) Visualization by confocal microscopy analysis (4 × digital zoom) of double-strand breaks in the DNA by γ-H2AX protein staining (green fluorescence), and DNA propidium iodide staining (red fluorescence) in differentiated macrophages after 24 h of incubation with 50 µg/mL fibres. Panels I-IV: M0-THP-1 macrophages; panels V-VIII: M1-THP-1 macrophages; panels IX-XII: M2-THP-1 macrophages. Panels I, V and IX: control; panels II, VI and X: CRO; panels III, VII and XI: CHR; panels IV, VIII and XII: ERI. The white bar represents 12 µm. (**B**) The quantitative analysis results of confocal microscopy acquisitions are expressed as the total number of double strand breaks in the DNA of M0-THP-1 cells challenged with 50 µg/mL fibres and are the mean ± SD of five microphotographs. Dotted bar: control; black bar: CRO; gray bar: CHR; white bar: ERI. Asterisks indicate significance in Tukey test (ANOVA $p < 0.000005$; Tukey vs. C, ** $p < 0.001$; Tukey vs. CRO, # $p < 0.001$, respectively). (**C**) Same analysis as (**B**) in M1-THP-1 macrophages (ANOVA $p < 0.0005$; Tukey vs. C, ** $p < 0.001$). (**D**) Same analysis as (**B**) in M2-THP-1 macrophages (ANOVA $p < 0.00005$; Tukey vs. C, ** $p < 0.001$).

The results clearly demonstrate that in the three types of macrophages, the mineral fibres showed different rates of toxicity and different proportions between plasma membrane lysis and apoptosis as causes of cell death (Figures 2–4), with CRO favouring the induction of cell death by apoptosis and CHR and ERI inducing cell death by both cell lysis and apoptosis. When it comes to DNA damage, all three fibres showed very similar behaviours, with a significant number of DSB foci already formed at 24 h in all treatments. This confirms that the onset of cell genomic instability induced by the fibres takes place shortly after their inhalation and that there is no apparent difference between the genetic damage caused by the three classified carcinogens.

6.4. INTRACELLULAR DISSOLUTION OF FIBRES AND METAL RELEASE

The interaction of mineral fibres with lung cells involves a wide range of biological processes and cellular responses in which professional phagocytes (e.g., macrophages and neutrophils) play a leading role. In the first hours after contact, the mineral fibre is partially or completely engulfed by phagocytes and enclosed in intracellular phagosomes, which undergo fusion with lysosomal vesicles (i.e., acidic compartments filled with different types of hydrolases) in a process called 'phagosome maturation', leading to the degradation of the phagolysosome content. Evidence from *in vivo* and *in vitro* studies has shown that mineral fibres can undergo partial or total dissolution during phagocytosis (Gualtieri et al., 2018b; Bernstein et al., 2020). This process is a function of the fibre biodurability (i.e., the resistance of the fibres to chemical/biochemical alteration). Indeed, recent *in vitro* acellular dissolution experiments showed that CRO, CHR and fibrous ERI display very different dissolution rates in the macrophage phagolysosome environment (Gualtieri et al., 2018b). For a 0.25 μm thick fibre, the estimated time for complete dissolution of chrysotile from Balangero is 0.3 y, which is very short if compared to that of UICC standard crocidolite (66 y) and fibrous erionite from Jersey, USA (181 y). Because mineral fibres can host toxic metals in their structure, fast-dissolving fibres such as chrysotile can act as carriers that release their metal cargos into the extracellular and intracellular environments more quickly. Conversely, biodurable crocidolite releases its metals slowly. Fibrous erionite is a biodurable zeolite that has an ion-exchange capacity. It can therefore release extra-framework cations by ion exchange even if dissolution does not occur (Gualtieri et al., 2019b).

To test this hypothesis and to measure the partial dissolution of the fibres inside macrophages at 24 h, polarised M0 THP-1 cells were treated with the three mineral fibres, and the intracellular content of silicic acid (as a measure of Si release in a soluble state) and the concentrations of selected trace elements (Mg, Al, Fe, Cr, Ni and Co) were detected (Figure 8). The basal intracellular soluble Si concentration in M0 THP-1 untreated macrophages was 46 μM (panel A, white bars), and only the

CRO and ERI treatments induced significant increases of 1.41- and 1.59-fold compared to control cells, respectively ($p < 0.001$ vs. C for both). CHR did not show a measurable soluble Si increase after 24 h of treatment, and this could be due to the different dissolution mode of this fibre compared to CRO and ERI (Gualtieri et al., 2018b). In fact, in the case of CHR, dissolution involves the brucite octahedral sheet (Gualtieri et al., 2018b; Ndlovu et al., 2011), while the Si-centred tetrahedral sheet is biodurable (Gualtieri et al., 2019b). These observations are confirmed by the fact that a significant increase in Mg intracellular content, originating from the dissolution of the brucite sheet of the mineral, was only measured in CHR-treated M0 THP-1 macrophages (1.6-fold increase, $p < 0.05$) as compared to control cells (basal intracellular Mg concentration of 27.4 µM) and to CRO- or ERI-treated cells (panel A, black bars). The homeostasis of Mg, both intracellular and extracellular, is tightly regulated in the body due to the pleiotropic functions of this ion in hundreds of enzymatic activities, particularly those involved in the storage, transfer and utilisation of energy (Touyz, 2004). Thus, changes in the intracellular concentration of free Mg are linked to imbalances of energy metabolism, which were indeed measured in the MTT tests (see Figure 3), ion transport, signal transduction and, ultimately, cellular stress. These effects can contribute not only to the acute toxicity of CHR but also to the onset of chronic disorders since the alteration of these important cellular activities is also linked to epigenetic changes that affect the long-term physiology of cells (Janke et al., 2015). Intracellular concentrations of Fe and Al (panel B) were also found in the micromolar range in untreated macrophages (0.2 and 0.5 µM, respectively). Furthermore, Fe was significantly increased in the cytoplasm of CRO- and CHR-treated cells (6.1- and 4.7-fold increases, respectively, white and striped bars, $p < 0.05$ for both), while Al was only significantly increased by ERI treatment (2.6-fold increase, $p < 0.05$) as compared to control cells. It is well known that both metals exert their toxic effects by creating an intracellular oxidative environment (Han et al., 2013; Eid et al., 2017) that leads to cellular dysfunctions such as mitochondrial impairment, protein and lipid oxidation and DNA damage, which indeed were also observed in our mineral-fibre-treated cells (see Figures 3, 6 and 7). Thus, the significant release of these metal ions from the fibres helps to explain the increased ROS production and the onset of the oxidative environment that we observed in differentiated M0, M1 and M2 macrophages (Figure 6) in the presence of the three different mineral species. Finally, it is noteworthy that CHR was also able to release traces of other toxic elements, such as Cr, Ni (panel C, grey and diamond bars, respectively) and Co (panel D), significantly increasing the very low basal intracellular content of these elements, which were in the nanomolar concentration range in untreated M0 cells (8.6 nM, 4.7 nM and 0.34 nM, respectively). The accumulation of these metals in the body, mainly in the lungs due to inhalation of polluted air, is related to the development of direct or indirect oxidative stress and

cancer promotion, as reviewed in Valko et al. (2006). Furthermore, the toxicity of Ni and Cr has also been recently demonstrated in the induction of nuclear epigenetic changes such as an increase in DNA and histone methylation at specific chromatin regions with the consequent downregulation of tumour suppressors such as p16, a cell cycle regulator (Arita and Costa, 2009). These findings explain how the release of these toxic metals promotes neoplastic cell transformation after inhalation. In CHR-treated macrophages, we measured a significant increase of 2.3-fold for intracellular Cr, 4.8-fold for Ni and 4.6-fold for Co as compared to control macrophages ($p < 0.05$ vs. C for all). These results agree with recent findings from acellular *in vitro* dissolution tests (Gualtieri et al., 2018b; 2019b). In fact, the dissolution of the chrysotile fibres involves the decomposition of the octahedral sheet with the leaching of Mg, Fe, Cr, Ni and Co. On the other hand, crocidolite is known to undergo slow dissolution with the formation of a nanometre-thick amorphous surface layer. Thus, the partial dissolution of crocidolite is responsible for the release of Fe in the CRO sample. The difference in the Fe content between Balangero chrysotile (2.50 wt% FeO and 0.40 wt% Fe_2O_3) and UICC crocidolite (17.4 wt% FeO and 17.9 wt% Fe_2O_3) accounts for the difference in the iron found in CHR-treated cells compared to CRO-treated cells. Once again, the results obtained for the Al content in ERI-treated macrophages confirm the previous acellular *in vitro* data.

These results may help to explain why, despite the low biodurability and the supposed lower toxicity potential of chrysotile relative to the other two mineral fibres, this mineral represents a hazard, especially for subjects exposed in work environments (Gulino et al., 2016; Ferrante et al., 2020). Thus, in contrast to the other two mineral fibres, CRO and ERI, whose carcinogenicity can be ascribed to their persistence in the lungs for years, the adverse effects of CHR seem to also be due to the dissolution process itself, with the release of metal ions such as Mg, Fe, Cr, Ni and Co. Indeed, the sum of all of these metals will amount to a significant concentration of oxidative stress, promoting the presence of ions in the cytoplasm of the affected cells and causing the onset of cellular dysfunctions and possibly neoplastic transformation due to both genetic and epigenetic changes. In addition to these interesting results, the microscale mechanisms underlying the dissolution of these mineral fibres in THP-1-derived cellular systems are currently investigated with synchrotron-based X ray imaging, combined with micro-XANES analyses and XRF elemental mapping, in order to obtain a more in-depth understanding of the metals mobilization mechanism by studying their intracellular spatial distribution and the changes in their valence state.

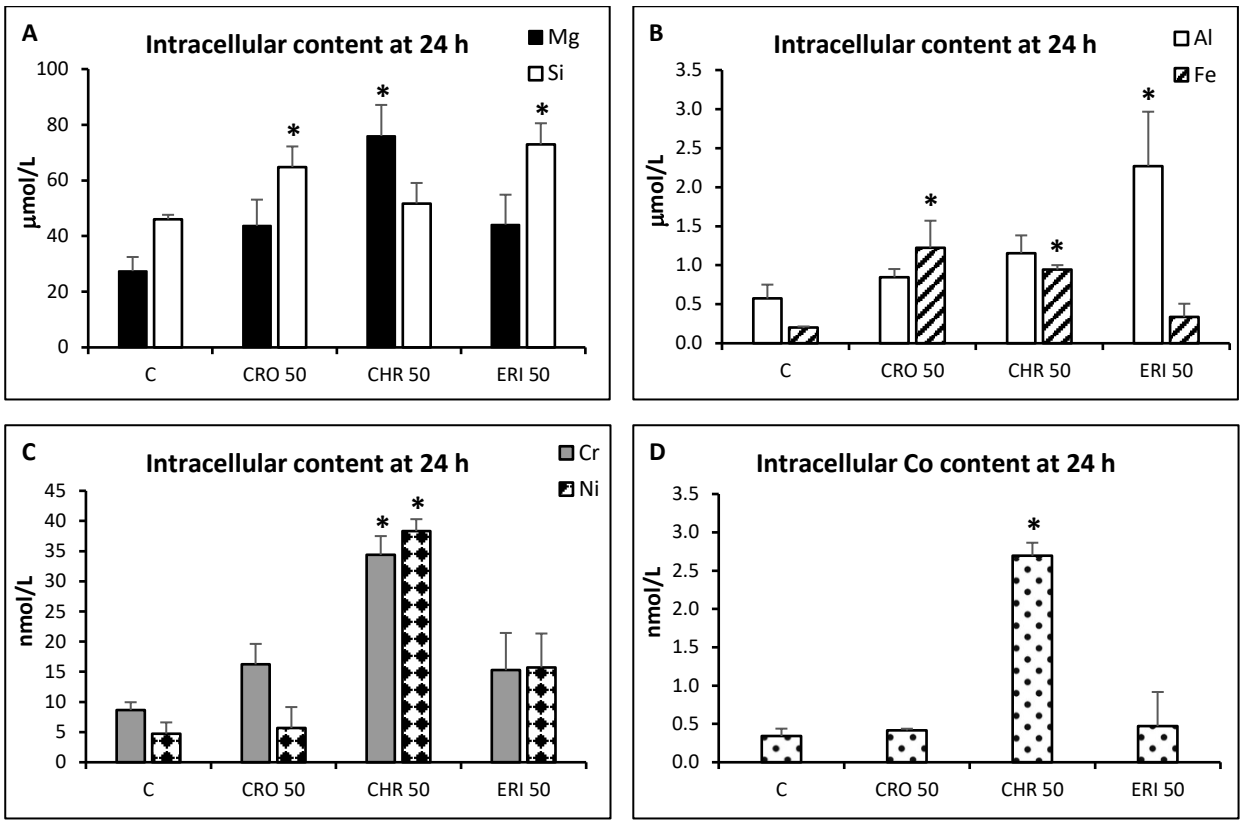

Figure 8. Intracellular silicic acid and toxic metal quantification. (**A**) Intracellular silicic acid content (white bars), measured by the Spectroquant® Silicate (Silicic Acid) Test, and Mg content (black bars), measured by inductively coupled plasma–mass spectrometry (ICP-MS), in M0 THP-1 macrophages incubated for 24 h with 50 µg/mL fibres. Results are the mean ± SD of two independent experiments performed in duplicate. Asterisks indicate significance in Tukey test (ANOVA for Si content $p < 0.0005$; Tukey vs. C, * $p < 0.05$, ANOVA for Mg content $p < 0.05$, Tukey vs. C * $p < 0.05$, respectively). (**B**) Intracellular Al content (white bars) and Fe content (striped bars) in M0 THP-1 cells in the same conditions as (**A**) measured by ICP-MS. ANOVA for Al $p < 0.01$; Tukey vs. C, * $p < 0.05$; ANOVA for Fe $p< 0.001$, Tukey vs. C * $p < 0.05$; respectively. (**C**) Intracellular Cr content (grey bars) and Ni content (diamond bars) in M0 THP-1 cells in the same conditions as (**A**) measured by ICP-MS. ANOVA for Cr $p < 0.0005$; Tukey vs. C, * $p < 0.05$; ANOVA for Ni $p < 0.0001$, Tukey vs. C, * $p < 0.05$. (**D**) Intracellular Co content (dotted bars) in M0 THP-1 cells in the same conditions as (**A**) measured by ICP-MS. ANOVA $p < 0.00005$; Tukey vs. C, * $p < 0.0001$.

6.5. INFLAMMATORY RESPONSE

Upon exposure to harmful stimuli, immune cells, especially macrophages, are responsible for both triggering and maintaining the inflammatory response (Gordon, 2007). For this reason, they have a fundamental role in the production of a number of cytokines that regulate the immune response in both acute and chronic conditions. The production of inflammatory cytokines is stimulated by the activation of the scavenger receptor A family upon the engagement and phagocytosis of foreign particles (Thakur et al., 2008) and is also sustained by the respiratory burst, mainly through the generation of H_2O_2. The latter is known to activate NF-κB and MAPK signalling pathways for the

upregulation of gene transcription (Iles and Forman, 2002), as well as to activate the NLRP3 inflammasome for the cleavage and maturation of cytoplasmically stored cytokines prior to their release in the extracellular milieu (Dostert et al., 2008). Thus, the result of this activation leads to the production of major inflammatory mediators (Min et al., 2007). According to the well-known fact that asbestos leads to chronic inflammation in the lung tissue, and since in our experimental conditions, we observed phagocytic events (Figures 1 and 2) and ROS production (Figure 6) in all three types of differentiated macrophages after only 24 h, the extracellular release of cytokines and the gene expression profile were evaluated by ELISA (Figure 9) and qPCR (Figure 10) tests, respectively, in M0, M1 and M2 cells in contact with the fibres. The reason to investigate both parameters is that while the rapid release of cytokines in the extracellular milieu indicates an acute response to the inflammatory stimulus, in the case of the mineral fibres, conversely, changes in the same cytokines at the transcriptional level may point to an exacerbated inflammatory response that persists over time and contributes to the onset of a chronic state of inflammation.

The pro-inflammatory protein IL-1β is particularly well known for its involvement in several cellular activities, such as cell proliferation, differentiation and apoptosis (Dinarello, 2018). In M0 macrophages (Figure 9A), basal IL-1β release amounted to 54.95 ± 4.77 pg/mL, which was increased by 1.6-fold by both CRO and ERI treatments and by 11.9-fold by CHR ($p < 0.0005$ and $p < 0.0001$ vs. C for CRO and CHR, respectively). Due to their pro-inflammatory role, M1 cells (Figure 9B) showed an overall higher basal production of this cytokine, which amounted to 406.5 ± 55 pg/mL of IL-1β in the untreated cells compared to M0 macrophages (7.4-fold increase compared to control M0 cells). Its release was further significantly elevated by all mineral fibres, exhibiting 2.4-fold and 2.3-fold increases in CRO- and ERI-treated cells ($p < 0.0001$ vs. C for both bars), respectively, and a 2.1-fold increase in CHR-treated cells ($p < 0.001$ vs. C). Regarding M2 macrophages (Figure 9C), the IL-1β quantified in the control cells was more similar to the release observed in M0 cells, and it amounted to 71.56 ± 6.45 pg/mL in the cellular medium (1.3-fold increase compared to control M0 cells). Again, its release was notably increased in all M2 cells in contact with the fibres, showing 5.1- and 5.5-fold increases for CRO and ERI, respectively ($p < 0.0001$ vs. C for both bars) and an 8.4-fold increase for CHR treatment ($p < 0.001$ vs. C). These data show that the three fibres induce very similar amounts of the pro-inflammatory cytokine IL-1β in M1 polarised macrophages. In M0 and M2 cells, CHR actually showed a much more relevant increase compared to the other two fibres, indicating that this fibre species can trigger a significantly stronger acute pro-inflammatory response after inhalation compared to CRO and ERI. Indeed, a significant IL-1β increase after CHR treatment has also been reported *in vivo* in a mouse model of CHR inhalation, where this cytokine was one of the highly expressed markers in the lungs

of treated animals (Sabo-Attwood et al., 2005), corroborating the hypothesis that CHR also exerts a strong acute inflammatory effect through the significant intracellular release of toxic metals, as we observed after only 24 h (Figure 8). IL-1β overproduction by inflammatory cells is a signal that promotes both carcinogenesis and tumour growth during chronic inflammation thanks to the stimulation of cell proliferation and anti-apoptotic pathways, and it also acts as an angiogenic factor (Bent et al., 2018). Thus, since CRO, CHR and ERI are able to stimulate the release of this cytokine not only in M0 and M1 macrophages but also, surprisingly, in the M2 phenotype, and knowing that these fibres persist for a long time in the lungs of exposed subjects (several months for CHR and years for CRO and ERI), it is reasonable to infer that chronically fibre-stimulated macrophages play a fundamental role in the carcinogenicity of asbestos and erionite fibres through the production of inflammatory cytokines that promote and maintain neoplastic cell transformation.

Another important cytokine involved in the inflammatory response is monocyte chemoattractant protein-1 (MCP-1), one of the key chemokines responsible for the regulation of migration and infiltration of monocytes/macrophages during the immune response (Deshmane et al., 2009). For this reason, we analysed MCP-1 production in all three types of polarised macrophages in the presence or absence of the investigated fibres. MCP-1 production was already very high in untreated M0, M1 and M2 macrophages. Nevertheless, it significantly increased with the fibre treatment in all differentiated macrophages. Indeed, in M0 cells (Figure 9, panel D), the levels of MCP-1 (1862.7 ± 631 pg/mL) significantly increased by 2.1-fold and 1.99-fold with CRO and CHR, respectively ($p < 0.005$ vs. C for both bars) and 1.55-fold with ERI ($p < 0.05$ vs. C). In M1 macrophages (Figure 9, panel E), the basal levels of MCP-1 released in the medium were higher than those of M0 control cells (1.9-fold increase), and they were significantly increased after exposure to CRO (1.33-fold, $p < 0.0005$ vs. C). In contrast, in M2 macrophages (Figure 9, panel F), basal MCP-1 release showed only a slight increase (1.3-fold) compared to M0 control cells. Furthermore, in M2 cells exposed to CRO and ERI fibres, the release of this chemokine was further significantly increased by 1.5- and 1.2-fold ($p < 0.0005$ and $p < 0.01$ vs. C, respectively). In general, it is possible to conclude that CRO is invariably the most effective in stimulating the release of this chemotactic protein in the three types of differentiated macrophages compared to the other two fibres. For MCP-1, as in the case of IL1β, the production of this chemokine has important consequences in the onset and progression of cancers other than those due to the development of the inflammatory process (Fridlender et al., 2011). In fact, MCP-1 production in the tumour microenvironment has been linked to a change in tumour-associated macrophages (TAMs) to an immunosuppressive phenotype, contributing to cancer cell proliferation and immunotherapy resistance (Mantovani et al., 2004b). As a matter of fact, this chemokine production also has an

important role in mesothelioma development (Chu et al., 2019). With this premise, our data demonstrate that the significant production of this chemokine by all three types of fibre-stimulated macrophages may contribute to the onset of conditions that are favourable to cancer progression in the lung because the release of this chemoattractant factor is able to suppress the immune system's ability to fight tumour cell proliferation in the long term.

TNF-α is also a well-recognised cytokine involved in the progression of inflammation and fibrosis in lung respiratory diseases (Lundblad et al., 2005). Indeed, the severity of the disease often correlates with TNF-α overexpression and release. Thus, this cytokine was also quantified in the cellular media of the three types of polarised macrophages incubated with the three fibres for 24 h. The results show that all of the fibres were able to significantly increase TNF-α production after only 24 h of incubation in the three types of macrophages. In particular, in unstimulated M0 macrophages (Figure 9G), the basal cytokine production amounted to 49.7 ± 0.3 pg/mL, and this further increased by 1.9-fold in the presence of both CRO and CHR ($p < 0.05$ and $p < 0.0005$ vs. C, respectively) and by 2.7-fold by ERI ($p < 0.05$ vs. C). In M1 cells (Figure 9H), the basal release of the cytokine in unstimulated cells was significantly higher than in M0 control cells (9.4-fold). The fibre treatment further increased this production by 1.5-fold and 1.24-fold for CRO and CHR, respectively ($p < 0.005$ vs. C for both), and by 1.6-fold for ERI ($p < 0.0005$). Furthermore, in M2 cells (Figure 9I), an increase in basal TNF-α production in unstimulated cells, as compared to M0 control cells, was also observed (1.8-fold). This production further increased by 2.3-, 1.7- and 1.1-fold in the presence of CRO, CHR and ERI, respectively ($p < 0.0001$ vs. C for the first two and $p < 0.001$ for the third). Once again, this cytokine, acting as a paracrine and autocrine growth factor, was demonstrated to have a role in tumour initiation, promotion, invasion and angiogenesis (Sethi et al., 2008). Thus, the significant TNF-α production measured in all three types of differentiated macrophages stimulated by the fibres once again shows the pro-tumour activity of these cells when recruited during the inflammatory response. Our data confirm that all of the fibres cause significant production of well-known inflammatory and chemotactic cytokines in all macrophage phenotypes, with some differences among the various fibres. These results also indicate that after immunosuppressive M2 macrophages are recruited to the site of inflammation in response to mineral inhalation, the inflammatory response cannot be quenched since these cell types will also contribute to the production of pro-inflammatory factors, leading to the chronicisation of the phenomenon. Since the production of these cytokines is also clearly involved in cancer progression (Coussens and Werb, 2002), these results confirm the hazard of all three mineral fibres investigated in this work.

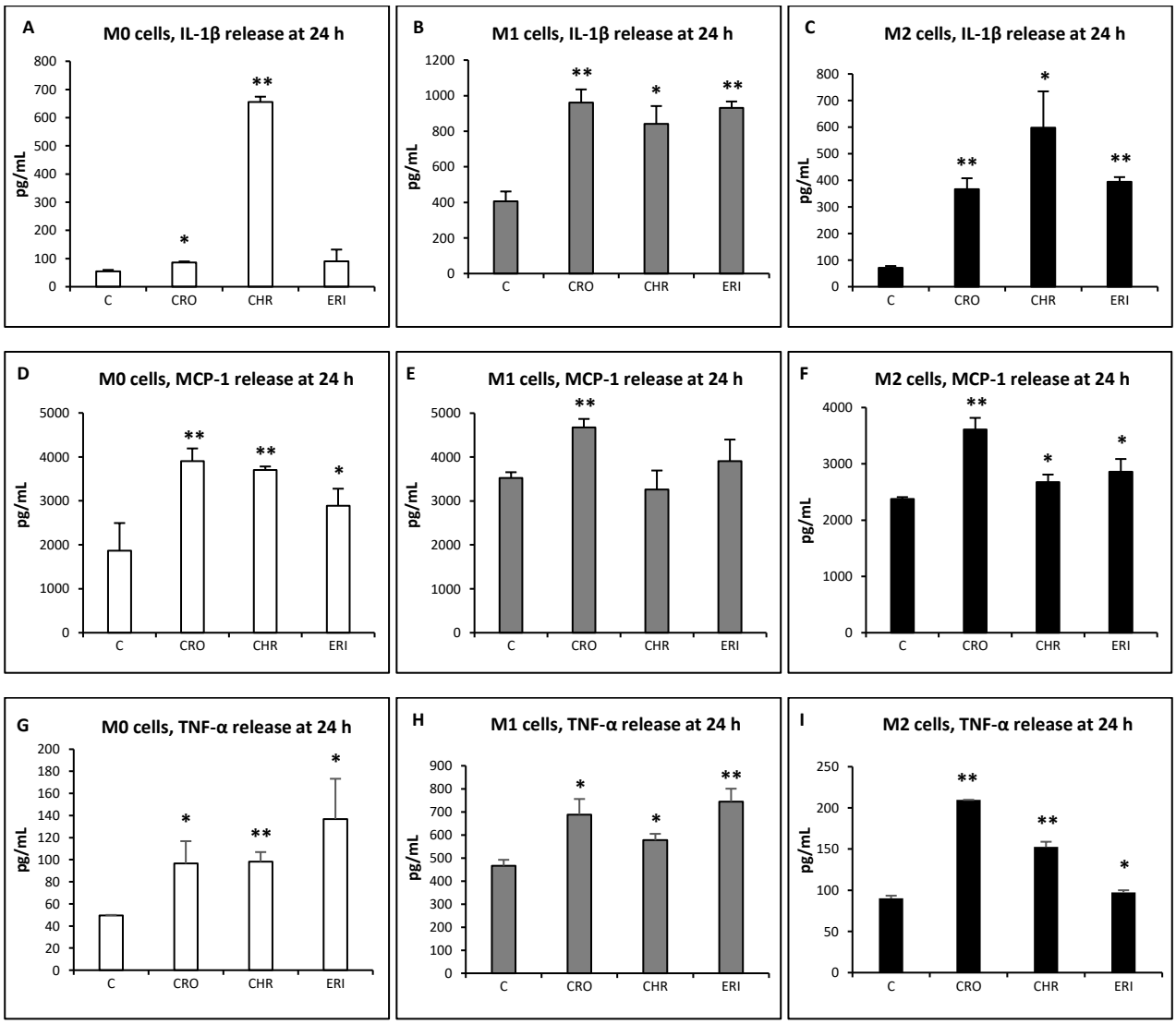

Figure 9. Extracellular release of inflammatory cytokines. (**A**) IL-1β release (in pg/mL) quantified by ELISA kit in M0 THP-1 macrophages incubated for 24 h with 50 µg/mL CRO, CHR and ERI. Results are the mean ± SD of two independent experiments performed in duplicate. Asterisks indicate significance in Tukey test (ANOVA $p < 0.000001$; Tukey vs. C, * $p < 0.0005$, ** $p < 0.0001$, respectively). (**B**) IL-1β release in M1 THP-1 macrophages in the same conditions as (**A**). ANOVA $p < 0.000005$; Tukey vs. C, * $p < 0.001$, ** $p < 0.0001$, respectively. (**C**) IL-1β release in M2 THP-1 macrophages in the same conditions as (**A**). ANOVA $p < 0.00005$; Tukey vs. C, * $p < 0.001$, ** $p < 0.0001$, respectively. (**D**) MCP-1 release (in pg/mL) quantified by ELISA kit in M0 THP-1 macrophages incubated as in (**A**). ANOVA $p < 0.0001$; Tukey vs. C, * $p < 0.05$, ** $p < 0.005$, respectively. (**E**) MCP-1 release in M1 THP-1 macrophages in the same conditions as (**A**). ANOVA $p < 0.001$; Tukey vs. C, ** $p < 0.0005$. (**F**) MCP-1 release in M2 THP-1 macrophages in the same conditions as (**A**). ANOVA $p < 0.00005$; Tukey vs. C, * $p < 0.01$, ** $p < 0.0005$, respectively. (**G**) TNF-α release (in pg/mL) quantified by ELISA kit in M0 THP-1 macrophages incubated in the same conditions as (**A**). ANOVA $p < 0.005$; Tukey vs. C, * $p < 0.05$, ** $p < 0.0005$, respectively. (**H**) TNF-α release in M1 THP-1 macrophages in the same conditions as (**A**). ANOVA $p < 0.00005$; Tukey vs. C, * $p < 0.005$, ** $p < 0.0005$, respectively. (**I**) TNF-α release in M2 THP-1 macrophages in the same conditions as (**A**). ANOVA $p < 0.00005$; Tukey vs. C, * $p < 0.001$, ** $p < 0.0001$, respectively.

Finally, we also analysed the gene expression profiles of interleukin-6 (IL-6) and interleukin-8 (IL-8), two other genes that are usually overexpressed in macrophages challenged with harmful stimuli and that are actively involved in the inflammatory response (Gabay, 2006; Qazi et al., 2011), together with the same inflammatory factors that were previously quantified by the ELISA tests in the different types of macrophages, displayed in Figure 9 (namely, IL-1β, MCP-1 and TNF-α). Both IL-6 and IL-8 were investigated because they are linked to detrimental effects of chronic inflammation. IL-6 sustains continuous monocyte recruitment to the site of inflammation, collagen synthesis and the anti-apoptotic effects of immune cells (Gabay, 2006), while IL-8 displays strong chemoattractant activity, mitogenic and angiogenic effects, collagen synthesis and tumour growth promotion (Qazi et al., 2011). On the other hand, the reason to investigate the cytokine release of IL-1β, MCP-1 and TNF-α (Figure 9) together with the relative mRNA production (Figure 10) is due to the fact that the synthesis and storage of these pro-inflammatory factors are already upregulated during M0 polarisation as compared to untreated THP-1 monocytes. Thus, the cellular response to asbestos treatment could be due to either (i) the neo-synthesis of cytokines from stabilised cytoplasmic mRNAs and their release in the extracellular milieu, (ii) an increase in mRNA transcription by the control of gene expression at the DNA level or (iii) a combination of the two processes (Lacy and Stow, 2011). Thus, to investigate the regulation of IL-1β, MCP-1 and TNF-α release stimulated by the fibres in differentiated THP-1 macrophages, their gene expression was investigated as well (Figure 10) at the 6 h time point. This time point was chosen because cells in contact with the mineral fibres are still alive but have perceived the inflammatory stimulus by phagocytosis and/or plasma membrane contact and have already shown a respiratory burst that produces enough ROS to activate the necessary signal transduction pathways (see Figures 2 and 6).

In M0 THP-1 macrophages, the mRNAs of all investigated cytokines (Figure 10A: IL-1β, IL-6 and IL-8; Figure 10B: MCP-1 and TNF-α) were significantly increased as compared to the undifferentiated control THP-1 monocytes in the absence of the fibres (IL-1β, 278-fold increase; IL-6, 53-fold increase; IL-8, 99-fold increase; MCP-1, 3-fold increase; and TNF-α, 10-fold increase). This means that, in M0 macrophages, the mRNA transcripts of the major inflammatory cytokines are already available for immediate translation in the cytoplasm upon receiving an inflammatory stimulus. Conversely, regarding the further increase in mRNA expression upon fibre treatment of M0 cells compared to untreated M0 cells, we observed different behaviours depending on the measured cytokine. In the case of IL-1β, significant inhibition of mRNA synthesis was observed for CRO and CHR treatment (panel A, black bars, 37% and 24% decrease, $p < 0.05$ vs. M0) but not for ERI. On the contrary, IL-6 mRNA (panel A, white bars) showed a significant increase only in the presence of CRO (3.4-fold, $p < 0.05$ vs. M0) compared to untreated M0 cells,

while IL-8 expression was always similar to untreated control M0 cells in all asbestos fibre-treated samples (panel A, grey bars). TNF-α mRNA was also found to be increased only in CRO-treated M0 cells (panel B, dotted bars, 1.3-fold, $p < 0.05$ vs. M0), while MCP-1 mRNA was not affected by treatment with any of the fibres compared to M0 cells (panel B, striped bars). These results indicate that in M0 cells, the significant cytokine production and release upon the addition of mineral fibres (Figure 9) are mainly due to protein synthesis from pre-existing cytoplasmic mRNA transcripts rather than the upregulation of transcription at the gene level, except for CRO, for which increases in IL-6 and TNF-α transcripts were also observed.

Even in M1 THP-1 macrophages, the mRNAs of all of the investigated cytokines were significantly increased as compared to undifferentiated THP-1 monocytes and thus immediately available for translation if needed (Figure 10, panel C: IL-1β, 1250-fold increase; IL-8, 421-fold increase; Figure 10, panel D: IL-6, 17-fold increase; MCP-1, 3.9-fold increase; and TNF-α, 3.6-fold increase). Moreover, a further increase in the expression of IL-1β, IL-6 and IL-8 cytokines in the M1 phenotype cells was observed upon CRO treatment. In particular, in the case of IL-1β mRNA (black bars), CRO treatment increased the synthesis by 1.3-fold ($p < 0.05$ vs. M1), while CHR and ERI inhibited the mRNA synthesis of this cytokine by 54% and 50%, respectively ($p < 0.05$ vs. M1 for both), although this reduction at the mRNA level did not affect the IL-1β cytokine release measured at 24 h, which indeed was relevant for all three types of fibres (Figure 9B). Regarding IL-8 mRNA expression (grey bars), CRO increased its synthesis by 1.8-fold ($p < 0.05$ vs. M1), while CHR and ERI diminished it by 50% in both cases ($p < 0.05$ vs. M1). In the case of IL-6 (white bars), again, its mRNA was increased by 1.5-fold by CRO treatment ($p < 0.05$ vs. M1), while CHR and ERI inhibited its synthesis by 40% in both cases ($p < 0.05$ vs. M1). Furthermore, in M1 cells, none of the fibre treatments was able to further increase the mRNA synthesis of TNF-α (dotted bars) or MCP-1 (striped bars) as compared to the untreated control M1 macrophages.

Finally, mRNA expression analysis in differentiated M2 THP-1 macrophages (Figure 10, panels E and F) once again revealed that the expression levels of IL-1β, IL-6, IL-8 and TNF-α were significantly increased compared to undifferentiated THP-1 monocytes (22-fold, 42-fold, 2-fold and 21-fold, respectively). Moreover, this mRNA production was further increased by both CRO and CHR treatment but not by ERI. Specifically, CRO and CHR increased IL-1β mRNA (panel E, black bars) by 2.4-fold and 1.7-fold ($p < 0.05$ vs. M2), IL-6 (panel E, white bars) by 2.7-fold and 4.8-fold ($p < 0.05$ vs. M2), IL-8 (panel F, grey bars) by 2.1-fold and 1.5-fold ($p < 0.05$ vs. M2), and TNF-α (panel F, dotted bars) by 1.5-fold and 1.4-fold, respectively ($p < 0.05$ vs. M2). Finally, in M2 cells, MCP-1 mRNA expression (panel F, striped bars) did not significantly differ from that of undifferentiated THP-1 monocytes in either the presence or absence of fibres. Noteworthy is the

increase in the expression of pro-inflammatory cytokines, especially IL-6 and IL-8, in these cell types. Indeed, since this macrophage phenotype should appear at the site of inflammation at a later stage to help resolve the inflammatory state, the fact that M2 cells instead produce IL-6 and IL-8 in the presence of CRO and CHR seems to demonstrate the opposite, as these cytokines stimulate the chronicisation of inflammation, eventually promoting fibrosis and cancer cell growth.

These intriguing results (Figures 9 and 10) suggest that the three macrophage phenotypes are able to respond to the detrimental stimuli of mineral fibres through the release of inflammatory mediators such as IL-1β, MCP-1 and TNF-α, mainly synthesised from pre-existing mRNA transcripts in the cytoplasm of the differentiated macrophages, with a minor contribution from upregulated transcription at the gene level. Notably, CRO seems to be able to also induce the upregulation of gene transcription of TNF-α in M0, M1 and M2 macrophages and of IL-1β, IL-6 and IL-8 in M1 and M2 fibre-stimulated macrophages. CHR is also able to partially induce this response at the transcriptional level by increasing IL-1β, IL-6, TNF-α and IL-8 only in M2 macrophages, while ERI never showed an upregulating effect at the transcriptional level of the investigated cytokines. As mentioned previously, there is a measurable decrease in Ca^{2+}, which acts as an intracellular second messenger, in ERI-stimulated macrophages in the hours immediately after the addition of the fibres (Di Giuseppe et al., 2021a), and this could contribute to the lack of sufficient transduction signals able to induce an effect at the regulatory regions of cytokine genes in the nucleus in the first hours of stimulation. Thus, ERI inhalation could create a milder chronic inflammatory state in the lungs relative to that induced by CRO and CHR, and its tumorigenic effect may be more associated with the DNA-damaging properties of the fibres (see Figure 6) and their high biodurability in organic fluids (Gualtieri, et al., 2018b). Quite surprisingly, M2 macrophages, which are usually associated with a more anti-inflammatory phenotype, instead showed significant production of pro-inflammatory cytokines in the presence of the three types of fibres, probably contributing to the enhancement rather than the mitigation of the inflammatory state of the tissue. This may reasonably occur in the lungs of mineral-exposed subjects due to the persistence and biodurability of the mineral fibres, which undergo cycles of *in situ* ingestion and re-ingestion by phagocytic cells for months, as in the case of chrysotile, or for years, as in the case of crocidolite and erionite. Furthermore, the observed behaviour in the presence of the mineral fibres confirms that the distinction between the M1 and M2 phenotypes of macrophages is not so clear-cut and that these cells may show more fluid behaviour depending on the stimuli encountered and the extracellular milieu of the tissues to which they are recruited, with certain phenotypes exacerbating the inflammatory processes despite being initially recruited to obtain the opposite effect.

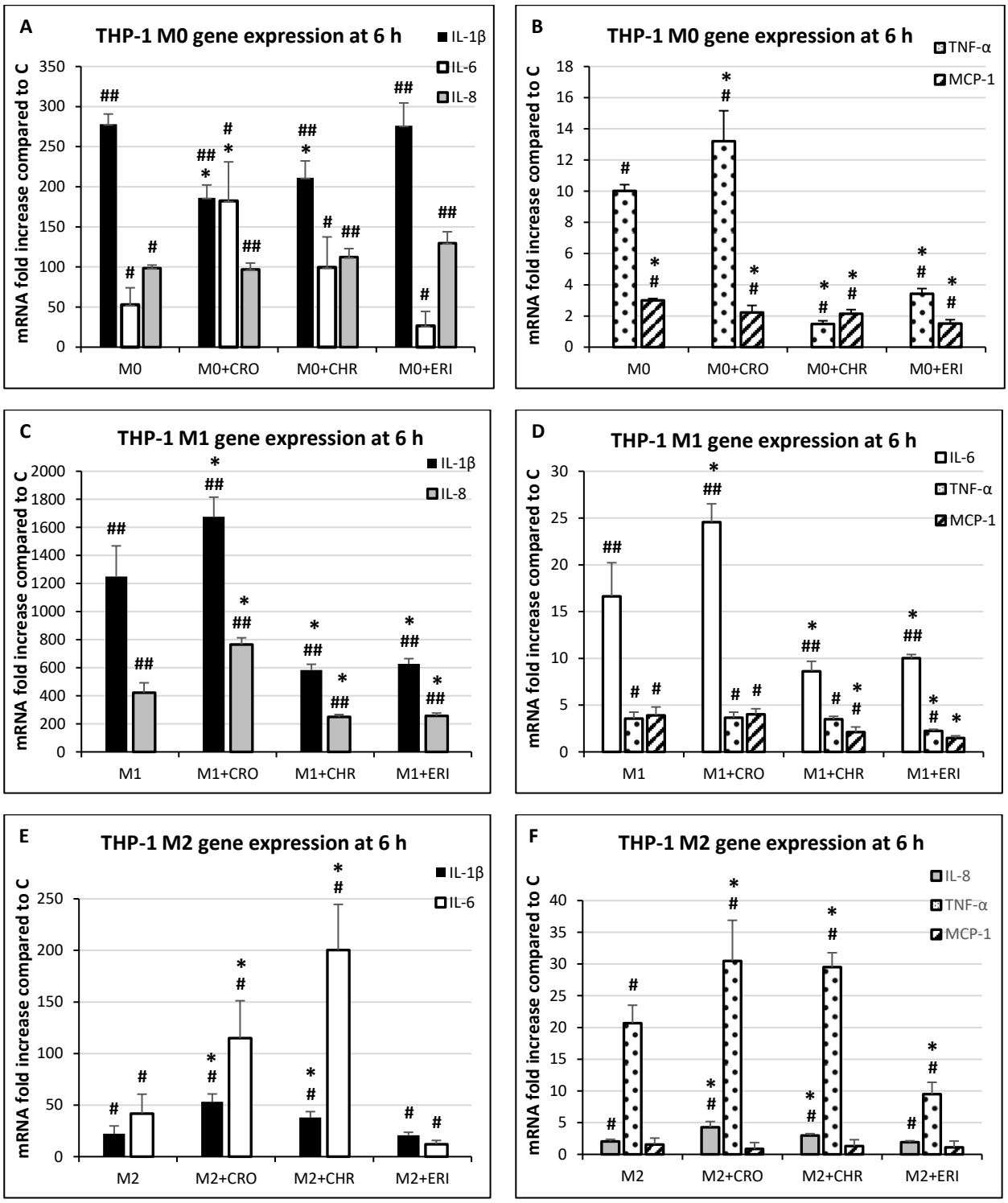

Figure 10. Gene expression of inflammatory mediators. (**A**) Gene expression of IL-1β, IL-6 and IL-8 measured by qPCR analysis after M0 THP-1 cell incubation for 6 h with 50 μg/mL mineral fibres (CRO, CHR and ERI). Data are normalised to the HPRT-1 housekeeping gene and expressed as mRNA fold increase compared to undifferentiated (control) THP-1 monocytes. Results are the mean ±SD of three experiments performed in triplicate. Asterisks indicate significance in Tukey test (IL-1β ANOVA $p<0.000001$, IL-6 ANOVA $p<0.0005$, IL-8 ANOVA $p < 0.000001$; Tukey vs. C # $p < 0.05$, ## $p < 0.0001$; Tukey vs. M0 * $p<0.05$, respectively). (**B**) Gene expression of TNF-α and MCP-1 measured by qPCR analysis in M0 THP-1 cell in the same conditions as (**A**). TNF-α ANOVA $p<0.000001$, MCP-1 ANOVA $p<0.00005$, Tukey vs. C # $p < 0.05$, Tukey vs. M0 * $p<0.05$, respectively. (**C**) Gene expression

of IL-1β and IL-8 measured by qPCR analysis in M1 THP-1 cells in the same conditions as (**A**). IL-1β ANOVA $p<0.000001$, IL-8 ANOVA $p<0.000001$, Tukey vs. C ## $p < 0.0001$, Tukey vs. M1 * $p<0.05$, respectively. (**D**) Gene expression of IL-6, TNF-α and MCP-1 measured by qPCR analysis in M1 THP-1 cells in the same conditions as (**A**). IL-6 ANOVA $p < 0.000001$ TNF-α ANOVA $p<0.0001$, MCP-1 ANOVA $p<0.0005$, Tukey vs. C # $p < 0.05$, C ## $p < 0.0001$, Tukey vs. M1 * $p<0.05$, respectively. (**E**) Gene expression of IL-1β and IL-6 measured by qPCR analysis in M2 THP-1 cells in the same conditions as (**A**). IL-1β ANOVA $p<0.000005$, IL-6 ANOVA $p<0.00005$, Tukey vs. C # $p < 0.05$, Tukey vs. M2 * $p<0.05$, respectively. (**F**) Gene expression of IL-8, TNF-α and MCP-1 measured by qPCR analysis in M2 THP-1 cell in the same conditions as (**A**). IL-8 ANOVA $p < 0.0001$ TNF-α ANOVA $p<0.000005$, Tukey vs. C # $p < 0.05$, Tukey vs. M2 * $p<0.05$, respectively.

7. ORENBURG CHRYSOTILE: RESULTS AND DISCUSSION

Due to the contradictory results of countless *in vitro*, *in vivo* and epidemiologic studies, the potential toxicity of short asbestos fibres—and in particular of short chrysotile fibres—remains a controversial issue in the scientific community. Indeed, in this endless debate, one side claims that all short asbestos fibres are toxic and carcinogenic (Egilman and Tran, 2016), while the other side argues that chrysotile fibres with lengths < 5 μm do not contribute to the negative effects of asbestos on human health (Bernstein, 2022). To this aim, representative batches of short (length < 5 μm) and long (length > 5 μm) chrysotile fibres were prepared from a commercial chrysotile extracted from an open pit mine near Yasny (Russia) by the Orenburg Minerals company. This sample was extensively characterised in a previous work, establishing its morphometric parameters, mineralogical composition, surface activity and chemical formula. Briefly, Orenburg chrysotile is composed of bundles of fibres that are easily split lengthwise, forming single fibres and thin bundles with a length ranging from 1.36 μm to 188.1 μm (mean length 33.9 μm) and a width varying from 0.05 μm to 2.79 μm (mean width 0.70 μm). Clino-chrysotile was the major phase detected in the sample, although minor contributions of ortho-chrysotile, lizardite, magnetite, hydromagnesite and calcite were also distinguished (Di Giuseppe et al., 2021c). The two fractions of Orenburg chrysotile were prepared by cryogenic milling, which produces fibres of a precise size while preventing structural defects or amorphization, thus preserving the physical-chemical properties of the original fibre. Since fibre length is strictly regulated by the milling time under cryogenic conditions, the short fraction (CHR-S, 95% L < 5 μm) was obtained by cryogenic milling for 40 min, while the long fraction (CHR-L, 88% L > 5 μm) required a milling time of 10 min (Scognamiglio et al., 2021).

The cytotoxic and genotoxic activity of these two size-separated fractions of chrysotile was then investigated *in vitro* in comparison to UICC crocidolite, an amphibole asbestos commonly employed as a positive carcinogenic standard, and to wollastonite NYAD G, a calcium inosilicate mineral characterised by non-biodurable fibres, scarce metal content and low toxicity (Di Giuseppe et al., 2021b). In particular, the cytotoxic activity of the two fractions of Orenburg chrysotile was evaluated by measuring the level of cell death by either cell lysis or apoptosis in THP-1-derived M0 macrophages and HECV endothelial cells. Subsequently, the intracellular oxidative state, the presence of DNA damage and the inflammatory response were studied in the two cell lines, since they are recognised factors that occur early during the inflammatory response and contribute to the onset of chronic diseases and malignancies in the long term. Finally, the effect of the pro-inflammatory mediators secreted by asbestos-treated M0 macrophages on HECV endotheliocytes was examined in a co-culture system at several time points (24 h, 48 h, and 7 days).

7.1. ACUTE TOXICITY OF MINERAL FIBRES

The cytotoxic effect of these mineral fibres was evaluated in M0 macrophages and in HECV endotheliocytes with the MTT assay, which measures mitochondrial enzyme activity by quantifying resultant alterations of energy metabolism and, ultimately, cell death. After 24 h and 48 h of exposure to CRO, WOL, CHR-S and CHR-L (Figure 1, panels A-B, dotted, white, gray and black bars, respectively), the viability index of M0 macrophages showed that both fractions of chrysotile induced a dose-dependent toxic effect which was comparable to CRO. Indeed, at 24 h (Figure 1, panel A) CRO at 50 µg/mL (dotted bar) caused a mortality rate of 25.6% compared to control cells (C), whereas CHR-S (grey bars) induced a dose-dependent cell death rate of 34.8%, 30.3% and 24.9%, at 100, 50 and 10 µg/mL, respectively, compared to C. At the same concentrations, CHR-L (black bars) determined a markedly higher cell death percentage, reaching a mortality rate of 49.3%, 40.5% and 36.5%, respectively. In M0 macrophages incubated with mineral fibres for 48 h (Figure 1, panel B), the dose-dependent mortality rate induced by the treatment with CHR-S (grey bars) similarly amounted to 37.7%, 35.2% and 37.6% at 100, 50 and 10 µg/mL, respectively. Instead, the prolonged exposure to CHR-L (black bars) at the same concentrations caused a sharp increase in the cell death percentage (57.9%, 54.5% and 46.0%, respectively). As expected, at both time points, wollastonite—which represented the negative control—displayed the lowest cytotoxic activity on M0 macrophages.

A similar trend was found in HECV endotheliocytes incubated with mineral fibres for 24 h and 48 h (Figure 1, panels C-D). In particular, at 24 h (Figure 1, panel C) both CHR-S (grey bars, 38.1%, 30.4% and 25.7%, at 100, 50 and 10 µg/mL, respectively, compared to C) and CHR-L (black bars, 49.4%, 41.9% and 36.3% at the same concentrations, respectively) induced a dose-dependent cell death rate which was significantly higher than CRO (dotted bar, 29.7%). The cytotoxic effect of these mineral fibres was exacerbated in HECV cells challenged at the same concentrations for 48 h (Figure 1, panel D), as evidenced by the increased mortality rate displayed by CHR-S (grey bars, 43.5%, 41.1% and 37.7%, respectively) and CHR-L (black bars, 53.3%, 53.0% and 50.9%, respectively), while the cell death rate of CRO-treated endotheliocytes reached 32.8% (dotted bar). Furthermore, wollastonite induced the less severe cytotoxic effects also in HECV cells, since it caused only a slight percentage of cell death at 48 h (22.0% compared to C).

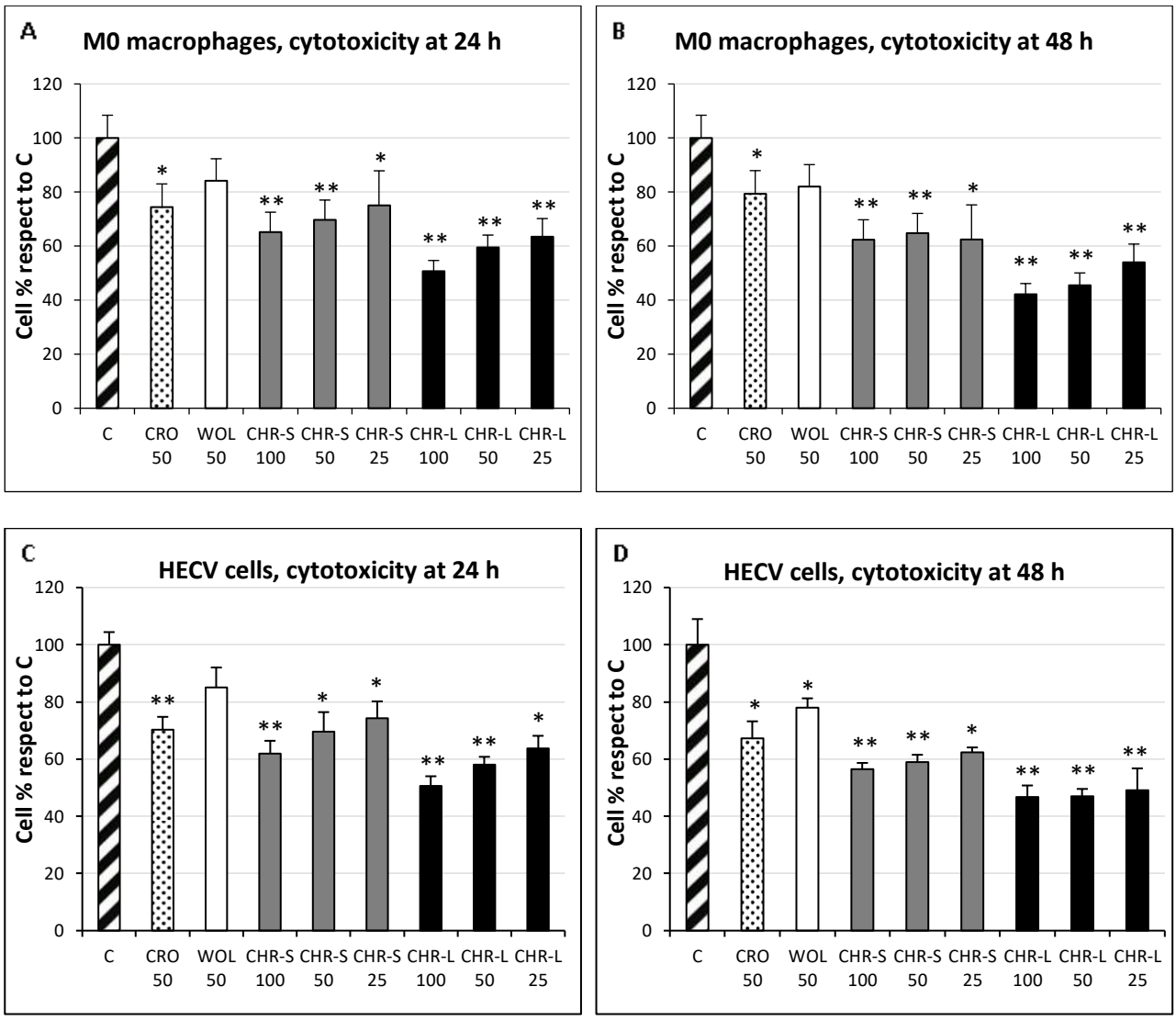

Figure 1. Cytoxicity quantification after exposure to mineral fibres. (**A**) M0 macrophage cytotoxicity quantification with the MTT test at 24 h in the presence of 100, 50 and 25 µg/mL of the mineral fibres CRO (dotted bar), WOL (white bar), CHR-S (grey bars) and CHR-L (black bars). Results are expressed as cell percentages relative to control cells (striped bar) and are the mean ± SD of three independent experiments performed in quadruplicate. Asterisks indicate the significance in a paired Tukey test (ANOVA, $p < 0.00001$; Tukey vs. C: * $p < 0.05$, ** $p < 0.005$, respectively). (**B**) M0 macrophage cytotoxicity quantification at 48 h in the same conditions as (**A**). ANOVA, $p < 0.00005$; Tukey vs. C: * $p < 0.05$, ** $p < 0.005$, respectively. (**C**) HECV endotheliocytes cytotoxicity quantification at 24 h in the same conditions as (**A**). ANOVA, $p < 0.0005$; Tukey vs. C: * $p < 0.005$, ** $p < 0.0005$, respectively. (**D**) HECV endotheliocytes cytotoxicity quantification at 48 h in the same conditions as (**A**). ANOVA, $p < 0.0005$; Tukey vs. C: * $p < 0.01$, ** $p < 0.0005$, respectively.

To investigate which type of cell death M0 macrophages and HECV endotheliocytes were undergoing, two analyses were performed: the lactate dehydrogenase (LDH) assay, which measures the plasma membrane damage by quantifying the leakage of this cytosolic enzyme in the cell medium, and the annexin/propidium iodide staining assay, which evaluates the level of cellular apoptosis by confocal microscopy. To assess the cell death caused by plasma membrane disturbance, the LDH assay was performed on M0 macrophages (Figure 2, panels A-B) and on HECV endotheliocytes (Figure 2, panels C-D) challenged with mineral fibres for 24 h and for 48 h. At both time points, the rates of cellular damage observed in M0 macrophages treated with CRO, WOL and CHR-S were comparable to the control (dotted, white and gray bars, respectively). Conversely, CHR-L (black bars) induced a dose-dependent plasma membrane disturbance, although a significant degree of cellular damage was only found after treatment with its highest concentration (1.55-fold and 1.47-fold higher than control cells at 24 h and 48 h, respectively). Overall, in M0 macrophages the exposure to CRO and CHR-S was not able to induce cell lysis, meaning that the high rates of cytotoxicity measured through the MTT test at 24 h and 48 h (Figure 1, panels A-B), are the result of other death mechanisms. In particular, in the case of CRO, these results are in agreement with the recent findings of our group, which demonstrated that, in all THP-1-differentiated macrophages, this fibre induced cell death mainly through an apoptotic mechanism (Mirata et al., 2022). On the other hand, the treatment with CHR-L determined significant levels of cell lysis, suggesting that this fibre may cause a multifactorial cytotoxic activity in which cell membrane alterations are at least partially capable of inducing cell death.

Regarding HECV endotheliocytes treated with mineral fibres for 24 h (Figure 2, panel C), a relevant increase in cell membrane-lysis events was found after the exposure to CRO and to WOL at 50 µg/mL (1.72-fold and 1.45-fold, respectively). In addition, CHR-L induced significant dose-dependent plasma membrane cell damage, with values 2.17-, 2.02- and 2.01-fold higher than control cells at 100, 50 and 10 µg/mL, respectively. The trend was similar after 48 h of treatment (Figure 2, panel D), as evidenced by the increased levels of cell lysis caused by CRO (1.84-fold at 50 µg/mL) and CHR-L (2.39-, 2.31- and 1.75-fold at 100, 50 and 10 µg/mL, respectively). Albeit to a lesser degree compared to CHR-L, CHR-S induced a significant degree of plasma membrane cell damage, with values 1.90-, 1.80- and 1.62-fold higher than control cells at 100, 50 and 10 µg/mL, respectively. Therefore, in HECV endotheliocytes, CRO and CHR-L caused a significant level of cell lysis suggesting that, with both fibres, the direct cell membrane damage is at least partially responsible for the high levels of cell death found with the MTT test (Figure 1, panels C-D). Moreover, compared to CHR-L, CHR-S requires a longer exposure time to induce plasma membrane damage in HECV cells, hinting that the length of Orenburg chrysotile fibres may be

correlated with differences in their cytotoxicity mechanism. Additionally, a certain degree of cell lysis was also observed in HECV cells treated with WOL for 24 h, suggesting that this fibre may cause cell membrane alterations, and thus death events, that are probably responsible for the small amount of cell death measured through the MTT test.

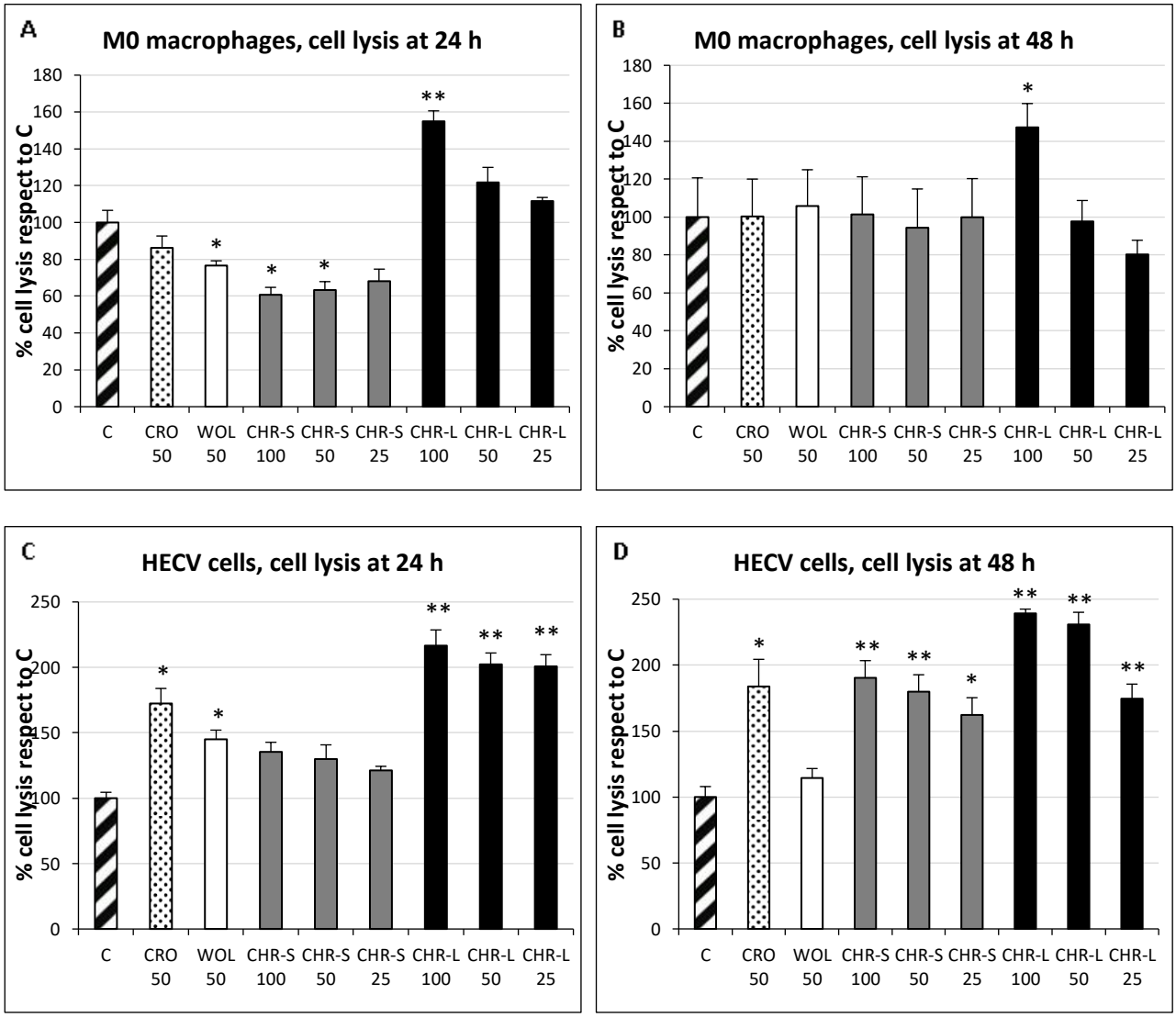

Figure 2. Cell plasma membrane damage assessment. (**A**) Cell lysis evaluation assayed by quantification of LDH release in the cell medium at 24 h in M0 macrophages in the presence of 100, 50 and 25 µg/mL of the mineral fibres CRO (dotted bar), WOL (white bar), CHR-S (grey bars) and CHR-L (black bars). Results are expressed as percentage of cell lysis relative to control cells (striped bar) and are the mean ± SD of three experiments performed in quadruplicate. Asterisks indicate the significance in paired Tukey test (ANOVA, $p < 0.0001$; Tukey vs. C: * $p < 0.05$, ** $p < 0.01$), respectively. (**B**) Cell lysis evaluation assayed at 48 h in M0 macrophages in the same conditions as (**A**). ANOVA, $p < 0.0001$; Tukey vs. C: * $p < 0.05$. (**C**) Cell lysis evaluation assayed at 24 h in HECV endotheliocytes in the same conditions as (**A**). ANOVA, $p < 0.00005$; Tukey vs. C: * $p < 0.05$, ** $p < 0.0005$, respectively. (**D**) Cell lysis evaluation assayed at 48 h in HECV endotheliocytes in the same conditions as (**A**). ANOVA, $p < 0.00005$; Tukey vs. C: * $p < 0.01$, ** $p < 0.005$, respectively.

To test this hypothesis, M0 macrophages and HECV endotheliocytes were challenged with the mineral fibres for 24 h and analysed by confocal microscopy after annexin/propidium iodide staining (Figure 3, panels A-C). In M0 macrophages (Figure 3, panel A) all fibres (Figure 3A: panels III-IV CRO, panels V-VI WOL, panels VII-VIII CHR-S and panels IX-X CHR-L, respectively) induced a certain degree of early (only green positivity) and/or late apoptosis (concomitant green/red positivity) compared to control cells (Figure 3A: panels I-II). The quantitative assessment of the apoptotic state (Figure 3, panel B) was obtained by counting and calculating the mean of only green (grey bars) and red–green cells (black bars) in five different fields of confocal microscope images for each treatment. In particular, CHR-S and CHR-L induced significant levels of early apoptosis (40% and 33%, respectively) that were comparable to the percentage of early apoptotic events found after treatment with CRO (36%). Moreover, the exposure to both fractions of chrysotile resulted in a significant amount of late apoptosis signals (20% for both CHR-S and CHR-L), suggesting that the apoptotic mechanism has also a fundamental role in causing the high levels of cytotoxicity highlighted by the MTT test (Figure 1, panels A-B). In particular, CHR-S exerts its cytotoxic activity mainly by apoptosis, as evidenced by the minimal levels of cell lysis measured in the LDH assay (Figure 2, panels A-B); conversely, CHR-L is characterised by a multifactorial cytotoxic activity to which both apoptosis and cell membrane damage contribute. Besides, WOL caused a small degree of early and late apoptosis (24% and 16%, respectively), hinting that the minimal amount of cell death measured in M0 macrophages through the MTT test is mainly the consequence of an apoptotic mechanism.

Regarding the apoptotic analysis of HECV endotheliocytes (Figure 3, panel C), these cells are characteristically organised in clusters, hindering the recognition of single annexin-positive cells and thus a quantitative evaluation of their apoptotic state. Nonetheless, the qualitative assessment of confocal microscope images showed no significant differences between the assayed fibres. Indeed, all mineral fibres (Figure 3C: panels III-IV CRO, panels V-VI WOL, panels VII-VIII CHR-S and panels IX-X CHR-L, respectively) induced a minimal amount of early apoptosis and no significant degree of late apoptosis compared to control cells (Figure 3C: panels I-II). Therefore, since the apoptotic mechanism seems to have only a marginal role in the induction of cell death, the high levels of cytotoxicity measured in fibre-treated HECV endotheliocytes with the MTT test (Figure 1, panels C-D) may be mainly ascribed to the direct cell membrane damage caused by the mineral fibres.

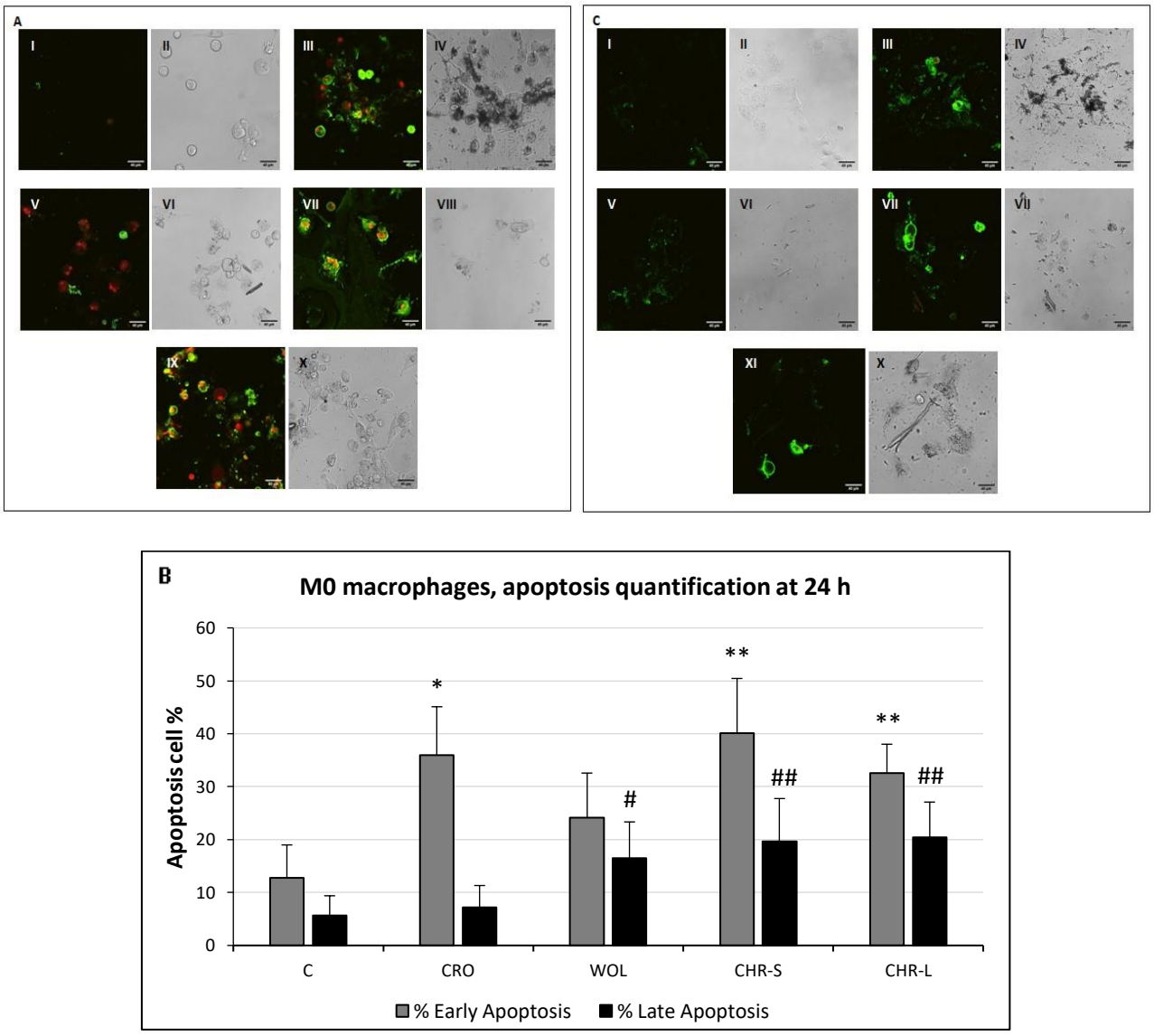

Figure 3. Cell apoptosis evaluation by confocal microscopy analysis. (**A**) Visualisation by confocal microscopy (2.5 × digital zoom) in fluorescence mode (panels I, III, V, VII and IX) and in phase contrast (panels II, IV, VI, VIII and X) of M0 macrophages following treatment with 50 µg/mL of mineral fibres for 24 h and staining of annexin–positive (green) and/or propidium iodide–positive (red) cells. Panels I-II: control; panels III-IV: CRO; panels V-VI: WOL; panels VII-VIII: CHR-S; panels IX-X: CHR-L. The white bar represents 40 µm. (**B**) Quantification of early (annexin–positive, grey bars) and late (both annexin–positive and propidium iodide–positive, black bars) apoptosis in M0 macrophages treated for 24 h with 50 µg/mL of CRO, WOL, CHR-S and CHR-L relative to the total number of cells observed by confocal microscopy; results are the mean ± SD of counts from five microphotograph. Asterisks indicate significance in Tukey test (ANOVA for white bars $p < 0.005$; Tukey vs. C: * $p < 0.005$, ** $p < 0.0005$, respectively; ANOVA for black bars $p < 0.005$, Tukey vs. C: # $p < 0.05$, ## $p < 0.01$, respectively). (**C**) Visualisation by confocal microscopy (2.5 × digital zoom) in fluorescence mode (panels I, III, V, VII and IX) and in phase contrast (panels II, IV, VI, VIII and X) of HECV endotheliocytes following treatment with 50 µg/mL of mineral fibres for 24 h and staining of annexin–positive (green) and/or propidium iodide–positive (red) cells. Panels I-II: control; panels III-IV: CRO; panels V-VI: WOL; panels VII-VIII: CHR-S; panels IX-X: CHR-L. The white bar represents 40 µm.

7.2. ROS PRODUCTION AND DNA DAMAGE

Lung-resident macrophages have a fundamental role in triggering and maintaining the inflammatory response that develops in the pulmonary tissue as a consequence of inhaled harmful stimuli (Aggarwal et al., 2014). In particular, ROS production is a documented early signal of inflammatory response. In fact, after the phagocytosis of harmful particles, macrophages rapidly undergo a respiratory burst, modifying their oxidative state through the intracellular production of ROS, with important consequences on several signalling pathways (Iles and Forman, 2002). The ROS increase can be further exacerbated by the physical-chemical characteristics of the phagocytosed particles, such as the presence of redox-active metals on their surface, which is a common occurrence in the case of mineral fibres. Additionally, the frustrated phagocytosis of long fibres induces a chronic ROS production which damages proteins and DNA, causes membrane damage through lipid peroxidation and prompts fibre encapsulation by collagen and iron-rich proteins (Manning et al., 2002).

After M0 macrophages and HECV endotheliocytes were incubated with 100 µg/mL of mineral fibres for 2 h, the intracellular ROS production was evaluated with the DCF fluorescent probe, revealing that all mineral fibres cause a significant increase of the intracellular ROS production (Figure 4, panels A-B). In M0 macrophages (Figure 4, panel A), CRO, CHR-S and CHR-L induced a similar overproduction of intracellular ROS (1.26-, 1.20-, 1.16-fold higher than untreated control cells, respectively), with values slightly lower than the positive control represented by cells treated with H_2O_2 (1.53-fold increase compared to untreated cells). Instead, in HECV cells (Figure 4, panel B), the exposure to CRO and CHR-L caused a similar increase in the intracellular ROS production (both 2.08-fold higher than untreated control cells), with values higher than the positive control of H_2O_2-stimulated cells (1.77-fold higher than untreated cells). Conversely CHR-S caused a lower, albeit still significant, level of ROS production (1.45-fold higher than untreated cells). Surprisingly, in both M0 macrophages and HECV endotheliocytes, the highest amount of intracellular ROS production was found with WOL (2.60- and 2.47-fold increase, respectively, compared to control cells). These differences in the cellular response are likely due to the different metal ion composition, as well as to the markedly different biodurability of these fibres. In fact, it has been recently demonstrated that crocidolite is able to release significant amounts of intracellular iron in M0 macrophages, while both fractions of Orenburg chrysotile present several redox-active metals in their chemical formula (i.e., Mg, Fe, Al, Cr and Ni) (Scognamiglio et al., 2021; Mirata et al., 2022). Conversely, wollastonite NYAD G is characterised by a relatively low amount of total iron and does not contain relevant amounts of metals that are commonly considered hazardous for human health (i.e., As, Co, Cr, Cd, Sb, Hg, Cu, Pb, Ni, Zn and V).

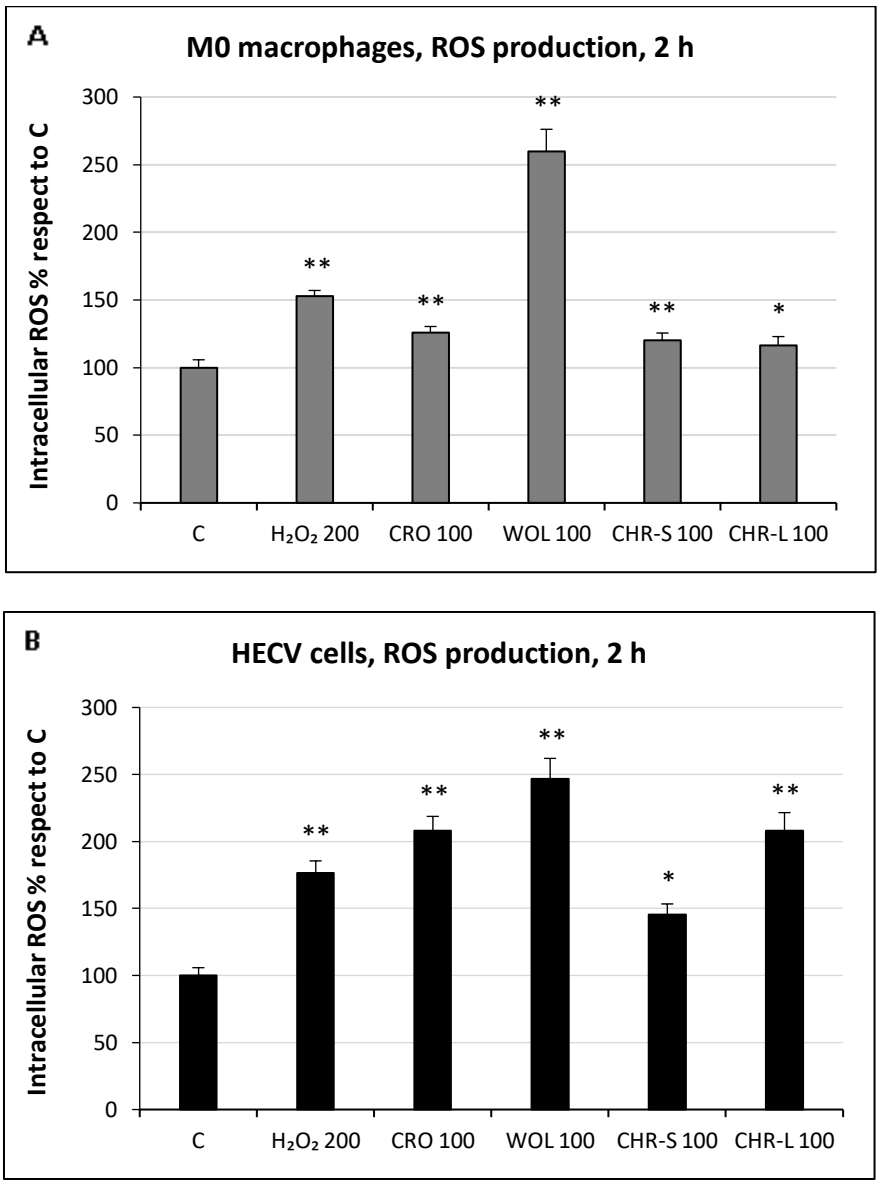

Figure 4. Intracellular ROS production. (**A**) Intracellular ROS production measured by 2',7' -dichlorodihydrofluorescein diacetate fluorometric analysis in M0 macrophages incubated for 2 h in the presence or absence of 100 µg/mL of the mineral fibres CRO, WOL, CHR-S and CHR-L. Cells stimulated with 200 µM H_2O_2 are the positive control. Results are expressed as percentages of ROS production compared to the untreated control (C) and are the mean ± SD of three experiments, in which each condition was tested eight times. Asterisks indicate significance in paired Tukey test (ANOVA $p < 0.000001$; Tukey vs. C: * $p < 0.001$, ** $p < 0.0001$). (**B**) Intracellular ROS production in HECV endotheliocytes treated in the same conditions as (**A**). ANOVA $p < 0.000001$; Tukey vs. C: * $p < 0.0005$, ** $p < 0.0001$, respectively.

However, wollastonite NYAD G exhibits an extremely fast dissolution rate with respect to chrysotile and amphibole asbestos. Indeed, for a 0.25 µm thick fibre, the estimated time for complete dissolution of wollastonite NYAD G is 30 days, which is very short in comparison to Orenburg chrysotile (0.4 y) and UICC standard crocidolite (66 y) (Di Giuseppe et al., 2021b). Since the structure of mineral fibres frequently contains toxic metals, fast-dissolving fibres such as wollastonite and chrysotile can release their metal cargos into the extracellular and intracellular environments more quickly (Gualtieri et al., 2019b). As a result of the fast dissolution rate of wollastonite, Ca^{2+} may be released from its fibres with important consequences on the intracellular ROS production, since Ca^{2+} is a fundamental mediator in cytoplasmic NADPH oxidase isoform activation and in mitochondria-mediated ROS production (Görlach et al., 2015). Therefore, the increase in Ca^{2+} caused by the fast dissolution of wollastonite may explain the higher levels of intracellular ROS generated by this fibre in comparison to Orenburg chrysotile and crocidolite.

This increment in the oxidative state of cells exposed to asbestos fibres is known to contribute to the induction of various forms of DNA damage. In particular, the inhalation of asbestos fibres commonly results in the appearance of DNA double-strand breaks (DSBs) in lung cells due to the overproduction of intracellular ROS that reach the cell nucleus causing damage to the DNA backbone, as well as to the four DNA bases. Thus, DSBs frequently lead to cell death through an apoptotic mechanism; however, in case the cell survives while the injury is not repaired (or is incorrectly repaired), the DNA information may be irrevocably compromised, eventually leading to the onset of various malignancies, such as diffuse malignant mesothelioma and lung cancer (Okayasu et al., 1999; Garcia-Canton et al., 2012).

In order to assess the potential genotoxic damage induced by these fibres, M0 macrophages were incubated with 50 µg/mL of mineral fibres for 24 h and the presence of DNA DSBs was evaluated by confocal microscopy through the staining of the DBS-derived γ-H2AX foci (Figure 5, panel A). Afterwards, the DNA DSBs were quantified by calculating the ratio between the number of foci in fibre-treated M0 cells and the number of foci in untreated M0 cells (Figure 5, panel B). As expected, the foci rate measured in CRO-treated macrophages denoted a significant amount of DSBs (8.98-fold increase compared to control cells), whereas WOL-treated cells displayed no such evidence of acute DNA damage (0.33-fold decrease compared to control cells). Regarding the two fractions of Orenburg chrysotile, both CHR-S and CHR-L induced a significant foci rate formation (6.48- and 10.92-fold increase compared to control cells, respectively), confirming their ability to cause DNA damage in M0 macrophages.

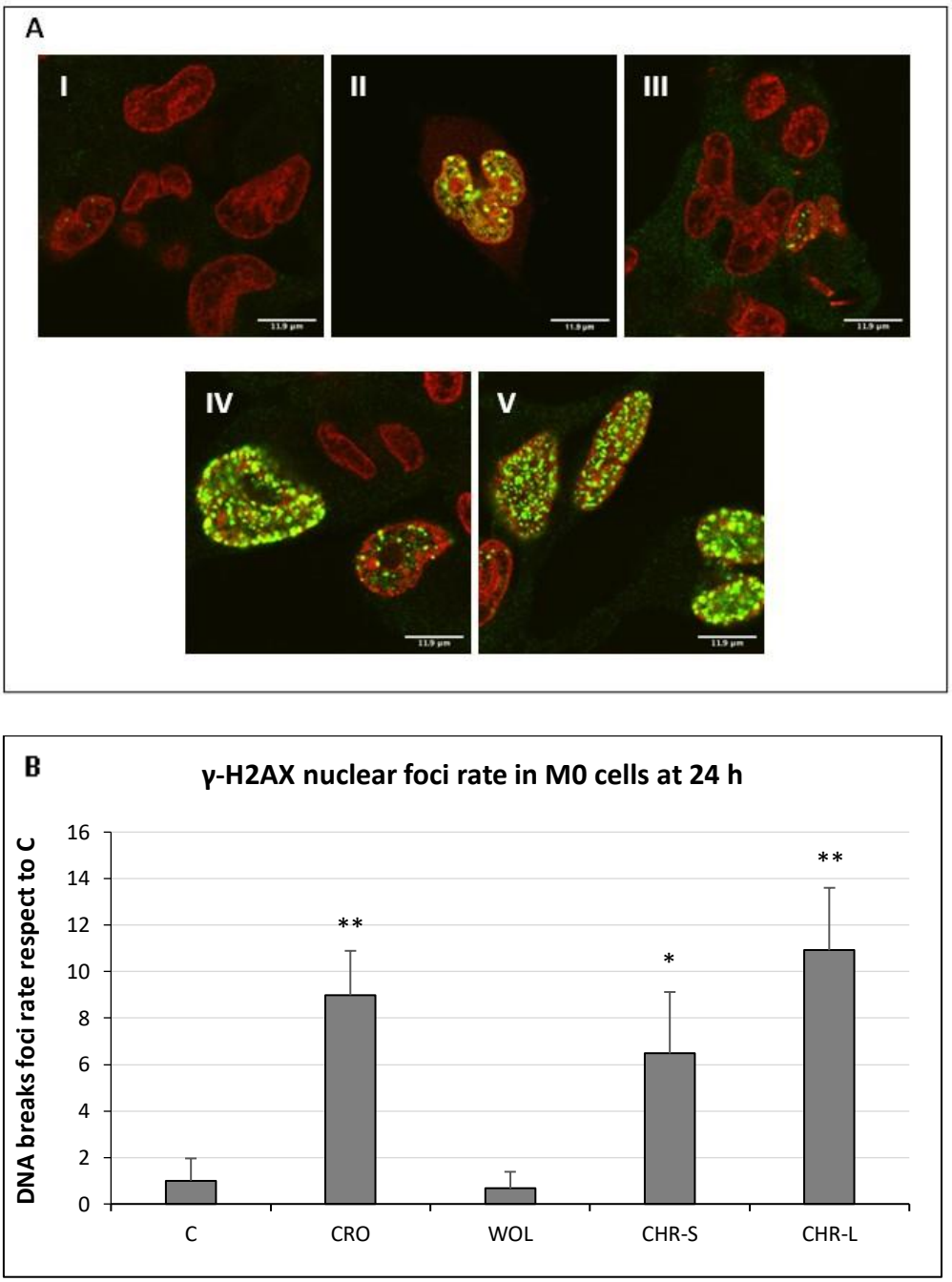

Figure 5. Quantification of the genotoxic damage. (**A**) Visualisation by confocal microscopy analysis (4 × digital zoom) of DNA double-strand breaks by γ-H2AX protein staining (green fluorescence), and DNA by propidium iodide staining (red fluorescence) in M0 macrophages after incubation with 50 µg/mL of mineral fibres for 24 h. Panel I: control; panel II: CRO; panel III: WOL; panel IV: CHR-S; panel V: CHR-L. The white bar represents 11.9 µm. (**B**) Quantification of the double-strand breaks in the DNA of M0 macrophages challenged with 50 µg/mL of mineral fibres for 24 h. The results are expressed as the ratio between the number of foci in fibre-treated M0 cells and the number of foci in untreated M0 cells. Data are the mean ± SD of five microphotographs. Asterisks indicate significance in Tukey test (ANOVA $p < 0.000001$; Tukey vs. C: * $p < 0.005$, ** $p < 0.0005$, respectively).

7.3. INFLAMMATORY RESPONSE

Due to their fundamental role in triggering and maintaining the inflammatory response caused by harmful stimuli, macrophages are known to produce an ample variety of cytokines that regulate the immune response in both acute and chronic conditions (Aggarwal et al., 2014). In particular, the phagocytosis of harmful particles results in the activation of the scavenger receptor A family, which promotes the production of pro-inflammatory cytokines (Thakur et al., 2008). Besides, the generation of H_2O_2 during the respiratory burst is known to stimulate NF-κB and MAPK signalling pathways contributing to the transcriptional upregulation of the inflammatory cytokines, and to activate the NLRP3 inflammasome promoting cleavage and maturation of the cytoplasmic-stored cytokines, that are ultimately released in the extracellular milieu (Iles and Forman, 2002; Dostert et al., 2008). Therefore, the gene expression profile of several pro-inflammatory cytokines (i.e., tumour necrosis factor-alpha (TNF-α), interleukin-1beta (IL-1β), interleukin-6 (IL-6), interleukin-8 (IL-8), monocyte chemoattractant protein-1 (MCP-1)) was evaluated by qPCR in M0 cells treated with mineral fibres for 6 h, 24 h, 48 h and 7 days (Figure 6, panels A-D, respectively). Additionally, these results were also plotted in Figure 7 according to the fibre treatment employed for M0 macrophages (panel A: CRO; panel B: WOL; panel C: CHR-S; panel D: CHR-L). For the shorter experimental times (6 h, 24 h and 48 h), the mineral fibres were employed at a final concentration of 50 µg/mL to assess the acute response. Instead, to investigate the inflammatory response after a semi-chronic exposure period (i.e., 7 days), the concentration of mineral fibres was reduced to 10 µg/mL so that most of the cells were still alive and not too damaged, as not to hinder the transcriptional process. To this aim, the cellular viability of M0 macrophages treated for 7 days with several concentrations of mineral fibres was assessed with the MTT test (data not shown), and the concentration of 10 µg/mL was ultimately chosen since it induced the less severe cytotoxicity (cell death rate of 12.3% with CRO, 10.2% with WOL, 16.6% with CHR-S and 26.7% with CHR-L, respectively, compared to control cells).

After 6 h (Figure 6, panel A), exposure to CRO induced a significant increase in the mRNA production of IL-8 and TNF-α (1.41- and 1.40-fold increase respect to untreated M0 macrophages, respectively), whereas the treatment with WOL increased the mRNA levels of IL-1β, IL-8 and TNF-α (1.45-, 1.54- and 1.83-fold increase, respectively). Moreover, the exposure to CHR-L caused the overproduction of IL-8 and MCP-1 mRNA (1.64- and 1.35-fold increase, respectively), in addition to a remarkably high increase in the mRNA production of IL-1β and TNF-α (2.15- and 2.44-fold increase, respectively). Conversely, CHR-S induced a slight but still significant decrease in IL-8 expression (0.29-fold decrease). After 24 h (Figure 6, panel B), CRO-treated macrophages displayed an increased level of TNF-α (1.70-fold increase) and diminished levels of IL-6 and MCP-

1 (0.33- and 0.20-fold decrease, respectively). Similarly, WOL-treated cells presented an increased level of TNF-α (1.71-fold increase) and a noticeably diminished level of IL-6 (0.64-fold decrease). The exposure to CHR-S caused high mRNA levels of both IL-6 and TNF-α (1.89- and 1.25-fold increase, respectively). Lastly, the treatment with CHR-L increased the mRNA production of IL-8 (1.25-fold increase), while decreasing the levels of MCP-1 (0.47-fold decrease). After 48 h (Figure 6, panel C), CHR-S induced a significant increase in the mRNA production of IL-8 (1.40-fold increase). CHR-L caused high mRNA levels of IL-1β and TNF-α mRNA (1.34- and 1.31-fold increase, respectively), as well as a remarkably high increase in the mRNA levels of IL-6 and IL-8 (2.66- and 2.28-fold increase, respectively).

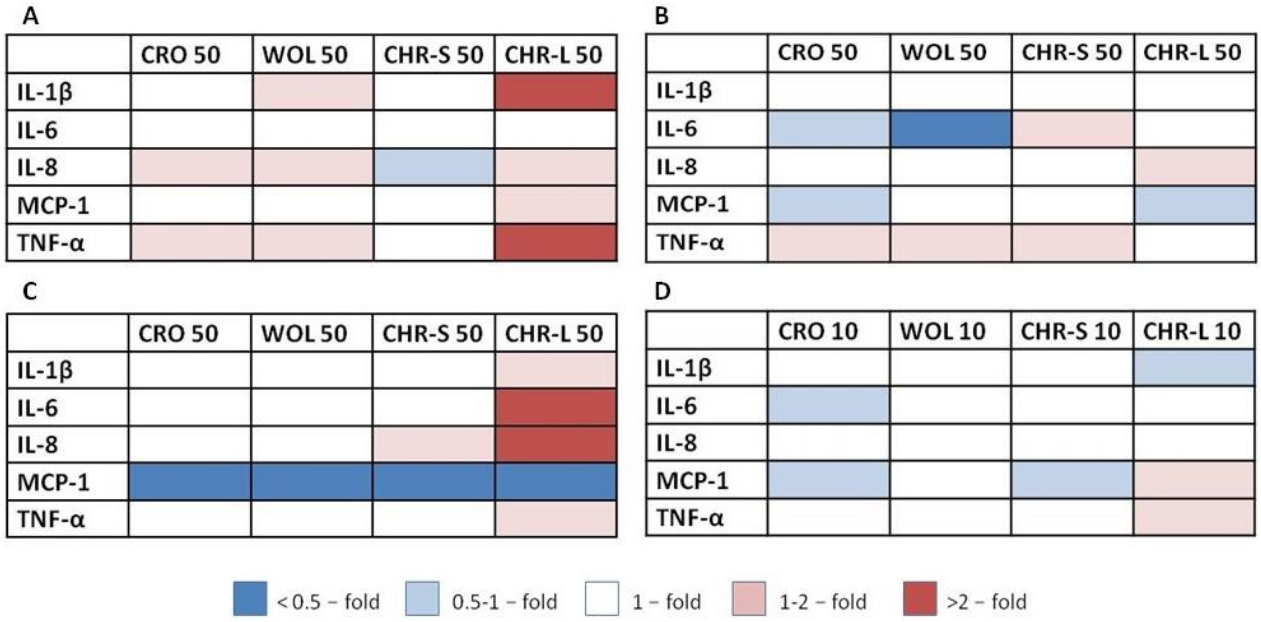

Figure 6. Gene expression of pro-inflammatory mediators in M0 macrophages per exposure time. (**A**) Gene expression of IL-1β, IL-6, IL-8, MCP-1 and TNF-α measured by qPCR analysis after M0 macrophages were incubated for 6 h with 50 µg/mL of mineral fibres (CRO, WOL, CHR-S and CHR-L). Data are normalised to HPRT-1 housekeeping gene and are the mean of three experiments performed in triplicate. (**B**) Gene expression of IL-1β, IL-6, IL-8, MCP-1 and TNF-α in M0 macrophages incubated for 24 h with 50 µg/mL of mineral fibres, measured in the same conditions as (**A**). (**C**) Gene expression of IL-1β, IL-6, IL-8, MCP-1 and TNF-α in M0 macrophages incubated for 48 h with 50 µg/mL of mineral fibres, measured in the same conditions as (**A**). (**D**) Gene expression of IL-1β, IL-6, IL-8, MCP-1 and TNF-α in M0 macrophages incubated for 7 days with 10 µg/mL of mineral fibres, measured in the same conditions as (**A**). Results are expressed as mRNA fold increase compared to untreated (control) M0 macrophages and colours different from white indicate significance in Tukey test (Tukey vs. C: $p < 0.05$). Results are colour-coded as follows: dark blue (< 0.5-fold decrease vs. C), light blue (between 0.5- and 1-fold decrease vs. C), pink (between 1- and 2-fold increase vs. C) and red (> 2-fold increase vs. C).

Moreover, all mineral fibres induced an outstanding reduction in the mRNA production of MCP-1 (0.78-, 0.62-, 0.60- and 0.72-fold decrease for CRO, WOL, CHR-S and CHR-L, respectively). After 7 days (Figure 6, panel D), macrophages exposed to CRO and CHR-S continued to display a decrease in the mRNA production of MCP-1 (0.30- and 0.27-fold decrease, respectively), albeit with lower values compared to 48 h-treated cells (Figure 7, panels A and C, respectively). Besides, CRO-treated macrophages presented a slight reduction of IL-6 mRNA levels (0.27-fold decrease). Finally, the exposure to CHR-L diminished the mRNA production of IL-1β (0.20-fold decrease) and augmented the levels of both MCP-1 and TNF-α (1.45- and 1.48-fold increase, respectively).

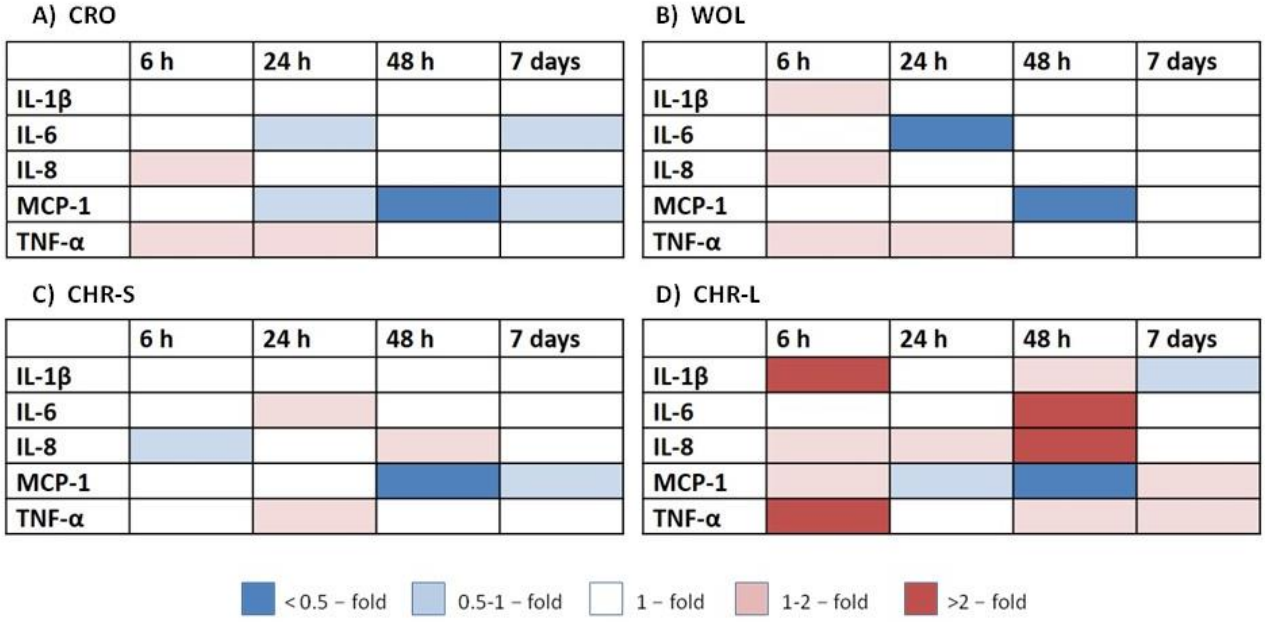

Figure 7. Gene expression of pro-inflammatory mediators in M0 macrophages per fibre treatment. (**A**) Gene expression of IL-1β, IL-6, IL-8, MCP-1 and TNF-α measured by qPCR analysis after M0 macrophages were incubated with CRO for 6 h, 24 h, 48 h and 7 days. Data are normalised to HPRT-1 housekeeping gene and are the mean of three experiments performed in triplicate. (**B**) Gene expression of IL-1β, IL-6, IL-8, MCP-1 and TNF-α in M0 macrophages incubated with WOL, measured in the same conditions as (**A**). (**C**) Gene expression of IL-1β, IL-6, IL-8, MCP-1 and TNF-α in M0 macrophages incubated with CHR-S, measured in the same conditions as (**A**). (**D**) Gene expression of IL-1β, IL-6, IL-8, MCP-1 and TNF-α in M0 macrophages incubated with CHR-L, measured in the same conditions as (**A**). Results are expressed as mRNA fold increase compared to untreated (control) M0 macrophages and colours different from white indicate significance in Tukey test (Tukey vs. C: $p < 0.05$). Results are colour-coded as follows: dark blue (< 0.5-fold decrease vs. C), light blue (between 0.5- and 1-fold decrease vs. C), pink (between 1- and 2-fold increase vs. C) and red (> 2-fold increase vs. C).

Inhalation of asbestos promotes the activation of the pulmonary endothelium with the subsequent production of pro-inflammatory molecules that contribute to the instauration of a persistent inflammatory state. In fact, the pulmonary vasculature can be damaged by the direct contact with asbestos fibres that accumulate along capillaries, embed into endothelial cells and penetrate within the capillary lumen. Besides, endothelial cells can be indirectly stimulated by pro-inflammatory factors secreted by other pulmonary cells in response to asbestos fibres (Garcia et al., 1988; Rom et al., 1991; Mossman and Gee, 1993; Treadwell et al., 1996).

Endothelial cells have a fundamental role in controlling the tissue inflammation since they interact with circulating immune cells in order to regulate their extravasation from the bloodstream into the tissue parenchyma. Therefore, in response to harmful stimuli, endothelial activation promotes the expression of cell surface proteins involved in the active recruitment of leukocytes, such as adhesion molecules (i.e., ICAM-1 and VCAM-1), selectins (i.e., E-selectin and P-selectin) and addressins (i.e., PNAd). Moreover, this process induces the activation of matrix metalloproteases (MMPs), which further regulate adhesion molecules by proteolytic cleavage of their extracellular domains. Furthermore, endothelial activation triggers the translocation of the transcription factors NF-κB and AP-1 to the nucleus, with the subsequent expression of genes encoding for various pro-inflammatory cytokines (i.e., IL-1β, IL-6, IL-8 and MCP-1) and co-stimulatory molecules (i.e., CD80 and CD86) (Shao et al., 2020). In this regard, the transcription factors AP-1 and NF-κB, as well as several MAPKs involved in endothelial activation, are known to be redox-sensitive. Therefore, ROS-mediated signalling contributes to several processes associated with endothelial activation, such as the upregulation of adhesion molecules and chemokines, increased proteolytic activity of MMP-2 and MMP-9, cytoskeletal actin reorganization, formation of intercellular gaps, increased endothelial permeability and leukocyte transmigration (Santiago-Delpin, 2004; Alom-Ruiz et al., 2008).

Moreover, endothelial cells contribute to the resolution of the acute inflammation by secreting cytokines and growth factors (e.g., VEGF and FGF) involved in the recruitment and activation of fibroblasts and macrophages. Arising from TGF-β-dependent differentiation from fibroblasts, myofibroblasts are characterised by the expression of the cytoskeletal proteins α-SMA and palladin; besides, they synthesise several ECM proteins, such as collagen types I and III, fibronectin, periostin and CTGF. After wound healing is complete, myofibroblasts are typically removed via apoptosis or deactivation; however, the persistence of asbestos fibres in the lung parenchyma due to their natural resistance to degradation leads to a continuous cycle of fibroblast activation, ECM deposition and increased tissue stiffness, frequently resulting in the development of asbestos-induced fibrosis (Hsu et al., 2019). Thus, endothelial cells participate in the initiation, and

subsequent progression, of lung fibrosis by increasing the myofibroblast pool, secreting pro-fibrotic mediators, promoting the recruitment of immune cells, participating in vascular rarefaction and decreasing angiogenesis. Furthermore, endothelial cells may directly contribute to the remodelling of the perivascular ECM by transitioning to mesenchymal cells in a process known as endothelial-to-mesenchymal transition (EndoMT). EndoMT is associated with the loss of endothelial markers (i.e., PECAM-1, Tie1, Tie2 and VE-cadherin) and with the corresponding acquisition of mesenchymal markers (i.e., α-SMA, FSP-1, N-cadherin and vimentin), forming mesenchymal cells that promote the synthesis of extracellular matrix proteins and contribute to the production of pro-inflammatory cytokines (i.e., IL-4, IL-6, IL-8, IL-13 and TNF-α) (Platel et al., 2019; Piera-Velazquez and Jimenez, 2019; Sun et al., 2020).

To obtain a more in-depth understanding of the transcriptional changes caused by asbestos fibres, the gene expression profile of HECV endotheliocytes focused on several markers involved in endothelial activation (ICAM-1 and VEGF), fibrosis (TGF-β and fibronectin), EndoMT (α-SMA, COL-1A and MMP-9), as well as several pro-inflammatory cytokines (IL-1β, IL-6, IL-8 and MCP-1). These markers were analysed in HECV cells treated for 24 h, 48 h and 7 days (Figure 8, panels A-C, respectively) with the same concentrations of mineral fibres reported for M0 macrophages. Moreover, these results were also plotted according to the fibre treatment employed for HECV cells in Figure 9. After 24 h (Figure 8, panel A), all mineral fibres induced a significant increase in the mRNA production of IL-1β, IL-6, IL-8 and VEGF, confirming their ability to promote the rapid insurgence of a pro-inflammatory state in HECV endotheliocytes. Moreover, CHR-S caused high transcriptional levels of two mediators involved in EndoMT, namely fibronectin and α-SMA (1.58- and 1.47-fold increase, respectively). Conversely, both fractions of Orenburg chrysotile diminished the mRNA production of TGF-β (0.22- and 0.31-fold decrease, respectively) and ICAM-1 (0.24- and 0.34-fold decrease, respectively). After 48 h (Figure 8, panel B), the mRNA production of the pro-inflammatory cytokines was still increased in the presence of CRO, WOL and CHR-L; conversely, their levels were significantly reduced by the treatment with CHR-S (Figure 9, panel C). Interestingly, the exposure to both fractions of chrysotile diminished the mRNA levels of VEGF compared to 24 h-treated cells, although CHR-L induced a significant overproduction of ICAM-1 mRNA (1.31-fold increase). Moreover, CHR-S and CHR-L caused a significant decrease in MCP-1, TGF-β, fibronectin and COL-1A expression. After 7 days (Figure 8, panel C), all mineral fibres induced a significant increase in the mRNA production of ICAM-1, confirming the activation of endothelial cells. Besides, both fractions of Orenburg chrysotile diminished the mRNA production of VEGF, TGF-β and fibronectin in a gene expression profile similar to CRO. Interestingly, while CHR-L reduced the mRNA levels of α-SMA (0.31-fold decrease), this EndoMT marker was

significantly increased with CRO, WOL and CHR-S (1.48-, 1.71- and 1.26-fold increase, respectively). Since the inhalation of large volumes of air causes a constant exposure of the pulmonary tissue to pathogens and pollutants, the lung displays a series of elaborate mechanisms that dampen the excessive immune activation following lung damage. In particular, the immunomodulatory role of endothelial cells is thought to have a major part in the regulation of the lung homeostasis.

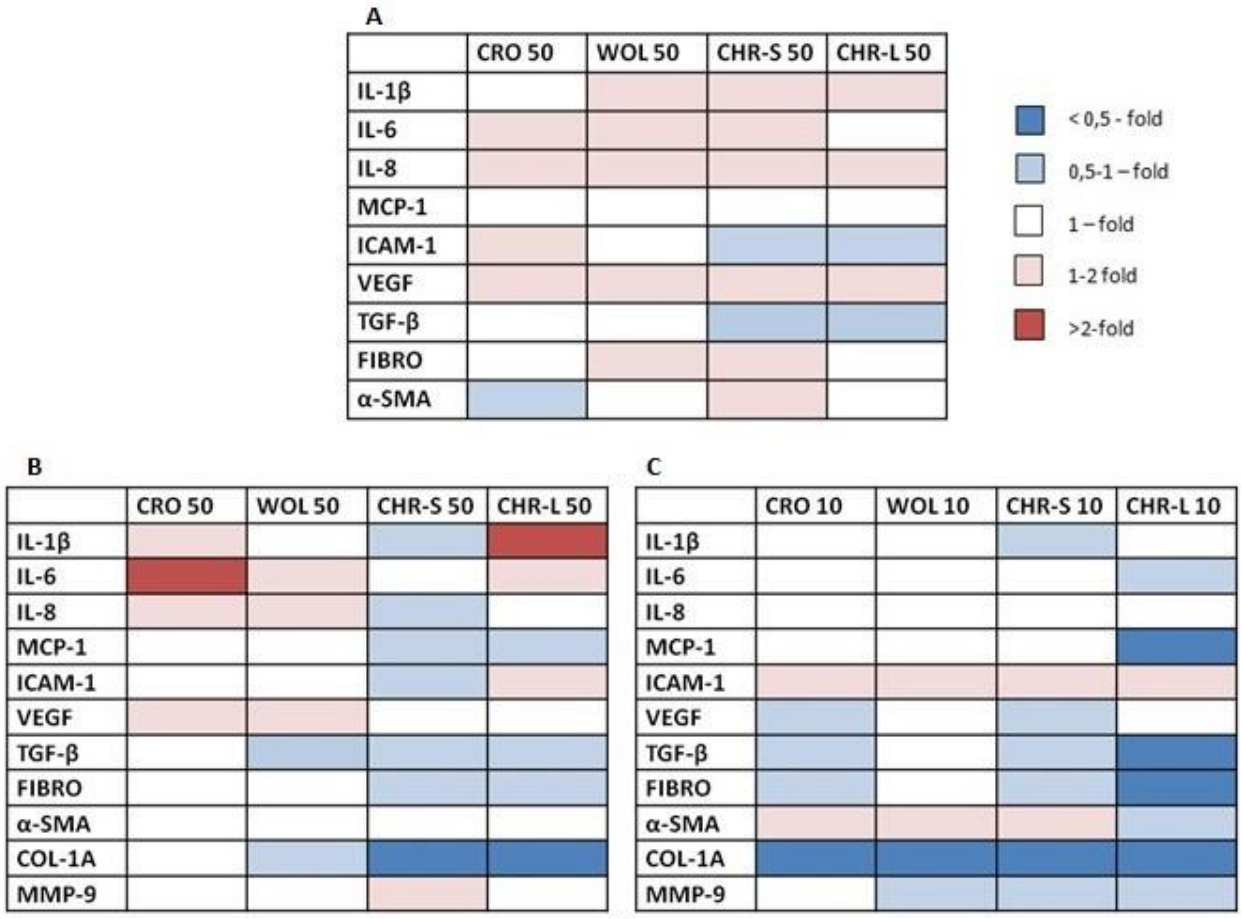

Figure 8. Gene expression of pro-inflammatory cytokines and endothelial mediators in HECV cells per exposure time. (**A**) Gene expression of markers involved in endothelial activation (ICAM-1 and VEGF), fibrosis (TGF-β and fibronectin), EndoMT (α-SMA, COL-1A and MMP-9), as well as several pro-inflammatory cytokines (IL-1β, IL-6, IL-8 and MCP-1), measured by qPCR analysis after HECV endotheliocytes were incubated for 24 h with 50 µg/mL of mineral fibres (CRO, WOL, CHR-S and CHR-L). Data are normalised to GAPDH housekeeping gene and are the mean of three experiments performed in triplicate. (**B**) Gene expression profile of the same markers measured in (**A**) in HECV endotheliocytes incubated for 48 h with 50 µg/mL of mineral fibres. (**C**) Gene expression profile of the same markers measured in (**A**) in HECV endotheliocytes incubated for 7 days with 10 µg/mL of mineral fibres. Results are expressed as mRNA fold increase compared to untreated (control) HECV cells and colours different from white indicate significance in Tukey test (Tukey vs. C: $p < 0.05$). Results are colour-coded as follows: dark blue (< 0.5-fold decrease vs. C), light blue (between 0.5- and 1-fold decrease vs. C), pink (between 1- and 2-fold increase vs. C) and red (> 2-fold increase vs. C).

In fact, the pulmonary tissue is highly vascularised with a specialised subset of microvascular endothelial cells that facilitate the gas exchange between the circulation on the apical side and the air stored in the alveoli on the basal side. In this regard, the immunosuppressive effects of VEGF-signalling in the alveolar microenvironment are thought to contribute to endothelial-mediated tolerance to airborne pathogens and particles in the lung (Amersfoort et al., 2022).

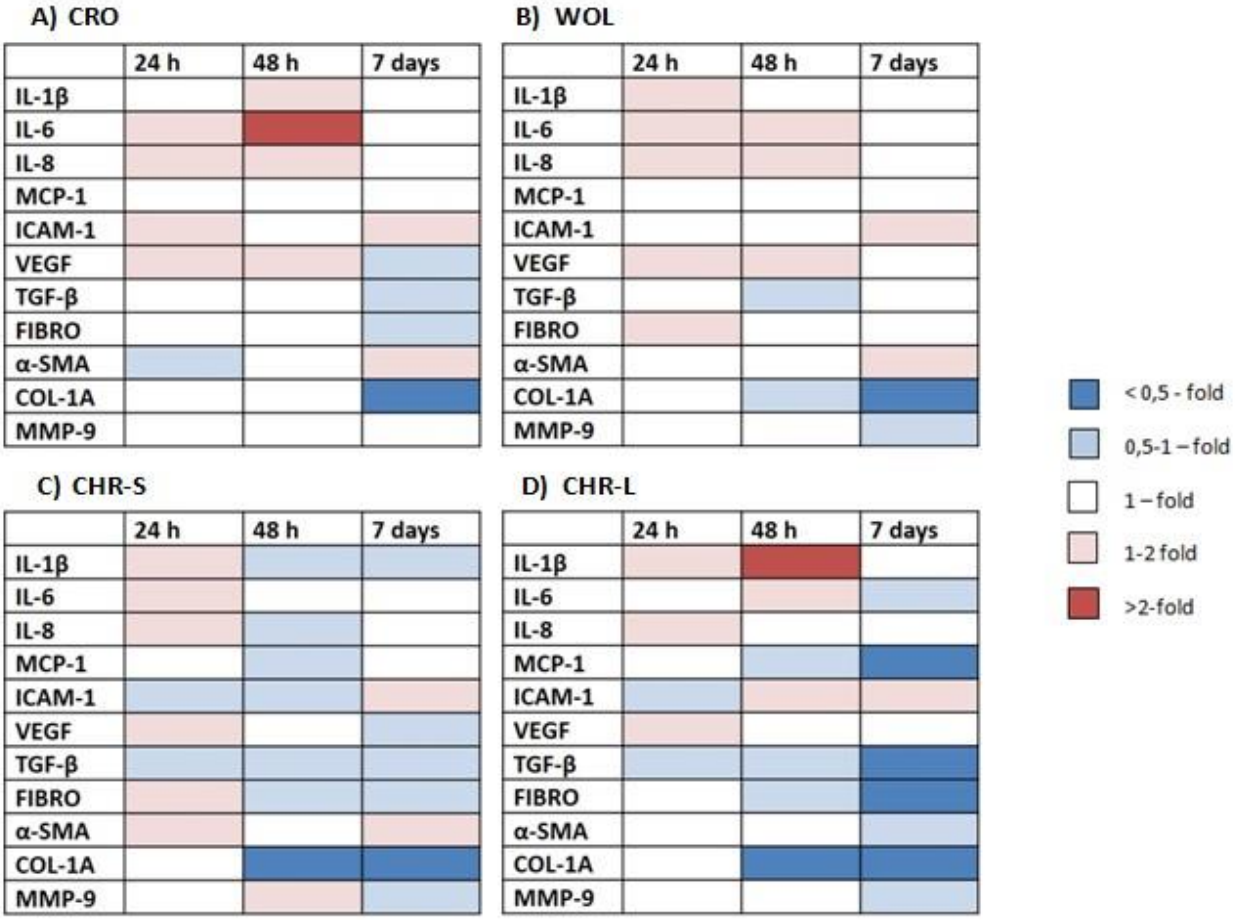

Figure 9. Gene expression of pro-inflammatory cytokines and endothelial mediators in HECV cells per fibre treatment. (**A**) Gene expression of markers involved in endothelial activation (ICAM-1 and VEGF), fibrosis (TGF-β and fibronectin), EndoMT (α-SMA, COL-1A and MMP-9), as well as several pro-inflammatory cytokines (IL-1β, IL-6, IL-8 and MCP-1), measured by qPCR analysis after HECV endotheliocytes were incubated with CRO for 24 h, 48 h and 7 days. Data are normalised to GAPDH housekeeping gene and are the mean of three experiments performed in triplicate. (**B**) Gene expression profile of the same markers measured in (**A**) in HECV endotheliocytes incubated with WOL. (**C**) Gene expression profile of the same markers measured in (**A**) in HECV endotheliocytes incubated with CHR-S. (**D**) Gene expression profile of the same markers measured in (**A**) in HECV endotheliocytes incubated with CHR-L. Results are expressed as mRNA fold increase compared to untreated (control) HECV cells and colours different from white indicate significance in Tukey test (Tukey vs. C: $p < 0.05$). Results are colour-coded as follows: dark blue (< 0.5-fold decrease vs. C), light blue (between 0.5- and 1-fold decrease vs. C), pink (between 1- and 2-fold increase vs. C) and red (> 2-fold increase vs. C).

7.4. CO-CULTURE VIABILITY AND GENE EXPRESSION PROFILE

During the inflammatory response to inhaled harmful stimuli, alveolar macrophages typically release several pro-inflammatory mediators in the surrounding microenvironment, affecting alveolar and endothelial cells. Therefore, to obtain a more in-depth understanding of how the secreted mediators produced by asbestos-treated macrophages affect the cell viability and the gene expression profile of endothelial cells, a co-culture setup with M0 macrophages and HECV endotheliocytes was investigated. Indeed, fibre-treated M0 macrophages were cultured in Transwell® PET inserts with a 0.4 μm-pore size that only enabled the flow through of soluble mediators, so that HECV cells were not directly exposed to the mineral fibres.

In this co-culture setup, the cell viability of M0 macrophages and HECV endotheliocytes was assessed with the MTT test at different time points, namely 24 h, 48 h and 7 days. In M0 macrophages directly exposed to mineral fibres (Figure 10, panels A-C), the viability index showed that both fractions of chrysotile induced a cytotoxic effect which was comparable to CRO at all considered time points. Indeed, at 24 h (Figure 10, panel A), CRO caused a mortality rate of 14.7% compared to control cells (C), whereas CHR-S and CHR-L induced a cell death percentage of 20.3% and 27.3% compared to C, respectively. Similarly, at 48 h (Figure 10, panel B), both CHR-S and CHR-L displayed a significant mortality rate (38.2% and 37.0% compared to C, respectively) which was comparable to the cell death rate of CRO-treated macrophages (39.5% compared to C). Moreover, a certain degree of cytotoxicity was also measured in WOL-treated macrophages (28.2% compared to C), confirming the results of the MTT assay performed in absence of co-cultured HECV cells (Figure 1, panel B). After 7 days of exposure to 10 μg/mL of mineral fibres (Figure 10, panel C), the mortality rate obtained with CHR-S and CHR-L (24.5% and 34.2% compared to C, respectively) was similar to the cytotoxic effect induced by CRO (22.4% compared to C), confirming the trend already observed at 24 h and 48 h. At all considered time points, HECV endotheliocytes co-cultured with M0 macrophages (Figure 10, panels D-F) displayed a significant decrease in the cell viability compared to HECV cells not grown in a co-culture setup (striped bar), probably due to an impairment in the growth of the endothelial monolayer due to the presence of cytokines physiologically released by M0 macrophages. Regarding HECV cells co-cultured with fibre-treated macrophages, at 24 h (Figure 10, panels D) all mineral fibres (CRO dotted bar, WOL white bar, CHR-S gray bar and CHR-L black bar, respectively) induced a slight but significant reduction in the cell number (values from 10.9% to 14.2% respect to C) in comparison with HECV cells cultured with untreated M0 macrophages (chequered bar). Conversely, at 48 h and 7 days, no significant differences in the cell number were measured between endotheliocytes co-cultured with fibre-treated and non-treated macrophages.

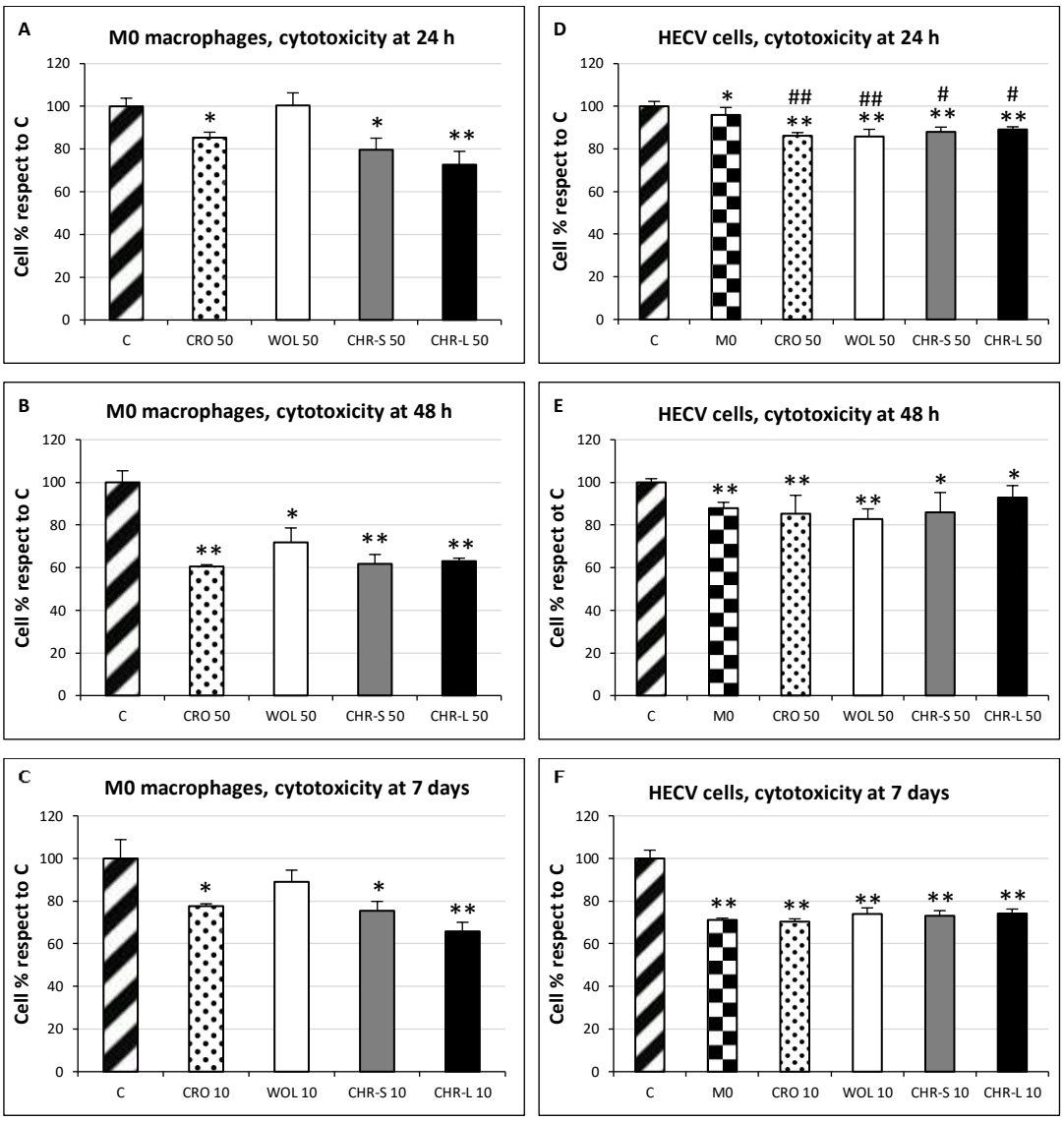

Figure 10. Cell toxicity evaluation of M0 macrophages and HECV endotheliocytes in a co-culture set up. (**A**) Cytotoxicity quantification of co-cultured M0 macrophages with the MTT test at 24 h in the presence of 50 µg/mL of the mineral fibres CRO (dotted bar), WOL (white bar), CHR-S (gray bar) and CHR-L (black bar). Results are expressed as cell percentages relative to control cells (striped bar) and are the mean ± SD of three independent experiments performed in quadruplicate. Asterisks indicate the significance in a paired Tukey test (ANOVA, $p < 0.00001$; Tukey vs. C: * $p < 0.01$, ** $p < 0.005$, respectively). (**B**) Cytotoxicity quantification of co-cultured M0 macrophages at 48 h in the same conditions as (**A**). ANOVA, $p < 0.00005$; Tukey vs. C: * $p < 0.01$, ** $p < 0.001$, respectively. (**C**) Cytotoxicity quantification of co-cultured M0 macrophages treated with 10 µg/mL of mineral fibres for 7 days. ANOVA, $p < 0.0005$; Tukey vs. C: * $p < 0.05$, ** $p < 0.005$, respectively. (**D**) Cytotoxicity evaluation of HECV endotheliocytes after 24 h in co-culture with M0 macrophages treated with 50 µg/mL of the mineral fibres CRO (dotted bar), WOL (white bar), CHR-S (gray bar) and CHR-L (black bar). Results are expressed as cell percentages relative to control cells (striped bar) and are the mean ± SD of three independent experiments performed in quadruplicate. Asterisks indicate the significance in Tukey test (ANOVA, $p < 0.00001$; Tukey vs. C: * $p < 0.05$, ** $p < 0.0001$; Tukey vs. M0: # $p < 0.005$, ## $p < 0.001$, respectively). (**E**) Cytotoxicity quantification of co-cultured HECV endotheliocytes at 48 h in the same conditions as (**A**). ANOVA, $p < 0.0005$; Tukey vs. C: * $p < 0.05$, ** $p < 0.005$, respectively. (**F**) Cytotoxicity quantification of HECV endotheliocytes in co-culture with M0 macrophages treated with 10 µg/mL of the mineral fibres for 7 days. ANOVA, $p < 0.000001$; Tukey vs. C: ** $p < 0.0001$.

Apart from being damaged by the direct contact with asbestos fibres, the endothelial cells of the pulmonary vasculature can be indirectly stimulated by the pro-inflammatory and pro-fibrotic mediators secreted by activated immune cells in response to asbestos fibres. In particular, TNF-α and IL-1β are the most important factors in inducing endothelial cell activation, stimulating the production of cytokines and adhesion molecules (e.g., E-selectin, P-selectin, ICAM-1, ELAM-1 and VCAM-1). Moreover, endothelial cells express receptors for other important immune molecules, such as C5a which, upon being upregulated by IL-6, is responsible for the increased production of MIP-2 and MCP-1 that are key chemokines responsible for the regulation of migration and infiltration of macrophages and neutrophils during the immune response. Furthermore, the importance of inflammatory cytokines in the induction of EndoMT has been described in multiple studies. For example, a short-term exposure to IL-1β or TNF-α promoted transient EndoMT in HDMEC, while a longer exposure prompted their permanent transformation to myofibroblasts. Similarly, IL-1β was shown to enhance the effect of TGF-β-mediated EndoMT in HUVEC cells, whereas TNF-α or IL-6 induced EndoMT in cardiac valve endothelial cells through the activation of the Akt and NF-κB pathways (Chaudhuri et al., 2007; Hsu et al., 2019).

To evaluate the transcriptional changes caused in endothelial cells by the pro-inflammatory cytokines released by fibre-treated M0 macrophages, the gene expression profile of the endothelial markers shown in Figures 8 and 9 was also analysed in HECV cells co-cultured for 24 h, 48 h and 7 days with M0 macrophages challenged with mineral fibres (Figure 11, panels A-C, respectively). Additionally, these results were plotted according to the fibre treatment employed for M0 macrophages (Figure 12). After 24 h (Figure 11, panel A), all fibre-treated M0 cells released soluble factors that induced a significant increase in the endothelial mRNA production of IL-1β, IL-6 and IL-8, confirming their ability to promote the rapid insurgence of a pro-inflammatory state in HECV endotheliocytes. Conversely, the endothelial mRNA levels of MCP-1 were increased only by M0 macrophages challenged with WOL and CHR-L, while they were diminished by the exposure to CRO and CHR-S. Interestingly, all fibre-treated M0 cells diminished the mRNA production of either ICAM-1 or VEGF in HECV cells. Regarding the mRNA levels of pro-fibrotic mediators, TGF-β was increased only with CHR-S-treated M0 macrophages (1.68-fold increase), whereas fibronectin was increased only with WOL-treated M0 cells (1.19- fold increase). After 48 h (Figure 11, panel B), the mRNA production of IL-1β was still significantly increased in the presence of M0 macrophages challenged with CRO, WOL and CHR-L (1.19-, 1.64- and 2.02-fold increase, respectively). Conversely, the mRNA levels of the pro-inflammatory cytokines IL-6 and IL-8 were decreased respect to 24 h, in particular after treatment with CHR-S (Figure 12, panel C). Interestingly, while the mRNA production of MCP-1, ICAM-1, VEGF and TGF-β was increased by

M0 macrophages treated with WOL, their levels were significantly reduced by the exposure to CRO and CHR-S. Besides, the mRNA production of TGF-β was also diminished in the presence of M0 cells treated with CHR-L (Figure 12, panel D). The mRNA levels of fibronectin, α-SMA and COL-1A were decreased to a certain degree by all treatments. After 7 days (Figure 11, panel C), the mRNA levels of VEGF and COL-1A were significantly diminished by soluble factors released by all fibre-treated M0 cells.

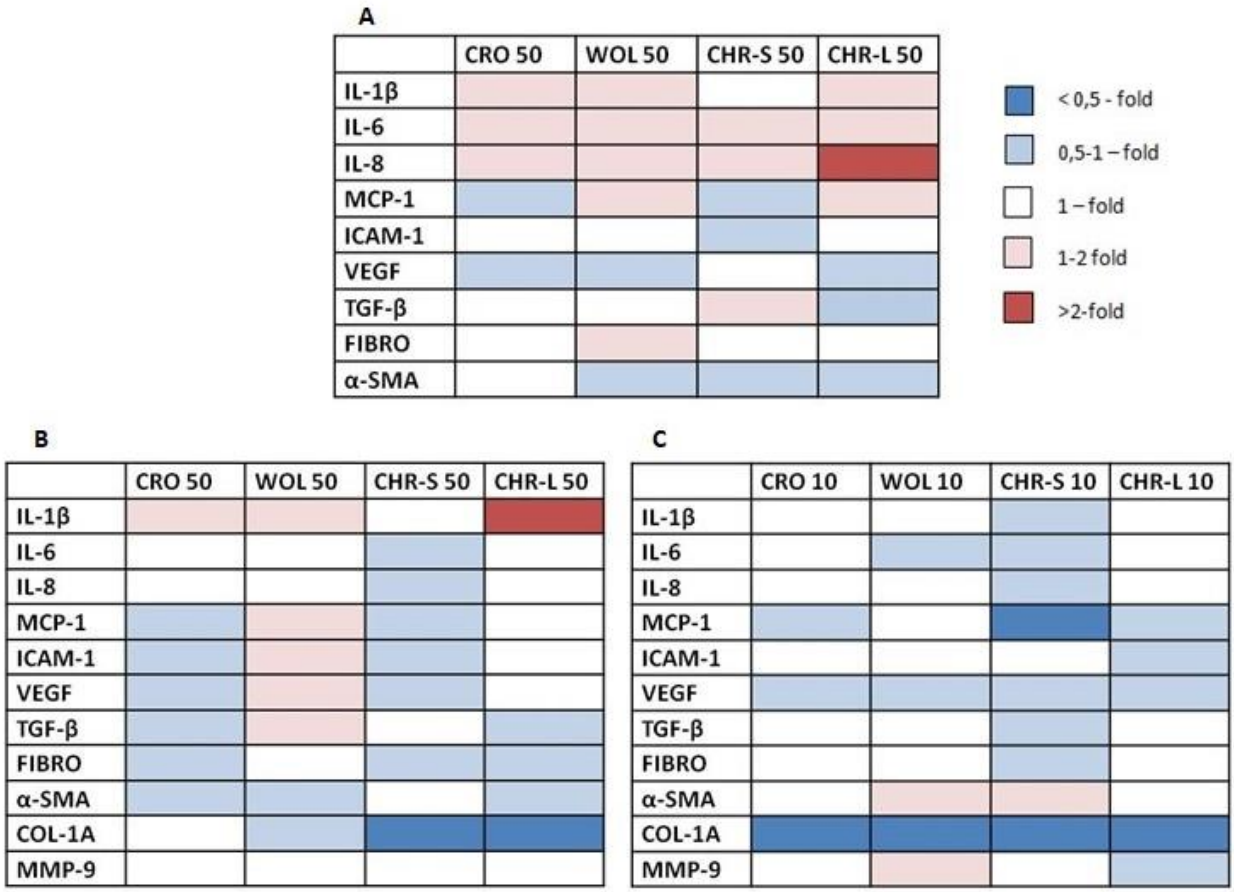

Figure 11. Gene expression profile in HECV cells co-cultured with fibre-treated M0 macrophages per exposure time. (**A**) Gene expression of markers involved in endothelial activation (ICAM-1 and VEGF), fibrosis (TGF-β and fibronectin), EndoMT (α-SMA, COL-1A and MMP-9), as well as several pro-inflammatory cytokines (IL-1β, IL-6, IL-8 and MCP-1), measured by qPCR analysis in HECV endotheliocytes incubated for 24 h with M0 macrophages treated with 50 µg/mL of mineral fibres (CRO, WOL, CHR-S and CHR-L). Data are normalised to GAPDH housekeeping gene and are the mean of three experiments performed in triplicate. (**B**) Gene expression profile of the same markers measured in (**A**) in HECV endotheliocytes incubated for 48 h with M0 macrophages treated with 50 µg/mL of mineral fibres. (**C**) Gene expression profile of the same markers measured in (**A**) in HECV endotheliocytes incubated for 7 days with M0 macrophages treated with 10 µg/mL of mineral fibres. Results are expressed as mRNA fold increase compared to untreated (control) HECV cells and colours different from white indicate significance in Tukey test (Tukey vs. C: $p < 0.05$). Results are colour-coded as follows: dark blue (< 0.5-fold decrease vs. C), light blue (between 0.5- and 1-fold decrease vs. C), pink (between 1- and 2-fold increase vs. C) and red (> 2-fold increase vs. C).

Moreover, the mRNA production of all pro-inflammatory cytokines, as well as of TGF-β and fibronectin, was still diminished in the presence of M0 cells challenged with CHR-S. Besides, CRO-treated M0 cells reduced the expression of MCP-1 (0.22-fold decrease) in HECV cells, while CHR-L-treated M0 macrophages decreased the endothelial mRNA production of both MCP-1 and ICAM-1 (0.50- and 0.16-fold decrease, respectively). Interestingly, both WOL and CHR-S increased the mRNA levels of α-SMA (1.23- and 1.34-fold, respectively) in HECV cells.

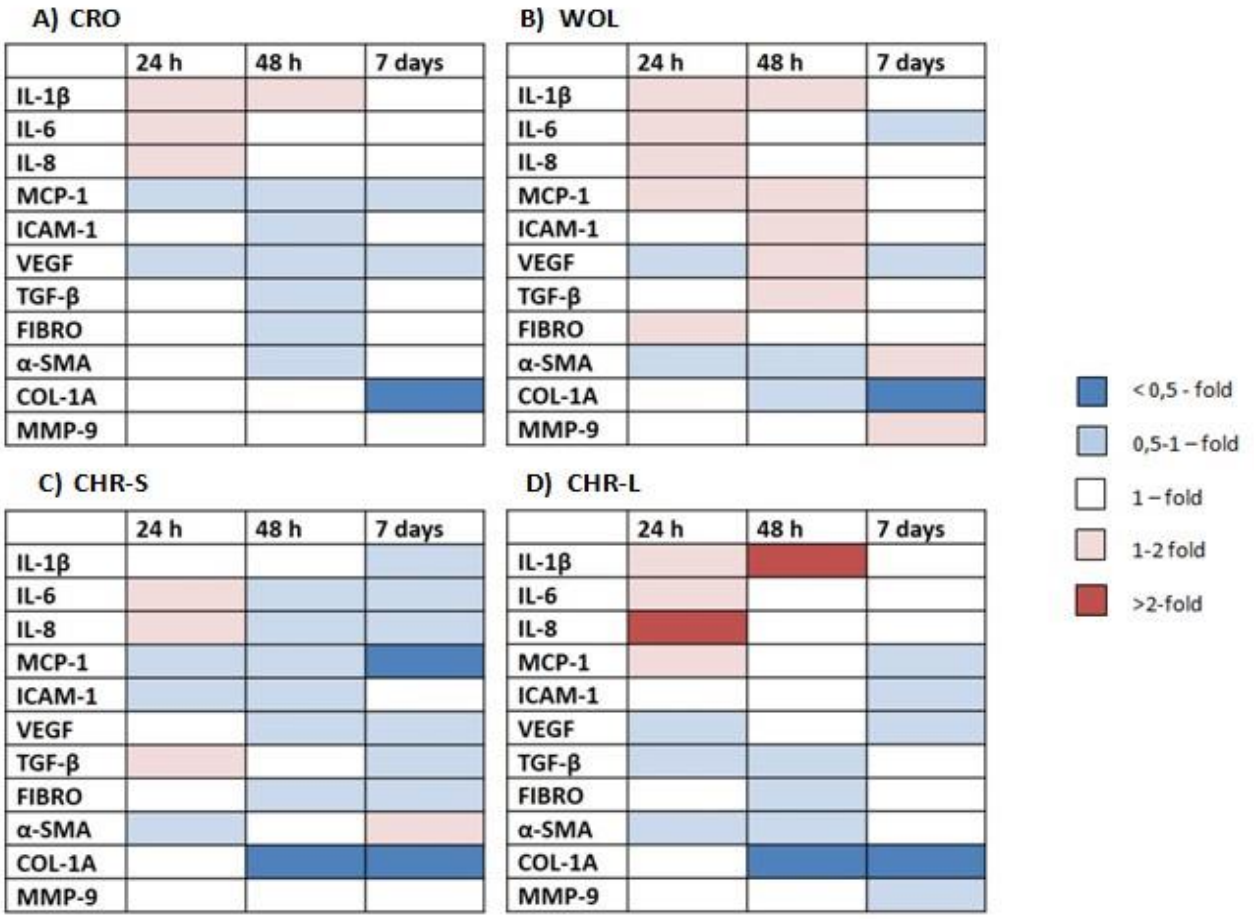

Figure 12. Gene expression profile of HECV cells co-cultured with fibre-treated M0 macrophages per fibre treatment. (**A**) Gene expression of markers involved in endothelial activation (ICAM-1 and VEGF), fibrosis (TGF-β and fibronectin), EndoMT (α-SMA, COL-1A and MMP-9), as well as several pro-inflammatory cytokines (IL-1β, IL-6, IL-8 and MCP-1), measured by qPCR analysis after HECV endotheliocytes were incubated with CRO for 24 h, 48 h and 7 days. Data are normalised to GAPDH housekeeping gene and are the mean of three experiments performed in triplicate. (**B**) Gene expression profile of the same markers measured in (**A**) in HECV endotheliocytes incubated with WOL. (**C**) Gene expression profile of the same markers measured in (**A**) in HECV endotheliocytes incubated with CHR-S. (**D**) Gene expression profile of the same markers measured in (**A**) in HECV endotheliocytes incubated with CHR-L. Results are expressed as mRNA fold increase compared to untreated (control) HECV cells and colours different from white indicate significance in Tukey test (Tukey vs. C: $p < 0.05$). Results are colour-coded as follows: dark blue (< 0.5-fold decrease vs. C), light blue (between 0.5- and 1-fold decrease vs. C), pink (between 1- and 2-fold increase vs. C) and red (> 2-fold increase vs. C).

8. CONCLUSIONS

Amphibole asbestos, serpentine asbestos and fibrous erionite have been widely recognised as carcinogenic to humans (Group 1) by the International Agency for Research on Cancer (IARC, 2012). However, despite being the focus of extensive research over the past few decades, the complex mechanisms through which these mineral fibres induce adverse effects *in vivo* are yet to be completely understood (Mossman and Gualtieri, 2020). In fact, the interpretation of their toxicity and carcinogenicity is complicated by the synergistic action of a multitude of crystal-chemical-physical factors, such as fibre length and width, crystal curvature and habit, fibre density, chemical composition, total iron and Fe^{2+} content, heavy metals presence, ability to produce ROS, surface activity, zeta potential, dissolution rate, velocity of iron and metals release, biopersistence and biodurability (Gualtieri, 2021). Therefore, understanding the complex mechanisms through which mineral fibres induce adverse effects *in vivo* constitutes a fundamental step towards the quantitative classification of the toxicity/pathogenicity of mineral fibres for preventive medicine and the development of effective treatments for both at-risk workers and the general population. On this matter, a multidisciplinary approach is of paramount importance to disclose the complex biogeochemical mechanisms through which the different mineral fibres induce toxicity and pathogenicity *in vivo*. In fact, the creation of a comprehensive model explaining at a molecular level the intricate mechanisms underlying fibre toxicity requires an innovative approach based on the combined experimental evidence of several research fields (i.e., biochemistry, mineralogy, physics, pathology, and toxicology). In this regard, the long-term project "*FIBRES: A multidisciplinary mineralogical, crystal-chemical and biological project to amend the paradigm of toxicity and cancerogenicity of mineral fibres*" has been in progress since 2017, with the aim of establishing a quantitative model which could evaluate the toxic and pathogenic potential of mineral fibres by correlating their crystal-chemical-physical characteristics to the adverse effects responsible for the ensuing pathological processes *in vivo*.

In this vein, the comparative study presented in the first part of this work provides an interesting insight into the early responses of human M0, M1, and M2 macrophages towards three well-known carcinogenic mineral fibres, namely crocidolite, chrysotile, and erionite. The acute damaging effects exerted by these fibres are highlighted in Table 1 and demonstrate that, although all three mineral fibres are able to cause lung diseases, they display different toxicity mechanisms in human macrophages. Indeed, crocidolite, chrysotile and erionite display distinctive biodurability rates, release characteristic toxic metal cargos, promote varying degrees of intracellular ROS and produce different levels of inflammatory mediators through the upregulation of their gene expression. All morphometric parameters being equal, crocidolite seems to exert its pathological effects mostly as a

result of its high biodurability and iron content, with significant levels of oxidative stress and DNA damage, as well as the transcriptional upregulation of mediators involved in the maintenance of a chronic state of inflammation. Conversely, chrysotile from Balangero shows detrimental effects mainly correlated to its low biodurability, which promotes the rapid release of several toxic metals hosted in its crystal structure (i.e., Mg, Fe, Ni, Cr, Co) both in the intracellular and extracellular environment, causing oxidative stress, promoting DNA damage and inducing the gene expression of pro-inflammatory mediators. Finally, biodurable erionite releases a minimal amount of toxic metals and produces low levels of oxidative stress in comparison to crocidolite and chrysotile, suggesting that other mechanisms are responsible for the adverse effects caused by the exposure to this fibre. Indeed, this zeolite seems to display a characteristic cation-exchange capacity which may alter the intracellular concentration of important cations (Di Giuseppe et al., 2021a), ultimately interfering with the biochemical processes involved in intracellular signalling. Nevertheless, treatment with erionite caused significant DNA damage and prompted the release of inflammatory cytokines, although this process was not simultaneously accompanied by the upregulation of gene transcription in the first hours of stimulation.

Interestingly, the behaviours of the three macrophage phenotypes towards the mineral fibres present several similarities, particularly in the production and release of pro-inflammatory mediators. In fact, it was observed that the M2 macrophage phenotype, which is characteristically known for being recruited at the site of injury to counteract the detrimental effects of the inflammatory state in the tissue, when in contact with the investigated mineral fibres, apparently continues to support local inflammation by supplying a pro-inflammatory secretome. Indeed, the results obtained in the presence of these mineral fibres confirm that macrophages may exhibit varying levels of M1/M2 markers and activities depending on the stimuli encountered during their recruitment (Laskin et al., 2019), resulting in certain phenotypes contributing to the enhancement of the inflammatory process

	Crocidolite	**Chrysotile**	**Erionite**
Biodurability	*** (66 yrs)	* (0.3 yrs)	*** (181 yrs)
Cell death	Mainly apoptosis	Apoptosis and cell lysis	Apoptosis and cell lysis
ROS production	***	**	**
Redox-active metal release	Fe	Mg, Fe, Ni, Cr, Co	Al
DNA damage	***	***	***
Cytokine release	***	***	***
Inflammatory gene upregulation	***	**	
Cation exchange capacity (CEC)			***

Table 1. Summary of the chemical-biological effects of UICC crocidolite, chrysotile from Balangero and fibrous erionite from Jersey.

despite being initially recruited to obtain its mitigation. This may reasonably occur in the lungs of mineral-exposed subjects, where the mineral fibres undergo cycles of *in situ* ingestion and re-ingestion by phagocytic cells for months, or even years, as a result of their biopersistence and biodurability, thus contributing to the instauration of a persistent pro-inflammatory environment.

Overall, the comparative data obtained studying the effects of crocidolite, chrysotile and erionite on the early stages of toxicity and macrophage activation provide an interesting insight on the different complex mechanisms that lead to the onset of pulmonary pathologies due to mineral fibre inhalation. In this regard, this *in vitro* model of human M0, M1, and M2 macrophages has proven to be extremely useful for performing accurate toxicity and inflammation studies on the effects of mineral fibres, contributing to a more accurate prediction of their pathogenic potential and making the proposed methodology a powerful tool to be further applied to other mineral fibres.

In order to develop a quantitative model to assess the toxicity and pathogenicity of mineral fibres, it is essential to shed light on the controversial issue regarding the potential toxicity of short asbestos fibres (< 5 μm). In fact, their potential toxicity is still widely debated in the scientific community due to the contradictory results of *in vitro*, *in vivo*, and epidemiologic studies concerning their harmful effects. Therefore, the second part of this study provides a comparative *in vitro* analysis of the citotoxic, genotoxic and inflammatory potential of two size-separated fractions of chrysotile asbestos fibres obtained by cryogenic milling from the same mineral source (i.e., a commercial chrysotile extracted from an open pit mine near Yasny). From the analyses performed on human M0 macrophages and HECV endotheliocytes, it was observed that both fractions of Orenburg chrysotile induce a significant acute cytotoxic and genotoxic effect, with results that are comparable to the well-known damaging effects of crocidolite. As evidenced by the results summarised in Table 2, the long fraction (> 5 μm) of chrysotile shows a notably higher cytotoxic potential, causing ROS production, DNA damage and the transcriptional upregulation of inflammatory mediators in THP-1-derived M0 macrophages. On the other hand, the short fraction (< 5 μm) of chrysotile displays a significant degree of cytotoxicity and genotoxicity *in vitro*, which is quite intriguing considering the ongoing debate regarding the potential toxicity of short asbestos fibres.

As expected, the two size-separated fractions of chrysotile display different toxicity mechanisms in human macrophages, confirming that their length and width have a fundamental role in determining differences in their behaviour. In fact, the short fraction of chrysotile seems to exert its cytotoxic activity mainly by apoptosis, in a manner similar to crocidolite; conversely, the long fraction of chrysotile is characterised by a multifactorial cytotoxic activity to which both apoptosis and plasma membrane damage contribute. These results may be reasonably explained by the fact that, although

THP-1-derived M0 macrophages are involved in the phagocytosis of both short and long fibres, the internalised fibres are typically shorter than 20 μm (Searl et al., 1999; Di Giuseppe et al., 2021a). Therefore, the short fraction of chrysotile is easily engulfed by M0 macrophages, prompting the release of toxic metals and the production of ROS in the intracellular environment, which ultimately promote the induction of an apoptotic mechanism (Redza-Dutordoir and Averill-Bates, 2016). On the other hand, due to their heterogeneous dimensions, the chrysotile fibres of the long fraction are only engulfed when they are shorter than 20 μm, whereas the fibres above this length are only partially internalised by M0 macrophages, causing frustrated phagocytosis and/or plasma membrane damage (Donaldson et al., 2010). It should also be noted that the assayed mineral fibres display different toxicity mechanisms in HECV endotheliocytes and in M0 macrophages. In fact, in HECV cells the mineral fibres cause cytotoxicity mainly as a result of direct cell membrane damage, while in M0 macrophages the apoptotic mechanism has a fundamental role in the induction of cell death. This is probably due to the different functions of these cells in the pulmonary tissue, since endothelial cells have the main function of lining the blood vessels, whereas macrophages are important effectors of the innate immune system that are characteristically recruited at the site of injury to remove harmful particles via phagocytosis.

As expected, the direct contact of HECV endotheliocytes with asbestos fibres stimulates the gene expression of several pro-inflammatory mediators (i.e., IL-1β, IL-6, IL-8 and VEGF), leading to the rapid insurgence of an inflammatory state that ultimately results in the overexpression of ICAM-1, which is known for promoting the leukocyte extravasation in the damaged tissue (Alom-Ruiz et al., 2008), and thus the maintenance of a chronic state of inflammation. Interestingly, as a consequence of the soluble mediators released by M0 macrophages after the exposure to mineral fibres, the co-cultured endotheliocytes develop a similar pro-inflammatory state that is instead progressively dampened over time. Therefore, our results are in agreement with the previous studies reporting that the immunomodulatory action of endothelial cells has a fundamental role in the regulation of the immune response triggered by inhaled harmful particles (Amersfoort et al., 2022).

	Crocidolite	**Chrysotile < 5 μm**	**Chrysotile > 5 μm**	**Wollastonite**
Biodurability	*** (66 yrs)	* (0.4 yrs)	* (0.4 yrs)	* (30 days)
Cell death in THP-1-M0	Mainly apoptosis	Mainly apoptosis	Apoptosis and cell lysis	Mainly apoptosis
ROS production	**	**	**	***
Redox-active metal release	Fe	Mg, Fe, Ni, Cr, Co	Mg, Fe, Ni, Cr, Co	Ca
DNA damage	***	***	***	
Inflammatory gene upregulation in THP-1-M0	**	*	***	

Table 2. Summary of the chemical-biological effects of UICC crocidolite, chrysotile from Orenburg and wollastonite NYAD G.

Finally, since the presence of a negative control is crucial when examining the adverse effects induced by the exposure to mineral fibres, this work also investigated wollastonite NYAD G as a potential negative control for *in vitro* toxicity tests. As expected, wollastonite shows minimal acute toxicity and no significant genotoxic effect, while the transcriptional upregulation of the inflammatory mediators produced by human macrophages is returned to its basal levels within a short amount of time (i.e., 7 days). These results suggest that, despite inducing a surprising amount of intracellular ROS, wollastonite could be suitably employed as a negative control for future *in vitro* experiments. In fact, in addition to its extremely low biodurability and scarce metal content (Di Giuseppe et al., 2021b), this mineral fibre appears to cause no detectable permanent damage in terms of both genotoxicity and chronic inflammation, although further studies are necessary to confirm these preliminary results.

Overall, the systematic approach used in this study elucidates the intricate mechanisms underpinning the acute toxicity, genotoxic damage, and inflammatory activation of the different macrophage phenotypes in contact with mineral fibres, while also investigating the damaging effects induced by their pro-inflammatory mediators on endothelial cells. In particular, our comparative data focus on the early stages of toxicity and macrophage activation caused by the exposure to different mineral fibres, clearly highlighting their different biogeochemical behaviour. Indeed, these results shed new light on the complex mechanisms that lead to the onset of pulmonary pathologies due to mineral fibre inhalation, making the proposed methodology a powerful tool to investigate the molecular mechanisms underlying the damaging effects caused by other harmful stimuli.

In particular, these data may contribute to the development of new prognostic tools for the ultimate classification of mineral fibre toxicity. Indeed, a general quantitative model explaining the toxicity and pathogenicity of mineral fibres is needed, both to resolve controversies on known mineral fibres with unclear classification and to help classify fibres with unknown toxicity. Within this framework, our data provide a clearer picture of the crystal-chemical-physical fibre parameters contributing to the adverse effects on the physiology of humans and could be employed for the development of a reliable fibre toxicity quantitative model. Additionally, further studies are necessary for modelling more advanced and/or prolonged states of inflammation upon fibre inhalation, possibly on 3D-reconstituted human lung tissues and organoids. These new human-relevant *in vitro* models will help to finally clarify the complex steps that lead to the long-lasting process of chronic pulmonary diseases and to produce new experimental tools for the classification of mineral fibres.

9. REFERENCES

Abdelaziz, M. H., Abdelwahab, S. F., Wan, J., Cai, W., Huixuan, W., Jianjun, C., Kumar, K. D., Vasudevan, A., Sadek, A., Su, Z., Wang, S., & Xu, H. (2020). Alternatively activated macrophages; a double-edged sword in allergic asthma. *Journal of translational medicine*, *18*(1), 58. https://doi.org/10.1186/s12967-020-02251-w

Acheson, E. D., Gardner, M. J., Pippard, E. C., & Grime, L. P. (1982). Mortality of two groups of women who manufactured gas masks from chrysotile and crocidolite asbestos: a 40-year follow-up. *British journal of industrial medicine*, *39*(4), 344–348. https://doi.org/10.1136/oem.39.4.344

Adelstein, D. J., Tomashefski, J. F., Jr, Snow, N. J., Horrigan, T. P., & Hines, J. D. (1986). Mixed small cell and non-small cell lung cancer. *Chest*, *89*(5), 699–704. https://doi.org/10.1378/chest.89.5.699

Aggarwal, N. R., King, L. S., & D'Alessio, F. R. (2014). Diverse macrophage populations mediate acute lung inflammation and resolution. *American journal of physiology. Lung cellular and molecular physiology*, *306*(8), L709–L725. https://doi.org/10.1152/ajplung.00341.2013

Alom-Ruiz, S. P., Anilkumar, N., & Shah, A. M. (2008). Reactive oxygen species and endothelial activation. *Antioxidants & redox signaling*, *10*(6), 1089–1100. https://doi.org/10.1089/ars.2007.2007

American Cancer Society. (2022). Lung Cancer Survival Rates. SEER*Explorer: An interactive website for SEER cancer statistics. *Surveillance Research Program*, National Cancer Institute. https://seer.cancer.gov/explorer/.

American Thoracic Society. (2004). Diagnosis and initial management of nonmalignant diseases related to asbestos. *American Journal of Respiratory and Critical Care Medicine, 170*(6), 691–715. https://doi.org/10.1164/rccm.200310-1436ST

Amersfoort, J., Eelen, G., & Carmeliet, P. (2022). Immunomodulation by endothelial cells - partnering up with the immune system?. *Nature reviews. Immunology*, *22*(9), 576–588. https://doi.org/10.1038/s41577-022-00694-4

Arita, A., & Costa, M. (2009). Epigenetics in metal carcinogenesis: nickel, arsenic, chromium and cadmium. *Metallomics: integrated biometal science*, *1*(3), 222–228. https://doi.org/10.1039/b903049b

Arora, S., Dev, K., Agarwal, B., Das, P., & Syed, M. A. (2018). Macrophages: Their role, activation and polarization in pulmonary diseases. *Immunobiology*, *223*(4-5), 383–396. https://doi.org/10.1016/j.imbio.2017.11.001

Auerbach, O., Stout, A. P., Hammond, E. C., & Garfinkel, L. (1961). Changes in bronchial epithelium in relation to cigarette smoking and in relation to lung cancer. *The New England journal of medicine*, *265*, 253–267. https://doi.org/10.1056/NEJM196108102650601

Auerbach, O., Saccomanno, G., Kuschner, M., Brown, R. D., & Garfinkel, L. (1978). Histologic findings in the tracheobronchial tree of uranium miners and non-miners with lung

cancer. *Cancer*, *42*(2), 483–489. https://doi.org/10.1002/1097-0142(197808)42:2<483::aid-cncr2820420216>3.0.co;2-e

Ballirano, P., Bloise, A., Gualtieri, A. F., Lezzerini, M., Pacella, A., Perchiazzi, N., Dogan, M., & Dogan, A. U. (2017). Chapter 2. The crystal structure of mineral fibres. *Mineral fibres: Crystal chemistry, chemical-physical properties, biological interaction and toxicity (A.F. Gualtieri, editor)*. 17–64. http://dx.doi.org/10.1180/EMU-notes.18.2

Banerjee, A. K. (2009). Preinvasive lesions of the bronchus. *Journal of Thoracic Oncology*, *4*(4), 545–551. https://doi.org/10.1097/JTO.0b013e31819667bd

Barlow, C. A., Grespin, M., & Best, E. A. (2017). Asbestos fiber length and its relation to disease risk. *Inhalation toxicology*, *29*(12-14), 541–554. https://doi.org/10.1080/08958378.2018.1435756

Barrett, J. C. (1994). Cellular and molecular mechanisms of asbestos carcinogenicity: Implications for biopersistence. *Environmental Health Perspectives*, *102*(SUPPL. 5), 19–23. https://doi.org/10.1289/ehp.94102s519

Baxter, E. W., Graham, A. E., Re, N. A., Carr, I. M., Robinson, J. I., Mackie, S. L., & Morgan, A. W. (2020). Standardized protocols for differentiation of THP-1 cells to macrophages with distinct M(IFNγ+LPS), M(IL-4) and M(IL-10) phenotypes. *Journal of immunological methods*, *478*, 112721. https://doi.org/10.1016/j.jim.2019.112721

Belluso, E., Cavallo, A., & Halterman D. (2017). Chapter 3. Crystal habit of mineral fibres. *Mineral fibres: Crystal chemistry, chemical-physical properties, biological interaction and toxicity (A.F. Gualtieri, editor)*, 17–64. http://dx.doi.org/10.1180/EMU-notes.18.3

Bent, R., Moll, L., Grabbe, S., & Bros, M. (2018). Interleukin-1 beta–A friend or foe in malignancies?. *International journal of molecular sciences*, *19*(8), 2155. https://doi.org/10.3390/ijms19082155

Bernstein, D. M., Chevalier, J., & Smith, P. (2005). Comparison of Calidria chrysotile asbestos to pure tremolite: final results of the inhalation biopersistence and histopathology examination following short-term exposure. *Inhalation toxicology*, *17*(9), 427–449. https://doi.org/10.1080/08958370591002012

Bernstein, D., Dunnigan, J., Hesterberg, T., Brown, R., Velasco, J. A. L., Barrera, R., Hoskins, J., & Gibbs, A. (2013). Health risk of chrysotile revisited. *Critical reviews in toxicology*, *43*(2), 154–183. https://doi.org/10.3109/10408444.2012.756454

Bernstein, D. M. (2014). The health risk of chrysotile asbestos. *Current Opinion in Pulmonary Medicine*, *20*(4), 366–370. https://doi.org/10.1097/MCP.0000000000000064

Bernstein, D. M., Toth, B., Rogers, R. A., Kling, D. E., Kunzendorf, P., Phillips, J. I., & Ernst, H. (2020). Evaluation of the exposure, dose-response and fate in the lung and pleura of chrysotile-containing brake dust compared to TiO_2, chrysotile, crocidolite or amosite asbestos in a 90-day quantitative inhalation toxicology study - Interim results Part 1: Experimental design, aerosol exposure, lung burdens and BAL. *Toxicology and applied pharmacology*, *387*, 114856. https://doi.org/10.1016/j.taap.2019.114856

Bernstein, D. M. (2022). The health effects of short fiber chrysotile and amphibole asbestos. *Critical Reviews in Toxicology 52*(2), 89-112. https://doi.org/10.1080/10408444.2022.2056430

Berry, G., Newhouse, M. L., & Wagner, J. C. (2000). Mortality from all cancers of asbestos factory workers in East London 1933-80. *Occupational and environmental medicine*, *57*(11), 782–785. https://doi.org/10.1136/oem.57.11.782

Bissardon, C., Reymond, S., Salomé, M., André, L., Bayat, S., Cloetens, P., & Bohic, S. (2019). Cell culture on silicon nitride membranes and cryopreparation for synchrotron X-ray fluorescence nano-analysis. *Journal of visualized experiments : JoVE*, *154*. https://doi.org/10.3791/60461

Bloise, A., Barrese, E., & Apollaro, C. (2009a). Hydrothermal alteration of Ti-doped forsterite to chrysotile and characterization of the resulting chrysotile fibres. *N. Jb. Miner. Mh*, *185*(3), 297–304. https://doi.org/10.1127/0077-7757/2009/0130

Bloise, A., Belluso, E., Barrese, E., Miriello, D., & Apollaro, C. (2009b). Synthesis of Fe-doped chrysotile and characterization of the resulting chrysotile fibers. *Cryst Res Technol*, *44*(6), 590–596. https://doi.org/10.1002/crat.200900135

Bloise, A., Belluso, E., Fornero, E., Rinaudo, C., Barrese, E., & Capella, S. (2010). Influence of synthesis conditions on growth of Ni-doped chrysotile. *Microporous and Mesoporous Materials*, *132*(1-2), 239–245. https://doi.org/10.1016/j.micromeso.2010.03.003

Bloise, A., Barca, D., Gualtieri, A. F., Pollastri, S., & Belluso, E. (2016). Trace elements in hazardous mineral fibres. *Environmental Pollution*, *216*, 314–323. https://doi.org/10.1016/j.envpol.2016.06.007

Bloise, A. (2019). Thermal behaviour of actinolite asbestos. *Journal of Materials Science*, *54*(18), 11784–11795. https://doi.org/10.1007/s10853-019-03738-8

Botham, S., & Holt, P.F. (1971). Development of asbestos bodies on amosite, chrysotile and crocidolite fibres in guinea-pig lungs. *The Journal of Pathology*, *105*(3), 159–167. https://doi.org/10.1002/PATH.1711050303

Boulanger, G., Andujar, P., Pairon, J. C., Billon-Galland, M. A., Dion, C., Dumortier, P., Brochard, P., Sobaszek, A., Bartsch, P., Paris, C., & Jaurand, M. C. (2014). Quantification of short and long asbestos fibers to assess asbestos exposure: a review of fiber size toxicity. *Environmental health*, *13*, 59. https://doi.org/10.1186/1476-069X-13-59

Boyles, M. S. P., Poland, C. A., Raftis, J., & Duffin, R. (2019). Assessment of the physicochemical properties of chrysotile-containing brake debris pertaining to toxicity. *Inhalation toxicology*, *31*(8), 325–342. https://doi.org/10.1080/08958378.2019.1683103

Byeon, I. J. L., Li, J., Ericson, K., Selby, T. L., Tevelev, A., Kim, H. J., O'Maille, P., & Tsai, M. D. (1998). Tumor suppressor p16INK4A: Determination of solution structure and analyses of its interaction with cyclin-dependent kinase 4. *Molecular Cell*, *1*(3), 421–431. https://doi.org/10.1016/S1097-2765(00)80042-8

Campbell, J. D., Alexandrov, A., Kim, J., Wala, J., Berger, A. H., Pedamallu, C. S., Shukla, S. A., Guo, G., Brooks, A. N., Murray, B. A., Imielinski, M., Hu, X., Ling, S., Akbani, R., Rosenberg, M., Cibulskis, C., Ramachandran, A., Collisson, E. A., Kwiatkowski, D. J., Lawrence, M. S., Weinstein, J. N., Verhaak, R. G. W., Wu, C. J., Hammerman, P. S., Cherniack, A. D., Getz, G.; Cancer Genome Atlas Research Network; Artyomov, M. N., Schreiber, R., Govindan, R., Meyerson, M. (2016). Distinct patterns of somatic genome alterations in lung adenocarcinomas and squamous cell carcinomas. *Nature genetics*, *48*(6), 607–616. https://doi.org/10.1038/ng.3564

Cancer Genome Atlas Research Network (2012). Comprehensive genomic characterization of squamous cell lung cancers. *Nature*, *489*(7417), 519–525. https://doi.org/10.1038/nature11404

Cancer Genome Atlas Research Network (2014). Comprehensive molecular profiling of lung adenocarcinoma. *Nature*, *511*(7511), 543–550. https://doi.org/10.1038/nature13385

Cangiotti, M., Salucci, S., Battistelli, M., Falcieri, E., Mattioli, M., Giordani, M., & Ottaviani, M. F. (2018). EPR, TEM and cell viability study of asbestiform zeolite fibers in cell media. *Colloids and surfaces. B, Biointerfaces*, *161*, 147–155. https://doi.org/10.1016/j.colsurfb.2017.10.045

Carbone, M., Adusumilli, P. S., Alexander, H. R., Jr, Baas, P., Bardelli, F., Bononi, A., Bueno, R., Felley-Bosco, E., Galateau-Salle, F., Jablons, D., Mansfield, A. S., Minaai, M., de Perrot, M., Pesavento, P., Rusch, V., Severson, D. T., Taioli, E., Tsao, A., Woodard, G., Yang, H., Zauderer, M. G., & Pass, H. I. (2019). Mesothelioma: Scientific clues for prevention, diagnosis, and therapy. *CA: a cancer journal for clinicians*, *69*(5), 402–429. https://doi.org/10.3322/caac.21572

Case, B. W., Abraham, J. L., Meeker, G., Pooley, F. D., & Pinkerton, K. E. (2011). Applying definitions of "asbestos" to environmental and "low-dose" exposure levels and health effects, particularly malignant mesothelioma. *Journal of toxicology and environmental health. Part B, Critical reviews*, *14*(1-4), 3–39. https://doi.org/10.1080/10937404.2011.556045

Case, B. W., & Marinaccio, A. (2017). Epidemiological approaches to health effects of mineral fibres: Development of knowledge and current practice. *Mineral Fibres: Crystal Chemistry, Chemical-Physical Properties, Biological Interaction and Toxicity. European Mineralogical Union-EMU Notes in Mineralogy*, *18*, 376–406. https://doi.org/10.1180/EMU-notes.18.11

Champaneria, M. C., Modlin, I. M., Kidd, M., & Eick, G. N. (2006). Friedrich Feyrter: a precise intellect in a diffuse system. *Neuroendocrinology*, *83*(5-6), 394–404. https://doi.org/10.1159/000096050

Chanput, W., Mes, J. J., & Wichers, H. J. (2014). THP-1 cell line: an in vitro cell model for immune modulation approach. *International immunopharmacology*, *23*(1), 37–45. https://doi.org/10.1016/j.intimp.2014.08.002

Chaudhuri, V., Zhou, L., & Karasek, M. (2007). Inflammatory cytokines induce the transformation of human dermal microvascular endothelial cells into myofibroblasts: a potential role in skin fibrogenesis. *Journal of cutaneous pathology*, *34*(2), 146–153. https://doi.org/10.1111/j.1600-0560.2006.00584.x

Chong, S., Lee, K. S., Chung, M. J., Han, J., Kwon, O. J., & Kim, T. S. (2006). Pneumoconiosis: comparison of imaging and pathologic findings. *Radiographics: a review publication of the Radiological Society of North America*, *26*(1), 59–77. https://doi.org/10.1148/rg.261055070

Chu, G. J., van Zandwijk, N., & Rasko, J. E. J. (2019). The immune microenvironment in mesothelioma: Mechanisms of resistance to immunotherapy. *Frontiers in oncology*, *9*, 1366. https://doi.org/10.3389/fonc.2019.01366

Churg, A. M., & Warnock, M. L. (1981). Asbestos and other ferruginous bodies. Their formation and clinical significance. *American Journal of Pathology*, *102*(3), 447–456.

Cigognetti, M., Lonardi, S., Fisogni, S., Balzarini, P., Pellegrini, V., Tironi, A., Bercich, L., Bugatti, M., Rossi, G., Murer, B., Barbareschi, M., Giuliani, S., Cavazza, A., Marchetti, G., Vermi, W., & Facchetti, F. (2015). BAP1 (BRCA1-associated protein 1) is a highly specific marker for differentiating mesothelioma from reactive mesothelial proliferations. *Modern pathology: an official journal of the United States and Canadian Academy of Pathology, Inc*, *28*(8), 1043–1057. https://doi.org/10.1038/modpathol.2015.65

Coffin, D. L., Cook, P. M., & Creason, J. P. (1992). Relative mesothelioma induction in rats by mineral fibers: comparison with residual pulmonary mineral fiber number and epidemiology. *Inhalat. Toxicol.*, *4*(3), 273–300. https://doi.org/10.3109/08958379209145671

Corti, A., Bonetti, J., Dominici, S., Piaggi, S., Fierabracci, V., Foddis, R., & Pompella, A. (2020). Induction of gamma-glutamyltransferase activity and consequent pro-oxidant reactions in human macrophages exposed to crocidolite asbestos. *Toxicological sciences*, *177*(2), 476–482. https://doi.org/10.1093/toxsci/kfz175

Coussens, L. M., & Werb, Z. (2002). Inflammation and cancer. *Nature*, *420*(6917), 860–867. https://doi.org/10.1038/nature01322

Craighead, J. E., Mossman, B. T., & Bradley, B. J. (1980). Comparative studies on the cytotoxicity of amphibole and serpentine asbestos. *Environmental Health Perspectives*, *VOL.34*(February), 37–46. https://doi.org/10.1289/ehp.803437

Croce, A., Arrais, A., & Rinaudo, C. (2018). Raman Micro-Spectroscopy identifies carbonaceous particles lying on the surface of crocidolite, amosite, and chrysotile fibers. *Minerals*, *8*(6), 249. https://doi.org/10.3390/min8060249

Currie, G. P., Watt, S. J., & Maskell, N. A. (2009). An overview of how asbestos exposure affects the lung. *BMJ (Clinical research ed.)*, *339*, b3209. https://doi.org/10.1136/bmj.b3209

D'Arcy, M. S. (2019). Cell death: a review of the major forms of apoptosis, necrosis and autophagy. *Cell biology international*, *43*(6), 582–592. https://doi.org/10.1002/cbin.11137

Davidson, B. (2015). Prognostic factors in malignant pleural mesothelioma. *Human Pathology*, *46*(6), 789–804. https://doi.org/10.1016/j.humpath.2015.02.006

Davis, J. M. (1970). Asbestos dust as a nucleation center in the calcification of old fibrous tissue lesions, and the possible association of this process to the formation of asbestos bodies. *Experimental and molecular pathology*, *12*(2), 133–147. https://doi.org/10.1016/0014-4800(70)90045-6

Dayen, C., Debieuvre, D., Molinier, O., Raffy, O., Paganin, F., Virally, J., Larive, S., Desurmont-Salasc, B., Perrichon, M., Martin, F., & Grivaux, M. (2017). New insights into stage and prognosis in small cell lung cancer: An analysis of 968 cases. *Journal of Thoracic Disease*, *9*(12), 5101–5111. https://doi.org/10.21037/jtd.2017.11.52

De La Fuente, G., Fontana, M., Asnaghi, V., Chiantore, M., Mirata, S., Salis, A., Damonte, G., & Scarfì, S. (2020). The remarkable antioxidant and anti-inflammatory potential of the extracts of the brown alga Cystoseira amentacea var. stricta. *Marine Drugs*, *19*(1), 2. https://doi.org/10.3390/md19010002

Deer, W. A., Howie, R. A., & Zussman, J. (2009). Rock Forming Minerals. 3B. Layered Silicates Excluding Micas and Clay Minerals, *2nd Edition, The Geological Society*, London.

Della Ventura, G., Vigliaturo, R., Gieré, R., Pollastri, S., Gualtieri, A. F., & Iezzi, G. (2018). Infra red spectroscopy of the regulated asbestos amphiboles. *Minerals*, *8*(9), 413. https://doi.org/10.3390/min8090413

Deshmane, S. L., Kremlev, S., Amini, S., & Sawaya, B. E. (2009). Monocyte chemoattractant protein-1 (MCP-1): an overview. *Journal of interferon & cytokine research: the official journal of the International Society for Interferon and Cytokine Research*, *29*(6), 313–326. https://doi.org/10.1089/jir.2008.0027

Devereux, T.R., Taylor, J.A., & Barrett, J.C. (1996). Molecular mechanisms of lung cancer. Interaction of environmental and genetic factors. *Chest*, *109*(Suppl 3), 14S–19S. https://doi.org/10.1378/chest.109.3_Supplement.14S

DeVita, V.T., Rosenberg, S.A., & Lawrence, T.S. (2008), *DeVita, Hellman, and Rosenberg's Cancer: Principles & Practice of Oncology, 8th Edition, Lippincott Williams & Wilkins*.

Di Giuseppe, D., Scarfì, S., Alessandrini, A., Bassi, A. M., Mirata, S., Almonti, V., Ragazzini, G., Mescola, A., Filaferro, M., Avallone, R., Vitale, G., Scognamiglio, V., & Gualtieri, A. F. (2021a). Acute cytotoxicity of mineral fibres observed by time-lapse video microscopy. Toxicology, 466, 153081. https://doi.org/10.1016/j.tox.2021.153081

Di Giuseppe, D., Scognamiglio, V., Malferrari, D., Nodari, L., Pasquali, L., Lassinantti Gualtieri, M., Scarfì, S., Mirata, S., Tessari, U., Hanuskova, M., & Gualtieri, A. F. (2021b). Characterization of fibrous wollastonite NYAD G in view of its use as negative standard for in vitro toxicity tests. *Minerals*, *11*(12), 1378. https://doi.org/10.3390/min11121378

Di Giuseppe, D., Zoboli, A., Nodari, L., Pasquali, L., Sala, O., Ballirano, P., Malferrari, D., Raneri, S., Hanuskova, M., & Gualtieri, A. F. (2021c). Characterization and assessment of the potential toxicity/pathogenicity of Russian commercial chrysotile. *American Mineralogist, 106* (10), 1606–1621. https://doi.org/10.2138/am-2021-7710

Dinarello, C. A. (2018). Overview of the IL-1 family in innate inflammation and acquired immunity. *Immunological reviews*, *281*(1), 8–27. https://doi.org/10.1111/imr.12621

Dodson, R. F., Williams, M. G., Jr, Corn, C. J., Idell, S., & McLarty, J. W. (1989). Usefulness of combined light and electron microscopy: evaluation of sputum samples for asbestos to determine past occupational exposure. *Modern pathology: an official journal of the United States and Canadian Academy of Pathology, Inc*, *2*(4), 320–322. PMID: 2548182.

Dodson, R. F., Atkinson, M. A., & Levin, J. L. (2003). Asbestos fiber length as related to potential pathogenicity: a critical review. *American journal of industrial medicine*, *44*(3), 291–297. https://doi.org/10.1002/ajim.10263

Dogan, A. U., Dogan, M., & Emri, S. (2005). Erionite. In P. Wexler (ed.), *Encyclopedia of toxicology, 2nd Edition*, 237–241. *Oxford: Elsevier*. https://doi.org/10.1016/B0-12-369400-0/00380-X

Dogan, A. U., Dogan, M., & Hoskins, J. A. (2008). Erionite series minerals: mineralogical and carcinogenic properties. *Environmental geochemistry and health*, *30*(4), 367–381. https://doi.org/10.1007/s10653-008-9165-x

Doll, R. (1955). Mortality from lung cancer in asbestos workers. *British Journal of Industrial Medicine*, *12*, 81–86. https://doi.org/10.1136/oem.50.6.485

Donaldson, K., Murphy, F. A., Duffin, R., & Poland, C. A. (2010). Asbestos, carbon nanotubes and the pleural mesothelium: a review of the hypothesis regarding the role of long fibre retention in the parietal pleura, inflammation and mesothelioma. *Particle and fibre toxicology*, *7*, 5. https://doi.org/10.1186/1743-8977-7-5

Dorling, M., & Zussman, J. (1987). Characteristics of asbestiform and non-asbestiform calcic amphiboles. *Lithos*, *20*(6), 469–489. https://doi.org/10.1016/0024-4937(87)90030-2

Dostert, C., Pétrilli, V., Van Bruggen, R., Steele, C., Mossman, B. T., & Tschopp, J. (2008). Innate immune activation through Nalp3 inflammasome sensing of asbestos and silica. *Science*, *320*(5876), 674–677. https://doi.org/10.1126/science.1156995

Egilman, D., & Tran, T. (2016). A commentary on Roggli's "The so-called short-fiber controversy." *International Journal of Occupational and Environmental Health*, *22*(3), 181–186. https://doi.org/10.1080/10773525.2016.1153866

Eid, R., Arab, N. T., & Greenwood, M. T. (2017). Iron mediated toxicity and programmed cell death: A review and a re-examination of existing paradigms. *Biochimica et biophysica acta. Molecular cell research*, *1864*(2), 399–430. https://doi.org/10.1016/j.bbamcr.2016.12.002

Epler, G. R., McLoud, T. C., & Gaensler, E. A. (1982). Prevalence and incidence of benign asbestos pleural effusion in a working population. *JAMA*, *247*(5), 617–622. https://doi.org/10.1001/JAMA.1982.03320300021016

Evans, B. W., & Ghiorso, M. S. (1995). Thermodynamics and petrology of cummingtonite. *American Mineralogist*, *80*(7–8), 649–663. https://doi.org/10.2138/am-1995-7-801

Evans, B. W., & Hexiong Yang. (1998). Fe-Mg order-disorder in tremolite-actinolite-ferro-actinolite at ambient and high temperature. *American Mineralogist*, *83*(5–6), 458–475. https://doi.org/10.2138/am-1998-5-606

Ferrante, D., Mirabelli, D., Silvestri, S., Azzolina, D., Giovannini, A., Tribaudino, P., & Magnani, C. (2020). Mortality and mesothelioma incidence among chrysotile asbestos miners in Balangero, Italy: A cohort study. *American journal of industrial medicine*, *63*(2), 135–145. https://doi.org/10.1002/ajim.23071

Frank, A. L. (2020). Global use of asbestos - Legitimate and illegitimate issues. *Journal of Occupational Medicine and Toxicology*, *15*(1), 1–6. https://doi.org/10.1186/s12995-020-00267-y

Fridlender, Z. G., Kapoor, V., Buchlis, G., Cheng, G., Sun, J., Wang, L. C., Singhal, S., Snyder, L. A., & Albelda, S. M. (2011). Monocyte chemoattractant protein-1 blockade inhibits lung cancer tumor growth by altering macrophage phenotype and activating CD8+ cells. *American journal of respiratory cell and molecular biology*, *44*(2), 230–237. https://doi.org/10.1165/rcmb.2010-0080OC

Fujimoto, N., Gemba, K., Aoe, K., Kato, K., Yokoyama, T., Usami, I., Onishi, K., Mizuhashi, K., Yusa, T., & Kishimoto, T. (2015). Clinical investigation of benign asbestos pleural effusion. *Pulmonary Medicine, 2015,* 416179. https://doi.org/10.1155/2015/416179

Fujimura N. (2000). Pathology and pathophysiology of pneumoconiosis. *Current opinion in pulmonary medicine*, *6*(2), 140–144. https://doi.org/10.1097/00063198-200003000-00010

Gabay, C. (2006). Interleukin-6 and chronic inflammation. *Arthritis research & therapy*, *8*(Suppl 2), S3. https://doi.org/10.1186/ar1917

Gainor, J. F., & Shaw, A. T. (2013). Novel targets in non-small cell lung cancer: ROS1 and RET fusions. *The oncologist*, *18*(7), 865–875. https://doi.org/10.1634/theoncologist.2013-0095

Gainor, J. F., Varghese, A. M., Ou, S. H., Kabraji, S., Awad, M. M., Katayama, R., Pawlak, A., Mino-Kenudson, M., Yeap, B. Y., Riely, G. J., Iafrate, A. J., Arcila, M. E., Ladanyi, M., Engelman, J. A., Dias-Santagata, D., & Shaw, A. T. (2013). ALK rearrangements are mutually exclusive with mutations in EGFR or KRAS: an analysis of 1,683 patients with non-small cell lung cancer. *Clinical cancer research: an official journal of the American Association for Cancer Research*, *19*(15), 4273–4281. https://doi.org/10.1158/1078-0432.CCR-13-0318

Garabrant, D. H., & Pastula, S. T. (2018). A comparison of asbestos fiber potency and elongate mineral particle (EMP) potency for mesothelioma in humans. Toxicology and applied pharmacology, 361, 127–136. https://doi.org/10.1016/j.taap.2018.07.003

Garcia, J. G., Gray, L. D., Dodson, R. F., & Callahan, K. S. (1988). Asbestos-induced endothelial cell activation and injury. Demonstration of fiber phagocytosis and oxidant-dependent toxicity. *The American review of respiratory disease*, *138*(4), 958–964. https://doi.org/10.1164/ajrccm/138.4.958

Garcia-Canton, C., Anadón, A., & Meredith, C. (2012). γ-H2AX as a novel endpoint to detect DNA damage: applications for the assessment of the in vitro genotoxicity of cigarette smoke. *Toxicology in vitro*, *26*(7), 1075–1086. https://doi.org/10.1016/j.tiv.2012.06.006

Germani, D., Belli, S., Bruno, C., Grignoli, M., Nesti, M., Pirastu, R., & Comba, P. (1999). Cohort mortality study of women compensated for asbestosis in Italy. *American journal of industrial medicine*, *36*(1), 129–134. https://doi.org/10.1002/(sici)1097-0274(199907)36:1<129::aid-ajim18>3.0.co;2-9

Ghio, A. J., LeFurgey, A., & Roggli, V. L. (1997). In vivo accumulation of iron on crocidolite is associated with decrements in oxidant generation by the fiber. *Journal of toxicology and environmental health*, *50*(2), 125–142. https://doi.org/10.1080/009841097160537

Ghio, A. J., Churg, A., & Roggli, V. L. (2004). Ferruginous bodies: Implications in the mechanism of fiber and particle toxicity. *Toxicologic Pathology*, *32*(6), 643–649. https://doi.org/10.1080/01926230490885733

Giacobbe, C., Di Giuseppe, D., Zoboli, A., Gualtieri, M. L., Bonasoni, P., Moliterni, A., Corriero, N., Altomare, A., Wright, J., & Gualtieri, A. F. (2021). Crystal structure determination of a lifelong biopersistent asbestos fibre using single-crystal synchrotron X-ray micro-diffraction. *IUCrJ*, *8*, 76–86. https://doi.org/10.1107/S2052252520015079

Gomes, A., Reis-Silva, M., Alarcão, A., Couceiro, P., Sousa, V., & Carvalho, L. (2014). Promoter hypermethylation of DNA repair genes MLH1 and MSH2 in adenocarcinomas and squamous cell carcinomas of the lung. *Rev Port Pneumol*, *20*(1), 20–30. https://doi.org/10.1016/j.rppneu.2013.07.003

Goodglick, L. A., & Kane, A. B. (1990). Cytotoxicity of long and short crocidolite asbestos fibers in vitro and in vivo. *Cancer research*, *50*(16), 5153–5163.

Gordon S. (2007). The macrophage: past, present and future. *European journal of immunology*, *37 Suppl 1*, S9–S17. https://doi.org/10.1002/eji.200737638

Görlach, A., Bertram, K., Hudecova, S., & Krizanova, O. (2015). Calcium and ROS: A mutual interplay. *Redox biology*, *6*, 260–271. https://doi.org/10.1016/j.redox.2015.08.010

Governa, M., & Rosanda, C. (1972). A histochemical study of the asbestos body coating. *British journal of industrial medicine*, *29*(2), 154–159. https://doi.org/10.1136/oem.29.2.154

Governa, M., Amati, M., Fontana, S., Visona I, Botta, G. C., Mollo, F., Bellis, D., & Bo, P. (1999). Role of iron in asbestos-body-induced oxidant radical generation. *Journal of toxicology and environmental health. Part A*, *58*(5), 279–287. https://doi.org/10.1080/009841099157241

Groppo, C., & Compagnoni, R. (2007). Metamorphic veins from the serpentinites of the Piemonte Zone, western Alps, Italy: a review. *Period Miner*, *76* (2–3), 127–153. http://doi.org/10.2451/2007PM0021

Gualtieri, A. F., Gandolfi, N. B., Pollastri, S., Pollok, K., & Langenhorst, F. (2016). Where is iron in erionite? A multidisciplinary study on fibrous erionite-Na from Jersey (Nevada, USA). *Scientific Reports*, *6*, 1–11. https://doi.org/10.1038/srep37981

Gualtieri, A. F., Gandolfi, N. B., Pollastri, S., Rinaldi, R., Sala, O., Martinelli, G., Bacci, T., Paoli, F., Viani, A., & Vigliaturo, R. (2018a). Assessment of the potential hazard represented by natural raw materials containing mineral fibres - The case of the feldspar from Orani, Sardinia (Italy). *Journal of hazardous materials*, *350*, 76–87. https://doi.org/10.1016/j.jhazmat.2018.02.012

Gualtieri, A. F., Pollastri, S., Bursi Gandolfi, N., & Gualtieri, M. L. (2018b). In vitro acellular dissolution of mineral fibres: A comparative study. *Scientific Reports*, *8*, 7071. https://doi.org/10.1038/s41598-018-25531-4

Gualtieri, A. F., Lusvardi, G., Pedone, A., Di Giuseppe, D., Zoboli, A., Mucci, A., Zambon, A., Filaferro, M., Vitale, G., Benassi, M., Avallone, R., Pasquali, L., & Lassinantti Gualtieri, M. (2019a). Structure model and toxicity of the product of biodissolution of chrysotile asbestos in the lungs. *Chemical Research in Toxicology*, *32*(10), 2063–2077. https://doi.org/10.1021/acs.chemrestox.9b00220

Gualtieri, A. F., Lusvardi, G., Zoboli, A., Di Giuseppe, D., & Lassinantti Gualtieri, M. (2019b). Biodurability and release of metals during the dissolution of chrysotile, crocidolite and fibrous erionite. *Environmental research*, *171*, 550–557. https://doi.org/10.1016/j.envres.2019.01.011

Gualtieri, A. F. (2021). Bridging the gap between toxicity and carcinogenicity of mineral fibres by connecting the fibre crystal-chemical and physical parameters to the key characteristics of cancer. *Current Research in Toxicology*, *2*, 42–52. https://doi.org/10.1016/j.crtox.2021.01.005

Gualtieri A. F. (2023). Journey to the centre of the lung. The perspective of a mineralogist on the carcinogenic effects of mineral fibres in the lungs. *Journal of hazardous materials*, *442*, 130077. https://doi.org/10.1016/j.jhazmat.2022.130077

Gulino, G. R., Polimeni, M., Prato, M., Gazzano, E., Kopecka, J., Colombatto, S., Ghigo, D., & Aldieri, E. (2016). Effects of chrysotile exposure in human bronchial epithelial cells: Insights into the pathogenic mechanisms of asbestos-related diseases. *Environmental health perspectives*, *124*(6), 776–784. https://doi.org/10.1289/ehp.1409627

Gupta, A., Harris, K., & Dhillon, S. S. (2019). Role of bronchoscopy in management of central squamous cell lung carcinoma *in situ*. *Annals of translational medicine*, *7*(15), 354. https://doi.org/10.21037/atm.2019.04.36

Han, S., Lemire, J., Appanna, V. P., Auger, C., Castonguay, Z., & Appanna, V. D. (2013). How aluminum, an intracellular ROS generator promotes hepatic and neurological diseases: the metabolic tale. *Cell biology and toxicology*, *29*(2), 75–84. https://doi.org/10.1007/s10565-013-9239-0

Hart, H. P. (1988). Asbestos in South Africa. *Journal of the South African Institute of Mining and Metallurgy*, *88*(6), 185–198. https://hdl.handle.net/10520/AJA0038223X_1875

Hawthorne, F. C., Oberti, R., Harlow, G. E., Maresch, W. V., Martin, R. F., Schumacher, J. C., & Welch, M. D. (2012). Ima report: Nomenclature of the amphibole supergroup. *American Mineralogist*, *97*(11–12), 2031–2048. https://doi.org/10.2138/am.2012.4276

Hawthorne, F. C. (2016). Short-range atomic arrangements in minerals. I: The minerals of the amphibole, tourmaline and pyroxene supergroups. *European Journal of Mineralogy*, *28*(3), 513–536. https://doi.org/10.1127/ejm/2016/0028-2538

Heppleston, A. G. (1988). Prevalence and pathogenesis of pneumoconiosis in coal workers. *Environmental Health Perspectives*, *78*(1), 159–170. https://doi.org/10.1289/ehp.8878159

Herbst, R. S., Morgensztern, D., & Boshoff, C. (2018). The biology and management of non-small cell lung cancer. *Nature*, *553*(7689), 446–454. https://doi.org/10.1038/nature25183

Herseth, J. I., Refsnes, M., Låg, M., Hetland, G., & Schwarze, P. E. (2008). IL-1β as a determinant in silica-induced cytokine responses in monocyte-endothelial cell co-cultures. *Human and Experimental Toxicology*, *27*(5), 387–399. https://doi.org/10.1177/0960327108094610

Hillerdal, G., & Ozesmi, M. (1987). Benign asbestos pleural effusion: 73 exudates in 60 patients. *European journal of respiratory diseases*, *71*(2), 113–121.

Hirsch, F. R., Franklin, W. A., Gazdar, A. F., & Bunn, P. A., Jr (2001). Early detection of lung cancer: clinical perspectives of recent advances in biology and radiology. *Clinical cancer research: an official journal of the American Association for Cancer Research*, *7*(1), 5–22.

Hirsch, F.R., & Bunn, P.A. (2009). EGFR testing in lung cancer is ready for prime time. *The Lancet. Oncology*, *10* (5), 432–433. https://doi.org/10.1016/s1470-2045(09)70110-x

Hodgson, J. T., & Darnton, A. (2000). The quantitative risks of mesothelioma and lung cancer in relation to asbestos exposure. *Annals of occupational hygiene*, *44*(8), 565–601. https://doi.org/10.1093/annhyg/44.8.565

Hsu, T., Nguyen-Tran, H. H., & Trojanowska, M. (2019). Active roles of dysfunctional vascular endothelium in fibrosis and cancer. *Journal of biomedical science*, *26*(1), 86. https://doi.org/10.1186/s12929-019-0580-3

Hume, L. A., & Rimstidt, J. D. (1992). The biodurability of chrysotile asbestos. *American Mineralogist*, *77*(9-10), 1125–1128.

Hussell, T., & Bell, T. J. (2014). Alveolar macrophages: plasticity in a tissue-specific context. *Nature reviews. Immunology*, *14*(2), 81–93. https://doi.org/10.1038/nri3600

IARC Working Group on the Evaluation of Carcinogenic Risks to Humans. (1987). Erionite. *IARC monographs on the evaluation of the carcinogenic risk of chemicals to humans*, *42*, 225–239.

IARC Working Group on the Evaluation of Carcinogenic Risks to Humans. (1988). Alcohol drinking. *IARC monographs on the evaluation of carcinogenic risks to humans, 44*, 1–378.

IARC Working Group on the Evaluation of Carcinogenic Risks to Humans. (1993). Beryllium, cadmium, mercury, and exposures in the glass manufacturing industry. *IARC monographs on the evaluation of carcinogenic risks to humans*, *58*, 1–415.

IARC Working Group on the Evaluation of Carcinogenic Risks to Humans (2004). Tobacco smoke and involuntary smoking. *IARC monographs on the evaluation of carcinogenic risks to humans*, *83*, 1–1438.

IARC Working Group on the Evaluation of Carcinogenic Risks to Humans (2012). Arsenic, metals, fibres, and dusts. *IARC monographs on the evaluation of carcinogenic risks to humans*, *100*(Pt C), 11–465.

Iles, K. E., & Forman, H. J. (2002). Macrophage signaling and respiratory burst. *Immunologic Research*, *26*, 95–105. https://doi.org/10.1385/ir:26:1-3:095

Institute of Medicine (US). (2006). Asbestos: Selected Cancers. *Committee on Asbestos: Selected Health Effects. National Academies Press (US)*. https://doi.org/10.17226/11665

International Labour Organization. (2011). Guidelines for the use of the ILO international classification of radiographs of pneumoconioses. *Occupational safety and health series*, No 22 (Revised edition 2011). https://www.ilo.org/global/publications/books/WCMS_168337/lang--en/index.htm

International Zeolite Association (2005). Erionite Series. *Commission on Natural Zeolites*. http://www.iza-online.org/natural/Datasheets/Erionite/erionite.htm

Ishizumi, T., McWilliams, A., MacAulay, C., Gazdar, A., & Lam, S. (2010). Natural history of bronchial preinvasive lesions. *Cancer and Metastasis Reviews*, *29*(1), 5–14. https://doi.org/10.1007/s10555-010-9214-7

Ito, F., Kato, K., Yanatori, I., Murohara, T., & Toyokuni, S. (2021). Ferroptosis-dependent extracellular vesicles from macrophage contribute to asbestos-induced mesothelial carcinogenesis through loading ferritin. *Redox biology*, *47*, 102174. https://doi.org/10.1016/j.redox.2021.102174

Janke, R., Dodson, A. E., & Rine, J. (2015). Metabolism and epigenetics. *Annual review of cell and developmental biology*, *31*, 473–496. https://doi.org/10.1146/annurev-cellbio-100814-125544

Jänne, P. A., Taffaro, M. L., Salgia, R., & Johnson, B. E. (2002). Inhibition of epidermal growth factor receptor signaling in malignant pleural mesothelioma. *Cancer Research*, *62*(18), 5242–5247.

Jaurand, M. C., Bignon, J., Sebastien, P., & Goni, J. (1977). Leaching of chrysotile asbestos in human lungs: Correlation with in vitro studies using rabbit alveolar macrophages. *Environmental Research*, *14*(2), 245–254. https://doi.org/10.1016/0013-9351(77)90036-6

Kamp, D. W. (2009). Asbestos-induced lung diseases: an update. *Translational Research*, *153*(4), 143–152. https://doi.org/10.1016/j.trsl.2009.01.004

Kawai, T., Tominaga, S., Hiroi, S., Ogata, S., Nakanishi, K., Kawahara, K., Sonobe, H., Hiroshima, K. (2016). Peritoneal malignant mesothelioma (PMM), and primary peritoneal serous carcinoma (PPSC) and reactive mesothelial hyperplasia (RMH) of the peritoneum. Immunohistochemical and fluorescence in situ hybridisation (FISH) analyses. *J Clin Pathol*, *69*(8), 706–712. https://doi.org/10.1136/jclinpath-2015-203211

Kee, S. T., Gamsu, G., & Blanc, P. (1996). Causes of pulmonary impairment in asbestos-exposed individuals with diffuse pleural thickening. *American journal of respiratory and critical care medicine*, *154*(3 Pt 1), 789–793. https://doi.org/10.1164/ajrccm.154.3.8810620

Keith, R. L., Miller, Y. E., Gemmill, R. M., Drabkin, H. A., Dempsey, E. C., Kennedy, T. C., Prindiville, S., & Franklin, W. A. (2000). Angiogenic squamous dysplasia in bronchi of individuals at high risk for lung cancer. *Clinical cancer research: an official journal of the American Association for Cancer Research*, *6*(5), 1616–1625.

Kelse, J. W., & Thompson, C. S. (1989). The regulatory and mineralogical definitions of asbestos and their impact on amphibole dust analysis. *American Industrial Hygiene Association Journal*, *50*(11), 613–622. https://doi.org/10.1080/15298668991375245

Klein, C., & Philpotts, A. (2016). Some selected earth materials resources. In *Earth Materials: Introduction to Mineralogy and Petrology* (pp. 499–522). *Cambridge: Cambridge University Press*. doi:10.1017/9781316652909.019

Kohyama, N., & Suzuki, Y. (1991). Analysis of asbestos fibers in lung parenchyma, pleural plaques, and mesothelioma tissues of North American insulation workers. *Annals of the New York Academy of Sciences*, *643*, 27–52. https://doi.org/10.1111/j.1749-6632.1991.tb24442.x

Kononova, S., Gubanova, G., Korytkova, E., Sapegin, D., Setnickova, K., Petrychkovych, R., & Uchytil, P. (2018). Polymer Nanocomposite Membranes. *Applied Sciences*, *8*(7), 1181. https://doi.org/10.3390/app8071181

Kris, M. G. (2005). How today's developments in the treatment of non-small cell lung cancer will change tomorrow's standards of care. *The Oncologist*, *10* (Suppl 2), 23–29. https://doi.org/10.1634/theoncologist.10-90002-23

Lacy, P., & Stow, J. L. (2011). Cytokine release from innate immune cells: Association with diverse membrane trafficking pathways. *Blood*, *118*(1), 9–18. https://doi.org/10.1182/blood-2010-08-265892

Langseth, H., Johansen, B. V., Nesland, J. M., & Kjaerheim, K. (2007). Asbestos fibers in ovarian tissue from Norwegian pulp and paper workers. *International journal of gynecological cancer: official journal of the International Gynecological Cancer Society*, *17*(1), 44–49. https://doi.org/10.1111/j.1525-1438.2006.00768.x

Larson-Casey, J. L., Gu, L., Kang, J., Dhyani, A., & Carter, A. B. (2021). NOX4 regulates macrophage apoptosis resistance to induce fibrotic progression. *The Journal of biological chemistry*, *297*(1), 100810. https://doi.org/10.1016/j.jbc.2021.100810

Laskin, D. L., Malaviya, R., & Laskin, J. D. (2019). Role of macrophages in acute lung injury and chronic fibrosis induced by pulmonary toxicants. *Toxicological Sciences*, *168*(2), 287–301. https://doi.org/10.1093/toxsci/kfy309

Leake, B. E. (1978). Nomenclature of amphiboles. *Mineralogical Magazine*, *42*, 533–563. https://doi.org/10.1180/MINMAG.1978.042.324.21

Leake, B. E., Woolley, A. R., Arps, C. E., Birch, W. D., Gilbert, M. C., Grice, J. D., Hawthorne, F. C., Kato, A., Kisch, H. J., Krivovichev, V. G., Linthout, K., Laird, J., Mandarino, J. A., Maresch, W. V., Nickel, E. H., Rock, N. M. S., Schumacher, J. C., Smith, D. C., Stephenson, N. C. N., Ungaretti, L., Whittaker, E. J. W., Youzhi, G. (1997). Nomenclature of amphiboles; report of the Subcommittee on Amphiboles of the International Mineralogical Association Commission on new minerals and mineral names. *Mineralogical magazine*, *61*(405), pp.295–310. https://doi.org/10.1127/ejm/9/3/0623

Lechner, J. F., Tesfaigzi, J., & Gerwin, B. I. (1997). Oncogenes and tumor-suppressor genes in mesothelioma–a synopsis. *Environmental health perspectives*, *105 Suppl 5*(Suppl 5), 1061–1067. https://doi.org/10.1289/ehp.97105s51061

Lee, D. K., Jeon, S., Han, Y., Kim, S. H., Lee, S., Yu, I. J., Song, K. S., Kang, A., Yun, W. S., Kang, S. M., Huh, Y. S., & Cho, W. S. (2018). Threshold rigidity values for the asbestos-like pathogenicity of high-aspect-ratio carbon nanotubes in a mouse pleural inflammation model. *ACS nano*, *12*(11), 10867–10879. https://doi.org/10.1021/acsnano.8b03604

Levallet, G., Vaisse-Lesteven, M., Le Stang, N., Ilg, A. G., Brochard, P., Astoul, P., Pairon, J. C., Bergot, E., Zalcman, G., & Galateau-Sallé, F. (2012). Plasma cell membrane localization of c-MET predicts longer survival in patients with malignant mesothelioma: a series of 157 cases from the MESOPATH Group. *Journal of thoracic oncology: official publication of the International Association for the Study of Lung Cancer*, *7*(3), 599–606. https://doi.org/10.1097/JTO.0b013e3182417da5

Lewis, I.R., Chaffin, N.C., Gunter, M.E., & Griffiths, P.R. (1996). Vibrational spectroscopic studies of asbestos and comparison of suitability for remote analysis. *Spectrochimica Acta Part A: Molecular and Biomolecular Spectroscopy*, *52*, 315–328. https://doi.org/10.1016/0584-8539(95)01560-4

Li, M., Gunter, M. E., & Fukagawa, N. K. (2012). Differential activation of the inflammasome in THP-1 cells exposed to chrysotile asbestos and Libby "six-mix" amphiboles and subsequent activation of BEAS-2B cells. *Cytokine*, *60*(3), 718–730. https://doi.org/10.1016/j.cyto.2012.08.025

Lin, A. L., & Gutmann, D. H. (2013). Advances in the treatment of neurofibromatosis-associated tumours. *Nature reviews. Clinical oncology*, *10*(11), 616–624. https://doi.org/10.1038/nrclinonc.2013.144

Lo, D., Zhang, Y., Dai, M. S., Sun, X. X., Zeng, S. X., & Lu, H. (2015). Nucleostemin stabilizes ARF by inhibiting the ubiquitin ligase ULF. *Oncogene*, *34*(13), 1688–1697. https://doi.org/10.1038/onc.2014.103

Longo, W. E., Rigler, M. W., & Slade, J. (1995). Crocidolite asbestos fibers in smoke from original Kent cigarettes. *Cancer Research*, *55*(11), 2232–2235.

Loomis, D., Dement, J. M., Wolf, S. H., & Richardson, D. B. (2009). Lung cancer mortality and fibre exposures among North Carolina asbestos textile workers. *Occupational and environmental medicine*, *66*(8), 535–542. https://doi.org/10.1136/oem.2008.044362

Loomis, D., Dement, J. M., Richardson, D. B., & Wolf, S. H. (2010). Asbestos fibre dimensions and lung cancer mortality among workers exposed to chrysotile. *Occupational and environmental medicine*, *67*(9), 580–584. https://doi.org/10.1136/oem.2009.050120

Loomis, D., Dement, J. M., Elliott, L., Richardson, D. B., Kuempel, E. D., & Stayner, L. T. (2012). Increased lung cancer mortality among chrysotile asbestos textile workers is more strongly associated with exposure to long thin fibres. *Occupational and Environmental Medicine*, *69*(8), 564–568. https://doi.org/10.1136/oemed-2012-100676

Lowers, H. A., & Meeker, G. P. (2002). Tabulation of asbestos-related terminology. *U.S. Geological Survey, Open-File Report 02–458*, 1−74. https://pubs.usgs.gov/of//2002/ofr-02-458/OFR-02-458-508.pdf

Lundblad, L. K., Thompson-Figueroa, J., Leclair, T., Sullivan, M. J., Poynter, M. E., Irvin, C. G., & Bates, J. H. T. (2005). Tumor necrosis factor-alpha overexpression in lung disease: a single cause behind a complex phenotype. *American journal of respiratory and critical care medicine*, *171*(12), 1363–1370. https://doi.org/10.1164/rccm.200410-1349OC

Lundborg, M., Johard, U., Johansson, A., Eklund, A., Falk, R., Kreyling, W., & Camner, P. (1995). Phagolysosomal morphology and dissolution of cobalt oxide particles by human and rabbit alveolar macrophages. *Experimental lung research*, *21*(1), 51–66. https://doi.org/10.3109/01902149509031744

Magnani, C., Ferrante, D., Barone-Adesi, F., Bertolotti, M., Todesco, A., Mirabelli, D., & Terracini, B. (2008). Cancer risk after cessation of asbestos exposure: a cohort study of Italian asbestos cement workers. *Occupational and environmental medicine*, *65*(3), 164–170. https://doi.org/10.1136/oem.2007.032847

Mamdani, H., Matosevic, S., Khalid, A. B., Durm, G., & Jalal, S. I. (2022). Immunotherapy in lung cancer: current landscape and future directions. *Frontiers in immunology*, *13*, 823618. https://doi.org/10.3389/fimmu.2022.823618

Mangum, M. D., Greco, F. A., Hainsworth, J. D., Hande, K. R., & Johnson, D. H. (1989). Combined small-cell and non-small-cell lung cancer. *Journal of clinical oncology: official journal of the American Society of Clinical Oncology*, *7*(5), 607–612. https://doi.org/10.1200/JCO.1989.7.5.607

Manning, C. B., Vallyathan, V., & Mossman, B. T. (2002). Diseases caused by asbestos: Mechanisms of injury and disease development. *International Immunopharmacology*, *2*(2–3), 191–200. https://doi.org/10.1016/S1567-5769(01)00172-2

Mantovani, A., Sica, A., Sozzani, S., Allavena, P., Vecchi, A., & Locati, M. (2004a). The chemokine system in diverse forms of macrophage activation and polarization. *Trends in immunology*, *25*(12), 677–686. https://doi.org/10.1016/j.it.2004.09.015

Mantovani, A., Allavena, P., & Sica, A. (2004b). Tumour-associated macrophages as a prototypic type II polarised phagocyte population: role in tumour progression. *European journal of cancer*, *40*(11), 1660–1667. https://doi.org/10.1016/j.ejca.2004.03.016

Martinez, F. O., Helming, L., & Gordon, S. (2009). Alternative activation of macrophages: an immunologic functional perspective. *Annual review of immunology*, *27*, 451–483. https://doi.org/10.1146/annurev.immunol.021908.132532

McCormack, V., Peto, J., Byrnes, G., Straif, K., & Boffetta, P. (2012). Estimating the asbestos-related lung cancer burden from mesothelioma mortality. *British Journal of Cancer*, *106*(3), 575–584. https://doi.org/10.1038/bjc.2011.563

McDonald, J. C., Harris, J., & Armstrong, B. (2004). Mortality in a cohort of vermiculite miners exposed to fibrous amphibole in Libby, Montana. *Occupational and environmental medicine*, *61*(4), 363–366. https://doi.org/10.1136/oem.2003.008649

McLemore, T. L., Mace, M. L., Jr, Roggli, V., Marshall, M. V., Lawrence, E. C., Wilson, R. K., Martin, R. R., Brinkley, B. R., & Greenberg, S. D. (1980). Asbestos body phagocytosis by human free alveolar macrophages. *Cancer letters*, *9*(2), 85–93. https://doi.org/10.1016/0304-3835(80)90111-1

Meeker, G.P., Bern, A.M., Brownfield, I.K., Lowers, H.A., Sutley, S.J., Hoefen, T.M., & Vance, J.S. (2003). The composition and morphology of amphiboles from the Rainy Creek complex, near Libby, Montana. *American Mineralogist, 88,* 1955–1969. https://doi.org/10.2138/am-2003-11-1239

Militello, G. M., Gaggero, L., & La Maestra, S. (2021). Asbestiform amphiboles and cleavage fragments analogues: overview of critical dimensions, aspect ratios, exposure and health effects. *Minerals*, *11*(5), 525. https://doi.org/10.3390/min11050525

Min, Y. D., Choi, C. H., Bark, H., Son, H. Y., Park, H. H., Lee, S., Park, J. W., Park, E. K., Shin, H. I., & Kim, S. H. (2007). Quercetin inhibits expression of inflammatory cytokines through attenuation of NF-κB and p38 MAPK in HMC-1 human mast cell line. *Inflammation research*, *56*(5), 210–215. https://doi.org/10.1007/s00011-007-6172-9

Mirata, S., Almonti, V., Di Giuseppe, D., Fornasini, L., Raneri, S., Vernazza, S., Bersani, D., Gualtieri, A. F., Bassi, A. M., & Scarfì, S. (2022). The acute toxicity of mineral fibres: a systematic in vitro study using different THP-1 macrophage phenotypes. *International journal of molecular sciences*, *23*(5), 2840. https://doi.org/10.3390/ijms23052840

Mitchell, R. N., Kumar, V., Robbins, S. L., & Fausto, N. (2007). "Ch. 13, box on morphology of small-cell lung carcinoma". *Robbins Basic Pathology, 8th Edition, Elsevier Saunders*.

Mitchell, R. N., Kumar, V., Robbins, S. L., & Fausto, N. (2007). "Ch. 13, box on morphology of adenocarcinoma". *Robbins Basic Pathology, 8th Edition, Elsevier Saunders*.

Morgan, A., & Holmes, A. (1985). The enigmatic asbestos body: its formation and significance in asbestos-related disease. *Environmental research*, *38* (2), 283–292. https://doi.org/10.1016/0013-9351%2885%2990092-1

Morón-Calvente, V., Romero-Pinedo, S., Toribio-Castelló, S., Plaza-Díaz, J., Abadía-Molina, A. C., Rojas-Barros, D. I., Beug, S. T., LaCasse, E. C., MacKenzie, A., Korneluk, R., & Abadía-Molina, F. (2018). Inhibitor of apoptosis proteins, NAIP, cIAP1 and cIAP2 expression during macrophage differentiation and M1/M2 polarization. *PloS one*, *13*(3), e0193643. https://doi.org/10.1371/journal.pone.0193643

Morris, G. F., Danchuk, S., Wang, Y., Xu, B., Rando, R. J., Brody, A. R., Shan, B., & Sullivan, D. E. (2015). Cigarette smoke represses the innate immune response to asbestos. *Physiological reports*, *3*(12), e12652. https://doi.org/10.14814/phy2.12652

Mossman, B. T., Bignon, J., Corn, M., Seaton, A., & Gee, J. B. L. (1990). Asbestos: scientific developments and implications for public policy. *Science*, *247*(4940), 294–301. https://doi.org/10.1126/science.2153315

Mossman, B. T. (1993). Mechanisms of asbestos carcinogenesis and toxicity: the amphibole hypothesis revisited. *Occupational and Environmental Medicine*, *50*, 673–676. http://doi.org/10.1136/oem.50.8.673

Mossman, B. T., & Gee, J. B. L. (1993). Pulmonary reactions and mechanisms of toxicity of inhaled fibers. In *Toxicology of the Lung* (D. E. Gardner, J. D. Crapo, and R. O. McClellan, Eds.), pp. 371–387. Raven Press, New York.

Mossman, B. T., Lippmann, M., Hesterberg, T. W., Kelsey, K. T., Barchowsky, A., & Bonner, J. C. (2011). Pulmonary endpoints (lung carcinomas and asbestosis) following inhalation exposure to asbestos. *Journal of Toxicology and Environmental Health, Part B*, *14*(1-4), 76–121. https://doi.org/10.1080/10937404.2011.556047

Mossman, B. T., Shukla, A., Heintz, N. H., Verschraegen, C. F., Thomas, A., & Hassan, R. (2013). New insights into understanding the mechanisms, pathogenesis, and management of malignant mesotheliomas. *American Journal of Pathology*, *182*(4), 1065–1077. https://doi.org/10.1016/j.ajpath.2012.12.028

Mossman, B. T. (2018). Mechanistic in vitro studies: What they have told us about carcinogenic properties of elongated mineral particles (EMPs). *Toxicology and applied pharmacology*, *361*, 62–67. https://doi.org/10.1016/j.taap.2018.07.018

Mossman, B. T., & Gualtieri, A. F. (2020). Lung cancer: mechanisms of carcinogenesis by asbestos. In: Anttila, S., Boffetta, P. *Occupational Cancers*. *Springer, Cham*. https://doi.org/10.1007/978-3-030-30766-0_12

Munson, P., Lam, Y. W., Dragon, J., MacPherson, M., & Shukla, A. (2018). Exosomes from asbestos-exposed cells modulate gene expression in mesothelial cells. *FASEB journal*, *32*(8), 4328–4342. https://doi.org/10.1096/fj.201701291RR

Nakajima, E. C., Vellanki, P. J., Larkins, E., Chatterjee, S., Mishra-Kalyani, P. S., Bi, Y., Qosa, H., Liu, J., Zhao, H., Biable, M., Hotaki, L. T., Shen, Y. L., Pazdur, R., Beaver, J. A., Singh, H., & Donoghue, M. (2022). FDA approval summary: Nivolumab in combination with Ipilimumab for the treatment of unresectable malignant pleural mesothelioma. *Clinical cancer research : an official journal of the American Association for Cancer Research*, *28*(3), 446–451. https://doi.org/10.1158/1078-0432.CCR-21-1466

National Institute for Occupational Safety and Health. (2011). Asbestos fibers and other elongate mineral particles: state of the science and roadmap for research. *Current intelligence bulletin 62*, 1–174. https://www.cdc.gov/niosh/docs/2011-159/pdfs/2011-159.pdf

National Toxicology Program. (2011). Erionite. *Report on Carcinogens : Carcinogen Profiles / U.S. Dept. of Health and Human Services, Public Health Service, National Toxicology Program*, *12*, 183–184. https://doi.org/10.1016/b978-044453067-7/50541-4

Ndlovu, B., Forbes, E., Becker, M., Deglon, D., Franzidis, J., & Laskowski, J. S. (2011). The effects of chrysotile mineralogical properties on the rheology of chrysotile suspensions. *Minerals Engineering*, *24*, 1004–1009. https://doi.org/10.1016/J.MINENG.2011.04.025

Nelson, D. B., Rice, D. C., Niu, J., Atay, S., Vaporciyan, A. A., Antonoff, M., Hofstetter, W. L., Walsh, G. L., Swisher, S. G., Roth, J. A., Tsao, A., Gomez, D., Giordano, S. H., Mehran, R., & Sepesi, B. (2017). Long-term survival outcomes of cancer-directed surgery for malignant pleural mesothelioma: propensity score matching analysis. *Journal of clinical oncology: official journal of the American Society of Clinical Oncology*, *35*(29), 3354–3362. https://doi.org/10.1200/JCO.2017.73.8401

Nemery, B. (1990). Metal toxicity and the respiratory tract. *The European respiratory journal*, *3*(2), 202–219. PMID: 2178966

Ni, Z., Liu, Y., Keshava, N., Zhou, G., Whong, W., & Ong, T. (2000). Analysis of K-ras and p53 mutations in mesotheliomas from humans and rats exposed to asbestos. *Mutation research*, *468*(1), 87–92. https://doi.org/10.1016/s1383-5718(00)00043-7

Nicholson, S. A., Beasley, M. B., Brambilla, E., Hasleton, P. S., Colby, T. V., Sheppard, M. N., Falk, R. & Travis, W. D. (2002). Small cell lung carcinoma (SCLC): a clinicopathologic study of 100 cases with surgical specimens. *Am. J. Surg. Pathol*, *26* (9), 1184–1197. https://doi.org/10.1097/00000478-200209000-00009

Nikolova, T., Christmann, M., & Kaina, B. (2009). FEN1 is overexpressed in testis, lung and brain tumors. *Anticancer research*, *29*(7), 2453–2459.

Nishiyama, Y., Suwa, H., Okamoto, K., Fukumoto, M., Hiai, H., & Toyokuni, S. (1995). Low incidence of point mutations in H-, K- and N-ras oncogenes and p53 tumor suppressor gene in renal cell carcinoma and peritoneal mesothelioma of Wistar rats induced by ferric nitrilotriacetate. *Japanese journal of cancer research: Gann*, *86*(12), 1150–1158. https://doi.org/10.1111/j.1349-7006.1995.tb03308.x

O'Brien, K. M., Tworoger, S. S., Harris, H. R., Anderson, G. L., Weinberg, C. R., Trabert, B., Kaunitz, A. M., D'Aloisio, A. A., Sandler, D. P., Wentzensen, N. (2020) Association of powder use in the genital area with risk of ovarian cancer. *JAMA*, *323*, 49–59. https://doi.org/10.1001/jama.2019.20079

Oberdörster, G. (2000). Determinants of the pathogenicity of man-made vitreous fibers (MMVF). *Int Archives Occup Environ health*, *73*, S60–S68. https://doi.org/10.1007/PL00014628

Okayasu, R., Takahashi, S., Yamada, S., Hei, T. K., & Ullrich, R. L. (1999). Asbestos and DNA double strand breaks. *Cancer research*, *59*(2), 298–300.

Ouelle, D. E., Zindy, F., Ashmun, R. A., & Sherr, C. J. (1995). Alternative reading frames of the INK4a tumor suppressor gene encode two unrelated proteins capable of inducing cell cycle arrest. *Cell*, *83*(6), 993–1000. https://doi.org/10.1016/0092-8674(95)90214-7

Pacella, A., Andreozzi, G.B., Nodari, L., & Ballirano, P. (2019). Chemical and structural characterization of UICC crocidolite fibres from Koegas Mine, Northern Cape (South Africa). *Period Miner*, *88*(3), 297–306. https://doi.org/10.2451/2019PM910

Panduri, V., Surapureddi, S., Soberanes, S., Weitzman, S. A., Chandel, N., & Kamp, D. W. (2006). P53 mediates amosite asbestos-induced alveolar epithelial cell mitochondria-regulated apoptosis. *American Journal of Respiratory Cell and Molecular Biology*, *34*(4), 443–452. https://doi.org/10.1165/rcmb.2005-0352OC

Panou, V., Vyberg, M., Weinreich, U. M., Meristoudis, C., Falkmer, U. G., & Røe, O. D. (2015). The established and future biomarkers of malignant pleural mesothelioma. *Cancer treatment reviews*, *41*(6), 486–495. https://doi.org/10.1016/j.ctrv.2015.05.001

Papp, T., Schipper, H., Pemsel, H., Bastrop, R., Muller, K. M., Wiethege, T., Weiss, D. G., Dopp, E., Schiffmann, D., & Rahman, Q. (2001). Mutational analysis of N-ras, p53, p16INK4a, p14ARF and CDK4 genes in primary human malignant mesotheliomas. *International journal of oncology*, *18*(2), 425–433. https://doi.org/10.3892/ijo.18.2.425

Pastis, N. J., Gonzalez, A. V., Silvestri, G. A. (2022). Lung Cancer: Diagnosis and Staging. In *Murray & Nadel's Textbook of Respiratory Medicine, 7th Edition, Elsevier*, pp. 1039–1051. https://doi.org/10.1016/C2011-1-08123-7

Pauling, L. (1930). The structure of the chlorites. *Proceedings of the National Academy of Sciences USA 16* (1930), 578–582. https://doi.org/10.1073/pnas.16.9.578

Pauly, J. L., O'Connor, R. J., Paszkiewicz, G. M., Cummings, K. M., Djordjevic, M. V., & Shields, P. G. (2009). Cigarette filter-based assays as proxies for toxicant exposure and smoking behavior - A literature review. *Cancer Epidemiology Biomarkers and Prevention*, *18*(12), 3321–3333. https://doi.org/10.1158/1055-9965.EPI-09-0925

Peacock, C., Copley, S.J., & Hansell, D.M. (2000) Asbestos-related benign pleural disease. *Clinical Radiology*, *55*(6), 422–432. https://doi.org/10.1053/crad.2000.0450

Petriglieri, J. R., Salvioli-Mariani, E., Mantovani, L., Tribaudino, M., Lottici, P. P., Laporte-Magoni, C., & Bersani, D. (2015). Micro-Raman mapping of the polymorphs of serpentine. *Journal of Raman Spectroscopy*, *46*(10), 953–958. https://doi.org/10.1002/jrs.4695

Piera-Velazquez, S., & Jimenez, S. A. (2019). Endothelial to mesenchymal transition: role in physiology and in the pathogenesis of human diseases. *Physiological reviews*, *99*(2), 1281–1324. https://doi.org/10.1152/physrev.00021.2018

Pikor, L., Ramnarine, V.R., Lam, S., & Lam, W.L. (2013). Genetic alterations defining NSCLC subtypes and their therapeutic implications. *Lung cancer*, *82*(2), 179–189. https://doi.org/10.1016/j.lungcan.2013.07.025

Pinato, D. J., Mauri, F. A., Lloyd, T., Vaira, V., Casadio, C., Boldorini, R. L., & Sharma, R. (2013). The expression of Axl receptor tyrosine kinase influences the tumour phenotype and clinical outcome of patients with malignant pleural mesothelioma. *British journal of cancer*, *108*(3), 621–628. https://doi.org/10.1038/bjc.2013.9

Piperno, S., Kaplan-Ashiri, I., Cohen, S. R., Popovitz-Biro, R., Wagner, H. D., Tenne, R., Foresti, E., Lesci, I. G. & Roveri, N. (2007). Characterization of Geoinspired and Synthetic Chrysotile Nanotubes by Atomic Force Microscopy and Transmission Electron Microscopy. *Advanced Functional Materials*, *17*(16), 3332–3338. https://doi.org/10.1002/adfm.200700278

Platel, V., Faure, S., Corre, I., & Clere, N. (2019). Endothelial-to-Mesenchymal Transition (EndoMT): roles in tumorigenesis, metastatic extravasation and therapy resistance. *Journal of oncology*, *2019*, 8361945. https://doi.org/10.1155/2019/8361945

Pollastri, S., Gualtieri, A. F., Gualtieri, M. L., Hanuskova, M., Cavallo, A., & Gaudino, G. (2014). The zeta potential of mineral fibres. *Journal of hazardous materials*, *276*, 469–479. https://doi.org/10.1016/j.jhazmat.2014.05.060

Pollastri, S., Perchiazzi, N., Lezzerini, M., Plaisier, J.R., Cavallo, A., Dalconi, M.C., Gandolfi, N.B., & Gualtieri, A.F. (2016). The crystal structure of mineral fibres. 1. Chrysotile. *Period Miner*, *85*, 249–259. https://doi.org/10.2451/2016PM655

Pooley, F. D. (1972). Asbestos bodies, their formation, composition and character. *Environmental Research*, *5*(4), 363–379. https://doi.org/10.1016/0013-9351(72)90039-4

Potter, R. M., & Mattson, S. M. (1991). Glass fiber dissolution in a physiological saline solution. *Glastechnische Berichte*, *64*(1), 16–28.

Pozzolini, M., Vergani, L., Ragazzoni, M., Delpiano, L., Grasselli, E., Voci, A., Giovine, M., & Scarfì, S. (2016). Different reactivity of primary fibroblasts and endothelial cells towards crystalline silica: A surface radical matter. *Toxicology*, *361-362*, 12–23. https://doi.org/10.1016/j.tox.2016.07.001

Putnis, A. (1992). The crystal structure of minerals II – Silicates. In *An Introduction to Mineral Sciences* (pp. 141–184). *Cambridge: Cambridge University Press*. doi:10.1017/CBO9781139170383.007

Qazi, B. S., Tang, K., & Qazi, A. (2011). Recent advances in underlying pathologies provide insight into interleukin-8 expression-mediated inflammation and angiogenesis. *International journal of inflammation*, *2011*, 908468. https://doi.org/10.4061/2011/908468

Qi, X. M., Luo, Y., Song, M. Y., Liu, Y., Shu, T., Liu, Y., Pang, J. L., Wang, J., & Wang, C. (2021). Pneumoconiosis: current status and future prospects. *Chinese Medical Journal*, *134*(8), 898–907. https://doi.org/10.1097/CM9.0000000000001461

Ramazzini, C. (2010). Asbestos is still with us: Repeat call for a universal ban. *Archives of Environmental and Occupational Health*, *65*(3), 121–126. https://doi.org/10.1080/19338241003776104

Rayess, H., Wang, M. B., & Srivatsan, E. S. (2012). Cellular senescence and tumor suppressor gene p16. *International journal of cancer*, *130*(8), 1715–1725. https://doi.org/10.1002/ijc.27316

Rdzanek, M., Fresco, R., Pass, H. I., & Carbone, M. (2006). Spindle cell tumors of the pleura: differential diagnosis. *Seminars in diagnostic pathology*, *23*(1), 44–55. https://doi.org/10.1053/j.semdp.2006.06.002

Redza-Dutordoir, M., & Averill-Bates, D. A. (2016). Activation of apoptosis signalling pathways by reactive oxygen species. *Biochimica et biophysica acta*, *1863*(12), 2977–2992. https://doi.org/10.1016/j.bbamcr.2016.09.012

Rinaudo, C., & Croce, A. (2019). Micro-Raman spectroscopy, a powerful technique allowing sure identification and complete characterization of asbestiform minerals. *Applied Sciences*, *9*(15), 3092. https://doi.org/10.3390/app9153092

Rivera, P., Mody, G. N., Weiner, A. A. (2022). "Lung Cancer: Treatment". In *Murray & Nadel's Textbook of Respiratory Medicine, 7th Edition, Elsevier*, pp. 1052–1065. https://doi.org/10.1016/C2011-1-08123-7

Robbins, S. L., Kumar, V., Cotran, R. S., Abbas, A. K., & Fausto, N. (2005). Robbins and Cotran pathologic basis of disease. *7th Edition, Elsevier Saunders*, p 759.

Roggli, V. L. (1995). Malignant mesothelioma and duration of asbestos exposure: correlation with tissue mineral fibre content. *The Annals of occupational hygiene*, *39*(3), 363–374. https://doi.org/10.1093/annhyg/39.3.363

Roggli, V. L., Sharma, A., Butnor, K. J., Sporn, T., & Vollmer, R. T. (2002). Malignant mesothelioma and occupational exposure to asbestos: a clinicopathological correlation of 1445 cases. *Ultrastructural pathology*, *26*(2), 55–65. https://doi.org/10.1080/01913120252959227

Roggli, V. L., & Vollmer, R. T. (2008). Twenty-five years of fiber analysis: what have we learned?. *Human pathology*, *39*(3), 307–315. https://doi.org/10.1016/j.humpath.2007.07.005

Roggli, V. L. (2013). Asbestos bodies and non-asbestos ferruginous bodies. *Pathology of Asbestos-Associated Diseases, 3rd Edition, Springer*, 25–53. https://doi.org/10.5005/jp/books/10591

Roggli, V. L. (2015). The so-called short-fiber controversy: Literature review and critical analysis. *Archives of pathology & laboratory medicine*, *139*(8), 1052–1057. https://doi.org/10.5858/arpa.2014-0466-RA

Rom, W. N., Travis, W. D., & Brody, A. R. (1991). Cellular and molecular basis of the asbestos-related diseases. *The American review of respiratory disease*, *143*(2), 408–422. https://doi.org/10.1164/ajrccm/143.2.408

Ross, M., & Nolan, R. P. (2003). History of asbestos discovery and use and asbestos-related disease in context with the occurrence of asbestos within ophiolite complexes. *Ophiolite concept and the evolution of geological thought. Geological Society of America*, *373*, 447–470. https://doi.org/10.1130/0-8137-2373-6.447

Ross, M., Langer, A. M., Nord, G. L., Nolan, R. P., Lee, R. J., Van Orden, D., & Addison, J. (2008). The mineral nature of asbestos. *Regulatory toxicology and pharmacology: RTP*, *52*(1 Suppl), S26–S30. https://doi.org/10.1016/j.yrtph.2007.09.008

Rosti, G., Bevilacqua, G., Bidoli, P., Portalone, L., Santo, A., & Genestreti, G. (2006). Small cell lung cancer. *Annals of oncology : official journal of the European Society for Medical Oncology*, *17 Suppl 2*, ii5–ii10. https://doi.org/10.1093/annonc/mdj910

Sabo-Attwood, T., Ramos-Nino, M.E., Bond, J.P., Butnor, K.J., Heintz, N.H., Gruber, A.D., Steele, C., Taatjes, D.J., Vacek, P., & Mossman, B.T. (2005). Gene expression profiles reveal increased mClca3 (Gob5) expression and mucin production in a murine model of asbestos-induced fibrogenesis. *The American journal of pathology*, *167*(5), 1243–1256. https://doi.org/10.1016/S0002-9440(10)61212-6

Saccomanno, G. (1982). Carcinoma in-situ of the lung: its development, detection, and treatment. *Semin Respir Med*, *4*(2), 156–160. https://doi.org/10.1055/s-2007-1012480

Sahtoe, D. D., van Dijk, W. J., Ekkebus, R., Ovaa, H., & Sixma, T. K. (2016). BAP1/ASXL1 recruitment and activation for H2A deubiquitination. *Nature communications*, *7*, 10292. https://doi.org/10.1038/ncomms10292

Santiago-Delpin, E. A. (2004). The endothelium and early immune activation: new perspective and interactions. *Transplantation proceedings*, *36*(6), 1709–1713. https://doi.org/10.1016/j.transproceed.2004.06.068

Scarfì, S., Magnone, M., Ferraris, C., Pozzolini, M., Benvenuto, F., Benatti, U., & Giovine, M. (2009). Ascorbic acid pre-treated quartz stimulates TNF-α release in RAW 264.7 murine macrophages through ROS production and membrane lipid peroxidation. *Respiratory research*, *10*(1), 25. https://doi.org/10.1186/1465-9921-10-25

Scarfì, S., Pozzolini, M., Oliveri, C., Mirata, S., Salis, A., Damonte, G., Fenoglio, D., Altosole, T., Ilan, M., Bertolino, M., & Giovine, M. (2020). Identification, purification and molecular characterization of chondrosin, a new protein with anti-tumoral activity from the marine sponge Chondrosia reniformis Nardo 1847. *Marine drugs*, *18*(8), 409. https://doi.org/10.3390/md18080409

Scognamiglio, V., Di Giuseppe, D., Gualtieri, M. L., Tomassetti, L., & Gualtieri, A. F. (2021). A systematic study of the cryogenic milling of chrysotile asbestos. *Applied Sciences (Switzerland)*, *11*(11), 4826. https://doi.org/10.3390/app11114826

Searl, A., Buchanan, D., Cullen, R. T., Jones, A. D., Miller, B. G., & Soutar, C. A. (1999). Biopersistence and durability of nine mineral fibre types in rat lungs over 12 months. *The Annals of occupational hygiene*, *43*(3), 143–153. https://doi.org/10.1093/annhyg/43.3.143

Sethi, G., Sung, B., & Aggarwal, B. B. (2008). TNF: a master switch for inflammation to cancer. *Frontiers in bioscience*, *13*, 5094–5107. https://doi.org/10.2741/3066

Shao, Y., Saredy, J., Yang, W. Y., Sun, Y., Lu, Y., Saaoud, F., Drummer, C., 4th, Johnson, C., Xu, K., Jiang, X., Wang, H., & Yang, X. (2020). Vascular endothelial cells and innate immunity. *Arteriosclerosis, thrombosis, and vascular biology*, *40*(6), e138–e152. https://doi.org/10.1161/ATVBAHA.120.314330

Sherr C. J. (2006). Divorcing ARF and p53: an unsettled case. *Nature reviews. Cancer*, *6*(9), 663–673. https://doi.org/10.1038/nrc1954

Skuland, T., Maslennikova, T., Låg, M., Gatina, E. M., Serebryakova, M. K., Trulioff, A. S., Kudryavtsev, I. V., Klebnikova, N., Kruchinina, I., Schwarze, P. E., & Refsnes, M. (2020). Synthetic hydrosilicate nanotubes induce low pro-inflammatory and cytotoxic responses compared to natural chrysotile in lung cell cultures. *Basic & clinical pharmacology & toxicology*, *126*(4), 374–388. https://doi.org/10.1111/bcpt.13341

Slomovitz, B., De Haydu, C., Taub, M., Coleman, R. L., & Monk, B. J. (2021). Asbestos and ovarian cancer: Examining the historical evidence. *International Journal of Gynecological Cancer*, *31*(1), 122–128. https://doi.org/10.1136/ijgc-2020-001672

Stanton, M. F., Layard, M., Tegeris, A., Miller, E., May, M., Morgan, E., & Smith, A. (1981). Relation of particle dimension to carcinogenicity in amphibole asbestoses and other fibrous minerals. *Journal of the National Cancer Institute*, *67*(5), 965–975. https://doi.org/10.1093/jnci/67.5.965

Stayner, L., Kuempel, E., Gilbert, S., Hein, M., & Dement, J. (2008). An epidemiological study of the role of chrysotile asbestos fibre dimensions in determining respiratory disease risk in

exposed workers. *Occupational and environmental medicine*, *65*(9), 613–619. https://doi.org/10.1136/oem.2007.035584

Sun, X., Nkennor, B., Mastikhina, O., Soon, K., & Nunes, S. S. (2020). Endothelium-mediated contributions to fibrosis. *Seminars in cell & developmental biology*, *101*, 78–86. https://doi.org/10.1016/j.semcdb.2019.10.015

Sung, H., Ferlay, J., Siegel, R. L., Laversanne, M., Soerjomataram, I., Jemal, A., & Bray, F. (2021). Global cancer statistics 2020: GLOBOCAN estimates of incidence and mortality worldwide for 36 cancers in 185 countries. *CA: a cancer journal for clinicians*, *71*(3), 209–249. https://doi.org/10.3322/caac.21660

Thakur, S. A., Hamilton, R. F., Jr, & Holian, A. (2008). Role of scavenger receptor A family in lung inflammation from exposure to environmental particles. *Journal of immunotoxicology*, *5*(2), 151–157. https://doi.org/10.1080/15476910802085863

Titulaer, M. K., van Miltenburg, J., Jansen, J. B., Geus, J. W. (1993). Characterization of tubular chrysotile by thermoporometry, nitrogen sorption, drifts, and TEM. *Clays and Clay Minerals*, *41*, 496–513. https://doi.org/10.1346/CCMN.1993.0410410

Titulaer, M. J., & Verschuuren, J. J. (2008). Lambert-Eaton myasthenic syndrome: tumor versus nontumor forms. *Annals of the New York Academy of Sciences*, *1132*, 129–134. https://doi.org/10.1196/annals.1405.030

Touyz, R. M. (2004). Magnesium in clinical medicine. *Frontiers in bioscience: a journal and virtual library*, *9*, 1278–1293. https://doi.org/10.2741/1316

Travis, W. D., Brambilla, E., Nicholson, A. G., Yatabe, Y., Austin, J. H. M., Beasley, M. B., Chirieac, L. R., Dacic, S., Duhig, E., Flieder, D. B., Geisinger, K., Hirsch, F. R., Ishikawa, Y., Kerr, K. M., Noguchi, M., Pelosi, G., Powell, C. A., Tsao, M. S., Wistuba, I., & WHO Panel (2015). The 2015 World Health Organization classification of lung tumors: impact of genetic, clinical and radiologic advances since the 2004 classification. *Journal of thoracic oncology: official publication of the International Association for the Study of Lung Cancer*, *10*(9), 1243–1260. https://doi.org/10.1097/JTO.0000000000000630

Treadwell, M. D., Mossman, B. T., & Barchowsky, A. (1996). Increased neutrophil adherence to endothelial cells exposed to asbestos. *Toxicol Appl Pharmacol*, *139*(1):62–70. https://doi.org/10.1006/taap.1996.0143

Tsai, Y.-L., Huang, E., Li, Y.-H., Hung, H.-T., Jiang, J.-H., Liu, T.-C., Fang, J.-N., & Chen, H.-F. (2021). Raman spectroscopic characteristics of zeolite group minerals. *Minerals*, *11*(2), 167. https://doi.org/10.3390/min11020167

Tsao, A. S., Harun, N., Fujimoto, J., Devito, V., Lee, J. J., Kuhn, E., Mehran, R., Rice, D., Moran, C., Hong, W. K., Shen, L., Suraokar, M., & Wistuba, I. (2014). Elevated PDGFRB gene copy number gain is prognostic for improved survival outcomes in resected malignant pleural mesothelioma. *Annals of diagnostic pathology*, *18*(3), 140–145. https://doi.org/10.1016/j.anndiagpath.2014.02.005

Tsou, C. L., Peters, W., Si, Y., Slaymaker, S., Aslanian, A. M., Weisberg, S. P., Mack, M., & Charo, I. F. (2007). Critical roles for CCR2 and MCP-3 in monocyte mobilization from bone

marrow and recruitment to inflammatory sites. *The Journal of clinical investigation*, *117*(4), 902–909. https://doi.org/10.1172/JCI29919

Utembe, W., Potgieter, K., Stefaniak, A. B., & Gulumian, M. (2015). Dissolution and biodurability: Important parameters needed for risk assessment of nanomaterials. *Part Fibre Toxicol*, *12*, 1–12. https://doi.org/10.1186/s12989-015-0088-2

Valko, M., Rhodes, C. J., Moncol, J., Izakovic, M., & Mazur, M. (2006). Free radicals, metals and antioxidants in oxidative stress-induced cancer. *Chemico-biological interactions*, *160*(1), 1–40. https://doi.org/10.1016/j.cbi.2005.12.009

Vandesompele, J., De Preter, K., Pattyn, F., Poppe, B., Van Roy, N., De Paepe, A., & Speleman, F. (2002). Accurate normalization of real-time quantitative RT-PCR data by geometric averaging of multiple internal control genes. *Genome biology*, *3*(7), RESEARCH0034. https://doi.org/10.1186/gb-2002-3-7-research0034

Vannella, K. M., & Wynn, T. A. (2017). Mechanisms of organ injury and repair by macrophages. *Annual review of physiology*, *79*, 593–617. https://doi.org/10.1146/annurev-physiol-022516-034356

Ventura, C., Pereira, J. F. S., Matos, P., Marques, B., Jordan, P., Sousa-Uva, A., & Silva, M. J. (2020). Cytotoxicity and genotoxicity of MWCNT-7 and crocidolite: assessment in alveolar epithelial cells versus their coculture with monocyte-derived macrophages. *Nanotoxicology*, *14*(4), 479–503. https://doi.org/10.1080/17435390.2019.1695975

Vimercati, L., Cavone, D., Delfino, M. C., Bruni, B., De Maria, L., Caputi, A., Sponselli, S., Rossi, R., Resta, L., Fortarezza, F., Pezzuto, F., & Serio, G. (2021). Primary ovarian mesothelioma: a case series with electron microscopy examination and review of the literature. *Cancers*, *13*(9), 2278. https://doi.org/10.3390/cancers13092278

Virta, R. L. (2002) Asbestos: Geology, mineralogy, mining, and uses: U.S. Geological Survey *Open-File Report 02- 149*, 35. https://doi.org/10.3133/ofr02149

Vogelzang, N. J., Rusthoven, J. J., Symanowski, J., Denham, C., Kaukel, E., Ruffie, P., Gatzemeier, U., Boyer, M., Emri, S., Manegold, C., Niyikiza, C., & Paoletti, P. (2003). Phase III study of pemetrexed in combination with cisplatin versus cisplatin alone in patients with malignant pleural mesothelioma. *Journal of clinical oncology : official journal of the American Society of Clinical Oncology*, *21*(14), 2636–2644. https://doi.org/10.1200/JCO.2003.11.136

Wagner, J. C., Sleggs, C. A., & Marchand, P. (1960). Diffuse pleural mesothelioma and asbestos exposure in the North Western Cape Province. *British Journal of Industrial Medicine*, *17*, 260–271. https://doi.org/10.1136/oem.17.4.260

Wagner, P. L., Kitabayashi, N., Yao-Tseng, C., & Saqi, A. (2009). Combined small cell lung carcinomas : Genotypic and immunophenotypic analysis of the separate morphologic components. *American Journal of Clinical Pathology*, *131*(3), 376–382. https://doi.org/10.1309/AJCPYNPFL56POZQY

Whittaker, E. J. (1953). The structure of chrysotile. *Acta Crystallographica*, *6*, 747–748. https://doi.org/10.1107/S0365110X53002118

Whittaker, E. J. (1957). The structure of chrysotile. V. Diffuse reflexions and fibre texture. *Acta Crystallographica*, *10*, 149–156. https://doi.org/10.1107/S0365110X57000511

Whittaker, E. J. (1960). The crystal chemistry of the amphiboles. *Acta Crystallographica*, *13*, 291–298. https://doi.org/10.1107/S0365110X60000741

Wienken, M., Dickmanns, A., Nemajerova, A., Kramer, D., Najafova, Z., Weiss, M., Karpiuk, O., Kassem, M., Zhang, Y., Lozano, G., Johnsen, S. A., Moll, U. M., Zhang, X., & Dobbelstein, M. (2016). MDM2 associates with Polycomb Repressor Complex 2 and enhances stemness-promoting chromatin modifications independent of p53. *Molecular cell*, *61*(1), 68–83. https://doi.org/10.1016/j.molcel.2015.12.008

Wignall, B. K., & Fox, A. J. (1982). Mortality of female gas mask assemblers. *British journal of industrial medicine*, *39*(1), 34–38. https://doi.org/10.1136/oem.39.1.34

Witkiewicz, A. K., Knudsen, K. E., Dicker, A. P., & Knudsen, E. S. (2011). The meaning of p16ink4a expression in tumors: Functional significance, clinical associations and future developments. *Cell Cycle*, *10*(15), 2497–2503. https://doi.org/10.4161/cc.10.15.16776

Wolff, H., Vehmas, T., Oksa, P., Rantanen, J., & Vainio, H. (2015). Asbestos, asbestosis, and cancer, the Helsinki criteria for diagnosis and attribution 2014: recommandations. *Scandinavian journal of work, environment & health*, *41*(1), 5–15. https://doi.org/10.5271/sjweh.3462

Xiao, G.-H., Gallagher, R., Shetler, J., Skele, K., Altomare, D. A., Pestell, R. G., Jhanwar, S., & Testa, J. R. (2005). The NF2 tumor suppressor gene product, Merlin, inhibits cell proliferation and cell cycle progression by repressing Cyclin D1 expression. *Molecular and Cellular Biology*, *25*(6), 2384–2394. https://doi.org/10.1128/mcb.25.6.2384-2394.2005

Yang, Z.Y., Liu. L., Mao, C., Wu, X.Y., Huang, Y.F., Hu, X.F., & Tang, J.L. (2014). Chemotherapy with cetuximab versus chemotherapy alone for chemotherapy-naive advanced non-small cell lung cancer (Review). *Cochrane Database Syst Rev* (11): CD009948. https://doi.org/10.1002/14651858.cd009948.pub2

Yates, D.H., Browne, K., Stidolph, P.N., & Neville, E. (1996). Asbestos-related bilateral diffuse pleural thickening: natural history of radiographic and lung function abnormalities. *American Journal of Respiratory and Critical Care Medicine*. *153*(1): 301–306. https://doi.org/10.1164/ajrccm.153.1.8542134

Zhang, Y., Xiong, Y., & Yarbrough, W. G. (1998). ARF promotes MDM2 degradation and stabilizes p53: ARF-INK4a locus deletion impairs both the Rb and p53 tumor suppression pathways. *Cell*, *92*(6), 725–734. https://doi.org/10.1016/s0092-8674(00)81401-4

Zhang, Y., & Lu, H. (2009). Signaling to p53: ribosomal proteins find their way. *Cancer cell*, *16*(5), 369–377. https://doi.org/10.1016/j.ccr.2009.09.024

Zhao, X., McCutcheon, J. N., Kallakury, B., Chahine, J. J., Pratt, D., Raffeld, M., Chen, Y., Wang, C., & Giaccone, G. (2018). Combined small cell carcinoma of the lung: is it a single entity?. *Journal of thoracic oncology: official publication of the International Association for the Study of Lung Cancer*, *13*(2), 237–245. https://doi.org/10.1016/j.jtho.2017.10.010